GAMMA RAY COMPTON SCATTERING
IN
TRANSITION METALS

by

Andrew J. Rollason

A thesis submitted for the degree of

Doctor of Philosophy of the University of Warwick

Department of Physics
University of Warwick

May 1984

ABSTRACT

The experimental technique of high energy γ-ray inelastic scattering has been investigated in great detail with respect to the influence of experimental factors on the Compton profiles of the transition metals Vanadium and Iron. New experimental procedures and analysis methods have yielded highly accurate data which throw doubt on the applicability of Local Density Approximations in the calculation of electron correlation effects in these materials. The concept of electron momentum density is developed as an observable which is particularly sensitive to such valence electron properties.

PREFACE

Since the development of solid-state detector systems in the early 1970's, experimental solid-state physics has progressed at a much accelerated rate. One technique which has only over the last half-dozen years started to show its true potential is that of Compton Scattering. The most important feature of this technqiue is that it measures the electron momentum density distribution of a system rather than the spatial density. Because of this, in a Compton Scattering experiment, the behaviour of the diffuse valence electron density is emphasised with respect to the inner core electrons and important properties of these electrons are readily observable.

The present work is concerned with the development of this technique for a high energy (400 keV) γ-ray system which is readily suited to the study of heavier materials (e.g. transition metals). In the context of this energy regime and for these materials, a rigorous study of the data correction procedures has been necessary and a number of significant new corrections have had to be introduced. The accuracy of the experimental results with these new corrections implemented is sufficient to show some interesting discrepancies with the predictions of contemporary band-structure calculations and throws new light on the problem of modelling electron correlation.

The ideas and terms of common usage are introduced in Chapter 1 with the definition of the Compton Profile and its relation to various types of system (e.g. atoms, molecules, etc). Chapter 2 presents an overview of the formal inelastic scattering theory with an emphasis

on the suitability of the so-called Impulse Approximation for high energy γ-rays. The experimental method and apparatus are described in Chapter 3 while Chapter 4 contains the investigation of the data correction analysis. Measurements and results for the transition metals Vanadium and Iron are presented in Chapters 5 and 6 respectively and it is here that the effects of electron correlation first appear. Chapter 7 tries to convey an overview of important Compton Scattering results, a discussion of the correlation problem and the author's opinion of the developments that can be expected in the near future.

Units

The system of units adopted in this work and in general use in Compton Scattering research is that of 'atomic units' where $|\hbar| = |m| = 1$ and $|c| = 137.036$.

Thus in relation to SI units, we have

1 au momentum $\equiv 1.9929 \times 10^{-24}$ kg m s^{-1}

1 au energy $\equiv 4.3598 \times 10^{-18}$ J

$\equiv 27.212$ eV

and 1 au length $\equiv 5.2918 \times 10^{-11}$ m

A. J. Rollason, 1984

on the suitability of the so-called Impulse Approximation for high energy γ-rays. The experimental method and apparatus are described in Chapter 3 while Chapter 4 contains the investigation of the data correction analysis. Measurements and results for the transition metals Vanadium and Iron are presented in Chapters 5 and 6 respectively and it is here that the effects of electron correlation first appear. Chapter 7 tries to convey an overview of important Compton Scattering results, a discussion of the correlation problem and the author's opinion of the developments that can be expected in the near future.

Units

The system of units adopted in this work and in general use in Compton Scattering research is that of 'atomic units' where $|\hbar| = |m| = 1$ and $|c| = 137.036$.

Thus in relation to SI units, we have

1 au momentum $\equiv 1.9929 \times 10^{-24}$ kg m s^{-1}

1 au energy $\equiv 4.3598 \times 10^{-18}$ J

$\equiv 27.212$ eV

and 1 au length $\equiv 5.2918 \times 10^{-11}$ m

A. J. Rollason, 1984

CONTENTS

ACKNOWLEDGEMENTS

The author wishes to acknowledge the support and encouragement of the following people during the performance of this research:

Dr. M. J. Cooper, Dr. R. S. Holt, Dr. J. R. Schneider, Miss S. Callanan, Mr. I. Bailey and Lesley.

A. J. Rollason, 1984

CHAPTER 1

ELECTRON DISTRIBUTIONS IN MOMENTUM SPACE

1.1. Introduction

In everyday life the world is usually perceived as a distribution of objects at specific locations. However, a description of one's environment completely in terms of the motion of the objects is equally valid and can sometimes be more useful. For example, a description of the position of every molecule of air in a room is meaningless but knowledge of the average speed of those molecules can lead to a determination of the temperature.

Compton scattering is an experimental technique that measures directly the distribution of velocities of electrons in matter. This therefore leads to a desire that the properties of the material be defined as functions of electron momentum rather than position. It must be emphasised that descriptions in either space are complementary and whichever description is applied is chosen only for convenience of use. A definition of the electronic Compton profile is first presented and then discussed with respect to aspects of electron behaviour in momentum space for various systems.

1.2. The Compton Profile

1.2.1. The Electron Momentum Distribution

Under certain conditions (see the discussion of the Impulse Approximation in §2.4) the energy spectrum of inelastically scattered photons can be related to the distribution of electron velocities in the target. If the target electrons are characterised by the momentum distribution

$n(\bar{p}) = \chi^*(\bar{p})\chi(p)$ (where χ is the electron momentum wavefunction per atom) and the required conditions hold, the second differential inelastic scattering cross section is proportional to the projection of this distribution onto the scattering vector, $\underline{K} = K\hat{z}$, i.e. $J(p_z)$ where

$$J(p_z) = \iint n(\bar{p})\, dp_x\, dp_y \qquad 1.1$$

$J(p_z)$ is called the Compton Profile (CP) of the electrons in the atom and represents the density of electrons (per unit momentum) having a component of momentum p_z along the z direction.

1.2.2. Historical Development of Compton Scattering

The discovery of X-rays (Röntgen, 1895) and γ-rays (Villard, 1900) posed some difficult problems for classical physics. Eve (1904) noticed that the γ radiation of a Radium source became very much softer (less penetrating) if it were scattered from a wide range of materials. Experiments by Bragg (1907) and Florance (1910) showed that the cross section did not follow Thomson's excess forward scattering $(1 + \cos^2\theta)$ law (which was usually true for classical, elastic scattering of electromagnetic plane waves - see §2.2), and it was later found (Barkla and White, 1917) to decrease at shorter wavelengths more rapidly than otherwise expected. There was confusion over whether the softening of the scattered radiation represented a new type of fluorescence in the target. Florance's conclusion was that it was due to the cross section preferentially selecting the longer wavelength components of the incident beam emitted by the polychromatic radium source. This conclusion was rejected by Gray (1913) who repeated Florance's work but went further showing that the spectral content of the incident and scattered radiation was different, thus

reasserting the possibility of a fluorescence-type situation. In 1921 Compton's work with crystal-reflected X-rays showed that even monochromatic radiation would undergo the softening interaction and he began to speculate on a mechanism for the generation of this fluorescence. His first approaches, made in a classical theme, considered the emitted radiation from electrons being accelerated forward by the incident wave and he obtained an expression for the change in wavelength depending on angle and the Doppler shift by some characteristic electron velocity. The velocity required to produce the observed shifts however was close to the velocity of light and Compton was finally forced to reject this idea and to experiment with the concepts of the new quantum physics.

After a number of false hypotheses he finally invoked the requirements for conservation of energy and momentum in a collision between a photon and an electron (Compton, 1923) and obtained the result which has served to justify the basis for modern quantum physics, i.e.

$$\Delta\lambda = \frac{2h}{m_o c} \sin^2 \frac{\theta}{2} \qquad 1.2$$

The energy loss of inelastically scattered radiation was thus explained although the reception of such non-classical ideas was reluctant rather than welcoming. Adding fuel to the resistance of the objectors was the observation in every experiment that the proposed "Compton line" was always much broader in energy than could be accounted for by the instrumental resolution or variation of the scattering angle in the apparatus. The first attempt to analyse the line shape in terms of electron motion was made by Jauncey (1924). However, his analysis relied too heavily on the precise position of the electrons in their orbits within a Bohr-Sommerfeld atomic model (semi-classical model) and he found no simple explanation of the broadening. DuMond (1929) finally

explained the effect in a very clear and completely general argument that evoked the Doppler shifting of the radiation from an assembly of electrons with a distribution of velocities. The conservation laws for a photon interaction with a moving electron led to the equation,

$$\Delta\lambda = \frac{2h}{m_0 c} \sin^2 \frac{\theta}{2} + 2(\lambda_1\lambda_2)^{\frac{1}{2}} \frac{p_z}{m_0 c} \sin \frac{\theta}{2} \qquad 1.3$$

where p_z is component of electron momentum in the direction of the scattering vector. DuMond applied his hypothesis to a free electron gas model (see §1.5.2.) of Beryllium and compared the result with his experimental data. The excellent agreement proved the theory and confirmed the correctness of Fermi statistics (on which his model was based) over the classical Maxwell-Boltzmann distribution law.

Experiments by DuMond and Kirkpatrick (1937) with an improved X-ray spectrometer on Helium agreed well with calculations by Hicks (1937) using Hylleraas wave functions and heralded the beginning of theoretical studies of momentum distributions. Due to the inordinately long times required to make a measurement using X-ray systems (the 1937 H,He measurement took several months!) experimental research fell into a decline until the advent of solid-state detectors in the early 1970's (Eisenberger and Reed, 1972). These brought the two-fold advantage of speed and the use of γ-ray sources. Measurements now took only a few days and the higher energies meant that heavier materials could be studied without infringing the a priori conditions for Compton Profile analysis - the Impulse Approximation (§2.4). To date, Compton Profiles of transition metals can be measured in a matter of days to an accuracy of a fraction of one percent of the peak value and comparisons with theory enable stringent tests of the relative merits of different band structure calculations to be made.

1.2.3. Alternative Momentum Representations

There are a number of momentum space quantities that are used to characterise the behaviour of electron systems. Eq. 1.1 defines the Compton profile for a general momentum distribution (EMD) $n(\bar{p})$ and may therefore be employed to exhibit directional differences (momentum anisotropies) for z aligned with different scattering vectors. If the EMD characterises a powder sample or a gas where the directional properties are lost, the distribution is described by an isotropic Compton profile defined as,

$$J(q) = 2\pi \int_q^\infty pn(p)dp \qquad 1.4$$

where n(p) is now the momentum density in any direction. J(q) is the experimentally observed sample of a radial distribution I(p) given by

$$I(p) = 4\pi p^2 n(p) \qquad 1.5$$

and derivable from a measurement by use of the equation

$$I(p) = -2q \frac{d}{dq} J(q)\Big|_{q=p} \qquad 1.6$$

Example of an isotropic Compton profile and the radial distribution function are shown in Figure 1.1 for a Slater-type Hydrogen 1s orbital, $\psi(r) = \pi^{-\frac{1}{2}} \exp(-r)$, normalised to one electron. The Compton profile, obtained as described in §1.3, is then given by

$$J(q) = \frac{8}{3\pi} \frac{1}{(1 + q^2)^3}$$

and the radial distribution is given by

$$I(p) = \frac{32}{\pi} \frac{p^2}{(1 + p^2)^4}$$

1.2.3. Alternative Momentum Representations

There are a number of momentum space quantities that are used to characterise the behaviour of electron systems. Eq. 1.1 defines the Compton profile for a general momentum distribution (EMD) $n(\bar{p})$ and may therefore be employed to exhibit directional differences (momentum anisotropies) for z aligned with different scattering vectors. If the EMD characterises a powder sample or a gas where the directional properties are lost, the distribution is described by an isotropic Compton profile defined as,

$$J(q) = 2\pi \int_q^\infty pn(p)dp \qquad 1.4$$

where n(p) is now the momentum density in any direction. J(q) is the experimentally observed sample of a radial distribution I(p) given by

$$I(p) = 4\pi p^2 n(p) \qquad 1.5$$

and derivable from a measurement by use of the equation

$$I(p) = -2q \frac{d}{dq} J(q)\Big|_{q=p} \qquad 1.6$$

Example of an isotropic Compton profile and the radial distribution function are shown in Figure 1.1 for a Slater-type Hydrogen 1s orbital, $\psi(r) = \pi^{-\frac{1}{2}} \exp(-r)$, normalised to one electron. The Compton profile, obtained as described in §1.3, is then given by

$$J(q) = \frac{8}{3\pi} \frac{1}{(1 + q^2)^3}$$

and the radial distribution is given by

$$I(p) = \frac{32}{\pi} \frac{p^2}{(1 + p^2)^4}$$

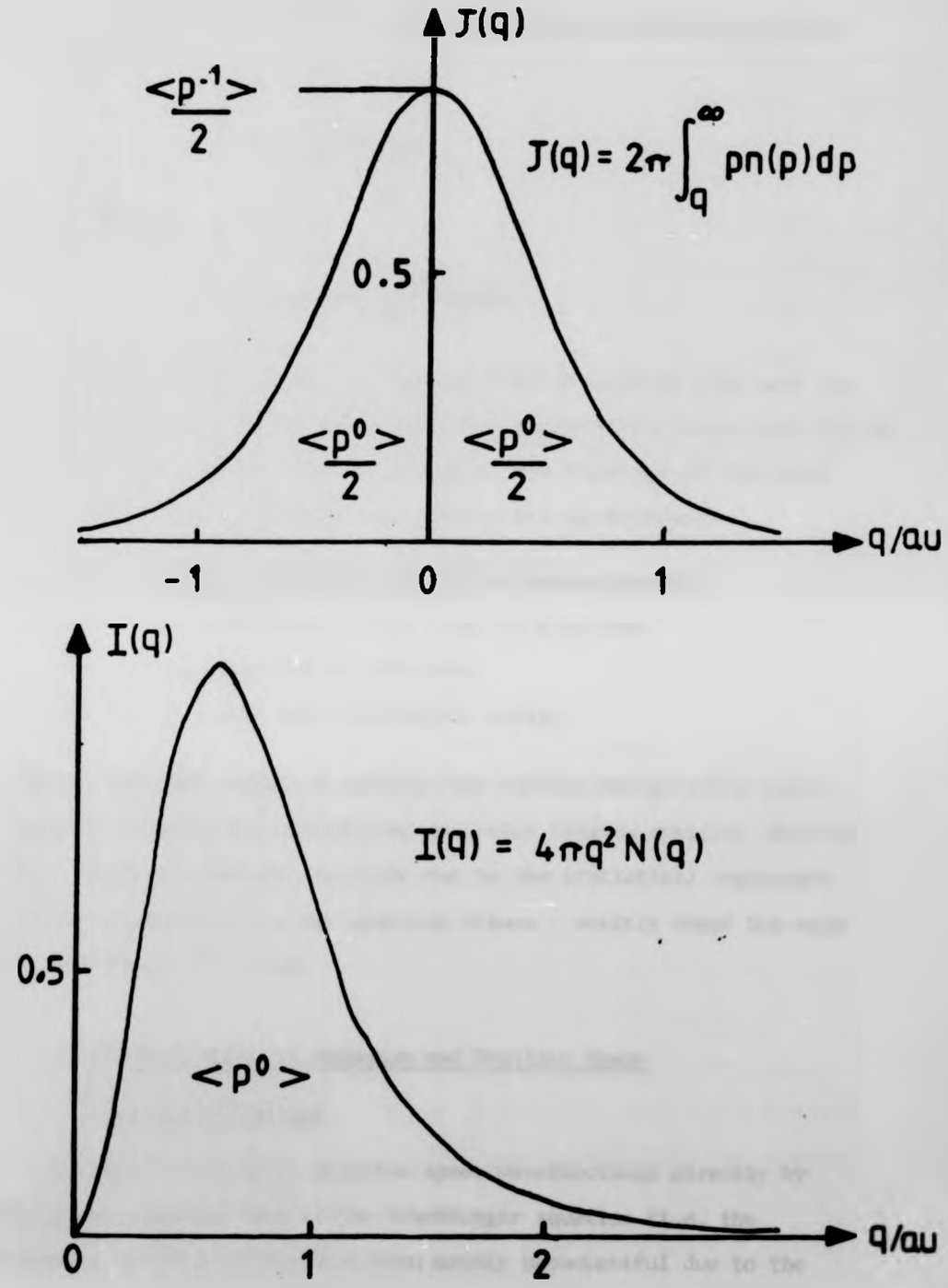

Figure 1.1. The Compton Profile, J(q), and Radial Momentum Distribution, I(q), for Atomic Hydrogen (1s)

The distributions are shown labelled with momentum expectation values $\langle p^n \rangle$ where

$$\langle p^n \rangle = \int_o^\infty p^n I(p) dp$$

or equivalently

$$\langle q^n \rangle = 2(n+1) \int_o^\infty q^n J(q) dq$$

It can be shown, assuming the correct form of n(p) at high and low momentum (see eg., table 1.1), that the expectation values are finite over only the limited range $-2 \leq n \leq 4$. The meanings of the most commonly encountered expectation values are as follows:-

$\langle p^{-1} \rangle$ = 2J(0), the peak value of the Compton profile

$\langle p^o \rangle$ = normalisation of J(p) = no. of electrons

$\langle p^1 \rangle$ = mean momentum of electrons

and $\langle p^2 \rangle$ = 2 x total electron kinetic energy.

Of these, the most useful is probably the kinetic energy value since it provides a means for determining molecular binding energies (Epstein, 1973). There are however, problems due to the statistical inaccuracy of measured profiles at large momentum values - exactly where the main contribution to $\langle p^2 \rangle$ arise.

1.3. Interrelationship of Momentum and Position Space

1.3.1. Dirac Transformation

Attempts to calculate momentum space wavefunctions directly by solving the momentum form of the Schrödinger equation (i.e. the Heisenberg representation) have been mainly unsuccessful due to the appearance of the potential energy term as an integral. For the one-electron hydrogenic atom the equation takes the form,

$$(p^2-2E)\chi(\bar{p}) = \frac{2}{\pi^2}\int \frac{\chi(\bar{p}')}{|\bar{p}-\bar{p}'|^2}\, d\bar{p}' \qquad 1.7$$

which has been solved exactly by Fock (1935). McWeeny and Coulson (1949) investigated solutions for the two electrons in H^- and He and encountered great difficulties in the analysis. The alternative approach (and perhaps the conceptually clearer one) is to first construct the position space wavefunctions and then to transform them to momentum space by applying the Dirac transformation.

For an n-electron system the Dirac transformation is simply a 3n-dimensional Fourier transform,

$$\chi(\bar{p}) = (2\pi)^{-\frac{3n}{2}} \int e^{-i\bar{p}.\bar{r}}\, \psi(\bar{r})\, d\bar{r} \quad , \qquad 1.8$$

where $\psi(\bar{r}) = \psi(\bar{r}_1,\bar{r}_2,\bar{r}_3,\ldots,\bar{r}_n)$ and $\bar{p}.\bar{r} = \bar{p}_1.\bar{r}_1+\bar{p}_2.\bar{r}_2+\ldots+\bar{p}_n.\bar{r}_n$. McWeeny and Coulson found that with electron correlations sufficiently well represented in the wavefunctions, the transformation integrals become extremely difficult but with an independent particle model, transformation of the individual wavefunctions by eq. 1.8 is quite straightforward. In particular, if the many electron wavefunction is represented by the Slater determinant of independent one-electron wavefunctions in position space, the transformation gives a many-electron momentum space wavefunction which is representable as a Slater determinant of the individually transformed basis functions. Indeed it is in the nature of the Dirac-Fourier transform that the form of the transformed function is the same in either space, i.e. considering the electrons for atomic hydrogen,

$$\psi(\bar{r}) = R_{n1}(r)\, Y_{lm}(\theta_r,\phi_r) \quad ,$$

these transform to

$$\chi(\bar{p}) = P_{n1}(p)\, Y_{lm}(\theta_p,\phi_p)$$

and the form of the individual s or p (etc) orbitals is retained in either space. The important difference arises from the radial function transformations, R(r) → P(p) and this will be discussed in detail in §1.3.3.

1.3.2. Interrelated Functions

As is shown in figure 1.2, the Dirac transformation enables pairs of functions in position and momentum space to be linked together. The diagram shows the usual functions encountered in X-ray diffraction (charge density measurements) in the top hemisphere and functions encountered in Compton scattering (momentum density measurements) in the lower hemisphere, with momentum space functions on the left and position space functions on the right. Projection back into the plane of the diagram corresponds to sampling a plane through the corresponding 3-dimensional function.

The four functions $\rho(\bar{r})$, $n(\bar{p})$, $B(\bar{t})$, $F(\bar{s})$ are related to the elements of the charge and momentum density matrices γ and $\hat{\gamma}$ as follows (Be nesch and Smith, 1973).

Charge density, $\rho(\bar{r}) = \gamma(\bar{r}|\bar{r}) \equiv \psi^*(\bar{r})\psi(\bar{r})$

Reciprocal form factor, $B(\bar{t}) = \int \gamma(\bar{r}|\bar{r}+\bar{t})d\bar{r} \equiv \int \psi^*(\bar{r}+\bar{t})\,\psi(\bar{r})d\bar{r}$

and

Momentum Density, $n(\bar{p}) = \hat{\gamma}\,(\bar{p}|\bar{p}) \equiv \chi^*(\bar{p})\chi(\bar{p})$

Form factor, $F(\bar{s}) = \int \hat{\gamma}(\bar{p}|\bar{p}+\bar{s})d\bar{p} \equiv \int \chi^*(\bar{p}+\bar{s})\chi(\bar{p})d\bar{p}$

The two density functions need no explaining but their relationship will be investigated in some detail in §1.3.3. since it is the behaviour of $n(\bar{p})$ that makes Compton scattering a useful technique. The form factor $F(\bar{s})$ derived from diffraction experiments is defined in eq. 2.6. as the

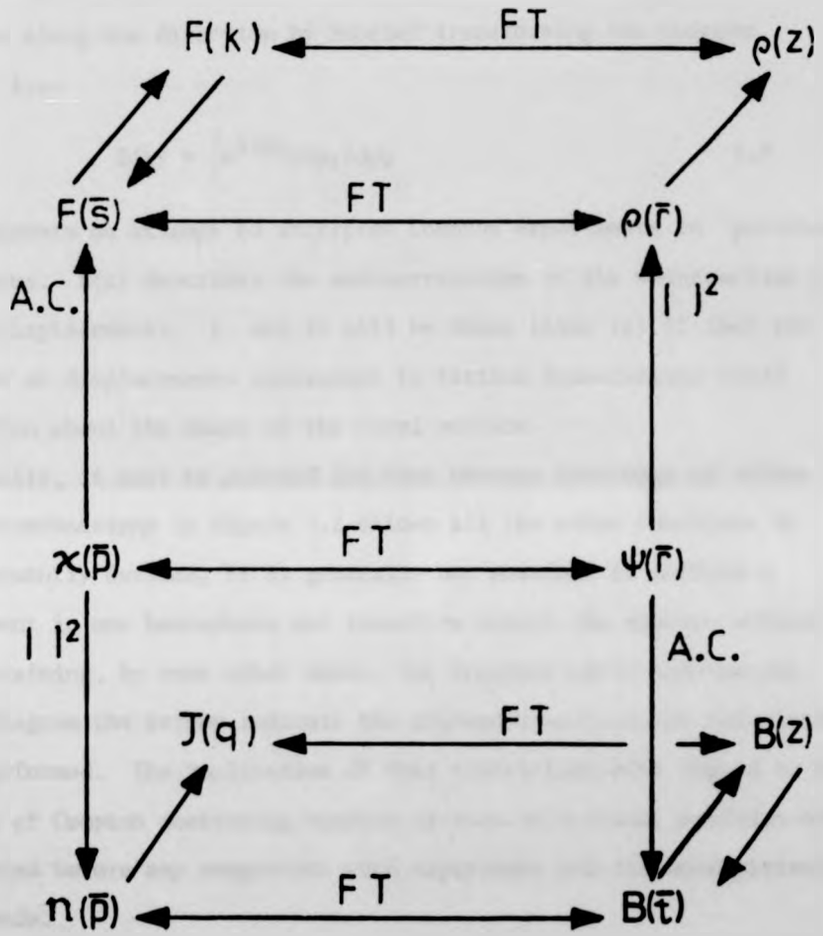

FT → Fourier transform

A.C. → Autocorrelation

Projection into diagram → Sampling in a plane

Figure 1.2. The Fourier Relationships of Common Momentum and Position Space Functions and Observables (see table 1.1.)

Fourier transform of the charge density. The function called the reciprocal form factor, $B(\bar{t})$, also commonly known as the B-function is rapidly gaining importance in Compton scattering. It can be evaluated along one direction by Fourier transforming the Compton profile, i.e.

$$B(z) = \int e^{izp_z} J(p_z) dp_z \qquad 1.9$$

and represents an attempt to interpret Compton experiments in position space terms. B(z) describes the autocorrelation of the wavefunction at varying displacements, z, and it will be shown later (§1.5) that its behaviour at displacements equivalent to lattice translations yield information about the shape of the Fermi surface.

Finally, it must be pointed out that whereas knowledge of either of the wavefunctions in figure 1.2 allows all the other functions to be subsequently derived, it is generally not possible to perform a measurement in one hemisphere and transform across the equator without first obtaining, by some other means, the required phase information. In the diagram the arrows indicate the allowed directions for calculations to be performed. The implication of this restriction with regard to the analysis of Compton scattering results is that theoretical profiles must be produced before any comparison with experiment and its interpretation can be made.

1.3.3. Complementarity of Representations

The importance of the momentum distribution description is that it emphasises the behaviour of electrons different to those emphasised in a position space description. Because of the nature of the Dirac-Fourier transform, functions which are strongly localised in one space become diffuse in the other. Consideration of Gaussian functions enables the properties of the transform to be studied with ease since the transform

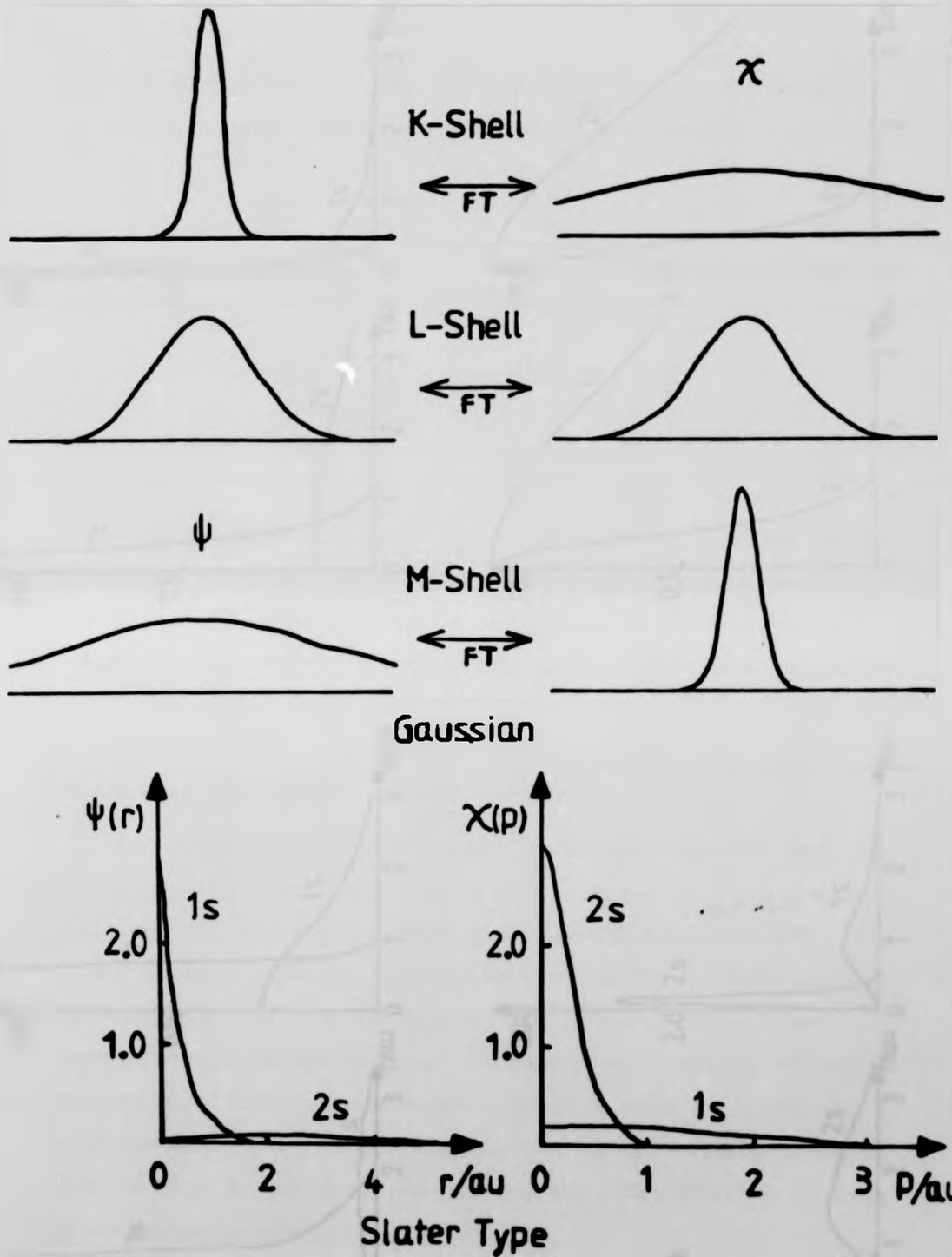

Figure 1.3a Position - Momentum Space Transformations of Simple Analytic Atomic Wavefunctions

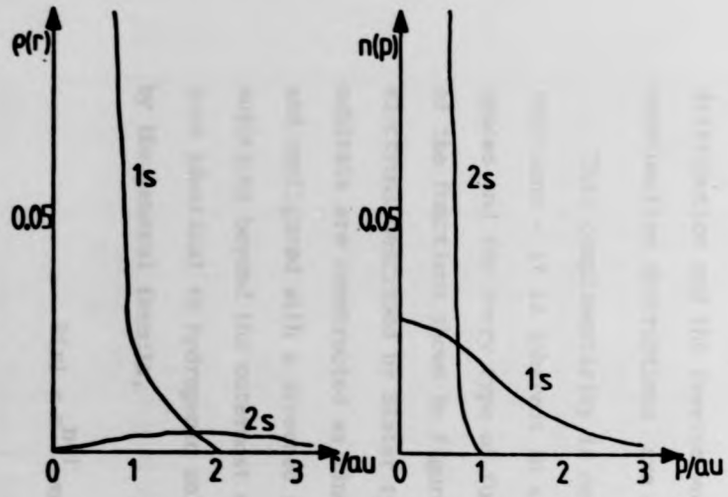

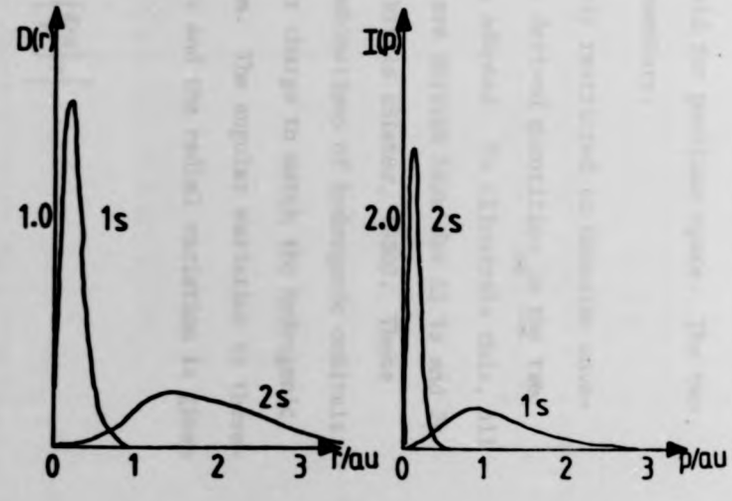

Figure 1.3b Corresponding p - r Isotropic Density Functions

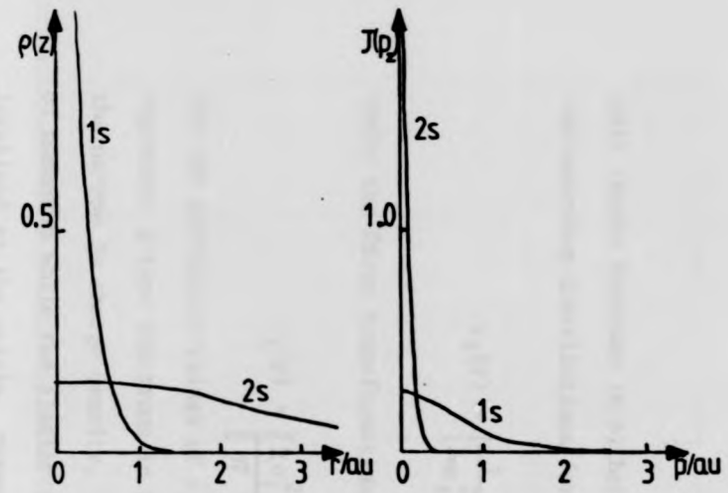

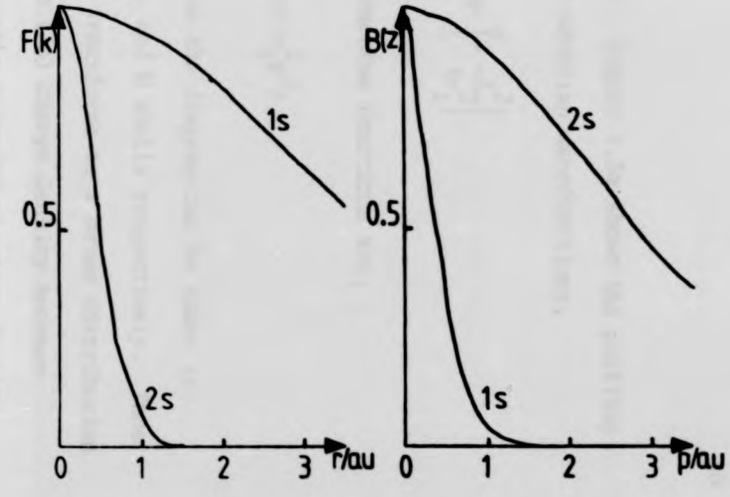

Figure 1.3c Corresponding p - r Directional Density Functions

pair remain Gaussian in either space. Figure 1.3a shows the position and momentum distributions for three Gaussian wavefunctions,

$$\psi_i(r) = \left(\frac{1}{2\pi\sigma_i^2}\right)^{1/4} \exp\left(-\frac{r^2}{4\sigma_i^2}\right)$$

Under the Dirac transformation the momentum functions are,

$$\chi_i(p) = \left(\frac{2\sigma_i^2}{\pi}\right)^{1/4} \exp(-\sigma_i^2 p^2)$$

For the particular values of σ_i chosen the diagram can be taken to represent s-type electrons in the K,L and M shells respectively. Thus the narrow 1s charge density, $|\psi_1|^2$, transforms to a broad distribution of momentum while the flatter valence (3s) charge density becomes localised at the origin. Summation over the occupied electron density would therefore lead to the valence electrons described by an exaggerated peak around the origin of momentum space surmounting a low core electron distribution and the reverse would hold for position space. The two wavefunction descriptions are complementary.

This complementarity is not merely restricted to Gaussian wavefunctions - it is inherent in all the derived quantities in the two spaces and for every type of function adopted. To illustrate this, all of the functions shown in figure 1.2 are derived here for Li 1s and 2s electrons described by Slater type orbitals (Slater, 1930). These orbitals are constructed as linear combinations of hydrogenic orbitals and configured with a screened nuclear charge to match the hydrogenic solutions beyond the outermost maximum. The angular variation is therefore identical to hydrogenic solutions and the radial variation is given by the general formula,

$$R(r) = r^{n-1} \exp\left|-\left(\frac{Z-s}{n}\right)r\right|$$

Function	$1s^2$	$2s^1$
γ_n	2.70	0.65
$\psi(r)$	$\sqrt{\frac{\gamma_1^3}{\pi}}\exp(-\gamma_1 r)$	$\sqrt{\frac{\gamma_2^5}{3\pi}}\, r\, \exp(-\gamma_2 r)$
$\chi(p)$	$\sqrt{\frac{8\gamma_1^5}{\pi^2}}\frac{1}{(\gamma_1^2 + p^2)^2}$	$\sqrt{\frac{8\gamma_2^5}{3\pi^2}}\frac{3\gamma_2^2 - p^2}{(\gamma_2^2 + p^2)^3}$
$\rho(r)$	$\frac{\gamma_1^3}{\pi}\exp(-2\gamma_1 r)$	$\frac{\gamma_2^5 r^2}{3\pi}\exp(-2\gamma_2 r)$
$n(p)$	$\frac{8\gamma_1^5}{\pi^2}\frac{1}{(\gamma_1^2 + p^2)^4}$	$\frac{8\gamma_2^5}{3\pi^2}\frac{(3\gamma_2^2 - p^2)^2}{(\gamma_2^2 + p^2)^6}$
$D(r)$	$4\gamma_1^3 r^2 \exp(-2\gamma_1 r)$	$\frac{4\gamma_2^5}{3} r^4 \exp(-2\gamma_2 r)$
$I(p)$	$\frac{32\gamma_1^5}{\pi}\frac{p^2}{(\gamma_1^2 + p^2)^4}$	$\frac{32\gamma_2^5}{3\pi}\frac{p^2(3\gamma_2^2 - p^2)^2}{(\gamma_2^2 + p^2)^6}$
$\rho'(z)$	$\gamma_1^2\left(z + \frac{1}{2\gamma_1}\right)\exp(-2\gamma_1 z)$	$\frac{2\gamma_2^5}{3}\left(\frac{z^3}{2\gamma_2} + \frac{3z^2}{(2\gamma_2)^2} + \frac{6z}{(2\gamma_2)^3} + \frac{6}{(2\gamma_2)^4}\right)\exp(-2\gamma_2 z)$
$J(q)$	$\frac{8\gamma_1^5}{3\pi}\frac{1}{(\gamma_1^2 + q^2)^3}$	$\frac{8\gamma_2^5}{9\pi}\frac{(5q^4 - 20\gamma_2^2 q^2 + 23\gamma_2^4)}{5(\gamma_2^2 + q^2)^5}$
$F(k)$	$16\gamma_1^4\frac{1}{(4\gamma_1^2 + k^2)}$	$64\gamma_2^6\frac{(4\gamma_2^2 - k^2)}{(4\gamma_2^2 + k^2)^2}$
$B(z)$	$\frac{\exp(-\gamma_1 z)}{6}(6 + 3\gamma_1 z + 2\gamma_1^2 z^2)$	$\exp(-\gamma_2 z)\, P_4(z)$

Table 1.1. Momentum Space - Position Space Function Pairs for Li 1s and 2s Slater Type Orbitals (Slater, J.C. : Phys.Rev. 16, 57, 1930)

where Z is the nuclear charge and s the shielding constant chosen according to Slater's semi-empirical rules. The orbitals have no nodes (unlike the hydrogenic solutions) and their simpler functional form enables analytic expressions for the required quantities to be easily derived. These are listed in Table 1.1 and the quantities are plotted in figures 1.3b and c as corresponding position/momentum space pairs. In all cases the relative emphasis of the 1s and 2s functions is reversed between the two representations.

Of particular interest are the functions J(q) and F(k) which are the measured quantities in Compton and diffraction (F^2) experiments respectively. In the charge density measurement the 2s contribution is completely submerged beneath the intensity scattered from the 1s electrons while in the Compton measurement the 1s profile is relegated to the level of a low background supporting the 2s profile. Since core electrons play very little role in bonding, remaining virtually unchanged between the free atom and the solid, it is clear that for the study of solid state effects the Compton technique is to be preferred. In the following sections the variation of the valence electron momentum distribution for atoms in different environments is discussed.

1.4. Electron Momentum Distributions for Simple Systems

1.4.1. Free Atoms

The discussion of §1.3 was restricted to the various momentum space properties of single electron wavefunctions to illustrate the complementary emphasis of representation in the two spaces brought about by the Dirac-Fourier transformation. The two Slater-type-orbital wavefunctions describing the 1s and 2s Li electrons in §1.3.3. were treated as if they were completely independent of one another

(apart from the average Coulomb screening effect included in the orbitals' exponents). In an atomic assembly of electrons this assumption is not entirely valid but serves to provide a first approximation to the atomic momentum distribution. The Compton profile for a single free atom of Ca ($1s^2 2s^2 2p^6 3s^2 3p^6 4s^2$) is shown in figure 1.4. This was calculated numerically in the non-relativisitic Hartree-Fock approximation (Biggs et al, 1975) which preserves the independence of the electrons. The separation of the total electron density into one-electron wavefunction is readily apparent as contributions to the profile from the separate K, L, M and N shells. Clearly the valence electron contributions are very prominent in this representation while the K and L shell core electrons are reduced to a flat background contribution over the range displayed.

While it is not possible to measure the profile of a single atom, the intuitive application of free atoms calculations is to the measurement of inert gases. The interesting aspect of such studies is the determination of the accuracy with which the free atom electron density can be approximated by the use of one-electron wavefunctions and the corresponding complexity of solving the Schrödinger equation for many electron systems. The problems encountered with free atoms also occur in an even more complicated form for molecules and solids.

He, N_2, Ar and Kr have been measured by Eisenberger and Reed (1972) using 159 KeV γ radiation from ^{123m}Te and compared with non-relativisitic analytic Hartree-Fock profiles calculated by Clementi (1965). Discrepancies in the profile height around q=0 have been attributed to electron correlation effects (Eisenberger et al, 1972), which are not included in the analytic Clementi wavefunctions.

Much work has been done on these calculations of many electron effects in one-electron representations of atomic distributions. The earliest calculations represented atomic electrons as individual hydro-

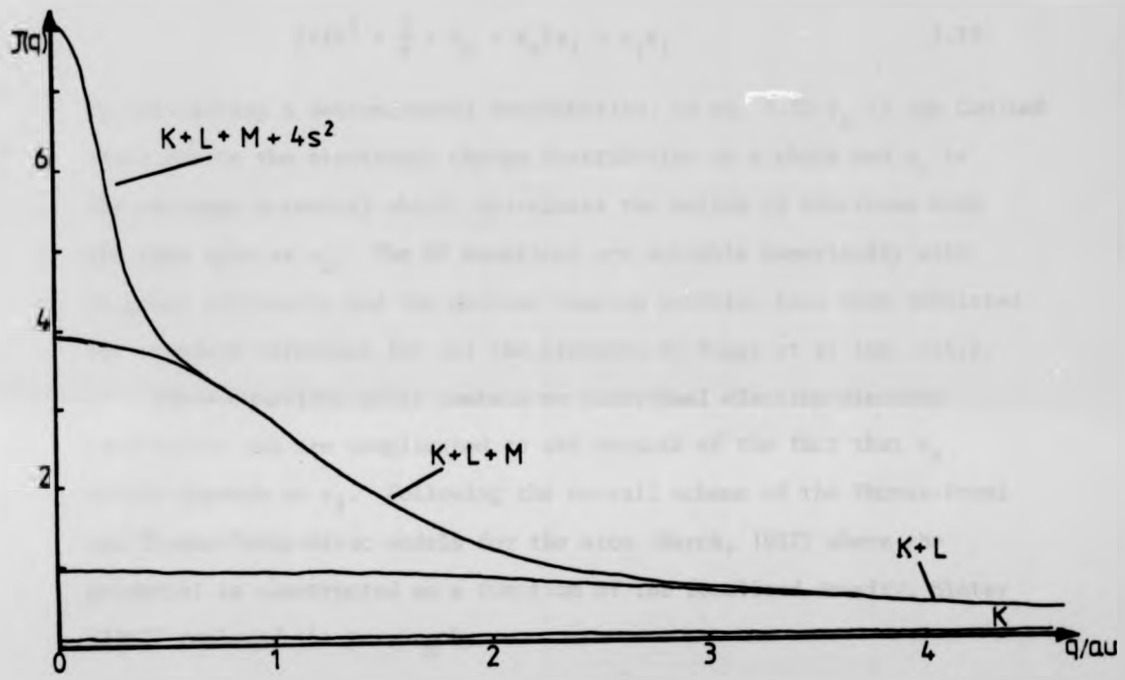

Figure 1.4. Free Atom Compton Profile of Ca (Z = 20) Showing the Contributions from Separate Shells

genic or Slater type orbitals which exhibit no electron correlation effects at all. In this case the many electron wavefunction is simply a product of the orbital basis functions. Electron spin and exchange effects were introduced by Slater with the Hartree-Fock (HF) equations

$$[-\tfrac{1}{2}\nabla^2 - \frac{Z}{r} + V_C + V_X]\phi_i = \varepsilon_i\phi_i \qquad 1.10$$

by considering a determinantal wavefunction. In eq. 1.10 V_C is the Coulomb field due to the electronic charge distribution as a whole and V_X is the exchange potential which correlates the motion of electrons with the same spin as ϕ_i. The HF equations are solvable numerically with no great difficulty and the derived Compton profiles have been tabulated for standard reference for all the elements by Biggs et al (op. cit.).

These equations still contain no individual electron-electron correlation and are complicated to use because of the fact that V_X itself depends on ϕ_i. Following the overall scheme of the Thomas-Fermi and Thomas-Fermi-Dirac models for the atom (March, 1957) where the potential is constructed as a function of the localised density, Slater (1951) replaced the term V_X by

$$V_X \rightarrow V_{X\alpha} = \alpha\, 2\left(\frac{3\rho(r)}{\pi}\right)^{1/3} \qquad 1.11$$

from consideration of an interacting electron gas. The parameter α has been investigated by various researchers and found to lie between $^2/_3$ and 1. This form represents the first introduction of the concept of density functional theory (Schlüter and Sham, 1982) to the solution of the many electron problem. Local density approximations for both exchange and correlation potentials are presently being employed in many calculations for all types of electronic systems.

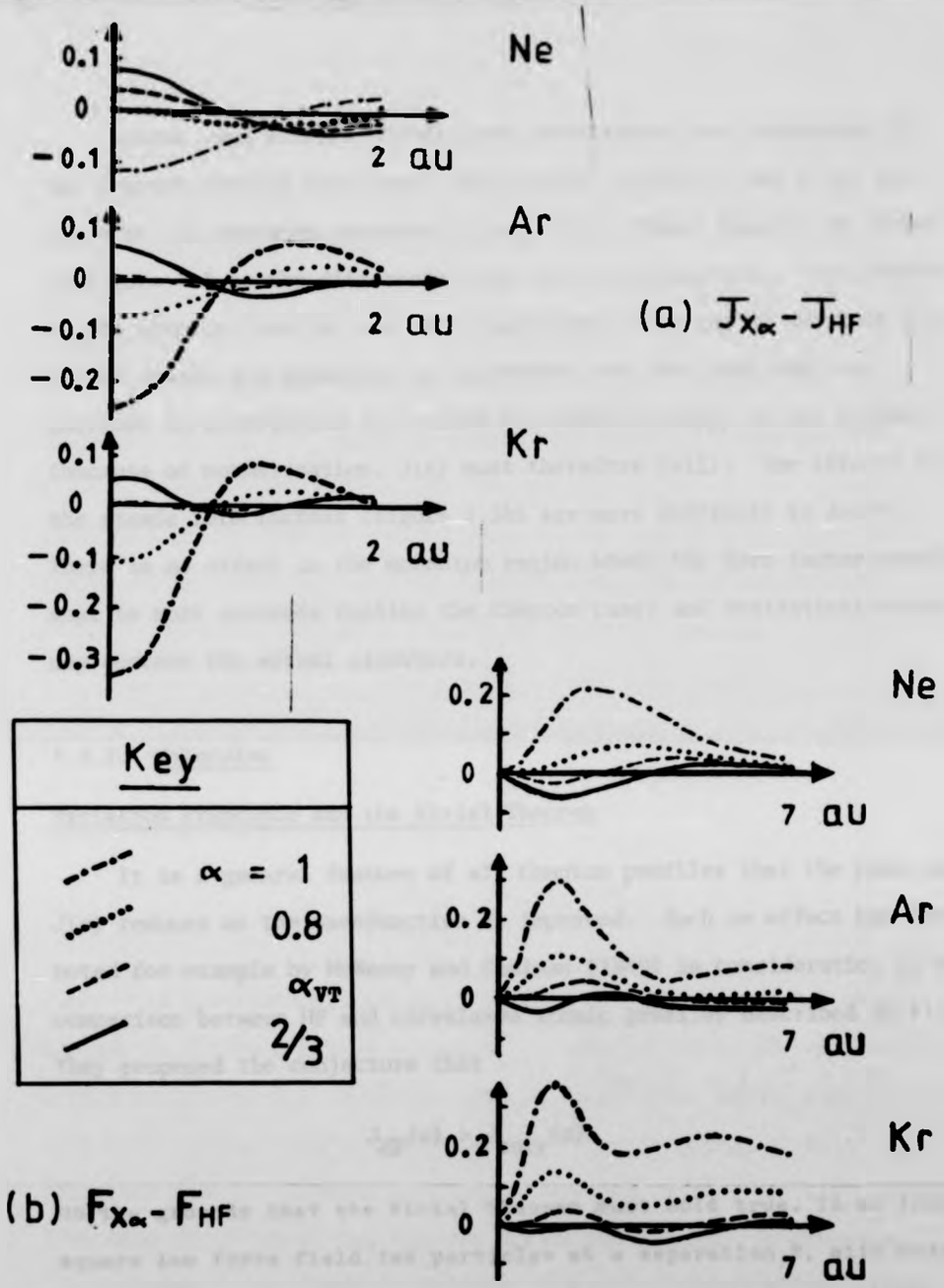

Figure 1.5. Investigation of Exchange-Correlation Effects in (a) the Compton Profile (b) Form Factor of the Noble Gases Ne, Ar and Kr. The differences represent a comparison between an X_α calculation for various α and the Hartree-Fock (HF) result made by Euwema and Surratt (1974). The value of α required by the Virial Theorem (α_{VT}) was found to be 0.72997 by Schwartz, K. (Phys. Rev. B, 5, 2466, 1972)

Euwema and Surratt (1974) have investigated the dependence of the Compton profile and atomic form factors of Ne, Ar and Kr on the value of the exchange parameter in eq. 1.11. Their results are shown in figure 1.5 as the difference from the HF calculations. The effects on the Compton profiles are very significant, varying by about 6% J(o) at the origin and generally in accordance with the idea that an increase in correlation (α) raises the kinetic energy of the systems (because of normalisation, J(o) must therefore fall). The effects in the atomic form factors (figure 1.5b) are more difficult to detect. There is no effect in the momentum region where the form factor measurement is most accurate (unlike the Compton case) and statistical errors may obscure the effect elsewhere.

1.4.2. Molecules

Variation Principle and the Virial Theorem

It is a general feature of all Compton profiles that the peak value J(o) reduces as the wavefunction is improved. Such an effect has been noted for example by McWeeny and Coulson (1949) in consideration of the comparison between HF and correlated atomic profiles described in §1.3. They proposed the conjecture that

$$J_{HF}(o) > J_{corr}(o)$$

on the grounds that the Virial Theorem must hold true. In an inverse square law force field two particles at a separation R, with potential, kinetic and total energy of V, T and E respectively must satisfy

$$2T + V + R\left(\frac{\partial E}{\partial R}\right) = 0$$

and at equilibrium $\frac{\partial E}{\partial R} = 0$ and this reduces to

$$2T + V = 0, \text{ the Virial Theorem} \qquad 1.12$$

The inclusion of correlation terms in the many-electron wavefunction describing a system of electrons and the minimisation of the total energy with respect to the correlation parameters (the Variation Principle) maintains the validity of the Virial Theorem (Feinberg and Ruedenberg, 1970). Since the total energy is lowered by this procedure, by the Virial Theorem the kinetic energy must increase. The correspondence of T to the momentum expectation value $\langle p^2 \rangle$ was described in §1.2.3, where it was stated that the main contributions to $\langle p^2 \rangle$ are contained in the high momentum region of the Compton profile. This region of the profile must therefore increase and, by normalisation ($\langle p^0 \rangle$ = constant), the peak value must therefore reduce.

Consideration of the Virial Theorem can also yield some insight into the effects of bonding on molecular Compton profiles. Finkelstein and Horowitz (1928) constructed a one-electron molecular orbital for H_2^+ by the LCAO method in the form

$$\psi = \frac{(\xi^3/\pi)^{\frac{1}{2}} e^{-\xi r_{A+}} \; (\xi^3/\pi)^{\frac{1}{2}} e^{-\xi r_B}}{\sqrt{2(1+s)}} \qquad 1.13$$

where ξ is a variational parameter and s the overlap integral between the atomic s-type orbitals ϕ_A and ϕ_B. Application of the variation method to determine ξ yields an orbital contraction around each atomic site (see figures 1.6a and b); i.e. for the free hydrogen atom ξ has the value 1 while the molecule ion H_2^+ has the value $\xi = 1.2387$. (The free atom obeys the Virial Theorem but as the molecule is formed and the interatomic separation decreased towards equilibrium the virial nature is temporarily lost until reestablished by the variation of ξ).

Feinberg and Ruedenberg gave a description of bond formation with the emphasis on the role of kinetic energy rather than potential energy. Both kinetic energy and potential energy increase in the bond region as electron density is redistributed there. This destroys the virial nature

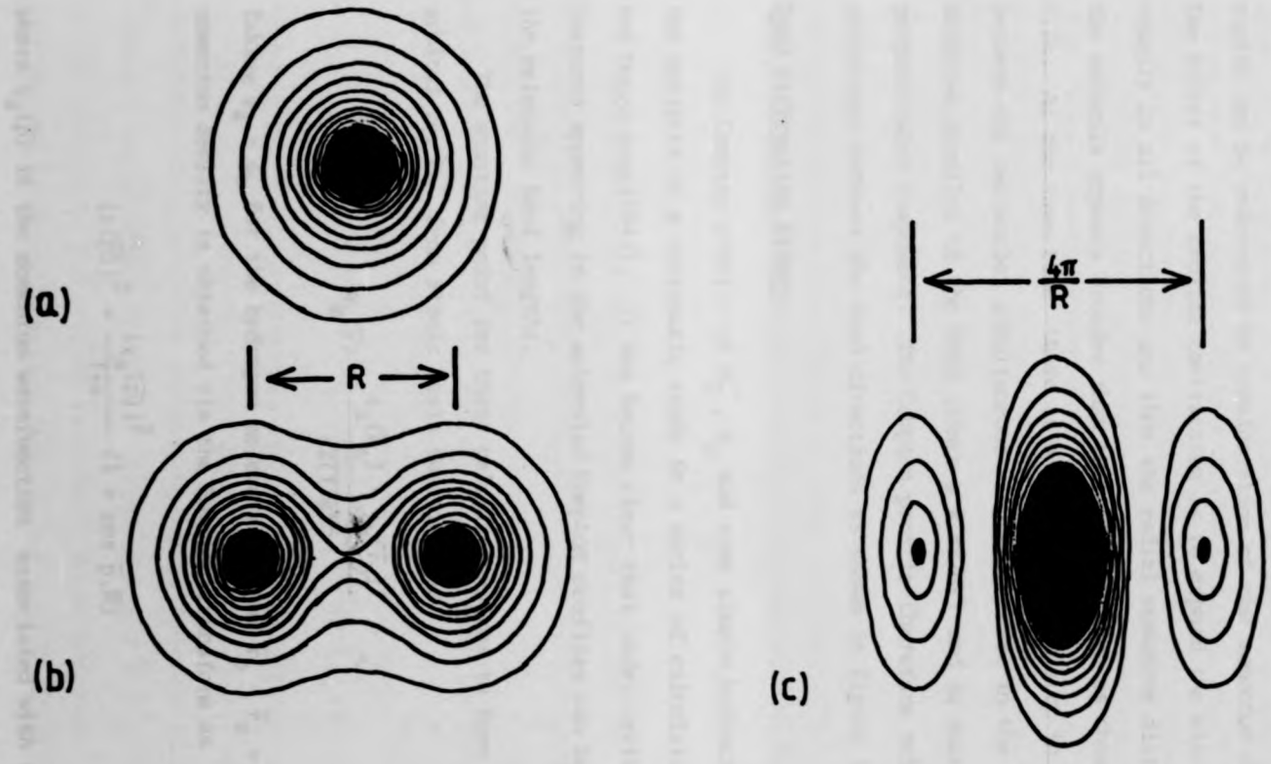

Figure 1.6. Electron Density Distribution for H_2^+ Molecular Orbitals: (a) 1s STO Charge Density (b) H_2^+ Charge Density Showing Contraction of Radial Exponent and (c) H_2^+ Momentum Density Distribution Showing the "Diffraction Effect"

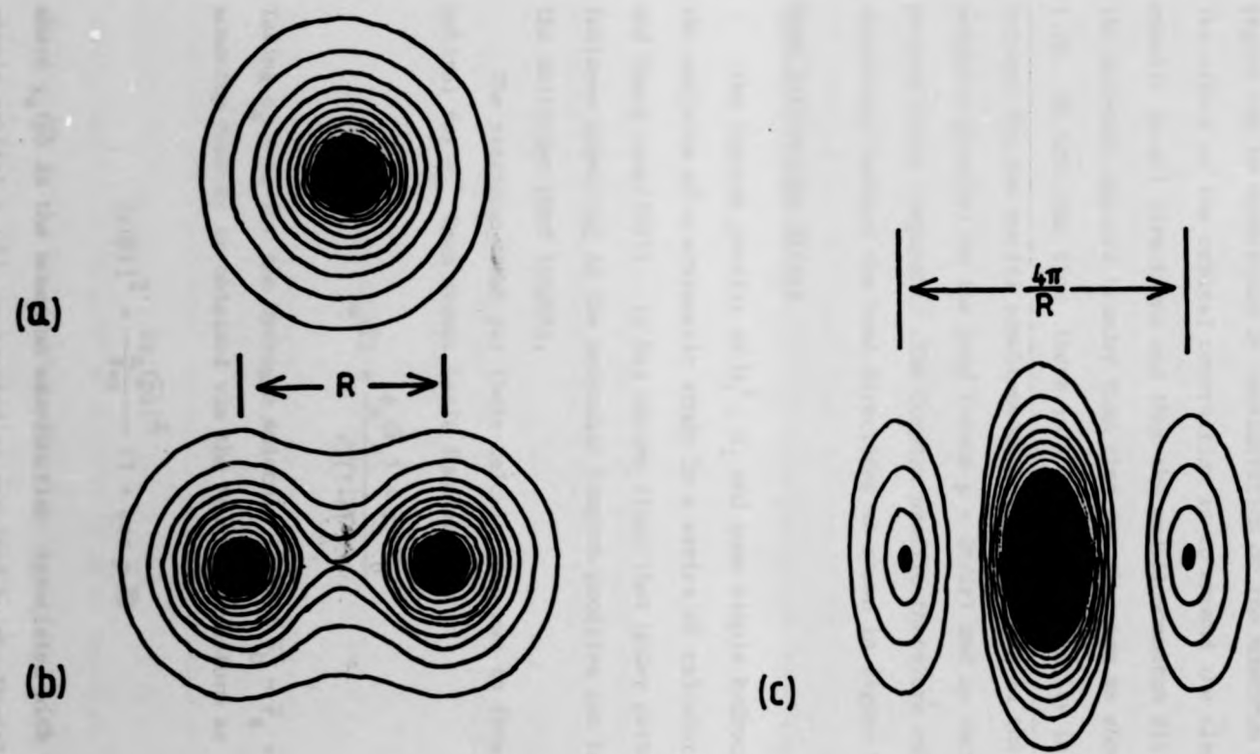

Figure 1.6. Electron Density Distribution for H_2^+ Molecular Orbital: (a) 1s STO Charge Density (b) H_2^+ Charge Density Showing Contraction of Radial Exponent and (c) H_2^+ Momentum Density Distribution Showing the "Diffraction Effect"

of the wavefunction which is reestablished as the charge density around each nuclear site contracts, again increasing the kinetic energy but reducing the potential energy. The movement of electrons into the bond region can be understood by consideration of the momentum distribution. The effect of the orbital contraction is to expand the electron momentum equally in all directions and thus the radial momentum distribution for the molecule appears broader than that for the atom as shown in figure 1.7a. At the same time there is a build up of density in the region between the two nuclei simultaneous with a decrease in the component of momentum parallel to the bond (since $p \propto d\Psi/dr$) and an increase in the perpendicular component. The Compton profile therefore exhibits an anisotropy between the bond directions as shown in figure 1.7b.

Bond Diffraction Effect

The Compton profile of H_2^+, H_2 and some simple hydrocarbons were the subjects of a systematic study in a series of calculations by Coulson and Dunca nson (1941). It has become clear that under certain restrictions features appearing in the molecular Compton profiles can be related to the molecular bond lengths.

The starting point for these calculations was to form a molecular orbital for H_2^+ from atomic basis functions as

$$\Psi_m(\bar{r}) = \frac{\phi_a(\bar{r}_a) + \phi_b(\bar{r}_b)}{\sqrt{2(1+s)}}$$

Taking $\phi_a = \phi_b$ for the hydrogen molecule ion and $\bar{r}_b - \bar{r}_a = \bar{R}$, the momentum density is obtained via the Fourier transform as

$$|\chi(\bar{p})|^2 = \frac{|\chi_a(\bar{p})|^2}{1+s} (1 + \cos \bar{p}.\bar{R}) \qquad 1.14$$

where $\chi_a(\bar{p})$ is the momentum wavefunction associated with the single atomic orbital $\phi_a(\bar{r}_a)$, contracted as required by the Virial Theorem

(figure 1.6). Clearly the momentum density of eq. 1.14 consists of an atomic, isotropic part and an interference part which has come to be known as the diffraction term. (Consideration of an anti-bonding molecular orbital would lead to a similar momentum density with the diffraction term of reversed sign). In general, the molecules would have a random distribution in a gas sample and the effective momentum density would be spherically symmetric. Averaging eq. 1.14 over all orientations of $\overline{R}$ with respect to $\overline{p}$ (along the scattering vector) we get,

$$|\chi(p)|^2 = \frac{|\chi_a(p)|^2}{1+s} \quad (1 + \frac{\sin pR}{pR})$$

The radial momentum distribution is shown in figure 1.7a for STO basis functions although the scale is too small for the oscillations of period $\frac{2\pi}{R}$ to be clearly seen. With this isotropic orientation no structure can be seen in the Compton profile.

If the molecular ions can all be aligned in some way, it is possible to measure the directional Compton profile parallel or perpendicular to the bond. When the scattering vector is parallel to the bond the diffraction density oscillations are picked out by the sampling plane and the profile is described by

$$J_{//}(p_z) = J_a(p) \quad (1 + \cos p_z R), \; p = p_z \qquad 1.15$$

where $J_a(p)$ is the isotropic contracted atomic profile. Snyder and Weber (1978) considered the conditions under which these oscillations would be detectable with particular emphasis on the F_2 molecule as a suitable choice. For an intera tomic bond length of $R \sim 2$ Å (e.g. N_2) the period of oscillation in the profile is about 15 au of momentum. Thus the diffraction structure arises a long way out in the profile tails and is unfortunately difficult to detect. The extent of the Compton profile tails can be roughly related to the size of the atoms by utilising the Heisenberg

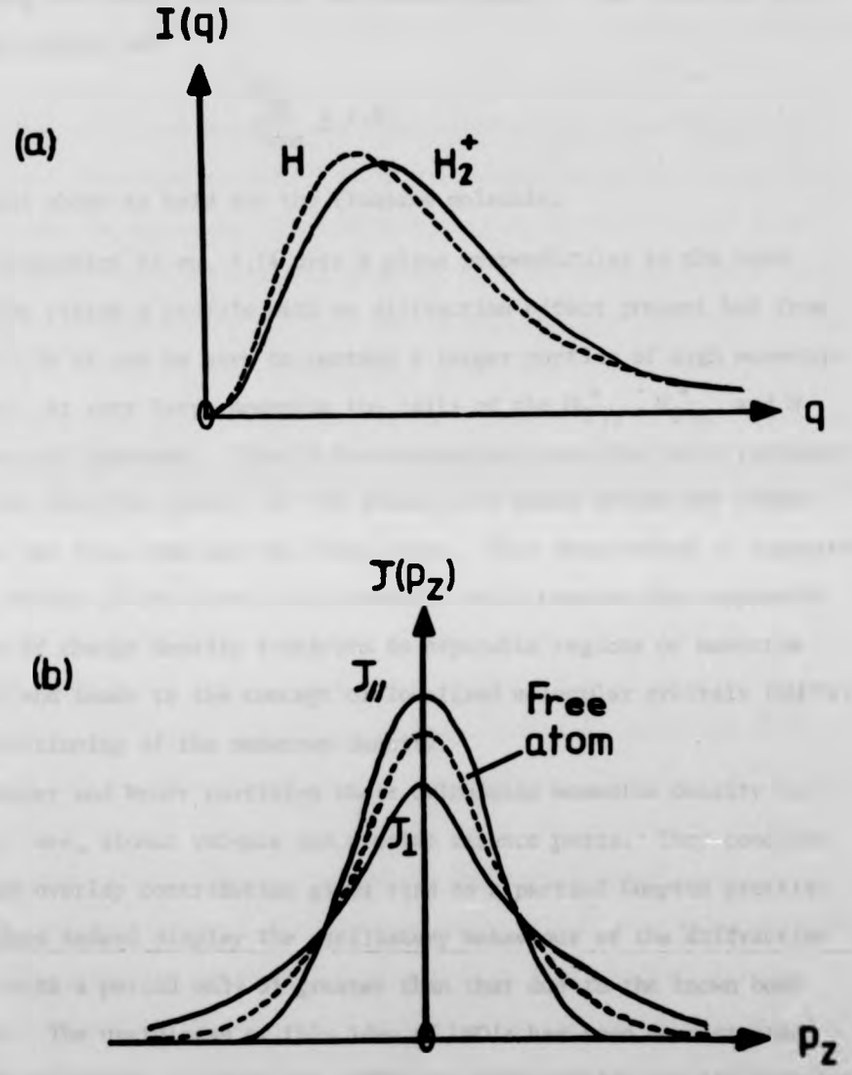

Figure 1.7. Bonding Effects on the Momentum Distribution (a) Increase in Mean Radial Momentum Density on Formation of the H_2^+ Molecule Ion (b) Directional Compton Profile Anisotropy w.r.t. Bond Orientation

relation $\Delta p \Delta x \sim \hbar$. It is therefore possible to predict which molecules would give rise to a detectable diffraction effect in the profile by comparing the atomic size with the bonding length. The criterion proposed by Snyder was

$$\frac{R_{ab}}{r_{rms}} \geq 2.4$$

which was shown to hold for the fluorine molecule.

Integration of eq. 1.14 over a plane perpendicular to the bond direction yields a profile with no diffraction effect present but from figure 1.7b it can be seen to contain a larger portion of high momentum density. At very large momentum the tails of the $H_{2//}^{+}$, $H_{2\perp}^{+}$ and H profiles all converge. This is to be expected since the tails represent the inner electron density of the atomic core which should not change between the free atom and the bound state. This observation is supported by the nature of the Dirac transformation which ensures that separable regions of charge density transform to separable regions of momentum density and leads to the concept of localised molecular orbitals (LMO's) and partitioning of the momentum density.

Snyder and Weber partition their calculated momentum density for F_2 into core, atomic valence and overlap valence parts. They conclude that the overlap contribution gives rise to a partial Compton profile which does indeed display the oscillatory behaviour of the diffraction effect with a period only 5% greater than that due to the known bond lengths. The usefulness of this idea of LMO's has been demonstrated further by Epstein and Lipscomb (1970) who have constructed the momentum distribution of large organic molecules from a series of elementary C-C and C-H bonds.

1.5. Electron Momentum Distributions for Solids

The sensitivity of Compton scattering to valence electron behaviour makes it a particularly suitable technique for investigating the electronic structure of solids. In the solid-state there is the opportunity to measure the anisotropy between momentum distributions along different directions. Such studies demand rigorous examination of the theoretical and experimental approach. Experimental studies of solids only became reliable after the development of penetrating γ-ray sources reduced the problems of absorption and multiple scattering. On the theoretical side, there is a need for highly sophisticated band structure calculations with detailed treatment of electron correlation effects. It is hoped that the experimental work described in this thesis will contribute to the understanding of these areas.

1.5.1. Ionic Crystals

Strongly ionic crystals are the simplest type of solid to be examined by Compton scattering due to the extreme localisation of covalent bonds around the atomic sites. Phillips and Weiss (1968) measured the X-ray profile of LiF and showed that it was reasonably well modelled by Hartree-Fock free ion wavefunctions, i.e. the overlap of charge density on neighbouring sites is negligible. The same is not true however for LiH. As a later measurement showed (Phillips and Weiss, 1969), the valence electron momentum distribution is about 50% broader than that prediction by a superposition of doubly occupied H^- and Li^+ free ion wavefunctions. This could be explained by allowing an overlap between pairs of H^- ions (not the Li^+, see later) which causes charge to be concentrated at these ion sites and thus broadens the momentum profile.

Pattison and Weyrich (1979) have shown that for a strongly ionic solid, Compton scattering measurements are better represented by transforming

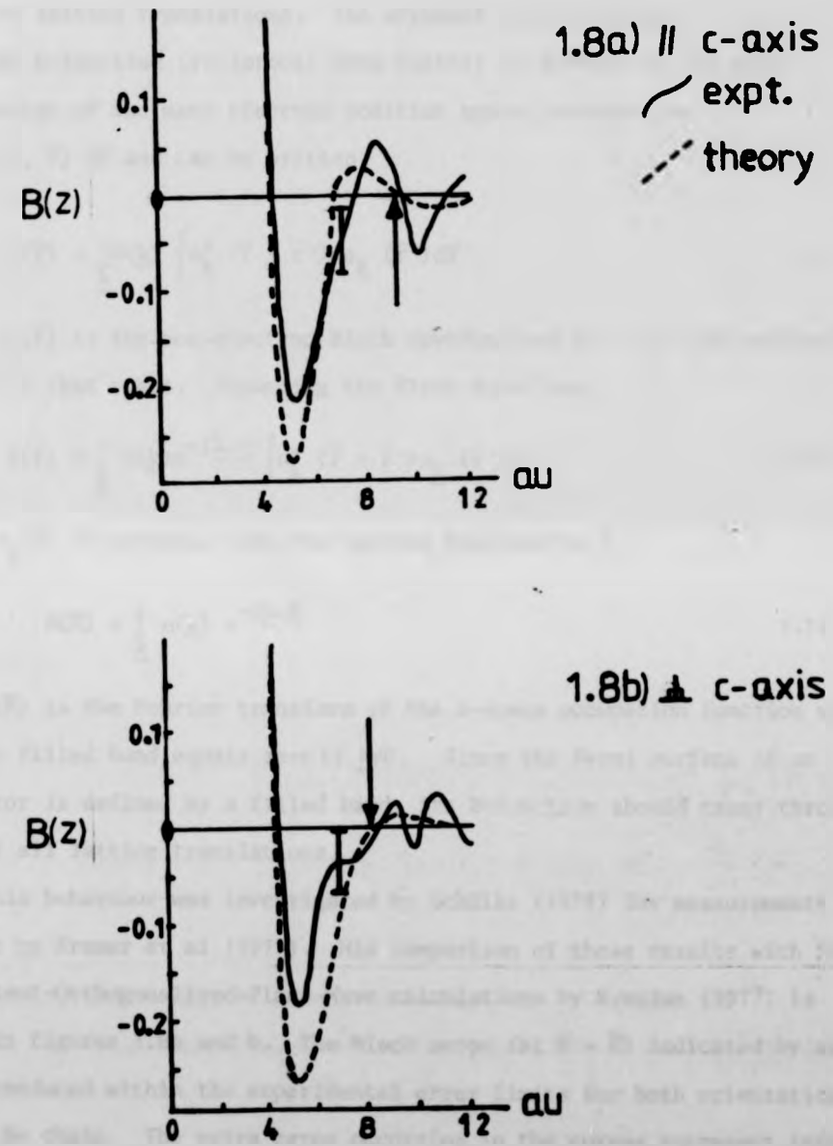

Figure 1.8. B - Functions for the Insulator Se : (a) Parallel and (b) Perpendicular to the Crystal Axis (The arrows indicate the expected positions of the Bloch zeros)

to position space and analysing the B-function (eq. 1.9). They showed that for an insulator the B-function should have zeros at distances equal to lattice translations. The argument is as follows.

The B-function (reciprocal form factor) is defined as the auto-correlation of the many electron position space wavefunction $\int \gamma(\bar{r} + \bar{t}, \bar{r})\, d\bar{r}$ and can be written

$$B(\bar{r}) = \sum_{\underline{k}} n(\underline{k}) \int \psi^*_{\underline{k}} (\bar{r} + \bar{r}') \, \psi_{\underline{k}} (\bar{r}') d\bar{r}' \qquad 1.16$$

where $\psi_{\underline{k}}(\bar{r})$ is the one-electron Bloch wavefunction and $n(\underline{k})$ the occupation number of that state. Expanding the Bloch functions,

$$B(\bar{r}) = \sum_{\underline{k}} n(\underline{k}) e^{-i\underline{k}.\underline{r}} \int u^*_{\underline{k}} (\bar{r} + \bar{r}') u_{\underline{k}} (\bar{r}') d\underline{r}' \qquad 1.17$$

where $u_{\underline{k}}(\bar{r})$ is periodic with the lattice translation $\underline{R}$.

$$\therefore \; B(\bar{R}) = \sum_{\underline{k}} n(\underline{k}) \, e^{-i\underline{k}.\underline{R}} \qquad 1.18$$

Thus $B(\bar{R})$ is the Fourier transform of the k-space occupation function which for any filled band equals zero if $\underline{R} \neq 0$. Since the Fermi surface of an insulator is defined by a filled band, its B-function should cross through zero at all lattice translations.

This behaviour was investigated by Schülke (1978) for measurements on Se made by Kramer et al (1977). His comparison of these results with Self-Consistent-Orthogonalised-Plane-Wave calculations by Krusius (1977) is shown in figures 1.8a and b. The Bloch zeros (at $\bar{r} = \bar{R}$) indicated by arrows are reproduced within the experimental error limits for both orientations of the Se chain. The extra zeros occurring in the curves represent information about the particular form of the Bloch wavefunctions.

The negative excursions of the curves of figure 1.8 may under certain circumstances contain information about antibonding contributions to the

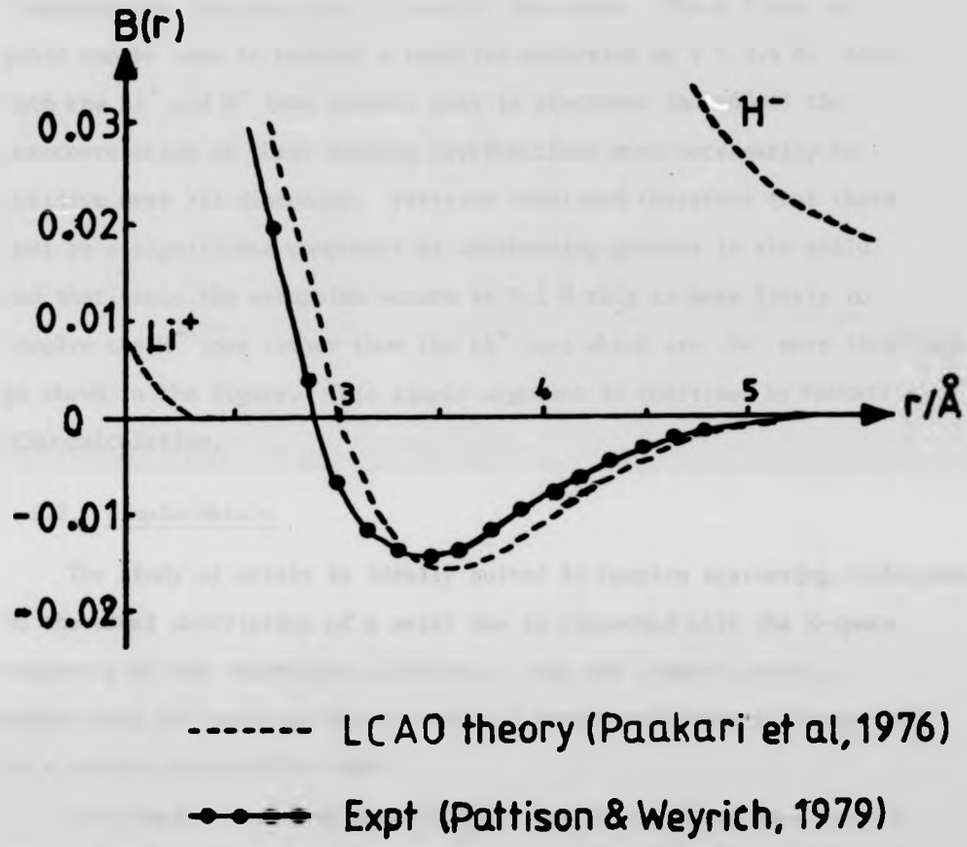

Figure 1.9. B-Function of LiH.(Both curves are damped by the experimental resolution function, $D(r) = \exp\left[-\left(\frac{r}{3.32}\right)^2\right]$)

autocorrelation function (ACF) as suggested by Pattison and Weyrich's investigation of the H^- ion overlap in LiH. Figure 1.9 displays the experimental and theoretical (LCAO, Paakari et al, 1976[108]) $B(\bar{r})$ for LiH alongside the functions for Li^+ and H^- free ions. The ACF for the solid can be seen to undergo a negative excursion at $r \sim 3.5$ Å. Since both the Li^+ and H^- ions possess only 1s electrons (no nodes) the autocorrelation of their bonding wavefunctions must necessarily be positive over all distances. Pattison concluded therefore that there must be a significant component of antibonding present in the solid and that since the excursion occurs at 3.5 Å this is more likely to involve the H^- ions rather than the Li^+ ions which are far more localised as shown in the figure. This simple argument is confirmed by Paakari's LCAO calculation.

1.5.2. Simple Metals

The study of metals is ideally suited to Compton scattering techniques. In the usual description of a metal one is concerned with the K-space behaviour of the conduction electrons. Thus the Compton profile, emphasising the momentum distribution of these conduction electrons, is in a readily discussible form.

The simplest model of a metal describes the electron density as a Hartree-Fock free ion core (unaffected by formation of the solid) and a homogeneous, non-interacting, free-electron gas forming the conduction band. The ground state momentum density can also be described by two distinct components - a broad flat base to the Compton profile due to the core electrons - and an isotropic contribution from the free electron gas defined by,

$$N(p) = \frac{I(p)}{4\pi p_1^2} = \begin{cases} N(0), & p \leq p_F \\ 0, & p > p_F \end{cases}$$

Eq. 1.4 then gives the Compton profile as

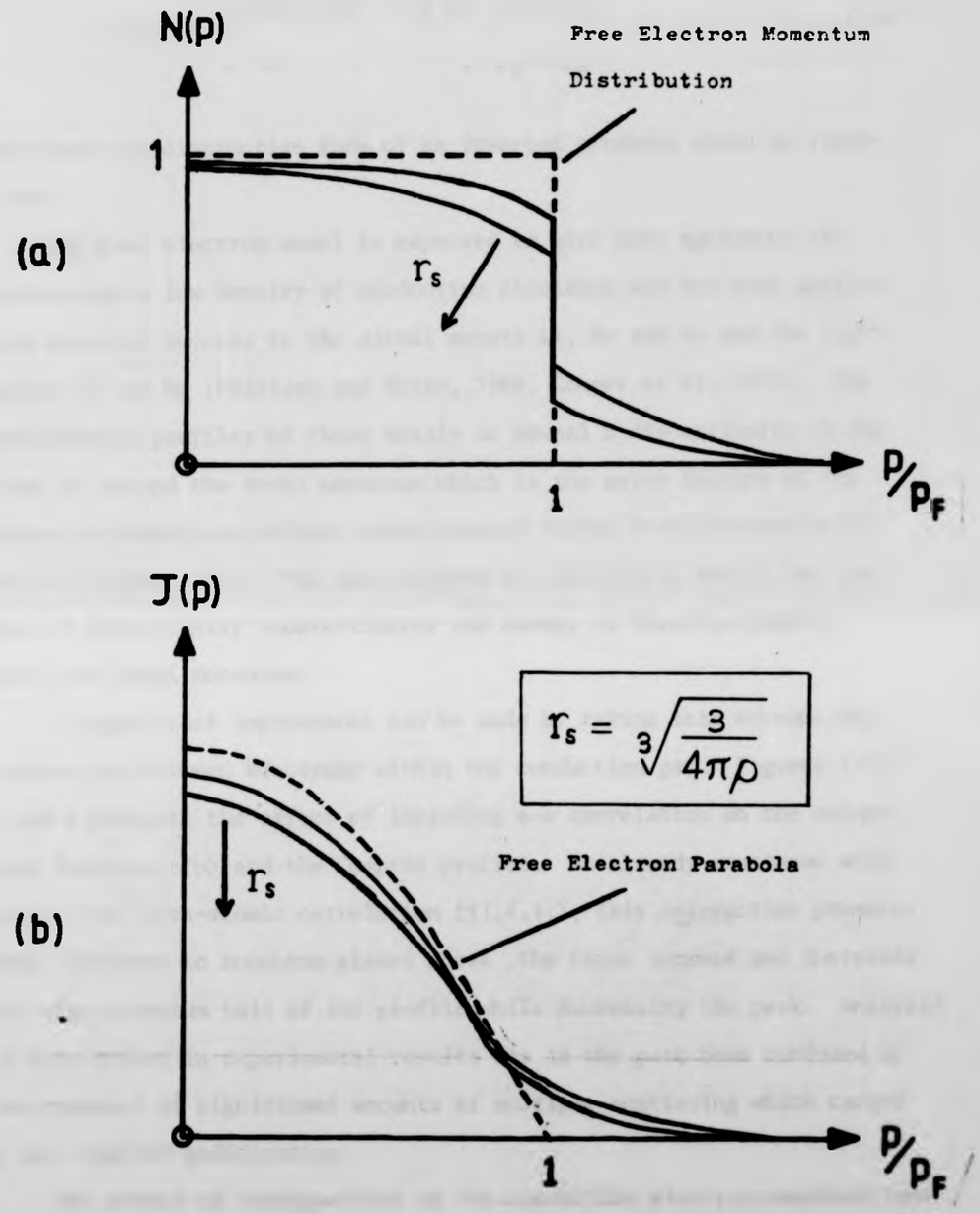

Figure 1.10. Effects of Electron Correlation in a Homogeneous Electron Gas on (a) Momentum Density (b) Compton Profile. The amount of correlation present can be related to the inverse electron density $1/\rho$ via the Wigner radius r_s (after Daniel, E. and Vosko, S.H. : Phys. Rev. 120, 2041, 1960)

$$J(p_z) = \begin{cases} \pi N(0)\ (p_F^2 - p_z^2), & p_z \leq p_F \\ 0 & , \ p_z > p_F \end{cases} \qquad 1.19$$

which has the distinctive form of an inverted parabola shown in figure 1.10b.

The free electron model is expected to give best agreement for metals with a low density of conduction electrons and has been applied with moderate success to the alkali metals Li, Be and Na and the light metals Al and Mg (Phillips and Weiss, 1968, Cooper et al, 1974). The experimental profiles of these metals do reveal a discontinuity in the slope at around the Fermi momentum which is the major feature of the theory and which can be seen quite clearly in the free electron model for Li (figure 1.11). The main failure of this simple theory has been that it consistently underestimates the amount of electron density above the Fermi momentum.

A significant improvement can be made by taking into account the interaction between electrons within the conduction gas. Figures 1.10 a and b indicate the effect of including e-e correlation on the occupation function n(p) and the Compton profile. As already mentioned with respect to intra-atomic correlation (§1.4.1.), this interaction promotes some electrons to momentum states above the Fermi surface and increases the high momentum tail of the profile while decreasing the peak. Analysis of this effect in experimental results has in the past been confused by the presence of significant amounts of multiple scattering which causes a very similar modification.

The effect of orthogonality of the conduction electron wavefunctions to the core states has also been investigated (Pandy and Lam, 1973). Experiments on Li and Na by Eisenberger et al (1972) showed a greater intensity in the tails of their profiles than was predicted by their theory based on an interacting electron gas into which the lattice

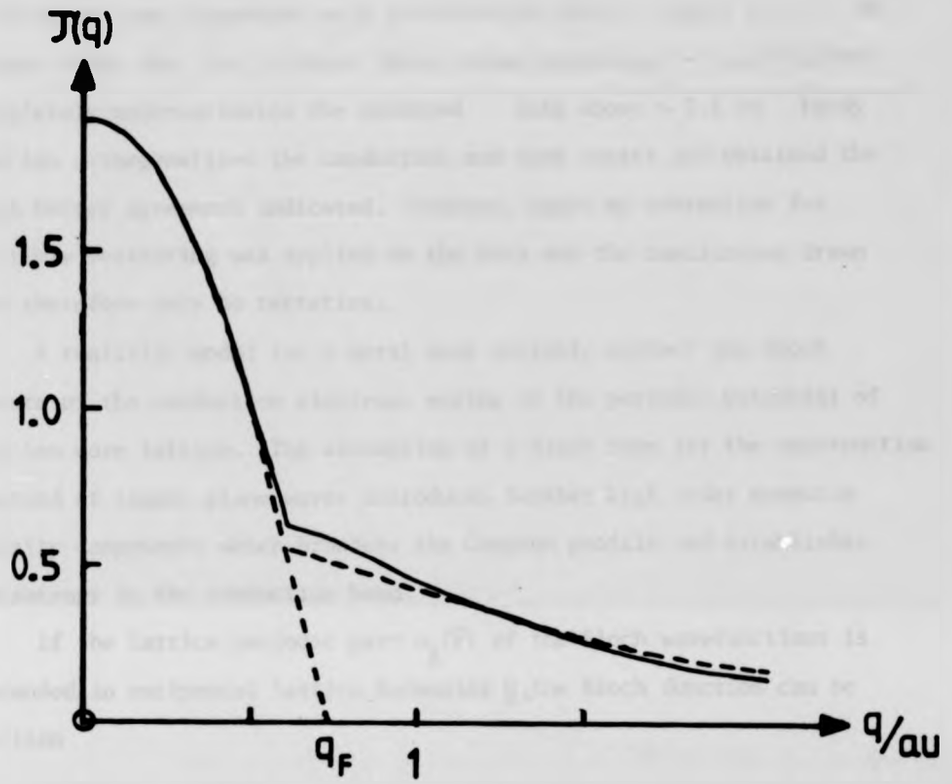

Figure 1.11. Simple Models of the Compton Profile of Li. Dashed Curve - Clementi Free Atom Core + Free Electron Gas, Full Curve - Band Structure Calculation (Borland & Cooper, 1970). (The two models have been normalised to the same value at q=0.)

interaction was introduced as a perturbation effect (figure 1.12). The figure shows that for Li their theory (even including e-e correlation) completely underestimates the measured data above ~ 0.5 au. Pandy and Lam orthogonalised the conduction and core states and obtained the much better agreement indicated. However, again no correction for multiple scattering was applied to the data and the conclusions drawn can therefore only be tentative.

A realistic model for a metal must suitably reflect the Bloch nature of the conduction electrons moving in the periodic potential of the ion core lattice. The assumption of a Bloch form for the wavefunction instead of simple plane waves introduces further high order momentum density components which broadens the Compton profile and establishes anisotropy in the conduction band.

If the lattice periodic part $u_{\underline{k}}(\bar{r})$ of the Bloch wavefunctions is expanded in reciprocal lattice harmonics $\underline{G}$, the Bloch function can be written

$$\psi_{\underline{k}}(\bar{r}) = \sum_{\underline{G}} a_{\underline{G}}(\underline{k}) \exp(i(\underline{k} + \underline{G}).\bar{r})$$

where $a_{\underline{G}}(\underline{k})$ are the expansion coefficients in reciprocal space.
By the Dirac transformation, the momentum space wavefunction is obtained as

$$\chi_{\underline{k}}(\bar{p}) = \int \sum_{\underline{G}} a_{\underline{G}}(\underline{k}) \exp(i(\underline{k}+\underline{G}).\bar{r}) \exp(-i\bar{p}.\bar{r}) d\bar{r}$$

$$= \sum_{\underline{G}} a_{\underline{G}}(\underline{k}) \delta(\bar{p}-\bar{k}-\underline{G})$$

The momentum density of an electron in state $\underline{k}$ is thus given by

$$\rho_{\underline{k}}(\bar{p}) = \sum_{\underline{G}} |a_{\underline{G}}(\underline{k})|^2 \delta(\bar{p}-\underline{k}-\underline{G})$$

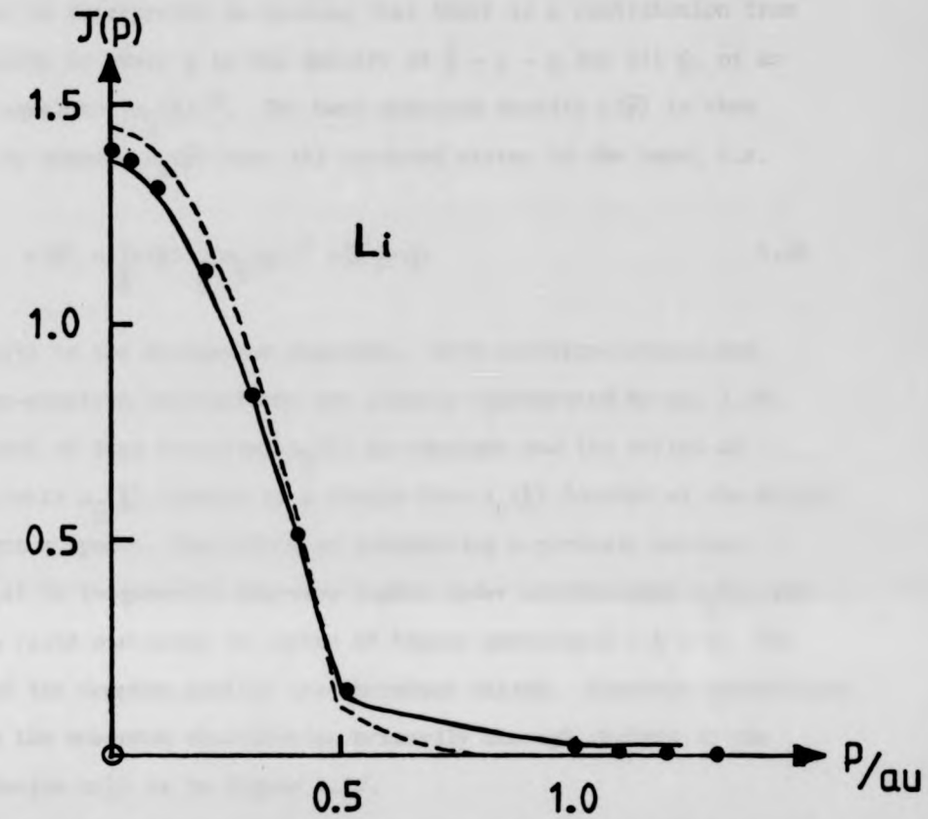

Figure 1.12. Effect of Orthogonalisation of Valence and Core States in J(p)

This can be interpreted as meaning that there is a contribution from an electron in state $\underline{k}$ to the density at $\overline{p} = \underline{k} + \underline{G}$ for all $\underline{G}$, of an amount equal to $|a_{\underline{G}}(\underline{k})|^2$. The band momentum density $\rho(\overline{p})$ is then formed by summing $\rho_{\underline{k}}(\overline{p})$ over all occupied states in the band, i.e.

$$\rho(\overline{p}) = \sum_{\underline{k}} n(\underline{k}) \sum_{\underline{G}} |a_{\underline{G}}(\underline{k})|^2 \, \delta(\overline{p}-\underline{k}-\underline{G}) \qquad 1.20$$

where $n(\underline{k})$ is the occupation function. Both electron-lattice and electron-electron interactions are clearly represented by eq. 1.20. For a band of free electrons $u_{\underline{k}}(\overline{r})$ is constant and the series of coefficients $a_{\underline{G}}(\underline{k})$ reduces to a single term $a_o(\underline{k})$ located at the origin of momentum space. The effect of introducing a periodic lattice potential is to generate non-zero higher order coefficients $a_{\underline{G}}(\underline{k})$ and thus to raise electrons to states of higher momentum $\overline{p} = \underline{k} + \underline{G}$. The tails of the Compton profile are therefore raised. Electron correlation affects the momentum distribution primarily through changes in the distribution $n(\underline{k})$ as in figure 1.10.

Figure 1.11 compares the free electron model for Li (HF free ion core and free electron conduction band) with an early band structure calculation by Borland and Cooper (1970). The latter employed Bloch functions composed of a free ion core ($1s^2$) and variationally determined tight binding bloch orbitals and plane waves ($2s^1$) through which the periodic potential, of Seitz form (Seitz, 1935), exerted its influence. In the figure both profiles have been calculated by Cooper et al (1970) and normalised to the same peak height. The most sig nificant effect on the profile of the introduction of the periodicity has been to shift 10% to 15% of the conduction electrons to a momentum above the Fermi surface.

It is interesting to note in passing that eq. 1.18 allows the Fermi surface of the metal to be found throughout the unfilled bands. The

procedure would be to examine $B(\underline{r})$ at $\underline{r}$ equal to lattice translations and compose a series of terms. Eq. 1.18 can then be inverted to give

$$n(\underline{k}) = \sum_{\underline{R}} B(\underline{R}) \exp(i\underline{k}.\underline{R}) \qquad 1.21$$

which is an expression of the Lock-Crisp-West (LCW) Theorem (Lock et al, 1973). However, this is a useful tool only when Compton profiles can be obtained with extremely good momentum resolution as is the case for Angular Correlation of Positron Annihilation Radiation (ACPAR) studies but not for γ-ray Compton scattering. This application is limited by the fact that the momentum resolution of a Compton profile transforms to a rapidly decaying, multiplicative damping function in position space. The number of terms $B(\underline{R})$ that can be discriminated from the noise level which is constant with r, is thus severely restricted (see, e.g. the B-function results for Vanadium in Chapter 5) and the corresponding representation of $n(\underline{k})$ from Compton scattering measurements is poor.

1.5.3. Transition Metals

The theoretical treatment of "simple" metals is relatively straightforward. The conduction electrons can be treated as nearly free and, due to their high density, electron correlation has only a small influence on the electron distribution. In transition metals however, the situation is complicated by the presence of unfilled d-bands at the Fermi surface. The momentum distribution is governed partly by the lattice potential and partly by the perturbation of the Fermi surface arising from strong electron correlation effects. Unpaired spins in the d-band, leading to the magnetic properties of the first transition series, are usually represented by separate spin-up and spin-down Fermi surfaces. These are very intricate and impossible to relate to the spin-independent

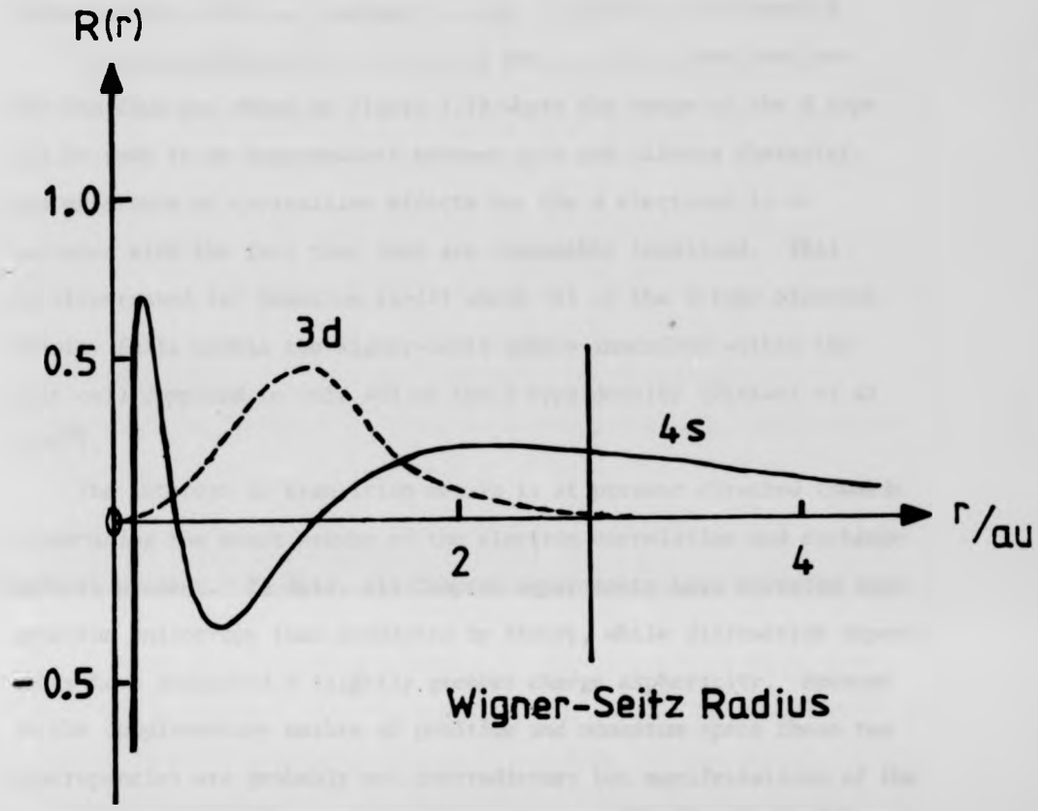

Figure 1.13. Radial Wavefunctions of the Transition Metal Vanadium (Free Atom) Showing the Intermediate Extent of the 3d Orbitals

Fermi surface which is relevant to γ-ray scattering measurements.

The comparable extents of the 3d and 4s radial wavefunctions for Vanadium are shown in figure 1.13 where the range of the d type can be seen to be intermediate between core and valence character. The existence of crystalline effects for the d electrons is at variance with the fact that they are reasonably localised. This is illustrated for Scandium (z=21) where 95% of the d-type electron density falls within the Wigner-Seitz sphere inscribed within the unit cell compared to only 40% of the s-type density (Paakari et al 1976[103]).

The interest in transition metals is at present directed towards determining the exact nature of the electron correlation and exchange effects present. To date, all Compton experiments have revealed less momentum anisotropy than predicted by theory, while diffraction experiments have indicated a slightly greater charge asphericity. Because of the complementary nature of position and momentum space these two discrepancies are probably not contradictory but manifestations of the same failure of the current theories - perhaps a failure of the Local Density Approximation in describing many electron effects.

One clear and simple evaluation of the role of d-electrons and their influence on electron correlation in Copper has been undertaken in an approximation based on the Seitz model, by Pattison et al (1982). By utilising eq. 1.20, they have separated the contributions to the Compton profile from correlation and lattice effects and illustrated that the momentum anisotropy depends strongly on the correlation produced by hybridisation of the 3d electrons and the 4s, 3p electrons in the valence band (Jepsen et al, 1981).

The Fermi surface of Copper is well known to be extremely simple compared to the other transition metals. It exists in only one energy band and is nearly spherically symmetric with short necks joining

adjacent zones. Jepsen showed that the existence of these necks is due to d-band mixing. In the Seitz models, the potential is assumed to be spherically symmetric within the unit cell and uniform everywhere else. The form of the valence electron wavefunction can then be taken to be

$$\psi_{\underline{k}}(\overline{r}) = U_o(|\overline{r}|) \exp(i\underline{k}.\underline{r})$$

where the periodic function is represented by the average for all states occupied in the band. With this assumption, the band momentum density (eq. 1.20) can be written

$$\rho(\overline{p}) = \sum_{\underline{G}} |a_{\underline{G}}|^2 \sum_{\underline{k}} n(\underline{k}) \delta(\overline{p}-\underline{k}-\underline{G})$$

and is represented in two dimensions for the case of entirely free electrons in figure 1.14. The momentum density is composed of free electron Fermi spheres n(k) repeated throughout the reciprocal lattice and weighted according to the probability of finding the high order component of momentum. The Compton profile is then obtained, as in the bottom half of the diagram, as the integral over a plane intersecting with these regions. Thus the lattice effects in the wavefunction give rise to maxima and minima as this plane of integration is moved out from the origin and the momentum distribution becomes anisotropic. Pattison et al found they could reproduce the general appearance of an LCAO band structure anisotropy (Bagayoko et al, 1980) by considering only 27 Fermi spheres (including the origin) at reciprocal lattice points of type (000), (111), (200) and (220). Repeating their calculations with electron correlation modifying the free electron occupation function caused a decrease in the amount of anisotropy of about 30% for an n(k) calculated for an interacting electron gas by Lundquist and Lyden (1971).

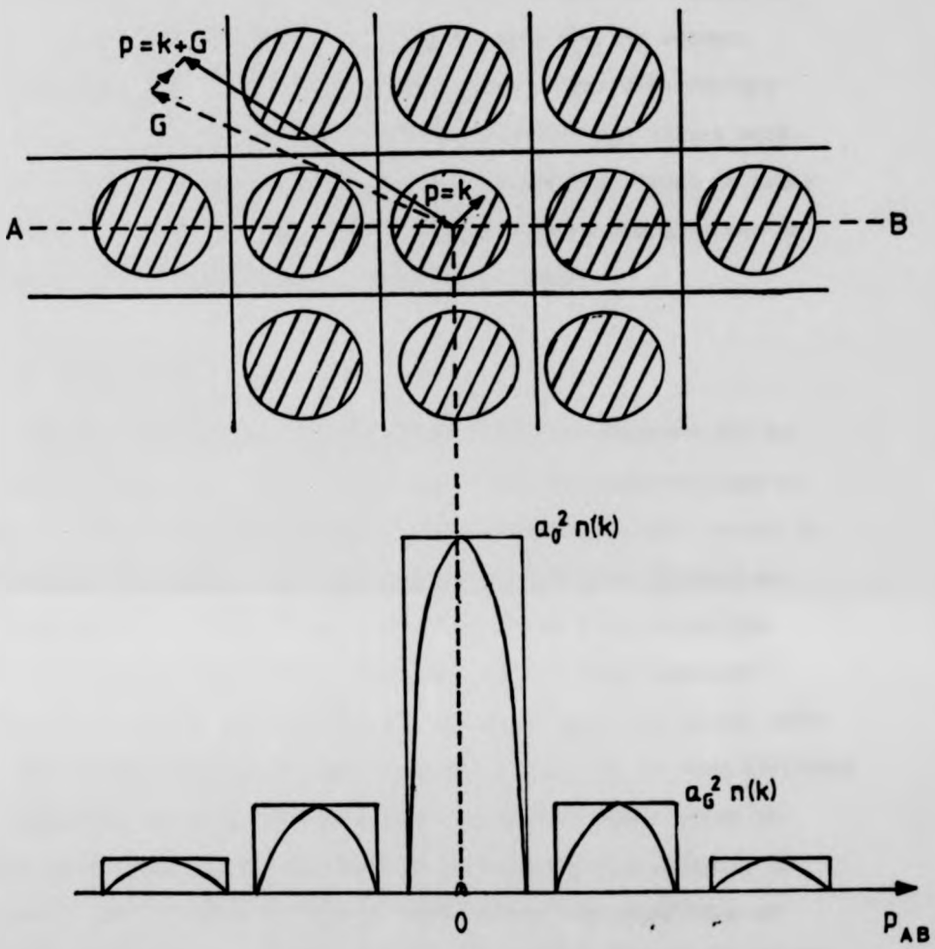

Figure 1.14. Seitz Model for Nearly Free Electrons in a Square Lattice (The lattice potential promotes electrons of wavenumber k from within the primary Fermi surface to the secondary surfaces with momenta p = k + G)

Thus the use of a very simple model has enabled the effects of electron correlation and mixing of d states into the s-p valence band to be examined. In other transition metals the Fermi surface is far more complicated and such simple models will not always work. Both theory and experiment need to be scrutinised for errors in order that clear conclusions may be drawn. Recent careful measurements on Vanadium and Iron are analysed in this present work.

1.6. Plan of Thesis

A number of properties of Compton profiles and features due to solid state effects have been discussed in the preceding sections of Chapter 1. The greater proportion of the remainder of this thesis is concerned with the development of Compton scattering as applied to transition metals. Such a study represents the Compton technique taken to its present day limit, restricted by available apparatus, suitable γ-ray sources and the sophistication of data processing software. The interpretation of transition metal profiles is very difficult and a comprehensive study of theoretical parameters would prove invaluable with regard to the delineation of many-electron effects in particular. Such a study is however well beyond the competence of the author and the scope of this thesis. Therefore, discussion of the prediction of band structure calculations is limited to those theoretical parameters which are readily accessible and to those calculations for which Compton profiles are available. The number of available calculations is not large but improvements in experimental techniques and accuracy are gaining respectability for Compton scattering and the number should increase dramatically. This thesis is concerned with a definition of those improvements.

Chapter 2 sets down the physical conditions under which the measured differential scattering cross section (inelastic) can be simply related to the ground state electron momentum distribution in the system and

specifies the cross-section correction function to be used for transition metals. The apparatus required to give these physical conditions is described in Chapter 3 with a consideration of the parameters affecting the measurement. The apparatus was designed and developed independently by Holt et al (1979) but this thesis represents the first studies using the new system. The apparatus - dependent correction scheme laid out in Chapter 3 is analysed minutely with reference to particular transition metal measurements in Chapter 4 until a final system of data reduction and processing is determined. In Chapter 5 and 6, measurements for Vanadium and Iron are reported and the accuracy and reproducibility are taken to justify the data processing scheme of Chapter 4. Chapter 7 discusses the results of recent Compton profile measurement made by other authors by γ-ray and other techniques providing a review of the scope of present day Compton measurements and suggestions for future investigations.

CHAPTER 2

PHOTON SCATTERING THEORY

2.1. General Inelastic Scattering Principles

The experimentalist interested in the fields of nuclear or condensed matter physics employs a variety of probes to analyse the target. High energy electron beams are used to investigate nuclear wave functions in solids (150 keV) and plasmons in metals; neutrons are used to measure the structure of liquids and atomic momentum distributions in solids or liquids; and X-rays have been used to measure the charge density in crystalline materials. The development of inelastic γ-ray scattering provides a tool for measuring electron momentum distributions in a wide range of materials. A general discussion of scattering techniques is given by Platzman (1972). The present work concentrates on the derivation of a cross-section to describe inelastic γ-ray scattering.

When the interaction between the scattering system and the probe is weak such that the effects of the scattered beam on the system are negligible, the scattering may be considered within the scope of the lowest order Born Approximation (Schiff, 1949). Under these conditions the cross-section is usually completely characterised by the momentum and energy transfer to the system, i.e.

$$\frac{d^2\sigma}{d\Omega d\omega} = \left(\frac{d\sigma}{d\Omega}\right)_o S(\underline{K},\omega) \qquad 2.1$$

where the basic coupling between the probe and the target is described by $\left(\frac{d\sigma}{d\Omega}\right)_o$ (e.g. the Thomson cross-section in the case of low energy X-rays scattering from a system of electrons) and

$$\underline{K} = \underline{k}_1 - \underline{k}_2 \text{ and } \omega = \omega_1 - \omega_2$$

are the momentum and energy transfers respectively. The function $S(\underline{K},\omega)$ generally describes the dynamics of the target and is the focus of attention for the study of condensed matter. All inelastic scattering experiments are included within this description by an interaction term and a dynamical correlation function and information obtained is distinguished by the region of $(\underline{K},\omega)$ space accessible to the probe.

Different probes which access the same region of $(\underline{K},\omega)$-space can give similar information. For example, inelastic X-ray and electron scattering and positron annihilation all provide information about the electron momentum distribution. Figure (2.1) gives an approximate delineation of the range of the main photon scattering processes in $(\underline{K},\omega)$-space referred to characteristic energies (ω_c) and wavelengths (λ_c) of the scattering system.

Considering a beam of low energy X-rays (λ_1 << the Compton wavelength, λ_c) scattering from slowly moving electrons, the Compton shift formula predicts only a very small change in wavelength on scattering,

i.e. $$\Delta\lambda_1 = 2\lambda_c \sin^2 \frac{\theta}{2} << \lambda_1 \quad ,$$

where θ is the scattering angle. Under this condition $|\underline{k}_1| \approx |\underline{k}_2|$ and the momentum transfer is given by

$$K = |\underline{k}_1 - \underline{k}_2| \approx 2|\underline{k}_1| \sin \frac{\theta}{2}$$

Thus the region of $(\underline{K},\omega)$ space being investigated can be selected by scanning the scattered radiation over the range of θ from 0 to π radians and varying K from 0 to a maximum of $2|\underline{k}_1|$. Below $K\lambda_c = 1$ the scattering involves many electrons and interference effects can occur. This is the regime of elastic scattering and photoelectric absorption. Above $K\lambda_c = 1$ the scattering takes place from individual electrons and Compton scattering dominates. At even larger energy and momentum transfer pair production occurs.

The magnitudes of the energy and momentum transfers play an important

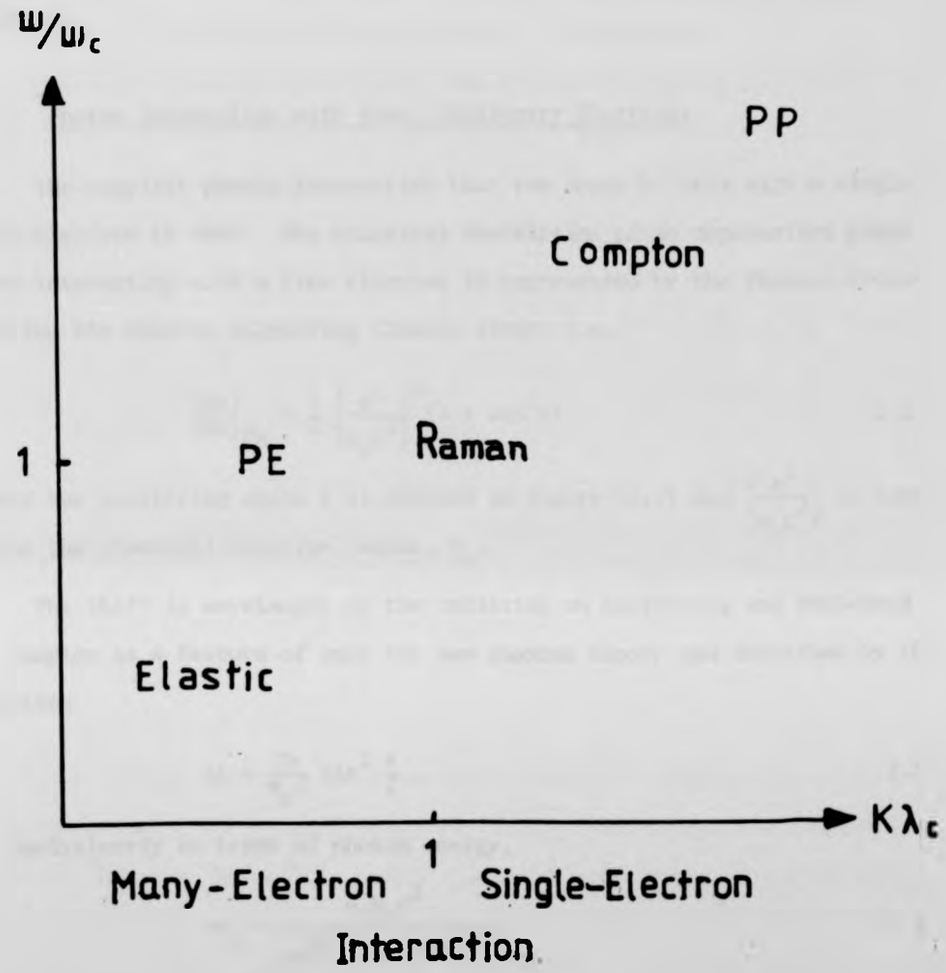

Figure 2.1. Characterisation of Type of Scattering Process According to the Region of (K,ω) - Space Sampled by the Incoherent Scattering Function, $S(K,\omega)$. The magnitude of the momentum and energy transfers are defined by the Compton shift at an angle θ. (ω_c and λ_c are characteristic energies and lengths of the target.)

role in the mathematical development of an inelastic scattering cross-section.

2.2. Photon Interaction with Free, Stationary Electrons

The simplest photon interaction that can occur is that with a single free electron at rest. The classical description of an unpolarised plane wave interacting with a free electron is represented by the Thomson cross-section for elastic scattering (James, 1948), i.e.

$$\left(\frac{d\sigma}{d\Omega}\right)_{Th} = \frac{1}{2}\left(\frac{e^2}{m_o c^2}\right)^2 (1 + \cos^2\theta) \qquad 2.2$$

where the scattering angle θ is defined in figure (2.2) and $\left(\frac{e^2}{m_o c^2}\right)$ is taken to be the classical electron radius, r_o.

The shift in wavelength of the radiation on scattering was explained by Compton as a feature of only the new quantum theory and described by the equation

$$\Delta\lambda = \frac{2h}{m_o c} \sin^2\frac{\theta}{2} \qquad 2.3$$

or equivalently in terms of photon energy,

$$\omega_2 = \frac{\omega_1 m_o c^2}{m_o c^2 + 2\omega_1 \sin^2\frac{\theta}{2}} \qquad 2.4$$

The Thomson cross-section was naturally unable to account for this effect - a relativistic theory was required. The relativistic scattering of unpolarised photons from a free, stationary electron is given by the well-known cross-section of Klein and Nishina (1929),

$$\left(\frac{d\sigma}{d\Omega}\right)_{KN} = \frac{1}{2} r_o^2 \left(\frac{\omega 2}{\omega_1}\right)^2 \left(\frac{\omega_1}{\omega_2} + \frac{\omega_2}{\omega_1} - \sin^2\theta\right) \qquad 2.5$$

where ω_2 is defined by eq. 2.4 and r_o is again the classical electron radius.

In the limit for low energy photons ($\omega_1 << m_o c^2$) $\omega_2 = \omega_1$ and the Klein Nishina cross-section reduces to the Thomson cross-section.

The shift in energy of photons from interaction with a stationary electron is important for its justification of quantum theory but it is the broadening of the Compton line about this shifted energy and ascribed by DuMond to the motion of the electrons that is of interest to the experimental solid-state physicist. Thus it was necessary to develop a theory that would describe the Compton scattering cross section for atomic electrons.

2.3. Cross Section for Bound Electrons

Scattering from electrons in an atom brings three new factors into consideration - the arrangement of the electrons about the nucleus, their motion and their degree of binding (ionisation probability). Discussion of the effects of electronic motion will be deferred to §2.4.

2.3.1. Electronic Arrangement.

Given a large assembly of atoms it is possible to define an average distribution of electron density around each nuclear site. The constant phase relationship of an elastically scattered wave to the in-coming wave (weak coupling approximation) means that interference of waves scattered from different electrons can occur. The amplitude of the resulting coherent radiation therefore depends on the direction of scattering relative to the electronic arrangement. The intensity is described in terms of an atom form factor f by

$$\frac{d\sigma}{d\Omega} = \left(\frac{d\sigma}{d\Omega}\right)_{Th} |f(\underline{s})|^2$$

where

$$f(\underline{s}) = \int \rho(\overline{r}) e^{i\underline{s}\cdot\underline{r}} d^3\underline{r} \qquad 2.6$$

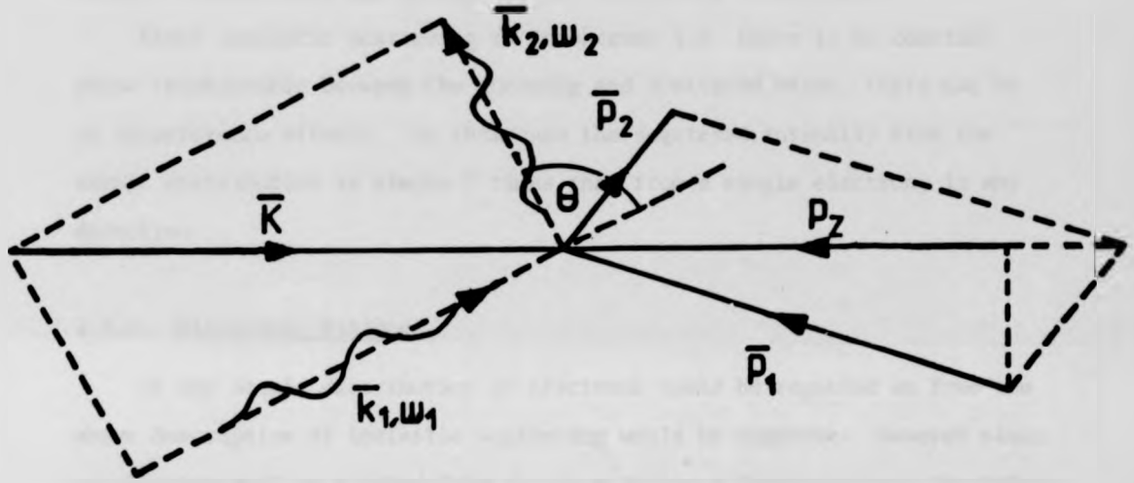

Figure 2.2. Schematic for Conservation of Momentum Process During the Interaction of a Photon $(\bar{k}_1, \omega_1)$ with an Electron $(\bar{p}_1, E_1)$. In a typical Compton experiment the γ-ray scattering vector is aligned with $\bar{K}$ and thus yields information about the initial electron momentum component p_z.

i.e. the Fourier transform of the charge density, ρ, and $\underline{s}$ is the scattering vector, $\underline{k}_1 - \underline{k}_2$. In the forward direction all the partial waves are in phase and $f(\underline{s})$ reduces to the number of electrons, Z. If each atom forms part of a regular array as in a single crystal, the intensity is further modulated by the structure factor, $S(\underline{k})$ defined in a similar way, as the Fourier transform of the charge density throughout the crystal.

Since inelastic scattering is incoherent i.e. there is no constant phase relationship between the incoming and scattered beams, there can be no interference effects. In this case the scattered intensity from the atomic distribution is simply Z times that from a single electron, in any direction.

2.3.2. Electronic Binding

If the atomic distribution of electrons could be regarded as free the above description of inelastic scattering would be complete. However since an electron must be ejected from the atom during a Compton event, the interaction is more likely to occur with lightly bound electrons than with those in the atom core. Thus the atomic cross section must be reduced in proportion. The calculation of the Incoherent Scattering Function S in eq. 2.1 for bound models has been performed by many authors (Nelms, 1953 and Hubbell et al, 1975). Calculations by Heisenberg and Bewilogua (1931) based on the Thomas-Fermi model (Fermi, 1928) have shown S can be written as a function of one variable proportional to $\frac{q}{Z^{\frac{2}{3}}}$ where q is the momentum transfer and Z the atomic number, i.e.

$$\left(\frac{d\sigma}{d\Omega}\right)_{atom} = \left(\frac{d\sigma}{d\Omega}\right)_{KN} \times Z \times S\left[\frac{q}{Z^{2/3}}\right] \qquad 2.7$$

When the momentum transfer is large compared with the atomic number (i.e. large compared to the inverse of some characteristic length of the system, e.g. electron orbit radius), the Incoherent Scattering Function tends

to unity and the Klein-Nishina cross section holds for the atom as a whole but when q is small not all the electrons may contribute equally. In this case the cross section is reduced and S represents the probability of ionisation of the atom given such an impulse. The function S has been calculated more accurately from the full relativistic second differential cross section $\frac{d^2\sigma}{d\Omega d\omega}$ by Ribberfors and Berggren (1982) and the same general conclusions are reached. The supposition of free electron interactions inherent in the Klein-Nishina cross section and fundamental to the theory of the Impulse Approximation (to be discussed in §2.4) is justified for low Z materials or high momentum transfers.

2.4. Second Differential Cross Section for Atomic Electrons

2.4.1. Origin of Energy Dependence of Compton Cross Section

DuMond explained the broadening of the Compton line in terms of the Doppler shifting of the scattered radiation by the motion of the electrons in the target. Figure 2.2 illustrates the dynamics of the interaction of a photon with a moving electron. Conservation of energy and momentum for non-relativistic electron motions leads to a wavelength shift given by

$$\Delta\lambda_1 = \frac{2h}{m_o c} \sin^2 \frac{\theta}{2} - \frac{2(\lambda_1\lambda_2)^{\frac{1}{2}}}{m_o c} \sin \frac{\theta}{2} p_z \qquad 2.8$$

where p_z is the component of electron momentum along the scattering vector $\underline{K} = \underline{k}_1 - \underline{k}_2$. This equation is split into two terms - the first describing the Compton shift and the second the DuMond broadening effect.

The advent of solid-state detectors and the accompanying use of high energy γ-ray sources meant that much heavier elements could be probed by Compton scattering. Under these more energetic conditions eq. 2.8 must be reformulated to account for relativistic electronic motions. The form of the equation remains unchanged but a scaling factor for the relativistic momentum component is introduced (Cooper and Williams, 1972):

i.e. $$\Delta\lambda = \frac{2h}{m_o c}\sin^2\frac{\theta}{2} - \frac{2\lambda_1}{m_o c}\sin\frac{\theta}{2}\,F(\lambda_1,\theta)p_z \qquad 2.9$$

where $$F(\lambda_1,\theta) = \left[1 + \frac{\Delta\lambda}{\lambda_1} + \left(\frac{\Delta\lambda}{2\lambda_1}\right)^2 \frac{1}{\sin^2\frac{\theta}{2}}\right]^{\frac{1}{2}}$$

The factor F introduces a momentum scale change of about 4% for MoKα X-rays.

If we now consider the scattered radiation from an atom characterised by a distribution of electron momentum component $J(p_z)$ (defined as in eq. 1.1) there will be a distribution of wavelengths present as in figure (2.3). Each wavelength point λ in the Compton cross section corresponds to scattering off electron density with a particular momentum component p_z given by inverting eq. 2.9; i.e. in natural units,

$$p_z = \frac{\omega_1\omega_2(1-\cos\theta) - E_1(\omega_1-\omega_2)}{(\omega_1^2 + \omega_2^2 - 2\omega_1\omega_2\cos\theta)^{\frac{1}{2}}} \qquad 2.10$$

It then becomes of great importance to determine under what conditions the second differential scattering cross section can be written as

$$\frac{d^2\sigma}{d\Omega d\omega} = C(\omega_1,\omega_2,\theta,p_z)J(p_z) \qquad 2.11$$

since if this equation can be shown to hold, the Compton Profile $J(p_z)$ can then be easily measured.

The circumstances under which it is possible to describe the inelastic cross section in the form 2.11 have come to be known as the Impulse Approximation (IA). The requirements are for the energy transfer to be much greater than any binding energy of the system (so that electrons are ejected into a continuum energy band) and secondly for the interaction to be completed before the electron has a chance to move in the Coulomb field of the atom, i.e. an "impulsive" interaction. These two conditions create a situation equivalent to the interaction of a photon with a system of free electrons having the same velocity distribution they would have in the target atom.

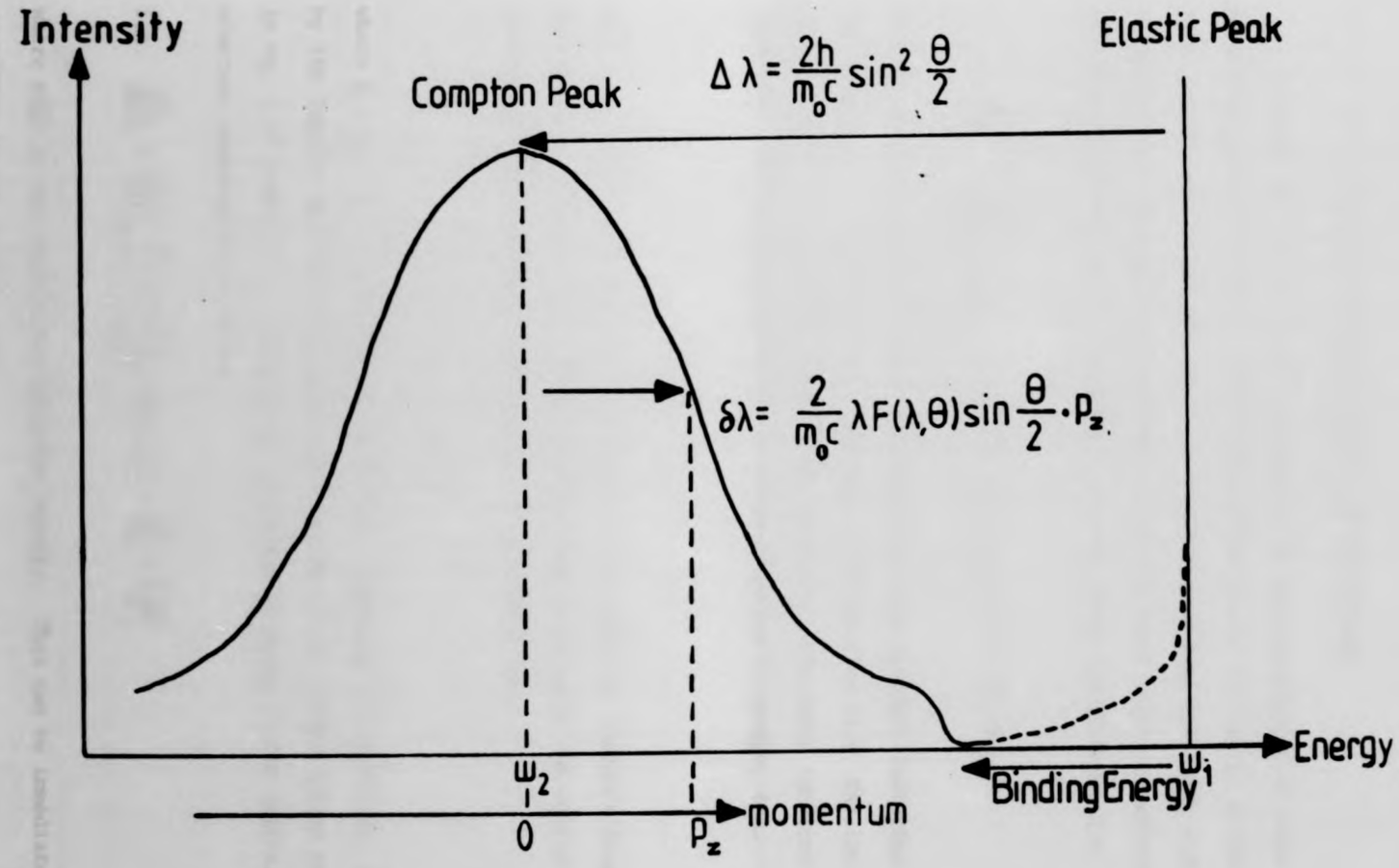

Figure 2.3. The Inelastically Scattered Intensity (Compton Cross-Section) from Atomic Electrons

2.4.2. Semi Classical Approximation to Cross Section

Platzman and Tzoar (1965) considered the perturbation of an atom by an unpolarised plane wave representing scattering of low energy X-rays. With a weak interaction described by the Born Approximation, they were able to employ time-dependent perturbation theory to first order to calculate the second differential cross section via the Fermi Golden Rule, i.e.

$$\frac{d^2\sigma}{d\Omega d\omega} = \left(\frac{d\sigma}{d\Omega}\right)_{Th} \frac{\omega_2}{\omega_1} \sum_f \sum_i |\langle f| \sum_j \exp(i\underline{K}.\underline{r}_j)|i\rangle|^2 \delta(E_f - E_i - \omega) \qquad 2.12$$

In this equation the basic interaction between the incident radiation and the electrons is described by the Thomson cross section (i.e. the low energy limit of the Klein-Nishina cross section). The delta function satisfies the necessary requirement of conservation of energy, i.e.

$$\omega = E_f - E_i$$

where ω is the energy transferred to the system from the incident beam. The probability of such a transition occurring is given by the matrix element of the perturbing potential of the incident wave,

$$|\langle f|\sum_j \exp(i\underline{K}.\underline{r}_j)|i\rangle|^2$$

where $\underline{K} = \underline{k}_1 - \underline{k}_2$ is the scattering vector. Assuming the conditions imposed by the Impulse Approximation, summation over the final states (plane waves) in eq. 2.12 leads to a cross section described in terms of the initial electron momentum distribution,

i.e. $$\frac{d^2\sigma}{d\Omega d\omega} = \left(\frac{d\sigma}{d\Omega}\right)_{Th} \frac{\omega_2}{\omega_1} \int \frac{d^3\bar{p}}{(2\pi)^3} n(\bar{p}) \delta \left(\omega - \frac{K^2}{2m} - \frac{\underline{K}.\bar{p}}{m}\right)$$

where $n(\bar{p})$ is the unperturbed momentum density. This can be immediately rewritten in the simpler form

$$\frac{d^2\sigma}{d\Omega d\omega} = \left(\frac{d\sigma}{d\Omega}\right)_{Th} \frac{\omega_2}{\omega_1} J(q) \qquad 2.13$$

where q is the electron momentum component along the scattering vector and ω_2 is defined as

$$\omega_2 = \omega_1 - \frac{K^2}{2m} - \frac{\bar{K}.\bar{p}}{m}$$

in analogy eq. 2.8 for the wavelength shift.

2.4.3. Validity of the Impulse Approximation

The assumption of the conditions implied by the Impulse Approximation in the preceeding section needs to be examined more closely. In eq. 2.12 it is obviously possible to choose more realistic final states for the ejected electron than plane waves and its initial energy could be assigned its actual bound value rather than just $p^2/2m$. The influence of more realistic assumptions on the accuracy with which the inelastic cross section explicitly represents the momentum distribution (Compton Profile) will be briefly discussed here.

Several measurements have been made with low energy spectrometer systems ($\leq$ 60 keV) to investigate deficiencies in the IA. Weiss (1975) and Weiss et al (1977) have studied Al, Polyethylene and Li with MoKα and β X-rays (17 keV) and discovered shifts of the order of 10 eV in the Compton Profile centre position away from the energy predicted by the Compton shift formula, eq. 2.3. A similar shift has also been detected in HEEIS (High Energy Electron Impact Spectroscopy) experiments by Barlas et al (1977). Using 60 keV γ-rays Holt et al (1979) have noted an asymmetry in the Compton Profile of Al around p_z = 1 au but detected no shift of the centre.

Early calculations by Eisenberger and Platzman (1970) and Mendelsohn and Biggs (1973) using Exact Hydrogenic (EH) states to describe s-type electron scattering showed negligible corrections to the IA until the energy transfer became comparable with the binding energy. Then it was noted that the Impulse

Hydrogenic (IH) result for the cross section exceeded the EH result. Even more realistic calculations by Currat et al (1971 [26,27]) employing a Herman Skillman model potential (EHS) to include electron correlation and exchange effects showed this same discrepancy. The EH investigation was expanded to cover a wider range of energies and higher electron shells (L and M) by Mendelsohn et al (1973), Bloch and Mendelsohn (1974) and Mendelsohn and Bloch (1975). They found that for the L shell the difference between the EH and the IH results was in the opposite direction, i.e. $J_{EH}(0) > J_{IH}(0)$. The effects of EHS calculations on individual s and p-type electrons in different shells were studied by Grossman and Mendelsohn (1975), and Mendelsohn and Grossman (1977). It was concluded (Mendelsohn, 1978) that the breakdown of the IA for individual s - and p - type electrons, producing opposing effects in the cross section, would tend to cancel from completely filled shells. The calculations were performed for a total Al profile with 60 keV radiation and the results were in agreement with experiment.

Thus it appears that at low energy transfers the IA does not hold for individual orbitals but only for the complete atom. There is therefore some danger in treating the Impulse Compton Profile contribution from each orbital separately when, for example, using a free atom core profile to describe a core in the crystalline state. The IA holds for loosely bound valence electrons but fails for the core if the energy transfer is too small. Fortunately the situation is partly rescued by the preferential sensitivity of the Compton measurement to valence electron behaviour which implies, as a corollary, that some error in the low, flat, core profiles can be tolerated.

The use of high energy (412 keV) γ-rays in the present work means that the IA is completely adequate for even the core electrons of transition metals and the Compton cross section is sensibly defined in terms of the initial electron momentum distribution.

2.4.4. Gamma Ray Inelastic Cross Section

The cross section of Platzman and Tzoar (eq. 2.13) adequately describes the Compton scattering of low energy X-rays but is inapplicable for γ-rays. The fundamental analysis of these high energy interactions requires the application of full relativistic-quantum field theory (Jauch and Rohrlich, 1955). Only an outline of the results will be presented here.

The Klein-Nishina cross section for stationary electrons (eq. 2.5) was generalised by Jauch and Rohrlich (op. cit.) to include a distribution of relativistically moving electrons, still retaining the assumption of the IA - that they could be treated as free. The derived cross section is in a form unsuited to the extraction of momentum distributions from measured spectra. Eq. 11.9 of Jauch and Rohrlich leads to

$$\frac{d^2\sigma}{d\Omega d\omega_2} = \frac{r_o^2 m^2 \omega_2}{2\omega_1 E_1 K + \frac{p_z}{E_1}\omega} \int dp_x dp_y n(\bar{p}_1) X \qquad 2.14$$

where $K = |\underline{k}_1 - \underline{k}_2|$ and $\omega = \omega_1 - \omega_2$. X is known as the flux factor and depends on E_1 and $\bar{p}_1$ and thus cannot be removed from the integration. The factor outside the integration also includes E_1 which depends on $\bar{p}_1$ rather than the z component of momentum. Therefore in its present form eq. 2.14 is unusable.

These two problems were tackled by Eisenberger and Reed (1974) and Manninen et al (1974). Considering the initial electronic motion to be only mildly relativistic the electron energy was replaced by the rest mass energy, $E_1 = m_o c^2$, i.e. neglecting terms of order $\left(\frac{p}{m}\right)^2$. To simplify the flux factor term, Manninen et al decided that since the majority of Compton experiments are performed in a configuration as close to backscattering as possible, X could be evaluated at the particular value of the scattering angle, $\theta = 180°$. With this assumption, X (180°) becomes a function of p_z alone and thus can be removed from the integration, i.e.

$$X(\bar{p}_1) + X(180°) = \frac{\omega_1 A_2}{\omega_1 A_1} + \frac{\omega_2 A_2}{\omega_1 A_1} + 2m\left[\frac{1}{\omega_1 A_1} - \frac{1}{\omega_2 A_2}\right]$$

$$- m^2\left[\frac{1}{\omega_1 A_1} - \frac{1}{\omega_2 A_2}\right]^2 \qquad 2.15$$

where $A_1 = 1 + p_z/m$

and $A_2 = 1 - p_z/m$, in natural units.

The cross section now has the desired form of eq. 2.11.

The derivation from this result of the exact cross section at angles other than 180° was considered by Ribberfors (1975). Extending the analysis of Manninen et al, he wrote the cross section as an expansion in a rapidly converging series of terms involving $J(p_z)$ and $\tilde{X}$ (see below), only the first two terms being at all significant. To first order the cross section is obtained in natural units as,

$$\frac{d^2\sigma}{d\Omega d\omega} = \frac{m^2\omega_2}{2\omega_1 K}\left\{\frac{\tilde{X}}{E(p_{min})} J(p_z) + \int_{p_{min}}^{\infty} \frac{J(p)}{E(p)} \frac{dX_{int}}{dp}\, dp\right\} \qquad 2.16$$

where $\tilde{X} = \frac{R}{R'} + \frac{R'}{R} + 2m^2\left(\frac{1}{R} - \frac{1}{R'}\right) + m^4\left(\frac{1}{R} - \frac{1}{R'}\right)^2$

and reduces to eq. 2.15 for $\theta = 180°$,

$$R = \omega\left[E + (\omega_1 - \omega_2 \cos\theta)\frac{p_z}{K}\right],$$

$$R' = R - \omega_1\omega_2(1-\cos\theta),$$

$$E = (p_z + m^2)^{\frac{1}{2}},$$

and $X_{int} = \frac{1}{2\pi}\int_0^{2\pi} X\, d\gamma$ and $p_{min} \approx p_z$.

The second term in eq. 2.16 is of order $\frac{p_z}{m}$ and can generally be ignored giving the usual zeroth order expression of the Ribberfors cross section,

$$\frac{d^2\sigma}{d\Omega d\omega} = \frac{m^2 r_o^2 \omega_2}{2\omega_1 KE} \tilde{X}\, J(p_z) \qquad 2.17$$

Eq. 2.17 has come to be accepted as the standard cross section for use by experimentalists and is completely general with respect to scattering angle. All measurements in the present work are analysed using this expression.

In the case of severe relativistic electronic motion, the second term in eq. 2.16 can be included to provide a rapidly converging iterative technique for Compton Profile extraction, viz.

$$J_1(p_{min}) = J_o(p_{min}) - \frac{E(p_{min})}{\tilde{X}} \int_{p_{min}}^{p_{max}} \frac{J_o(p)}{E(p)} \frac{dX_{int}}{dp}\, dp \qquad 2.18$$

However for present experimental purposes with error characteristics of $\sim$ 1% J(o), the zeroth order expression is completely adequate.

2.5. Multiple Scattering

In a typical Compton experiment the accumulated spectrum of inelastically scattered radiation contains a portion that is attributable to photons undergoing more than one collision in the target (DuMond, 1930). These multiple scattering events (of which at least one is inelastic) may easily contribute as much as 15% to the accumulated profile. The proportion of multiple scattering depends on the dimensions of the target compared with the mean free path for the radiation. There is no simple relationship between the cross section of multiply scattered radiation and the dynamics of the electron distribution and therefore this contribution must be removed from the measured spectrum before the Compton Profile can be defined. The

current technique for effecting this correction is described in Chapter 4 and will be dealt with only briefly here.

Two approaches to a solution have been considered. One is to perform the experiment in such a way that multiple scattering is not present (or at least minimised) and the other is to determine the contribution in a given situation and then remove its effect in some way.

Assuming a certain geometry and an average cross section for scattering (elastic and inelastic) for all energies, Williams and Halonen (1972) have shown the ratio of double to single scattering to be proportional to an effective length λ, such that

$$\lambda = \int_0^t \exp(-\mu z)dz \qquad 2.19$$

where t is the thickness of the target and μ the average absorption coefficient. At large t the ratio tends to a constant value proportional to $\frac{1}{\mu}$ and for small thicknesses it varies as t. Thus reducing t in general reduces the amount of multiple scattering present. This unfortunately has the effect of reducing the single cross section too and the signal usually becomes too small compared with the background noise. The required accumulation time also grows inconveniently large.

The existence of an expression like eq. 2.19 suggests that a way of removing a multiple contribution would be to make several measurements on targets of different thickness and then to extrapolate the data to zero t. However the true dependence of the multiple spectrum on t is far from simple (and not general) and indeed the shape of the spectrum can vary with thickness as noted in measurements on silicon by Reed and Eisenberger (1972). A point by point (in momentum or energy space) extrapolation of a Compton profile to zero thickness cannot therefore be performed.

Such an extrapolation implies an implicit determination of the intensity of multiply scattered radiation. This can be measured explicity by using a displaced beam technique so that collimation excludes the detection of

singly scattered photons (Hulubei, 1934). Again however the multiple spectrum depends strongly on the displacement adopted and extrapolation cannot be considered exact. The most successful explicit determinations have arisen from analytical or numerical calculations. Of these, analytical results can only be produced for the very simplest of geometries whereas the numerical techniques of the Monte-Carlo method (Felsteiner et al, 1974) are quite general in their applicability.

There are two main Monte-Carlo correction methods in current use. The first, adopted throughout this present work, generates a scattered spectrum of both double and triple events which can then be subtracted from the renormalised measured profile (see §4.2). This method requires only one measurement and one calculation and is therefore quite efficient of time. The second approach involves a series of measurements on targets of varying thickness and a separate calculation for each. It has been found experimentally (Felsteiner & Pattison, 1980) that the value of J(q) observed at each momentum point varies nearly linearly with the proportion of multiple events present, i.e.

$$J_{obs}(q) = J(q)\left[1 + a(q)\frac{N_{mult}}{N_s}\right]$$

where N_{mult} = normalisation of multiple events

N_s = normalisation of single events.

This second technique then allows a straightforward linear extrapolation for each J(q) to zero proportion of multiple scattering. The accuracy of this technique is not yet sufficiently well substantiated for the requirement of several time consuming measurements to be overlooked. For this reason the former and earlier devised technique has been preferred for this work.

CHAPTER 3

EXPERIMENTAL METHOD AND ANALYSIS PROCEDURE

3.1. Consideration of the Method

Chapter 2 discussed the theory of interaction of γ-rays with matter and defined the conditions under which the measured differential scattering cross-section can be simply related to the Compton profile of the scatterer. This chapter examines the apparatus required to make a measurement under these conditions and introduces the factors which enhance the expression - eq. 2.11 describing the measurement. The general procedure for removing these effects is set out in §3.3. A brief mention is made of the alternative scattering techniques for obtaining Compton profiles with an emphasis on the different experimental and theoretical problems encountered. This allows the particular advantages of the γ-ray method to be more clearly understood and thus indicates the areas where the data analysis should be performed with care. Two new experimental Compton spectrometers are briefly described and the performance of the high energy system is examined with reference to early measurements of Vanadium, the data having been processed only in a cursory fashion. This served as an indication that the final achievable accuracy would be consistent with the design aims for the new system.

3.1.1. Gamma Ray System Design

The Compton spectrometer employed to measure the electron momentum distributions of transition metals described in this present work consists of a ^{198}Au γ-ray source (412 keV) of rectangular cross-section

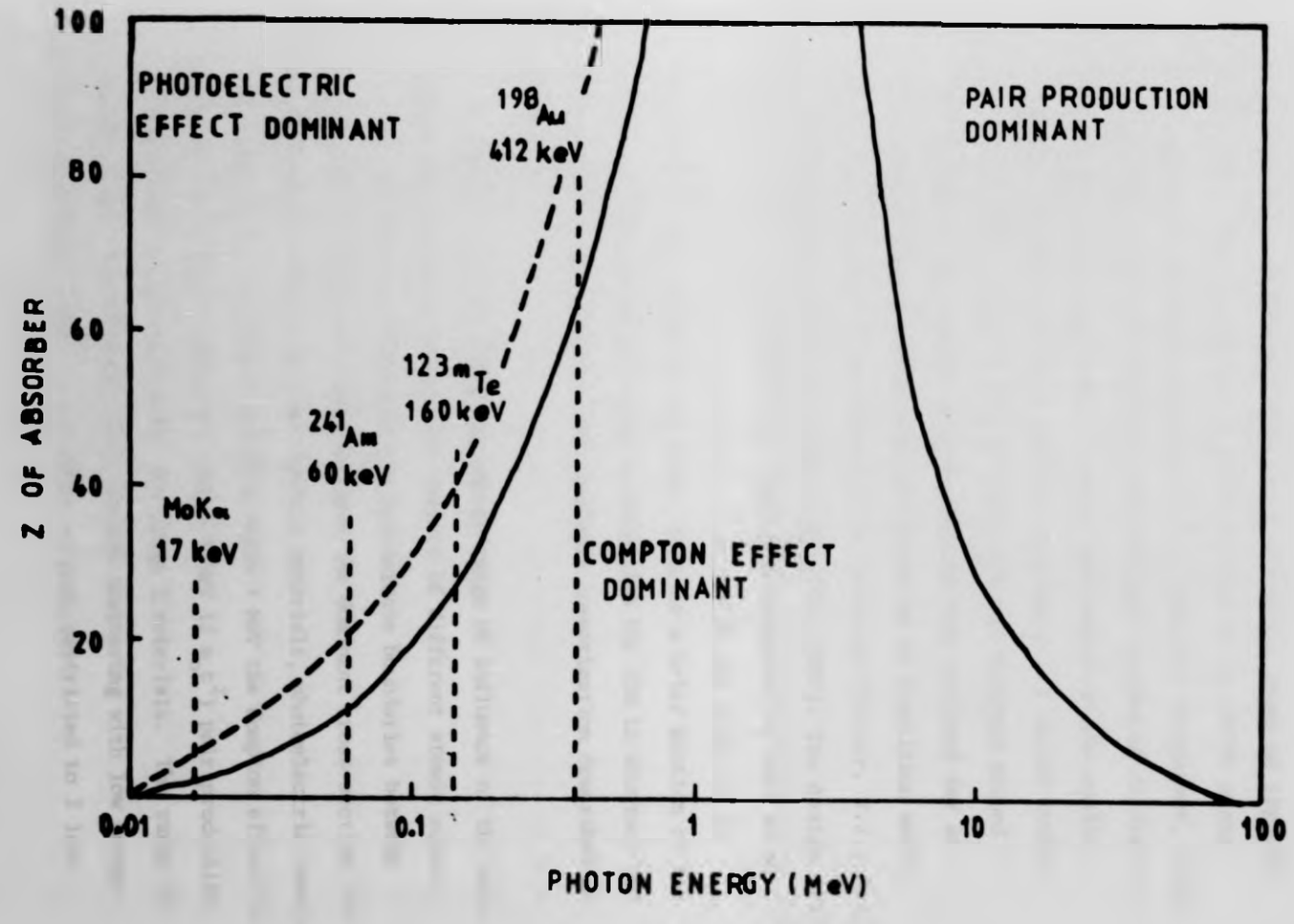

Figure 3.1. Regions of Dominance of Photon-Electron Cross-Sections (solid boundaries). The dashed curve roughly denotes a 1% error in the Impulse Approximation result

and an intrinsic Ge solid-state detector feeding a pulse height analyser (multi-channel analyser). The target sample is located in an evacuated chamber and subtends a scattering angle of approximately 167°. The system was designed by Holt et al (1979) along the lines of an existing apparatus at ILL, Grenoble (Schneider, 1974) but dedicated primarily to Compton experiments instead of diffractometry as the latter had been. A great improvement in the quality of results was expected with this new instrument. A second system intended for the study of lighter materials was designed around a ^{241}Am annular γ-ray source (60 keV) and has been utilised for an investigation into the cross-section variation of transition metal alloys as a method of non-destructive analysis (Cooper, M.J., Rollason, A.J. and Tuxworth, R.W.: J.Phys.E, 15, 568, 1982). The design criteria for these two systems have been extensively analysed by Holt et al (op. cit.), Holt (1978) and Cooper et al (1978) and need not be reproduced in any great detail here. However a brief mention of the more basic principles will help to establish the aim in accuracy and the context of the rigorous data analysis investigation described in Chapter 4.

Figure 3.1 illustrates the energy range of influence of the major photon interaction processes for targets of different atomic number, Z. The solid curves represent the approximate boundaries between regions where different processes have the dominant cross-section. At low energies, for all but the lightest materials, photoelectric absorption dominates. At higher energies below 1 MeV the Compton effect is dominant for Z up to about 80. Above 1 MeV ($2 m_o c^2$) pair production can occur and is more efficient for large Z materials. The range of materials that can be studied by Compton scattering with low energy X-rays ($\sim Mo K_\alpha$, 17 keV) is therefore severely restricted to Z less

than about 10. The penalty for attempting to extend the range of measurement with X-rays is a strong reduction in scattered intensity, failure to eject inner electrons and of the Impulse Approximation.

The use of γ-ray sources, and in particular ^{198}Au, enables measurements to be made up to $Z \sim 80$. The energies of several commonly available γ-ray sources are shown on the diagram. The dashed curve is an approximate indication of the locus of a 1% error in the Compton cross-section due to a failure of the IA. The error in the IA was found by Eisenberger and Platzman (see §2.4.3.) to be of the order $\left(\frac{E_B}{E_R}\right)^2$ where E_B is the binding energy of an electron and E_R the recoil energy after the photon has been scattered. The maximum error occurs for the two K-shell electrons which contribute a low background to the Compton profile. The error in the total profile is therefore of the order $\frac{2}{Z}\left(\frac{E_B}{E_R}\right)^2$. Requiring that this error be less than 1% means that the range of targets that can be investigated with a given energy must be restricted to the area below the dashed curve.

Table 3.1 lists the half lives of the common γ-ray sources along with both the primary and secondary energies and also those lines due to any contaminants usually present. (Data obtained from Lederer, 1967). Up to the present, most experimental work has concentrated on the three sources 123m Te, 241 Am and 198 Au, with 51 Cr recently being examined. The source 241 Am is very convenient to use because of the long half life making it a 'permanent' source, whereas the gold source must be renewed every two weeks. The usefulness of each of these sources depends on other factors than just their energy and specific activity I_o given by

$$I_o = \frac{N_A \ln 2}{A T_{\frac{1}{2}} M} \text{ photons/unit time/g over } 4\pi \text{ s.r.}$$

Source	Half Life	Main Energy (keV)	Relative Intensity	Other Energies (keV)	Relative Intensity
$^{51}_{24}Cr$	27.7d	320.1	-	-	-
$^{123m}_{52}Te$	119.7d	159.0	100	247.5 88.5	10 0.11
$^{137}_{55}Cs$	30.2y	662.0	-	-	-
$^{198}_{79}Au$	2.7d	411.8	100	1088.0 676.0	0;16 0.97
$^{199}_{79}Au$	3.1d	158.2	100	208.2 49.8	22.1 0.64
$^{203}_{80}Hg$	46.8d	279.2	-	-	-
$^{241}_{95}Am$	458y	59.6	100	43.4 33.2 26.4	8.3 0.6 0.6

Table 3.1. γ - Ray Sources for Compton Spectrometers (Data from Lederer et al, 1967)

where M = atomic mass, N_A = Avogadro's constant and $T_{\frac{1}{2}}$ = half life. Their limitations are also governed by the purity and the presence of other γ-ray emissions. The low energy of the Americium line and strong self-absorption is responsible for limiting the maximum surface activity to about 0.8 Ci cm^{-2} (1 Curie, Ci ≡ 3.7×10^{10} Bq, Becquerel) whereas activities of several hundred Curies can be obtained with current gold sources produced by neutron irradiation of 197 Au.

The gold source was chosen as the basis for the new spectrometer system. Under neutron bombardment in the Dido Reaction at Harwell, the rectangular gold foils 0.25 mm thick undergo the reactions

$$^{197}Au\ (n,\gamma) \rightarrow {}^{198}Au \xrightarrow[T_{\frac{1}{2}}=2.7d]{} {}^{198}Hg + \gamma\ (412\ keV) + \beta^-$$

and

$$^{198}Au\ (n,\gamma) \rightarrow {}^{199}Au \xrightarrow[T_{\frac{1}{2}}=3.2d]{} {}^{199}Hg + \gamma\ \begin{matrix}(208\ keV)\\(158\ keV)\end{matrix} + \beta^-$$

Holt et al (op. cit.) found that irradiation of one foil 6.5 mm square for 2 days would produce a useful activity of ∿ 100 Ci. However this was accompanied by almost 50 Ci of the 158 keV emission which was unacceptable. Due to the difference in neutron cross-section for the 197 Au and 198 Au isotopes it was found possible to reduce this secondary emission drastically by irradiating 4 foils for only one quarter of the time. Thus after 12 hours irradiation 120 Ci of 412 keV emission are produced and, reduced further by stronger self absorption, the 158 keV emission is negligible.

By using solid state detectors feeding multi channel analysers a complete spectrum can be measured in a few days - dependent on the sample size and cross-section. For the Americium system the detection efficiency is very good, remaining at 100% over the entire range of the

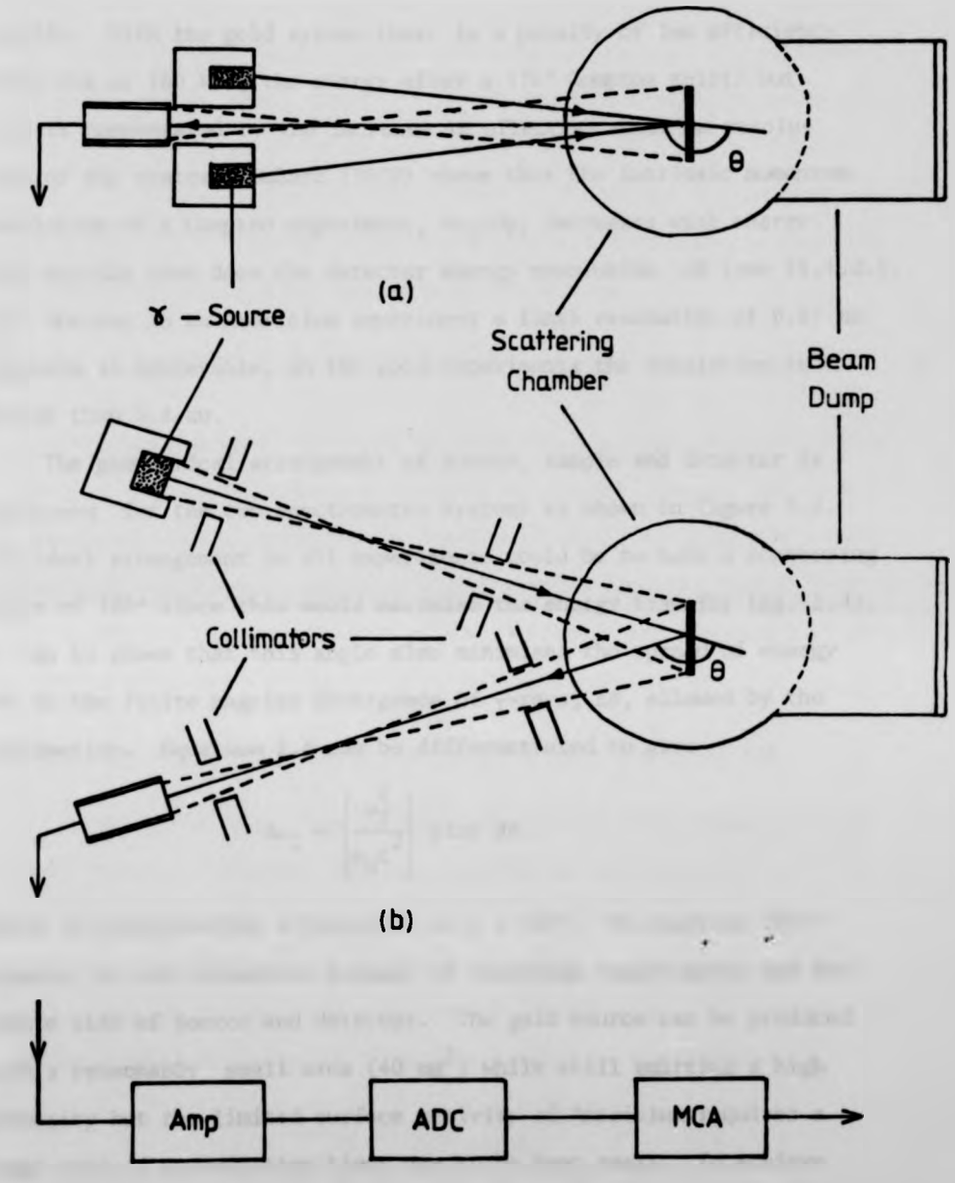

Figure 3.2. Compton Spectrometer Geometries (a) Annular Source (Americium Spectrometer) and (b) Planar Geometry (Gold Spectrometer). The lower part of the figure shows the standard data – logging electronics.

profile. With the gold system there is a penalty of low efficiency (only 20% at 160 keV, the energy after a 170° Compton shift) but this is compensated by the increase in effective momentum resolution of the system. DuBard (1979) shows that the intrinsic momentum resolution of a Compton experiment, $d\omega_2/dp$, increases with energy more quickly than does the detector energy resolution, ΔE (see §4.1.2.). Thus whereas in an Americium experiment a final resolution of 0.57 au momentum is achievable, in the gold experiments the resolution is better than 0.4 au.

The geometrical arrangement of source, sample and detector is different for the two spectrometer systems as shown in figure 3.2. The ideal arrangement in all experiments would be to have a scattering angle of 180° since this would maximise the energy transfer (eq. 2.4). It can be shown that this angle also minimises the spread of energy due to the finite angular divergence of γ-rays, $\Delta\theta$, allowed by the collimation. Equation 2.4 can be differentiated to give

$$d\omega_2 = \left(\frac{\omega_2^2}{m_o c^2}\right) \sin\theta \, d\theta$$

which is minimised for a finite $\Delta\theta$ at $\theta = 180°$. In practice 180° geometry is not achievable because of shielding requirements and the finite size of source and detector. The gold source can be produced with a reasonably small area (40 mm^2) while still emitting a high intensity but the limited surface activity of Americium requires a large area if accumulation times are to be kept small. To achieve this while keeping θ close to 180° and $\Delta\theta$ as small as possible an annular source is used as in figure 3.2a with the detector aligned with the axis. Because of this arrangement the two systems are not equivalent. With the Americium system the scattering vector is not uniquely defined and lies along the generator of a cone with the sample

at the apex. This means that the annular system is not very suitable for measuring directional Compton profiles but rather for isotropic materials of low atomic number. The layout of the gold system which utilises a planar geometry is represented schematically in figure 3.2.b. In this case the scattering vector is defined within the limits allowed by angular divergence alone and the system is suitable for measuring anisotropic momentum distributions.

3.1.2. Alternative Experimental Methods of Obtaining the Compton Profile

Strictly speaking, the term 'Compton Profile' applies only to the result of a photon-electron scattering experiment, however there are a number of related experimental techniques which also measure a projection of the electron momentum density - the Impulse Compton profile. The advantages and restrictions of these methods are discussed in detail by Reed (1976) and will be briefly described here.

ACPAR (Angular Correlation of Positron Annihilation Radiation)

A positron (e.g. from a ^{64}Cu source) is injected into a target where it rapidly achieves thermal equilibrium with the material. At some later time it annihilates with a target electron to emit two photons, generally of very different energy, at an angle depending upon the transverse component of momentum of the electron. The two photons are detected in coincidence to give a measure of the function

$$\rho(\bar{p}) = \left| \int e^{i\bar{p}.\bar{r}} \psi_+(\bar{r}) \psi(\bar{r}) d^3\bar{r} \right|^2 \qquad 3.1$$

(see West, 1973 for a detailed derivation). Apart from the term $\psi_+(\bar{r})$ describing the positron wavefunction, this expression is just the electron momentum density as in a photon scattering experiment.

This technique has a number of advantages over Compton scattering. First the resolution obtainable is an order of magnitude better, depending on the angular precision with which the coincidence counters can be manoeuvered. Secondly, although the usual parameter measured is the projection of eq. 3.1 onto a line (long slit geometry) as in the Compton experiment, it is also possible to measure the projection in a plane (by using point slit geometry). Investigations have also been made (Dauwe et al, 1972) into the detection of the photons' energies. This would yield the third component of momentum and the three dimensional function $\rho(\bar{p})$ could be measured directly.

Unfortunately the disadvantages of ACPAR are also numerous. The greatest problem arises with evaluating $\psi_+(\bar{r})$ which is not uniform and must be solved self consistently within the crystal potential and field of the other electrons. Apart from this mathematical difficulty there is also the physical problem due to the fact that $\psi_+(\bar{r})$ always avoids the positively charged nuclei and this does not sample the inner and outer electrons to the same extent. There is also introduced a significant component of $e^+ - e^-$ correlation which acts in a manner opposed to the effects of electron-electron correlation in the pure material. Furthermore, unless the sample contains no crystalline defects, the positron will be preferentially trapped at the defect sites and will not sample the average ground state electron distribution.

HEEIS (High Energy Electron Impact Spectroscopy)

A second method of obtaining information about the electron momentum distribution was first investigated by Hughes and Mann (1938). This involves the inelastic scattering of high energy electrons and under the conditions of the Binary Encounter Approximation (equivalent to the IA of Compton Scattering) leads to a measurement of J(q). This method has the advantage of very good momentum resolution and the high cross-

section for electron interactions ensures rapid accumulation of data - about 1 hour is required for 0.5% accuracy in each profile. Unfortunately exchange and correlation effects between the incident and scattered electrons and large amounts of multiple scattering limit the use of the technique to low Z, gaseous samples and it is therefore completely unsuitable for the study of metals.

(e,2e) Method

In this recent electron scattering technique, the recoil electron is detected in coincidence with the scattered electron. McCarthy (1973) has shown that, as a result of the extra information about the target that can be obtained in this way, the cross-section is proportional to $\rho(\bar{p})$ itself rather than any projection. In one mode of operation, the incident electron energy can be varied and the recoil electrons are ejected from different ionisation shells. This implies that it is possible to measure the momentum density of individual electron orbitals directly - a very useful facility. However, as with HEEIS, the energy transfer is low and the technique is again restricted to gases with electrons of low binding energies.

To summarise then, γ-ray Compton scattering is the most generally applicable technique with no fundamental restrictions as to the type of system that can be studied. For a particular range of materials other techniques can yield the Compton profile more readily but with regard to Transition Metals only CS and ACPAR can be employed - and the latter is less sensitive to the more localised 3d electrons. Experimentally, the CS apparatus is the simplest in construction and operation and also the cheapest. The statistical accuracy obtainable is reasonably good but may require several days accumulation depending on the sample size. The only disadvantage of this technique is the limited momentum resolution obtainable with current solid state detectors

but this is a severe restriction only when Fermi surfaces are to be measured - in all other cases of comparison with theory, resolutions of $\sim$ 0.4 au are quite adequate.

3.2. Gold Spectrometer System

3.2.1. Apparatus

The high energy Compton spectrometer located at the Rutherford Appleton Laboratory recently designed and described by Holt et al (1979) is shown in plan view in figure 3.3. The 198 Au source, contained in a transportable tungsten alloy block, consists of a rectangular foil sandwich originally 6.5 mm square x 1 mm thick, facing the sample direction. The source dimensions were later changed to 5 mm high x 3 mm wide x 2 mm thick to cut down the emission of 159 keV γ-rays and also to reduce the geometric divergence of the incident beam (see §4.2.2.). In either case the source was activated to $\sim$ 120 Ci by bombardment with neutrons for $\sim$ 12 hours in the Dido reactor at Harwell.

A great improvement in both signal strength and signal to noise ratio over the existing system at ILL, Grenoble was one of the design aims for this spectrometer. This was mainly achieved by reduction of the incident and scattered beam path lengths. The system was designed to have two alternative sets of collimation lengths. In the long geometry configuration shown, these were

source to sample	476 mm
sample to detector	594 mm

and in the shorter configuration (for which it is necessary to remove the two tungsten alloy plates between the source block and the scattered beam collimator) they are

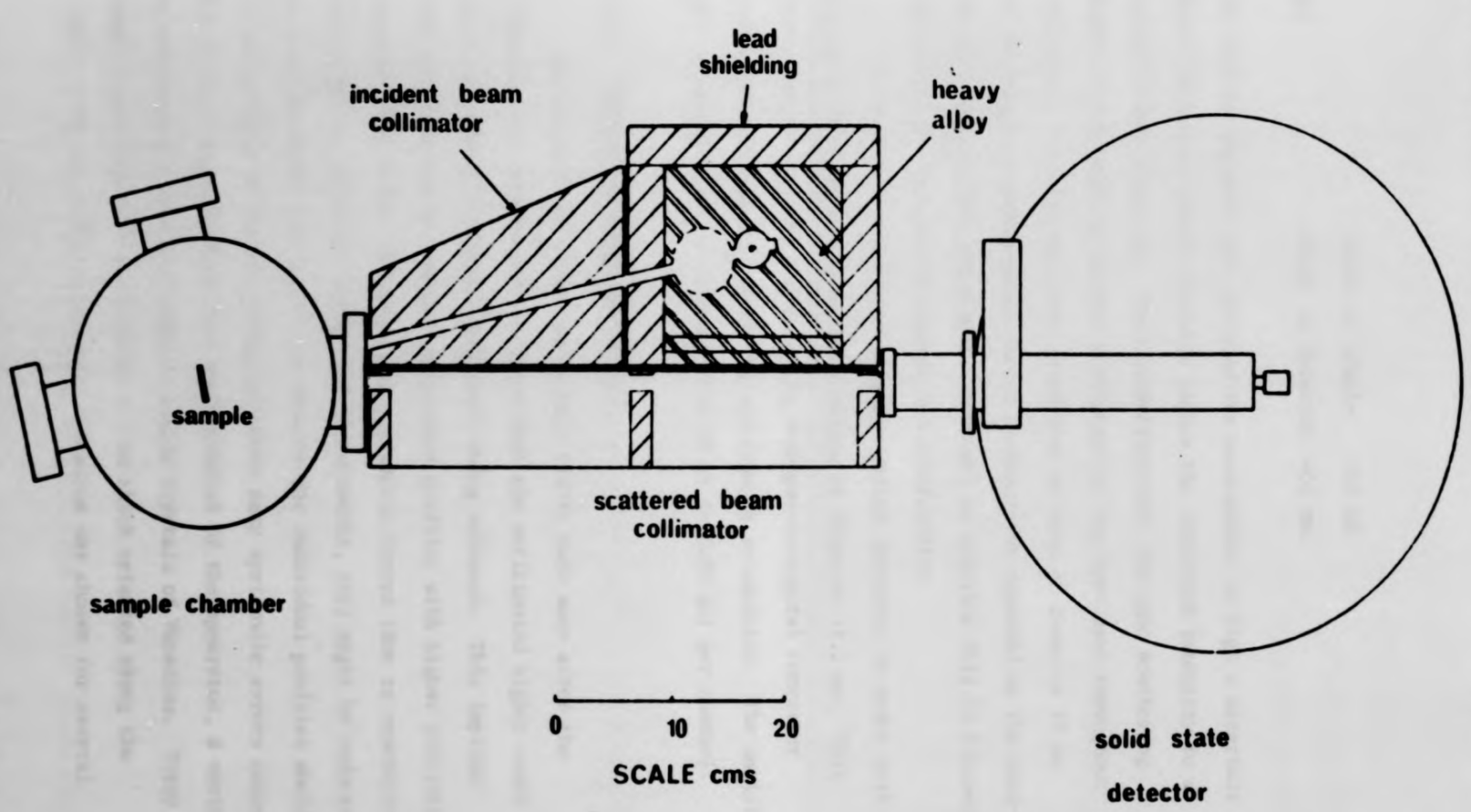

Figure 3.3. Plan View of the ^{198}Au (Rutherford Laboratory) Compton Spectrometer

(Diagram taken from Holt, 1978)

source to sample 363 mm

and sample to detector 462 mm.

The shorter geometry was provided for measurement of high z materials where absorption would otherwise reduce the scattered intensity to a prohibitively low level. Both geometries have the same scattering angle of 167° and the shorter configuration has been used throughout this work. The incident beam irradiates an area of diameter 18 mm at the sample position which should therefore be regarded as the minimum size desired for any sample. However, in practice this is frequently impossible for reasons of expense and availability.

The detector is a liquid nitrogen cooled intrinsic Ge model with a crystal thickness of 8 mm and a window of diameter 11.2 mm. This feeds signals via amplifiers and an Analogue-to-Digital Converter into a 4096 channel MCA where the spectrum is accumulated. The amplifier gain is usually set to correspond to 50 eV ($\sim$ 0.03 au) per channel.

3.2.2. Initial Proving Experiments

Measurements of aluminium by Holt (1978) made soon after the apparatus was constructed confirmed that the anticipated higher count rates and signal to noise levels were being achieved. This implied that it would now be possible to measure profiles with higher statistical accuracy than before and also that systematic errors (due to resolution tail effects, incorrect background measurements, etc) might be reduced to a sufficiently low level that results for individual profiles would be as reliable as for anisotropies (where many systematic errors cancel). For a first investigation into the potential of the apparatus, a series of measurements were performed on single crystals of Vanadium. These samples were discs 10 mm diameter x 2 mm thick oriented along the (100), (110) and (111) directions. Vanadium was chosen for several

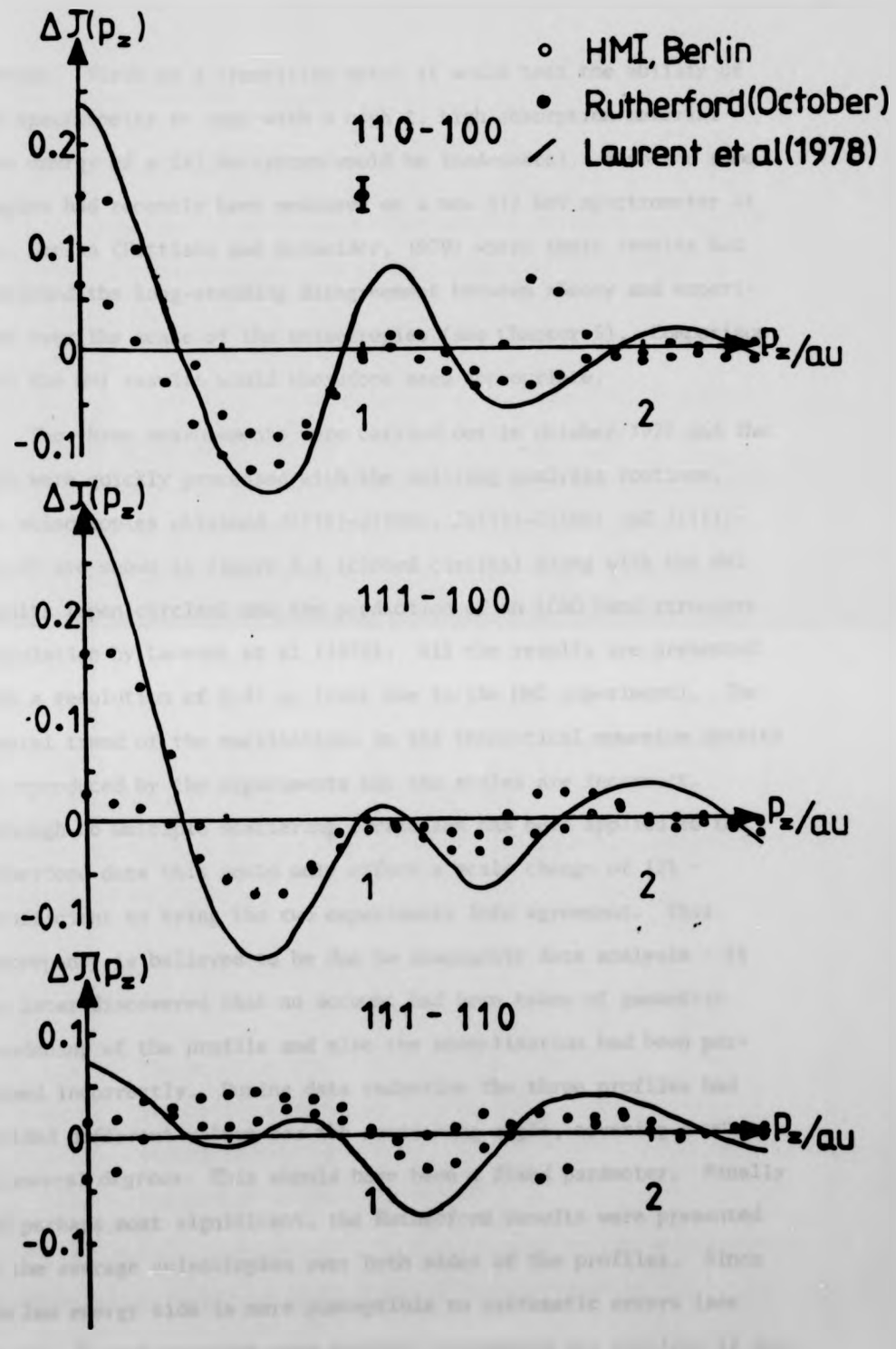

Figure 3.4. Preliminary Measurement of Vanadium Profile Anisotropy

reasons. First as a transition metal it would test the ability of the spectrometer to cope with a high Z, high absorption material (the energy of a 241 Am system would be inadequate). Also the same samples had recently been measured on a new 412 keV spectrometer at HMI, Berlin (Pattison and Schneider, 1979) where their results had confirmed the long-standing disagreement between theory and experiment over the scale of the anisotropies (see Chapter 5). Comparison with the HMI results would therefore seem appropriate.

The three measurements were carried out in October 1979 and the data were quickly processed with the existing analysis routines. The anisotropies obtained J(110)-J(100), J(111)-J(100) and J(111)-J(110) are shown in figure 3.4 (closed circles) along with the HMI results (open circles) and the prediction of an LCAO band structure calculation by Laurent et al (1978). All the results are presented with a resolution of 0.41 au (that due to the HMI experiment). The general trend of the oscillations in the theoretical momentum density is reproduced by the experiments but the scales are incorrect. Although no multiple scattering correction has been applied to the Rutherford data this would only effect a scale change of 12% - insufficient to bring the two experiments into agreement. This discrepancy is believed to be due to inaccurate data analysis - it was later discovered that no account had been taken of geometric broadening of the profile and also the normalisation had been performed incorrectly. During data reduction the three profiles had yielded different values for the scattering angle, covering a range of several degrees. This should have been a fixed parameter. Finally and perhaps most significant, the Rutherford results were presented as the average anisotropies over both sides of the profiles. Since the low energy side is more susceptible to systematic errors (see Chapter 4) more rigorous data analysis procedures are required if data

in this region is to be considered reliable.

3.3. Data Reduction Procedure

Data reduction in the Compton scattering experiment starts with eq. 2.11 which can be written in terms of the scattered energy as

$$D(\omega) = C(\omega)\ J(\omega) \qquad 3.2$$

where $D(\omega)$ is the second differential cross section, $C(\omega)$ describes the interaction (e.g. Ribberfors cross section) and $J(\omega)$ is the Compton profile. During the data processing one attempts to extract $D(\omega)$ from the measured spectrum $M(\omega)$ by removing the effects of all contributing experimental parameters which are either additive, factoral or convolutive. A general description of the corrections required is given in Williams (1977). An analysis of these and other corrections is reported in Chapter 4 and has led to a better understanding of the experimental effects and a corresponding improvement in accuracy of the final profile, particularly in the low-energy side.

The overall strategy is represented by the equation describing the measured spectrum,

$$M(\omega) = R(\omega) * G(\omega)A(\omega)D(\omega) + B(\omega) \qquad 3.3$$

where

- $R(\omega)$ → the total system resolution function
- $G(\omega)$ → the detector efficiency function
- $A(\omega)$ → sample absorption
- $B(\omega)$ → background noise distribution

and * represents a convolution. The Compton profile can be calculated from the measured data by application of the equation

$$J(\omega) = NC^{-1}(\omega)A^{-1}(\omega)R(\omega)^{*-1}G^{-1}(\omega)[M(\omega)-B(\omega)] \qquad 3.4$$

	SUBJECT INVESTIGATED	FUNCTION / RESULT		
PRELIMINARY SYSTEM MEASUREMENTS	(1) Se source spectrum & energy calibration (2) Te source line spectrum & energy calibration	(1) Detector efficiency function, G (2) Detector energy resolution function, R_1		
SUBSIDIARY CALCULATIONS	(1) γ source emission line (2) Apparatus collimation (3) Free atom normalisation (4) Sample multiple scattering	(1) Source broadening function, R_A (2) Geometry broadening function, R (3) N, fixed p range (4) Spectrum & proportion of multiple events	Data Reduction Procedures	J (p) with momentum resolution Δp
EXPERIMENTAL DATA MEASUREMENTS	(1) Sample spectrum (2) Background spectrum (3) Exposure timings	(1) Data, M (2) Noise, B (3) Background time - correction ratio		
OTHER DATA	(1) Sample parameters (2) System parameters			

Table 3.2. Compton Scattering Experiment Structure

(N is a suitable normalisation constant). Reading from right to left this is interpreted as

(1) Subtract a background spectrum from the data

(2) Correct for varying detector efficiency

(3) Remove the convolution due to finite system resolution

(4) Correct for absorption in the sample

(5) Apply the Ribberfors cross section correction

(6) Normalise the data.

It should be noted that up to this point no account is made for multiple scattering effects in the spectrum. This correction is applied later after renormalisation of the data. Also, the total system resolution function has previously been taken to be due solely to the detector energy resolution. The contributions from angular dispersion and source line broadening are discussed in §4.2.

Table 3.2 tries to illustrate the structure of a Compton experiment with regard to the several measurements and calculations which must be made in order to obtain a single Compton profile. Fortunately, all of these determinations do not have to be repeated for each experiment. The data describing the spectrometer apparatus need be obtained only once with an occasional check to ensure that the system (e.g. detector energy resolution) has not degraded. At present the subsidiary calculations of angular divergence and the normalisation condition are performed during the data reduction procedures and the data analysis does not strictly follow the order of the chart. The complete set of data reduction procedures are listed in the order they are now performed in table 3.3. Stage (q) is carried out twice, the second iteration occuring after redefinition of the energy calibration. This ensures that the energy at the centre of the profile is correctly reproduced

	OPERATION / MEASUREMENT	COMMENTS
a	Measure detector efficiency	PE absorption curve fit
b	Measure detector energy resolution and calibration	^{121m}Te source (159keV)
c	Measure data and record timings	Compton Spectrum
d	Measure background and record timings	
e	Determine initial energy calibration for data	From Compton Spectrum
f	Calculate angular divergence profile in energy scale of data	Monte Carlo Simulation
g	Correct resolution function for detector efficiency	
h	Convert resolution function to energy scale of data	
i	Convolute above with angular divergence profile	Numeric Convolution
j	Determine total FWHM	Exp. Resolution in au
k	Subtract time corrected background from data	
l	Correct for detector efficiency	
m	Deconvolute data with total resolution function	FFT
n	Convolute with chosen FWHM	Profile resolution
o	Evaluate normalisation for chosen FWHM	Area of free atom CP
p	Correct data for sample / air absorption	
q	Convert to p scale and apply cross section correction	$p = p(\omega_2, \theta, \omega_1)$ Ribberfors
r	Normalise data	
s	Procedures for multiple scattering	Monte Carlo Simulation
t	Procedures for source line broadening	Monte Carlo Simulation - Deconvolution required

Table 3.3. Compton Profile Extraction Data Reduction Procedure

	OPERATION / MEASUREMENT	COMMENTS
a	Measure detector efficiency	PE absorption curve fit
b	Measure detector energy resolution and calibration	^{125m}Te source (159keV)
c	Measure data and record timings	Compton Spectrum
d	Measure background and record timings	
e	Determine initial energy calibration for data	From Compton Spectrum
f	Calculate angular divergence profile in energy scale of data	Monte Carlo Simulation
g	Correct resolution function for detector efficiency	
h	Convert resolution function to energy scale of data	
i	Convolute above with angular divergence profile	Numeric Convolution
j	Determine total FWHM	Exp. Resolution in au
k	Subtract time corrected background from data	
l	Correct for detector efficiency	
m	Deconvolute data with total resolution function	FFT
n	Convolute with chosen FWHM	Profile resolution
o	Evaluate normalisation for chosen FWHM	Area of free atom CP
p	Correct data for sample / air absorption	
q	Convert to p scale and apply cross section correction	$p = p(\omega_1, \theta, \omega_1)$ Ribberfors
r	Normalise data	
s	Procedures for multiple scattering	Monte Carlo Simulation
t	Procedures for source line broadening	Monte Carlo Simulation - Deconvolution required

Table 3.3. Compton Profile Extraction Data Reduction Procedure

by the predominant scattering angle calculated in stage (f). (As yet no attempt has been made to actually remove the effects of source-line broadening during stage (t) - this is anticipated in the near future.

The difference between the two spectrometer system configurations, their respective energy regimes and the absorption properties of the materials studied with each become apparent through the degree to which they affect the processes listed in table 3.3. For example, within the energy regime of the Americium system up to 60 keV, the detector efficiency correction is negligible since it remains constant (less than 1% variation) over this entire range. The general data analysis scheme can therefore be tailored to suit the specific applications as is done for the treatment of geometric broadening described in §4.2. The investigation of Chapter 4 into the accuracy of the individual data reduction procedures is therefore strongly biased towards optimisation for the analysis of transition metals. The results of these investigations are employed for the measurements of Vanadium and Iron in Chapters 5 and 6.

CHAPTER 4

DATA ANALYSIS

Chapter 3 presented the general approach towards extraction of a Compton Profile from the measured spectrum of a γ-ray scattering experiment. The physical processes which, untreated, would give rise to significant systematic errors were included in the scheme of table 3.2. They are analysed here in the simplest manner compatible with the required accuracy (e.g. as for the treatment of detector efficiency in §4.1.1.) and therefore the corrections need to be reviewed periodically, with the demand for more accurate results.

In the recent past the level of accuracy was such (∿ 1% J(o) on the high energy side of the profile) that it was possible to separate the corrections into two categories dependent on the ease of implementation. Thus energy calibrations were considered easy while multiple scattering corrections were considered problematical. The aim for greater accuracy engendered by the development of the new high energy spectrometer system has meant that even the "simple" corrections have become critical and the heuristic simple/difficult categorisation has had to be abandonned. In order to clarify the presentation of the problems of data analysis therefore, the strict order of processing has been rejected in favour of the generic scheme of table 3.2.

The following sections describe the developments that have been made to the existing procedures with the aim of regularly achieving systematic accuracies for profiles better than 0.5% J(o) over all the data - a statistical limitation currently imposed by the time available for accumulation of data. Those features which are more important with regard to transition metals are emphasized.

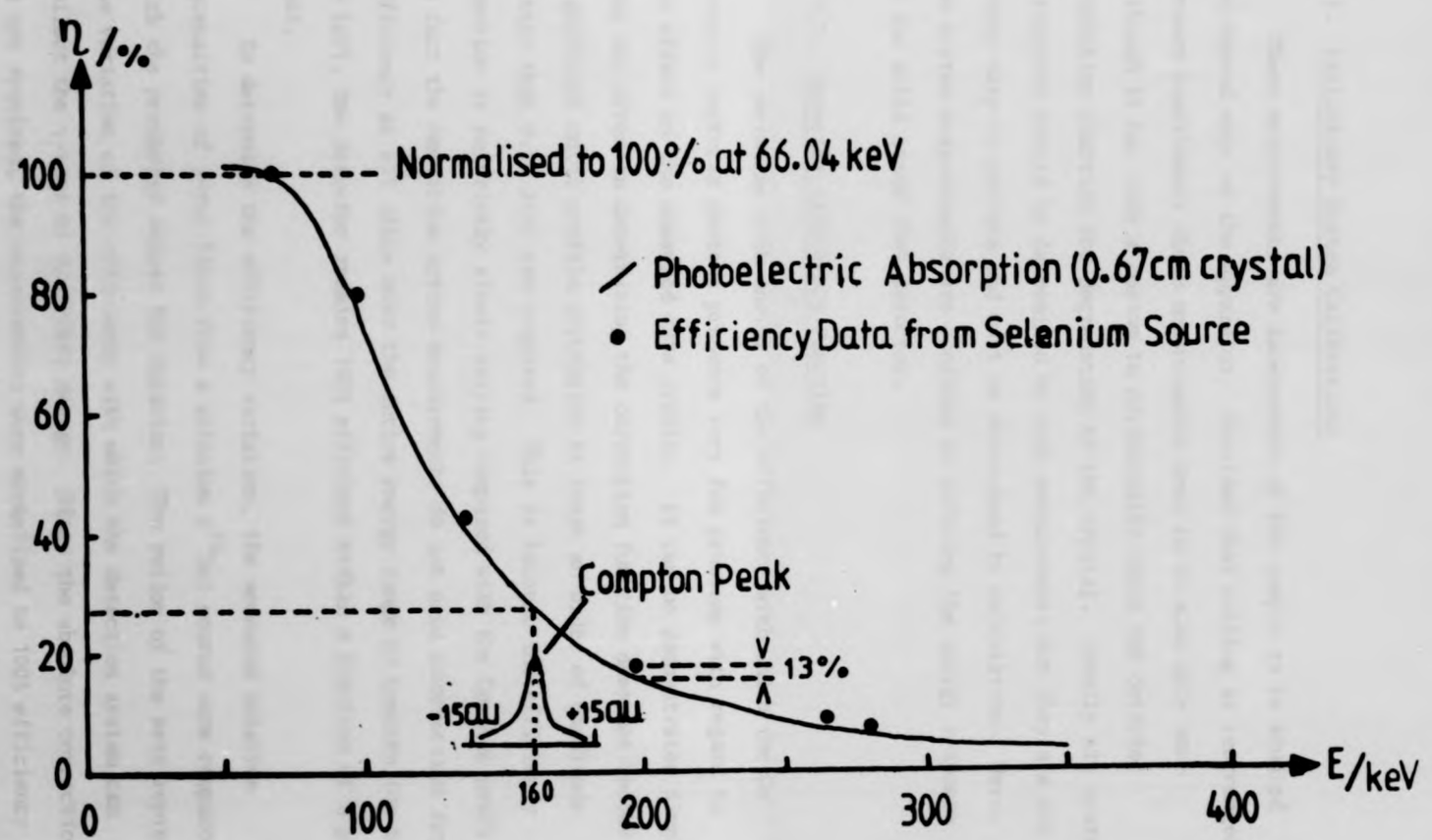

Figure 4.1. Germanium Detector Efficiency Determination

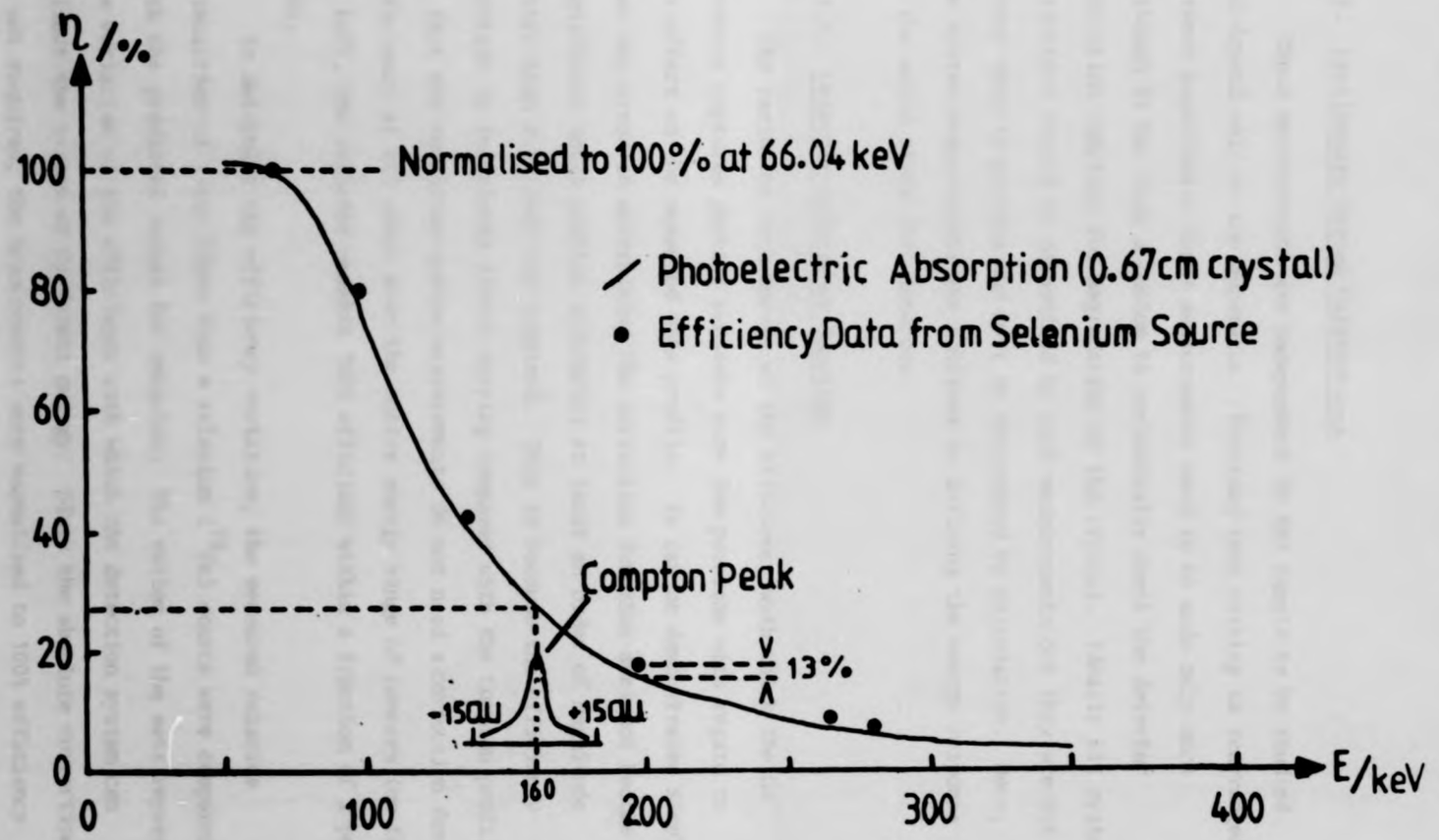

Figure 4.1. Germanium Detector Efficiency Determination

4.1. Preliminary System Calibrations

These measurements are independent of the sample to be studied and depend only on the apparatus. Provided that nothing is rearranged between experiments these measurements need to be made only once although it has been a custom to periodically check the detector resolution function for degradation of the crystal. Ideally all system parameters should be determined by such measurements but they are not always easy to perform and must be determined by calculation. Here, the system measurements are confined to defining the energy response of the solid state (Ge) detector.

4.1.1. Detector Efficiency Function

The variation with energy of the efficiency with which the Ge detector captures photons presents very few problems with regard to its effect on the measured data profile. It can be demonstrated simply that any error in determining the correction function does not become significant until profile accuracies at least an order of magnitude better than 0.5% J(o) are required. This is because the efficiency function is relatively slowly varying compared with the Compton profile. In fact the Americium system measurements do not need a correction for efficiency at all since over the entire energy range of concern (up to 60 keV), the detector remains 100% efficient within a fraction of a percent.

To determine the efficiency variation, the measured relative intensities of γ-ray lines from a selenium (^{75}Se) source were compared with the predicted values for emission. The ratios of the sets represents the variation of the efficiency with which the detection system can collect the γ-rays of different energy. Since the absolute correction is not required, the measurements were normalized to 100% efficiency

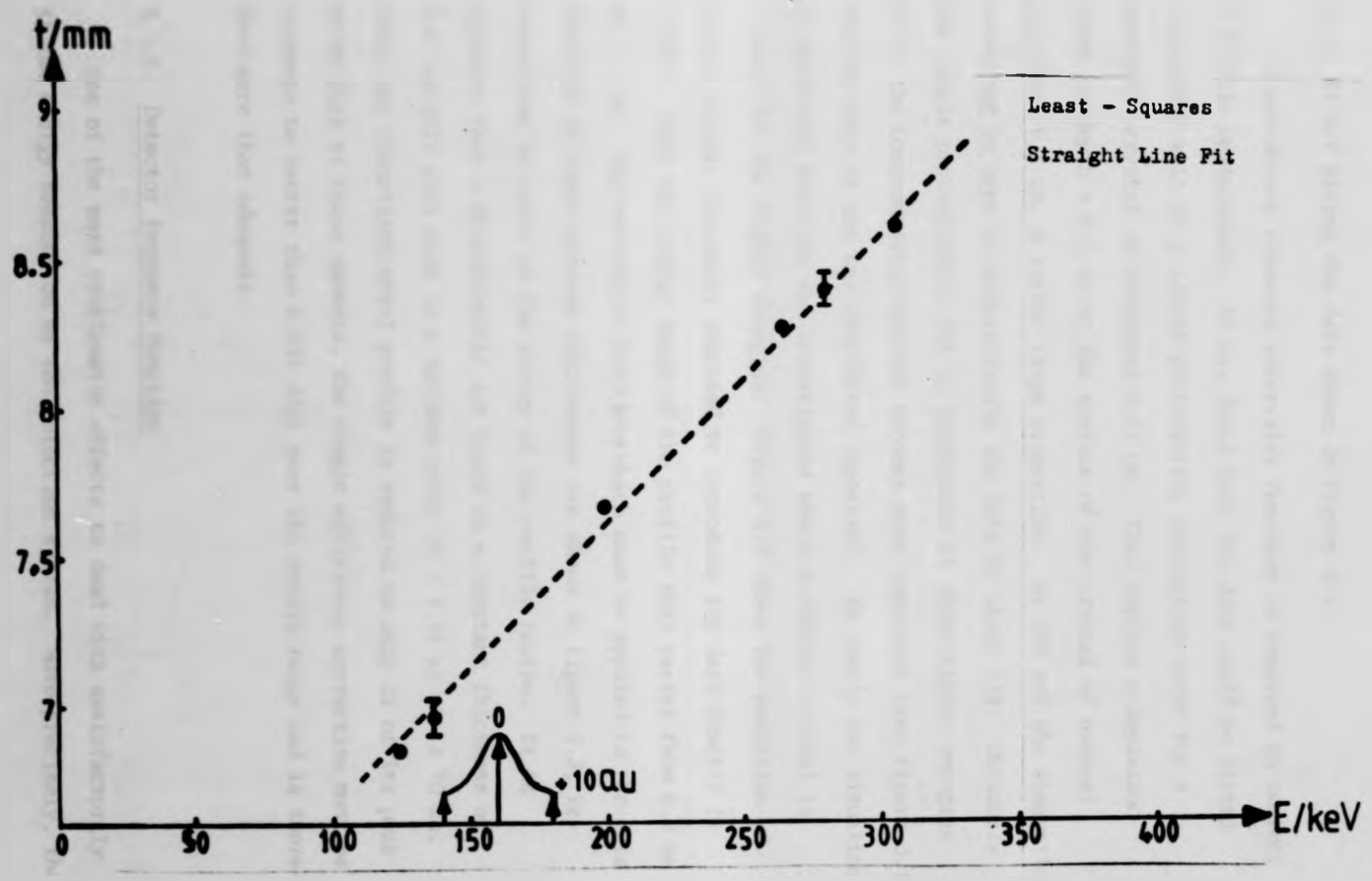

Figure 4.2. Empirical Photoelectric - Absorptive Crystal (Ge) Thickness. The data points represent the detector crystal thickness required to reproduce the measured detector efficiency at varying energy, considering PE absorption only.

at 66.04 keV giving the data shown in figure 4.1.

A continuous (channel intervals) function is required to correct a profile measurement. It was found that the data could be fitted reasonably well by a simple photelectric absorption curve for a germanium crystal of thickness 0.67 cm. This implies a depletion layer of depth $\sim$ 0.2 cm at the surface of the crystal of nominal thickness 0.8 cm, a rather large proportion. At 200 keV the absorption curve can be seen to underestimate the data by about 13%. Obviously the simple photoelectric fit is inadequate at these higher energies where the Compton cross-section becomes more important (see figure 3.1) but the ease of use was considered important. To remedy the situation an empirical function was investigated where a thicker crystal is assumed for the higher energies. Figure 4.2 shows the variation of active crystal thickness required to reproduce the data exactly (± 0.03%). Over the energy range of the profile this varies from 6.9 mm to 7.6 mm. The correction functions which must be applied to the data for each of these extreme thicknesses are shown in figure 4.3, re-normalised to unity at the energy of the profile centre. It is apparent that a photoelectric fit based on a constant thickness of 0.67 cm will give rise to a maximum error of $\sim$ 1.5% at $p' = \pm$ 10 au. Since any transition metal profile is reduced to only 2% of its peak value J(o) at these momenta, the simple efficiency correction must be accurate to better than 0.03% J(o) over the entire range and is therefore more than adequate.

4.1.2. Detector Response Function

One of the most problematic effects to deal with satisfactorily is the energy resolution of the detection system. More precisely, the

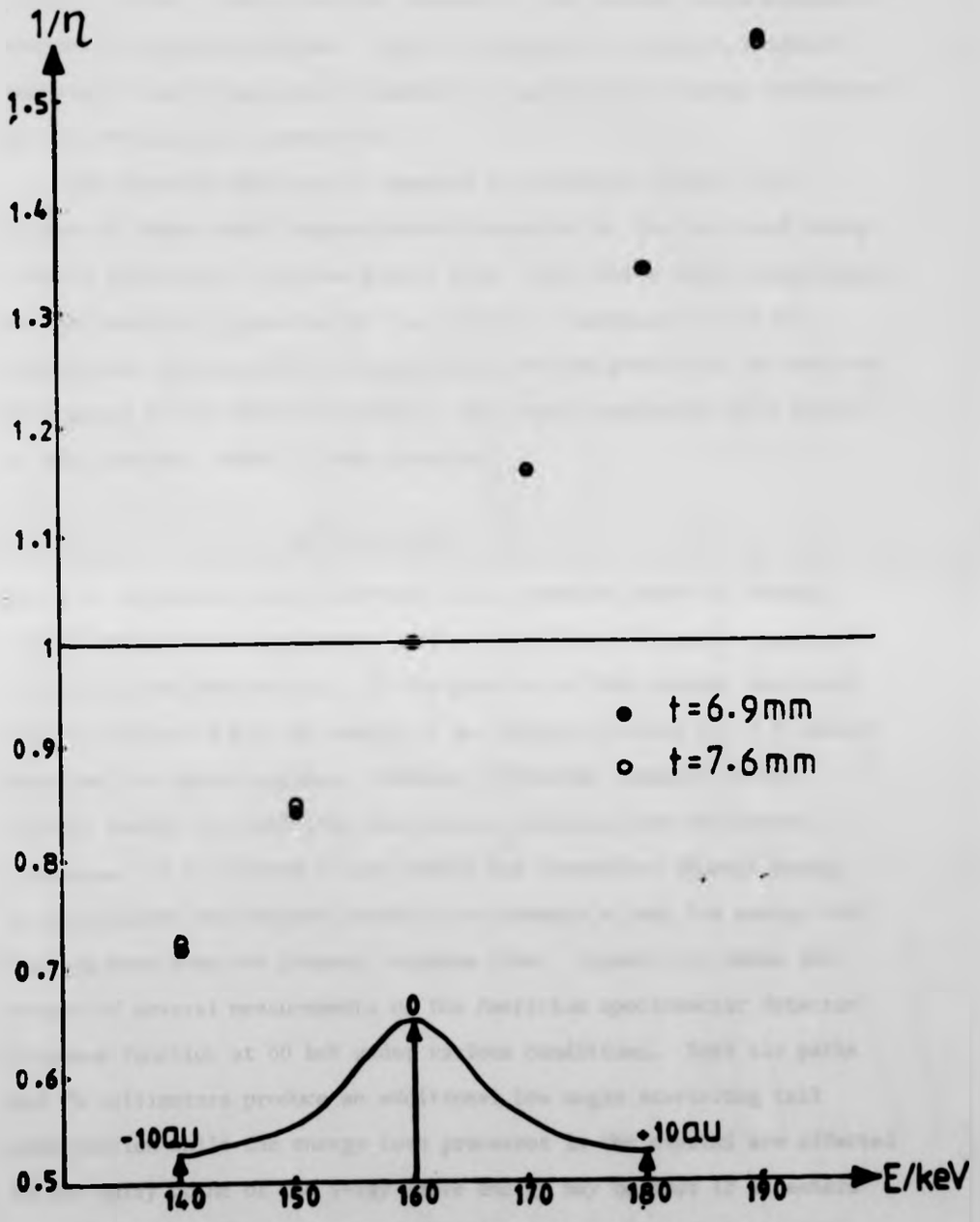

Figure 4.3. Detector Efficiency Correction Functions for Two Photoelectric Absorption Thicknesses (Ge)

problem is how to determine the response of the system to monochromatic sources at various energies. Once the response is defined, numerical techniques can be employed to handle it, and the final energy resolution of the profile can be specified.

The response function is composed of two parts (figure 4.4) - a line of finite width (approximately Gaussian) at the principal energy - and a long tail on the low energy side. The finite width (resolution) of the function is governed by two effects - electronic noise and statistical counting effects associated with the production of electron hole pairs in the detector crystal. The total resolution (full width at half maximum, FWHM) is then given by

$$\Delta E^2 = \alpha + \beta E \qquad 4.1.$$

where α represents the electronic noise, constant over all energy, and βE reflects the properties of the crystal with β another constant related to the Fano Factor. If the geometry of the crystal were such that it collected all the energy of any incident γ-ray, eq. 4.1. would describe the whole response. However, differing amounts of the primary energy are lost from the crystal, carried away by ejected electrons or as emitted X-rays (which may themselves deposit energy as they leave) and the net result is to produce a long low energy tail falling away from the primary response line. Figure 4.4. shows the result of several measurements of the Americium spectrometer detector response function at 60 keV under various conditions. Both air paths and Pb collimators produce an additional low angle scattering tail contribution while the energy loss processes in the crystal are affected by the entry point of the γ-ray (more energy may be lost if it enters near the edge). Obviously the definitive measurement of the response function must be made in a fashion that resembles the experimental configuration as closely as possible.

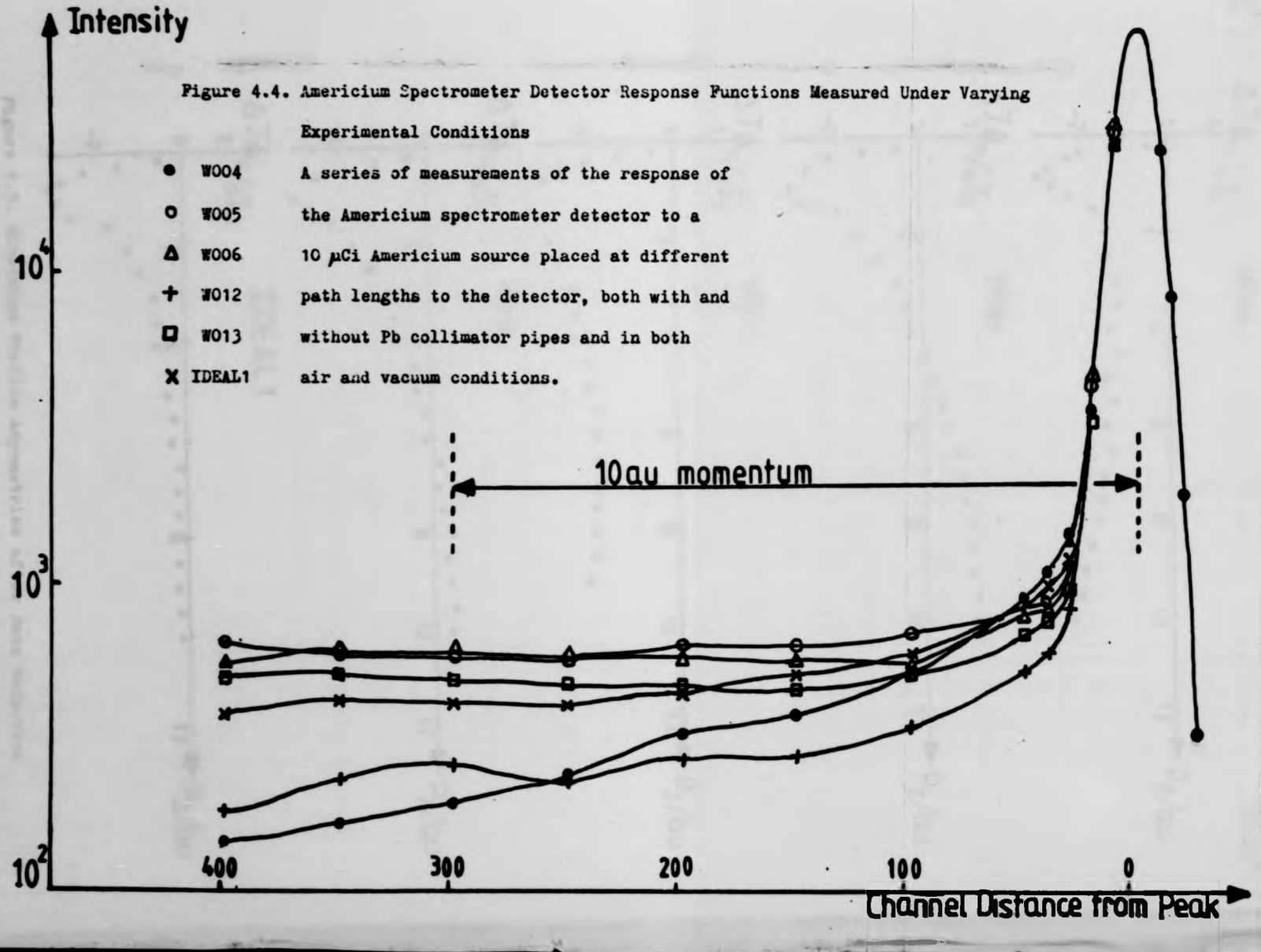

Figure 4.4. Americium Spectrometer Detector Response Functions Measured Under Varying Experimental Conditions

● W004
○ W005
△ W006
\+ W012
□ W013
X IDEAL1

A series of measurements of the response of the Americium spectrometer detector to a 10 μCi Americium source placed at different path lengths to the detector, both with and without Pb collimator pipes and in both air and vacuum conditions.

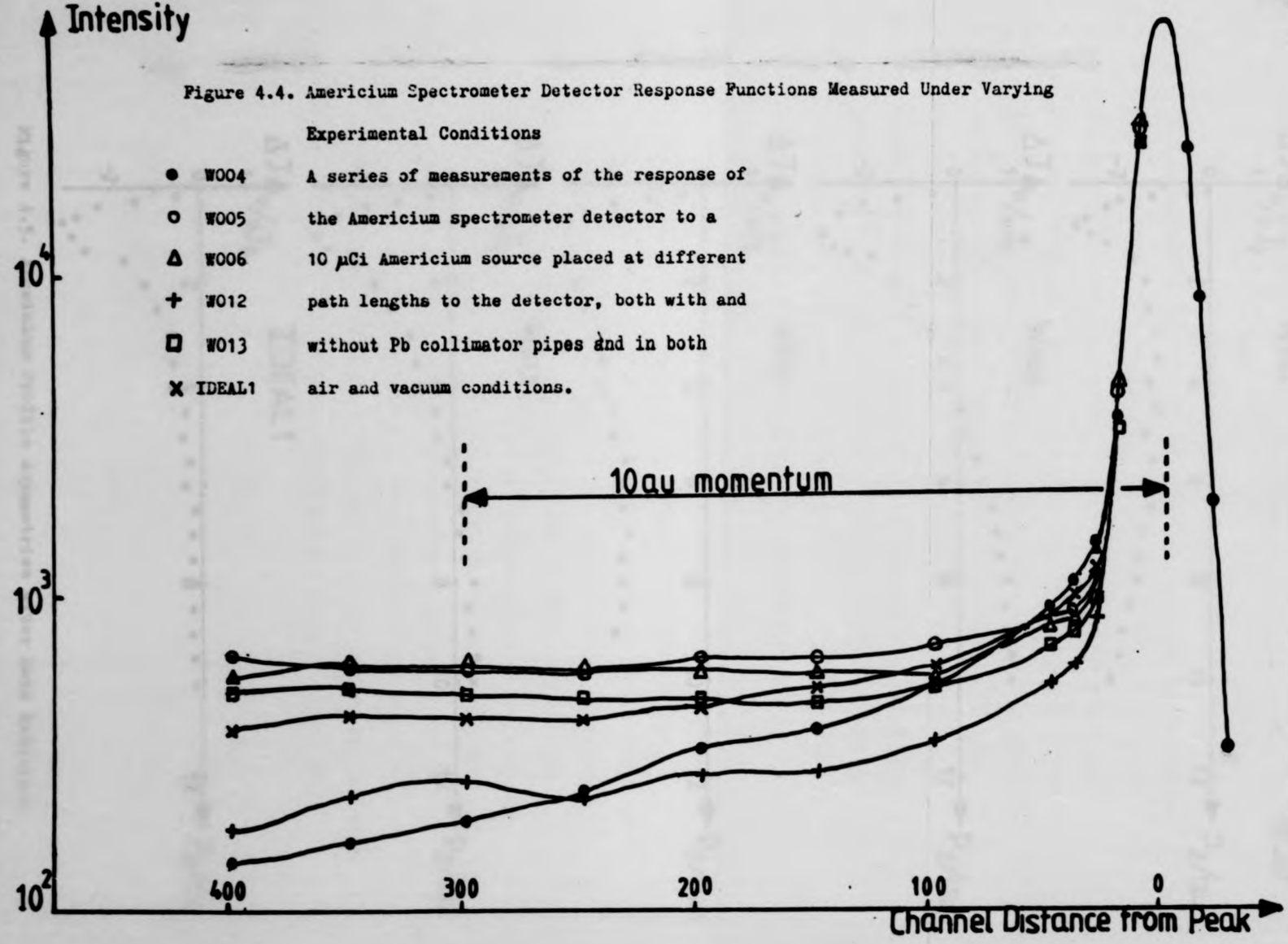

Figure 4.4. Americium Spectrometer Detector Response Functions Measured Under Varying Experimental Conditions

● W004
○ W005
△ W006
\+ W012
□ W013
× IDEAL1

A series of measurements of the response of the Americium spectrometer detector to a 10 μCi Americium source placed at different path lengths to the detector, both with and without Pb collimator pipes and in both air and vacuum conditions.

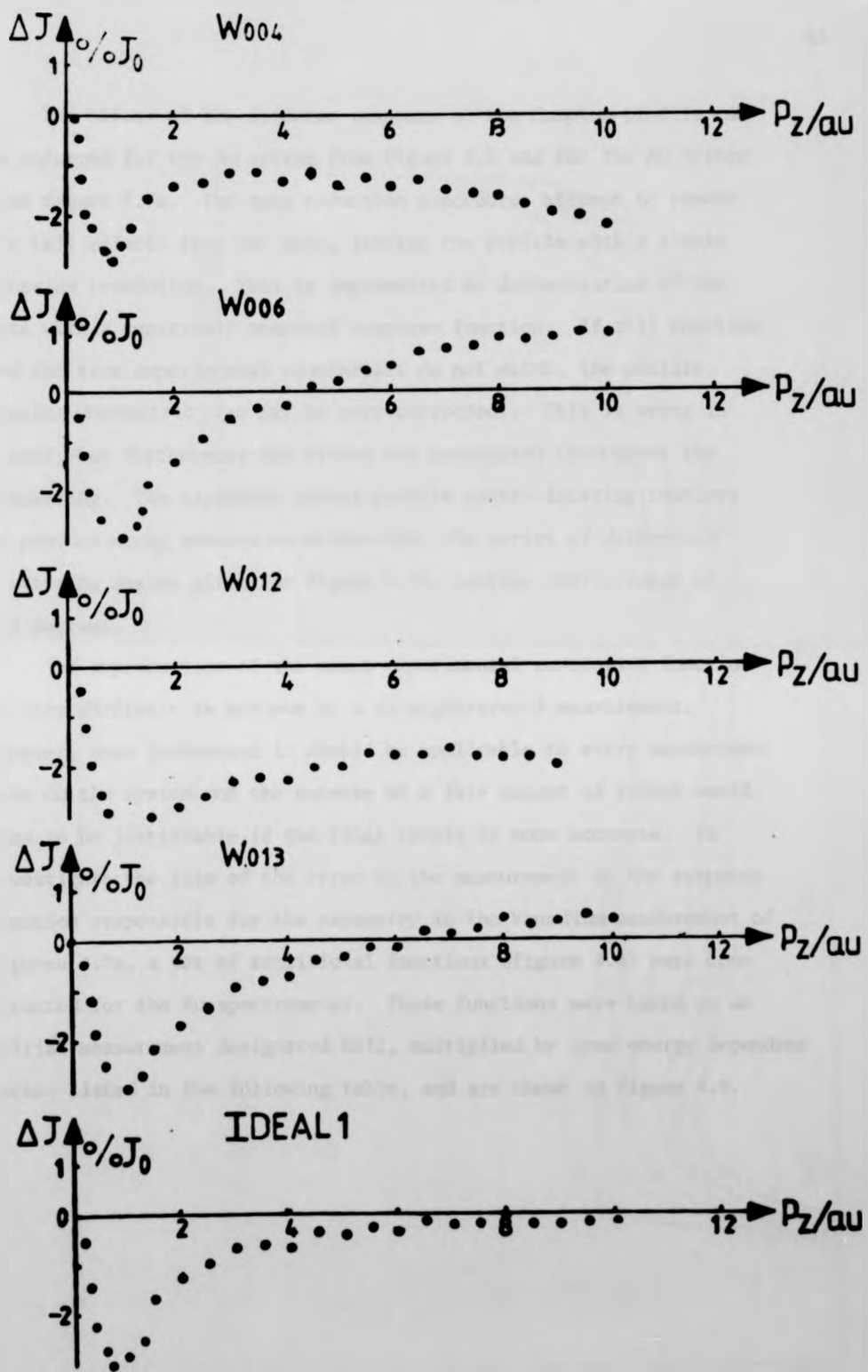

Figure 4.5. Aluminium Profile Asymmetries after Data Reduction

The effect of the detector response on the Compton profile can be inferred for the Am system from figure 4.5 and for the Au system from figure 4.7a. The data reduction procedures attempt to remove the tail effects from the data, leaving the profile with a simple Gaussian resolution. This is implemented by deconvolution of the data with a separately measured response function. If this function and the true experimental counterpart do not match, the profile remains asymmetric (or may be over-corrected). This is wrong in itself, but furthermore the errors are propagated throughout the processing. The asymmetry causes profile centre locating routines to produce wrong answers as evidencedby the series of determined scattering angles given for figure 4.7b, varying over a range of 0.4 degrees.

The reproduction of the exact experimental resolution function is very difficult to achieve by a straightforward measurement. However, once determined it should be applicable to every measurement made on the system and the expense of a fair amount of effort would seem to be justifiable if the final result is more accurate. To investigate the size of the error in the measurement of the response function responsible for the asymmetry in the Vanadium measurement of figures 4.7a, a set of ar tificial functions (figure 4.6) were constructed for the Au spectrometer. These functions were based on an initial measurement designated R012, multiplied by some energy dependent factor listed in the following table, and are shown in figure 4.6.

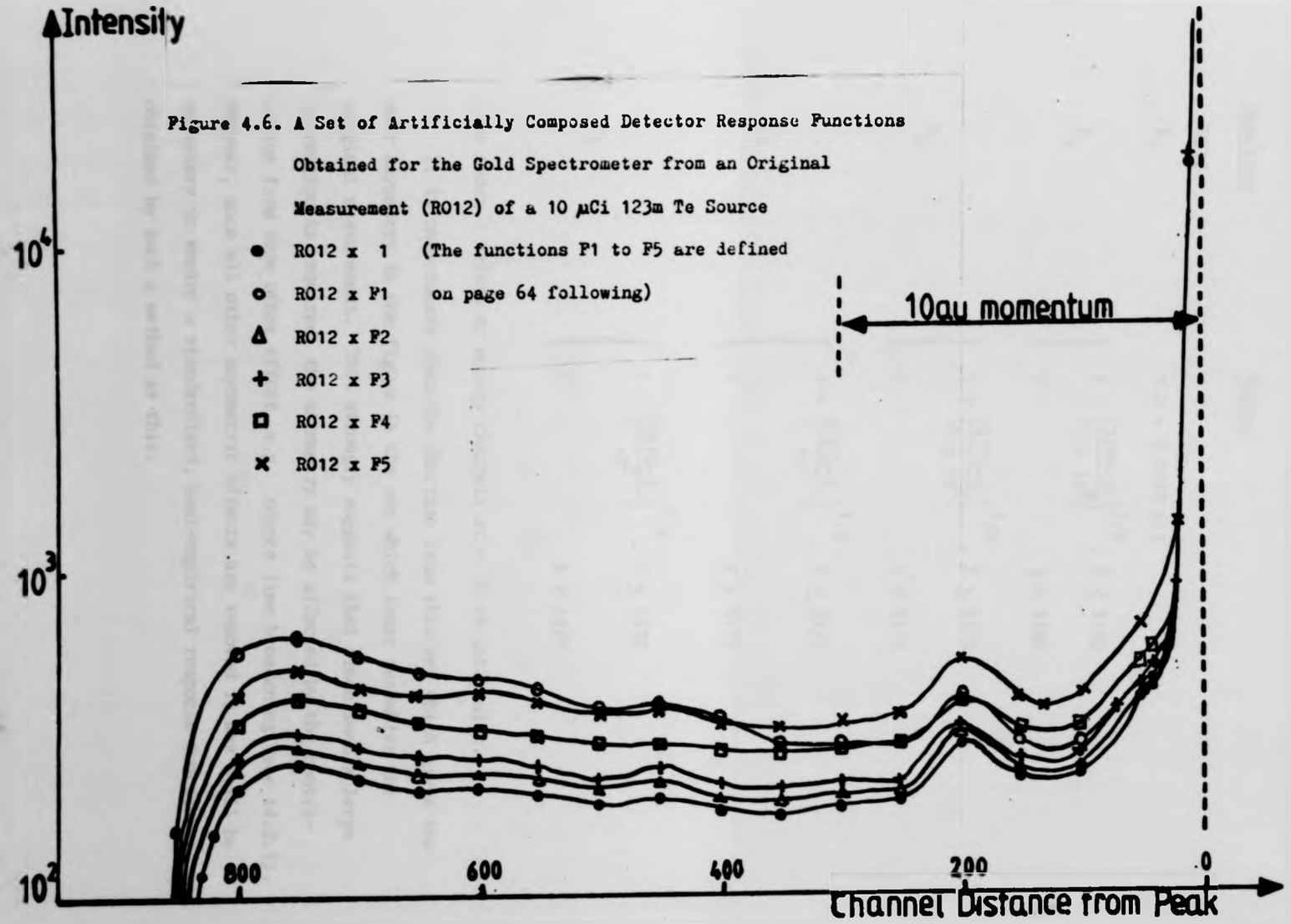

Figure 4.6. A Set of Artificially Composed Detector Response Functions Obtained for the Gold Spectrometer from an Original Measurement (RO12) of a 10 μCi 123m Te Source

(The functions P1 to P5 are defined on page 64 following)

Function	Factor
R012	1
F_1	$7.0 - 0.0019 \times I$
F_2	$\begin{cases} 1 + \left(\frac{3180-I}{7 \times 10^6}\right)^{1/8}, & I \leq 3180 \\ 1, & I > 3180 \end{cases}$
F_3	$\begin{cases} 1 + \left(\frac{3175-I}{7 \times 10^6}\right)^{1/8}, & I \leq 3175 \\ 1, & I > 3175 \end{cases}$
F_4	$\begin{cases} 1 + \left(\frac{3175-I}{10^3}\right)^{1/8}, & I \leq 3175 \\ 1, & I > 3175 \end{cases}$
F_5	$\begin{cases} 1 + \left(\frac{3170-I}{10^3}\right)^{1/8}, & I \leq 3170 \\ 1, & I > 3170 \end{cases}$

(The index I refers to energy channels at ∿ 50 eV intervals).

It is unfortunate that the function from this set which gives the best asymmetry in the figure is the one which least resembles the original measurement. This strongly suggests that since such a large correction is required, the asymmetry may be affected by the contribution from some other effect, e.g. source line broadening (see §4.2.1). However, once all other asymmetric effects are removed it may still be necessary to employ a standardised, semi-empirical response function obtained by such a method as this.

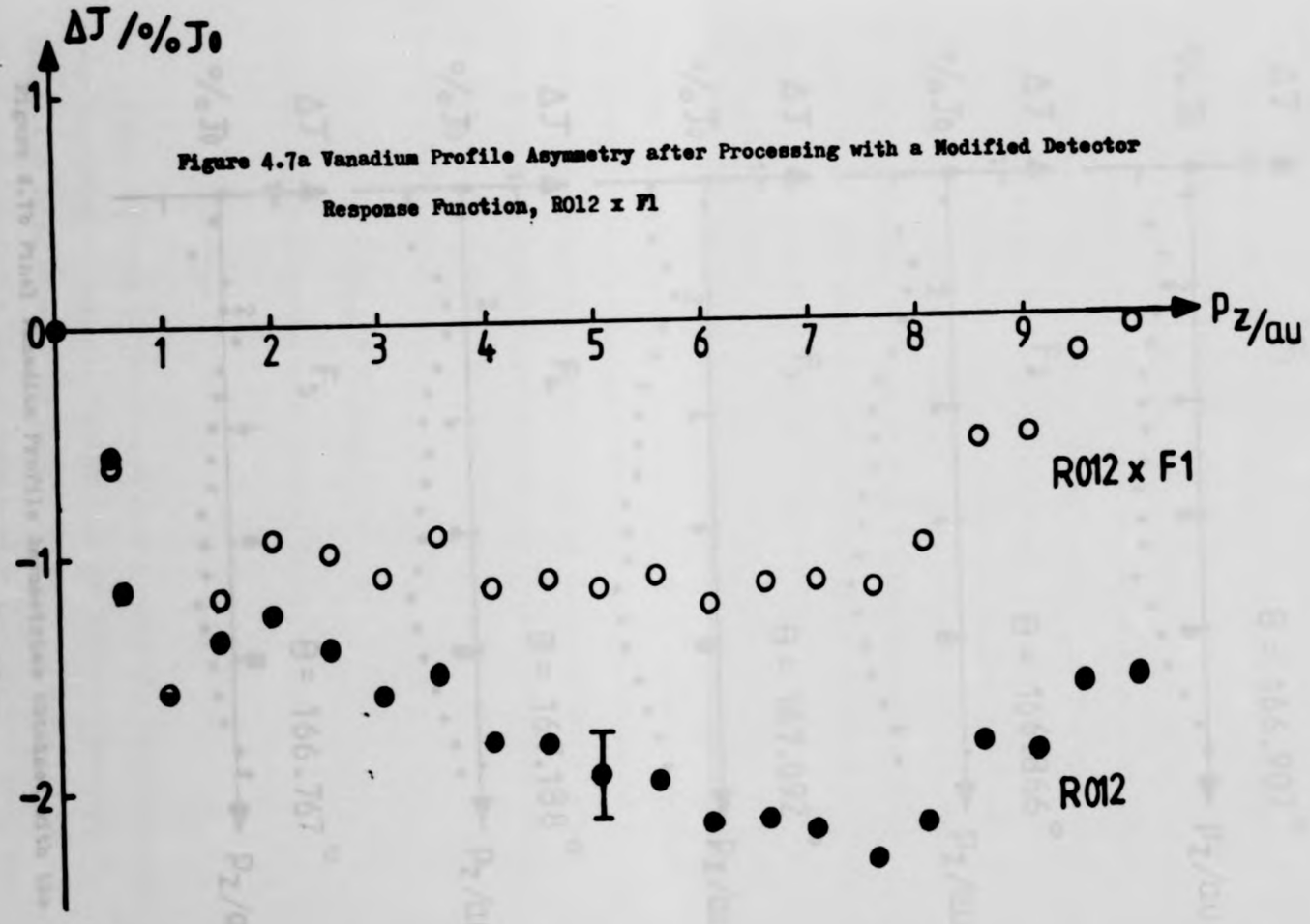

Figure 4.7a Vanadium Profile Asymmetry after Processing with a Modified Detector Response Function, R012 x F1

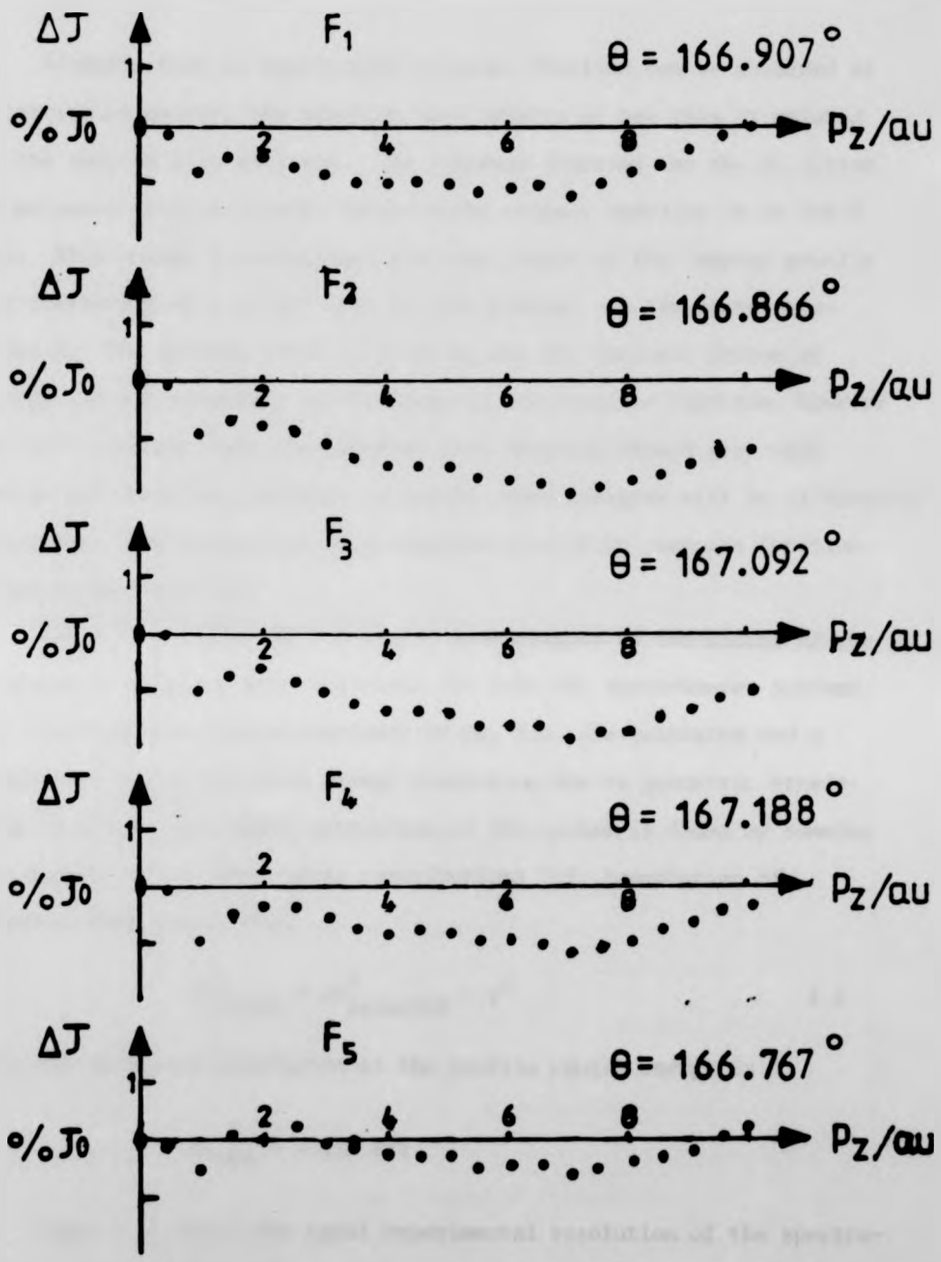

Figure 4.7b Final Vanadium Profile Asymmetries Obtained with the Series of Detector Response Functions

Assuming that an appropriate response function can be obtained at a particular energy, the question then remains of how this is related to the smeared data spectrum. The response function for the Au system is measured using a ^{123m}Te source whose primary emission is at 159.0 keV. This energy is coincident with the centre of the Compton profile for scattering at $\theta = 167°$ with 412 keV photons - a fortunate coincidence. The detector thus distributes all the incident photon of energy 159 keV according to the shape of the response function. However eq. 4.1. predicts that the width of this function should vary with energy and therefore incident γ-rays of other energies will be differently dispersed. The assumption of a constant resolution response function needs to be justified.

Table 4.1. lists the results of measurements of the widths of the response to single energy emissions for both the spectrometer systems. The resolution variation constants of eq. 4.1. are evaluated and a figure for the approximate energy dispersion due to geometric broadening is given. The total resolution of the system is found by summing the squares of the individual contributions (cf. convolution of Gaussian functions), viz,

$$\Delta E^2_{total} = \Delta E^2_{detector} + \gamma^2 \qquad 4.2$$

Thus the Au system resolution at the profile centre energy is

$$\Delta E_{tot} = 0.639 \text{ keV}$$

Figure 4.8 shows the total experimental resolution of the spectrometer (ignoring the response function tail but including geometric broadening) in relation to the Compton profile. The value for the final energy resolution usually considered is that appropriate to the centre position, i.e. $\Delta E_{nominal} = 0.639$ keV. However, the effects of

Assuming that an appropriate response function can be obtained at a particular energy, the question then remains of how this is related to the smeared data spectrum. The response function for the Au system is measured using a ^{123m}Te source whose primary emission is at 159.0 keV. This energy is coincident with the centre of the Compton profile for scattering at $\theta = 167°$ with 412 keV photons - a fortunate coincidence. The detector thus distributes all the incident photon of energy 159 keV according to the shape of the response function. However eq. 4.1. predicts that the width of this function should vary with energy and therefore incident γ-rays of other energies will be differently dispersed. The assumption of a constant resolution response function needs to be justified.

Table 4.1. lists the results of measurements of the widths of the response to single energy emissions for both the spectrometer systems. The resolution variation constants of eq. 4.1. are evaluated and a figure for the approximate energy dispersion due to geometric broadening is given. The total resolution of the system is found by summing the squares of the individual contributions (cf. convolution of Gaussian functions), viz,

$$\Delta E^2_{total} = \Delta E^2_{detector} + \gamma^2 \qquad 4.2$$

Thus the Au system resolution at the profile centre energy is

$$\Delta E_{tot} = 0.639 \text{ keV}$$

Figure 4.8 shows the total experimental resolution of the spectrometer (ignoring the response function tail but including geometric broadening) in relation to the Compton profile. The value for the final energy resolution usually considered is that appropriate to the centre position, i.e. $\Delta E_{nominal} = 0.639$ keV. However, the effects of

^{198}Au(412keV)			^{241}Am(60keV)		
Name	Energy	Width	Name	Energy	Width
PbKα_1	74.969	0.5044	Amγ_2	26.36	0.3353
Teγ_1	159.000	0.5960	Amγ_1	59.54	0.3855
Resolution Variation Parameters, $\Delta E^2 = \alpha + \beta E$					
α	0.1646 (keV)		α	0.0836 (keV)	
β	0.00120(keV)		β	0.00109(keV)	
Geometric Broadening					
γ	0.230 (keV)		γ	0.067 (keV)	

Table 4.1. Detector Resolution Variation Parameters

Figure 4.8. Variation of Energy and Momentum Resolution Across the Range of the Compton Profile for Scattering at 167° of 412 keV Primary Radiation

Energy Resolution –

ΔE_{exp} – Existing experimental resolution

ΔE_{nom} – Assumed constant energy resolution

$\Delta E_{req'd}$ – Required energy resolution for constant momentum resolution

Momentum Resolution –

Δp_{exp} – Existing momentum resolution

Δp_{nom} – Momentum resolution corresponding to assumed constant energy resolution

$\Delta p_{req'd}$ – Desired constant momentum resolution

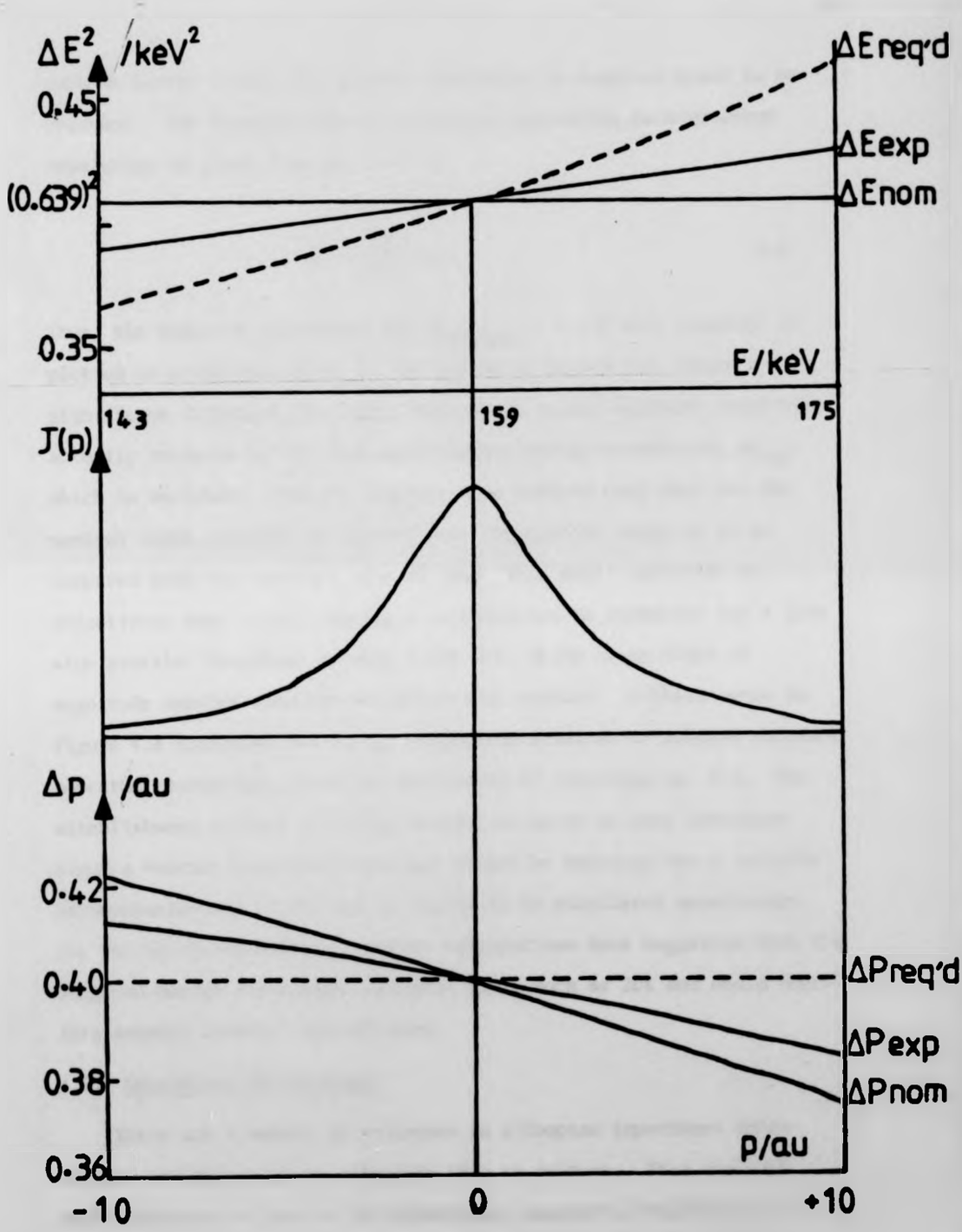
ΔE² /keV²
0.45
(0.639)²
0.35
ΔEreq'd
ΔEexp
ΔEnom
E/keV
143
159
175
J(p)
Δp /au
0.42
0.40
0.38
0.36
ΔPreq'd
ΔPexp
ΔPnom
p/au
-10
0
+10

such an energy resolution must be considered in momentum space to be relevant. The transposition of an energy resolution to a momentum resolution is given from eq. 2.10 by

$$\Delta p = \left(\frac{\partial p_z}{\partial \omega_2}\right) \Delta\omega_2 \qquad 4.3$$

Thus, the momentum resolution for $\Delta E_{nominal}$ = 0.639 keV, constant is plotted as a function of p_z at the bottom of figure 4.8. where a significant variation is clear. Also shown is the momentum resolution actually produced by the true experimental energy resolution, ΔE_{exp} which is variable. This is slightly more uniform than that for the nominal value, varying by only 6% over the profile range of 20 au compared with the previous case of 10%. This small variation is effectively negligible, causing a contribution to asymmetry for a free atom profile (Vanadium) of only 0.03% J(o) which is an order of magnitude smaller than can be detected at present. A third curve in figure 4.8 indicates the energy resolution required to achieve constant momentum resolution, which was determined by inverting eq. 4.3. The establishment of such an energy resolution would be very laborious since a Fourier transform technique cannot be employed for a variable deconvolution and so for the Au system it is considered unnecessary. For the Am system however, similar calculations have suggested that the required energy resolution variation is as much as 20% and would therefore require careful consideration.

4.2. Subsidiary Calculations

There are a number of processes in a Compton experiment whose effects are more easy to calculate than to measure. This includes such processes as source line broadening, geometric broadening and multiple scattering. Calculations for the latter two effects have

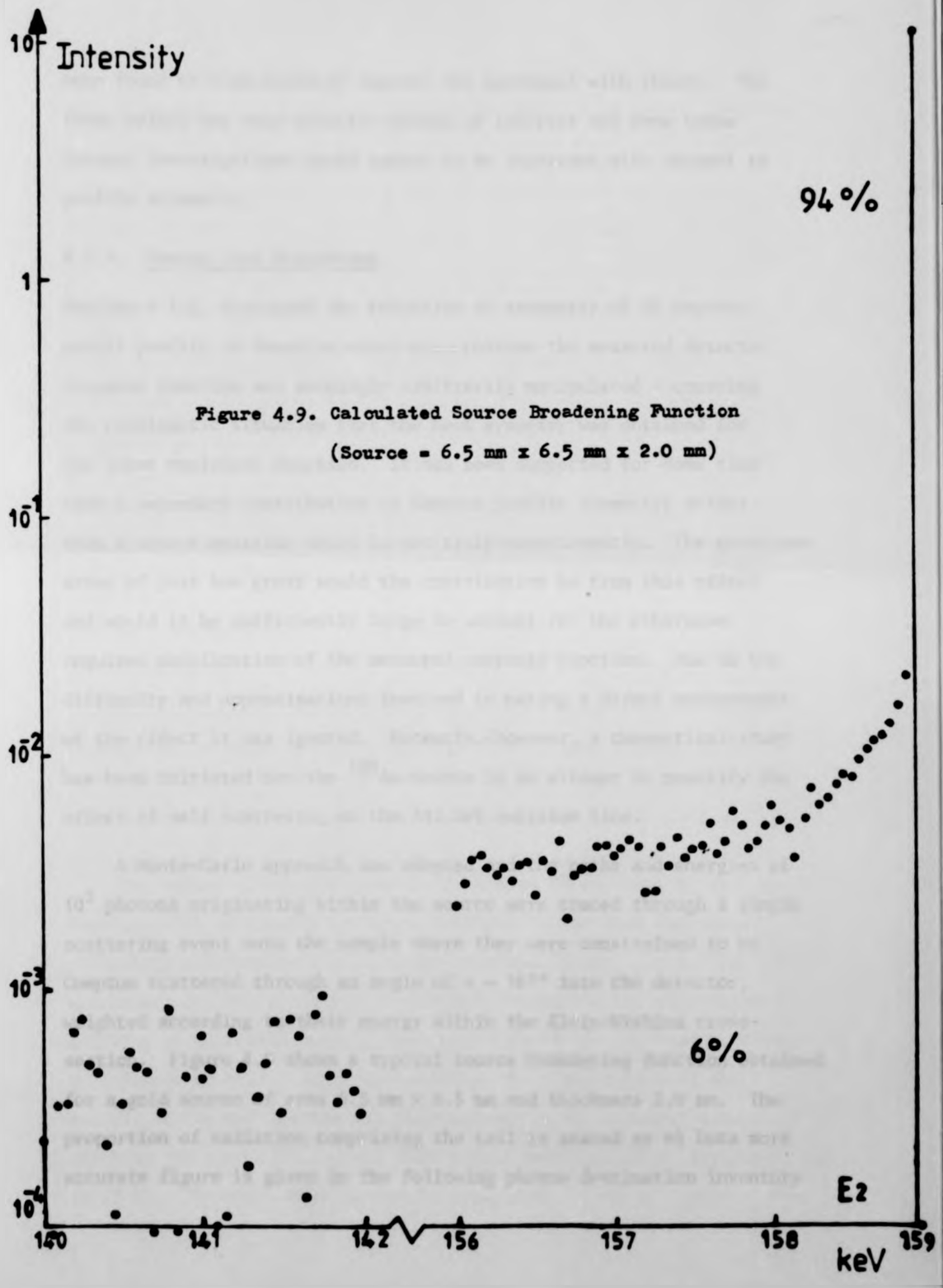

Figure 4.9. Calculated Source Broadening Function

(Source = 6.5 mm x 6.5 mm x 2.0 mm)

been found to significantly improve the agreement with theory. The first effect has only recently become of interest and from these present investigations would appear to be important with respect to profile asymmetry.

4.2.1. Source Line Broadening

Section 4.1.2. discussed the reduction in asymmetry of an experimental profile of Vanadium which occurredwhen the measured detector response function was seemingly arbitrarily manipulated - creating the problematic situation that the best symmetry was obtained for the least empirical function. It has been suspected for some time that a secondary contribution to Compton profile asymmetry arises from a source emission which is not truly monochromatic. The questions arose of just how great would the contribution be from this effect and would it be sufficiently large to account for the otherwise required modification of the measured response function. Due to the difficulty and approximations involved in making a direct measurement of the effect it was ignored. Recently, however, a theoretical study has been initiated for the ^{198}Au source in an attempt to quantify the effect of self scattering on the 412 keV emission line.

A Monte-Carlo approach was adopted and the paths and energies of 10^5 photons originating within the source were traced through a single scattering event onto the sample where they were constrained to be Compton scattered through an angle of $\theta = 167°$ into the detector, weighted according to their energy within the Klein-Nishina cross-section. Figure 4.9 shows a typical source broadening function obtained for a gold source of area 6.5 mm x 6.5 mm and thickness 2.0 mm. The proportion of radiation comprising the tail is stated as 6% buta more accurate figure is given in the following photon destination inventory

for various source thicknesses. It is immediately obvious that the tail proportion of the source function increases with source thickness.

Source Size/mm^3 6.5 x 6.5 x	1	2	10
Before Scattering from Sample			
Absorbed (No scattering)	15.1%	21.8%	35.9%
Absorbed (After scattering)	5.2	9.0	19.9
Emitted in Forward Direction	39.9	34.6	22.1
Incident on Sample	0.007	0.006	0.003
After Scattering from Sample			
Primary Intensity	96.7	94.7	88.0
Tail Intensity	3.3	5.3	12.0

Inventory of emission from range of ^{198}Au sources falling on a sample of diameter 10 mm at a distance 36 cm.

The effect of the tail was to be studied by convoluting the source function with originally symmetric profiles rather than immediately attempting a deconvolution of an experimental result. As a crude first approximation, the symmetric profile was represented by a Gaussian matching at the tails and the peak (the FWHM of this is inappropriate by a factor of ~ 3). After convolution, the right hand side (high energy) of the new profile was renormalised to the original area - which is the condition imposed during data reduction of an experiment (§4.2.3). The difference profiles (convoluted - original) should then

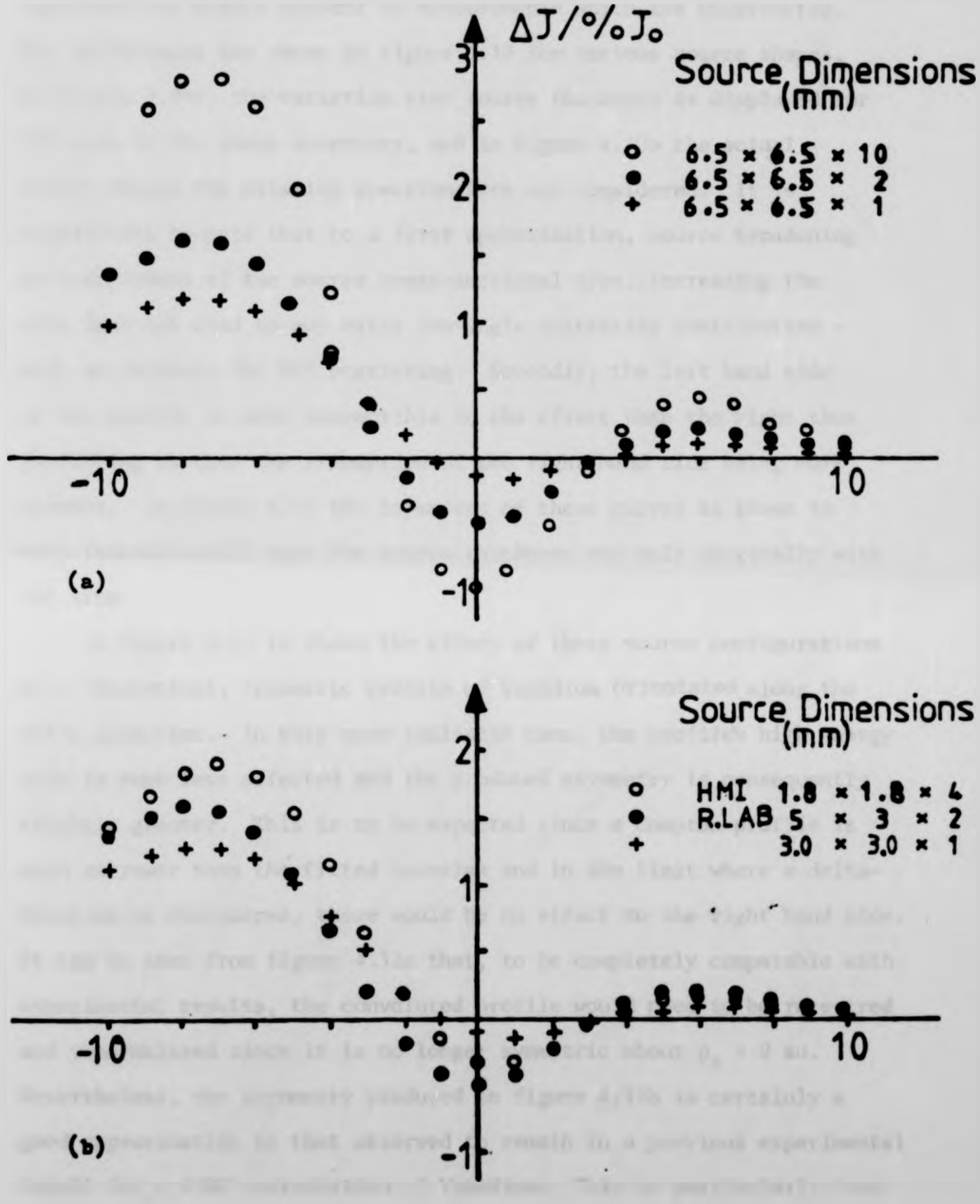

Figure 4.10. Differences between Gaussian Model Profiles Convoluted with a Source Broadening Function and Unconvoluted

represent the errors present in measurements which are uncorrected. The differences are shown in figure 4.10 for various source shapes. In figure 4.10a, the variation with source thickness is displayed for the data in the above inventory, and in figure 4.10b the actual source shapes for existing spectrometers are considered. It is significant to note that to a first approximation, source broadening is independent of the source cross-sectional area; increasing the area does not lead to any extra low-angle scattering contribution - only an increase for 90° scattering. Secondly, the left hand side of the profile is more susceptible to the effect than the right thus justifying further the assumption of the right hand side being more correct. In figure 4.11 the asymmetry of these curves is shown to vary systematically with the source thickness and only marginally with the area.

In figure 4.12 is shown the effect of these source configurations on a theoretical, symmetric profile of Vanadium orientated along the (111) direction. In this more realistic case, the profile's high energy side is even less affected and the produced asymmetry is consequently slightly greater. This is to be expected since a Compton profile is much narrower than the fitted Gaussian and in the limit where a delta-function is considered, there would be no effect to the right hand side. It can be seen from figure 4.12a that, to be completely comparable with experimental results, the convoluted profile would need to be recentred and renormalised since it is no longer symmetric about $p_z = 0$ au. Nevertheless, the asymmetry produced in figure 4.12b is certainly a good approximation to that observed to remain in a previous experimental result for a (100) orientation of Vanadium. This is particularly true near the origin ($p_z < 1$ au) and a little consideration shows that recentring and further renormalisation would tend to improve the agreement. Furthermore, all recent measurements with the Au spectrometer

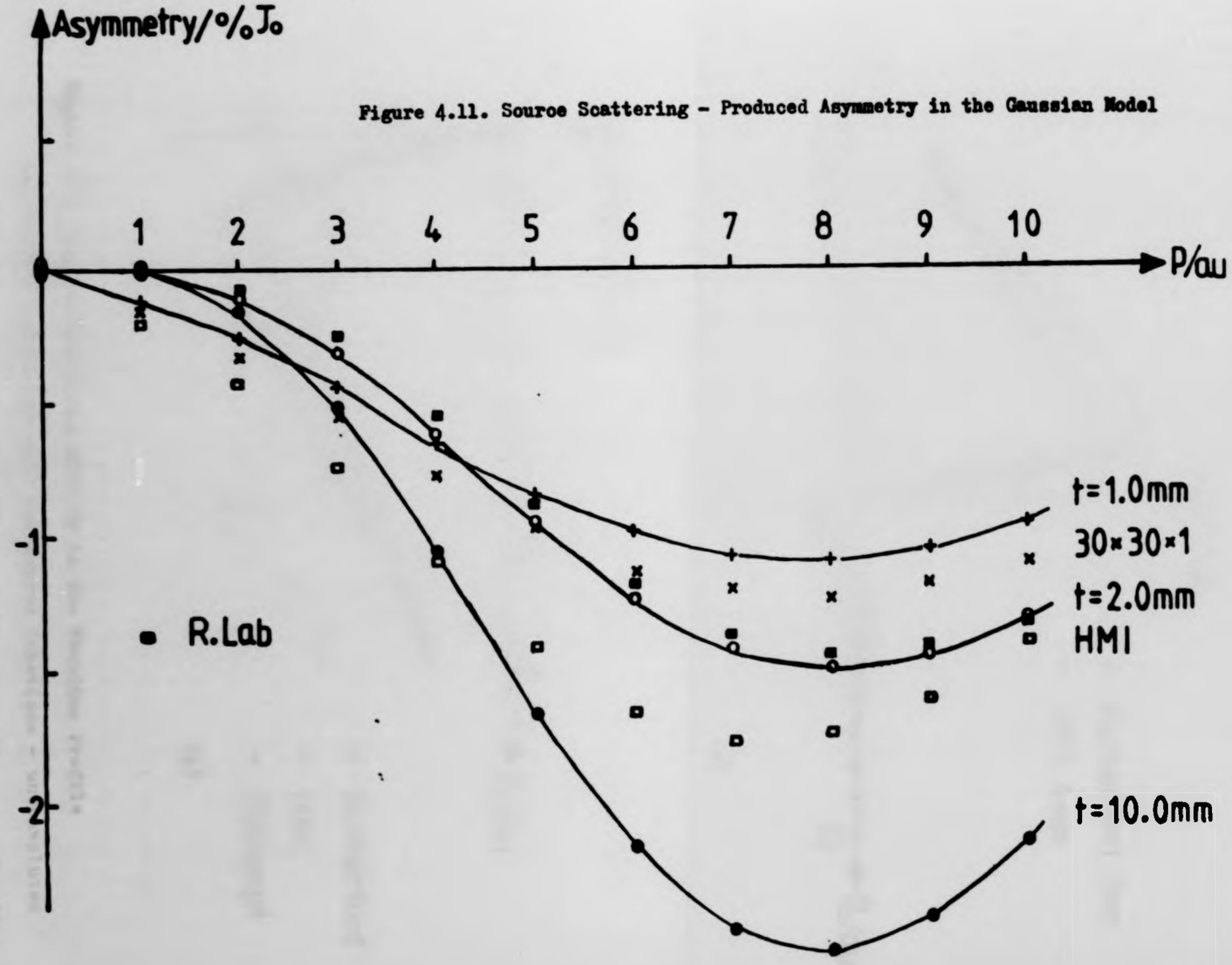

Figure 4.11. Source Scattering - Produced Asymmetry in the Gaussian Model

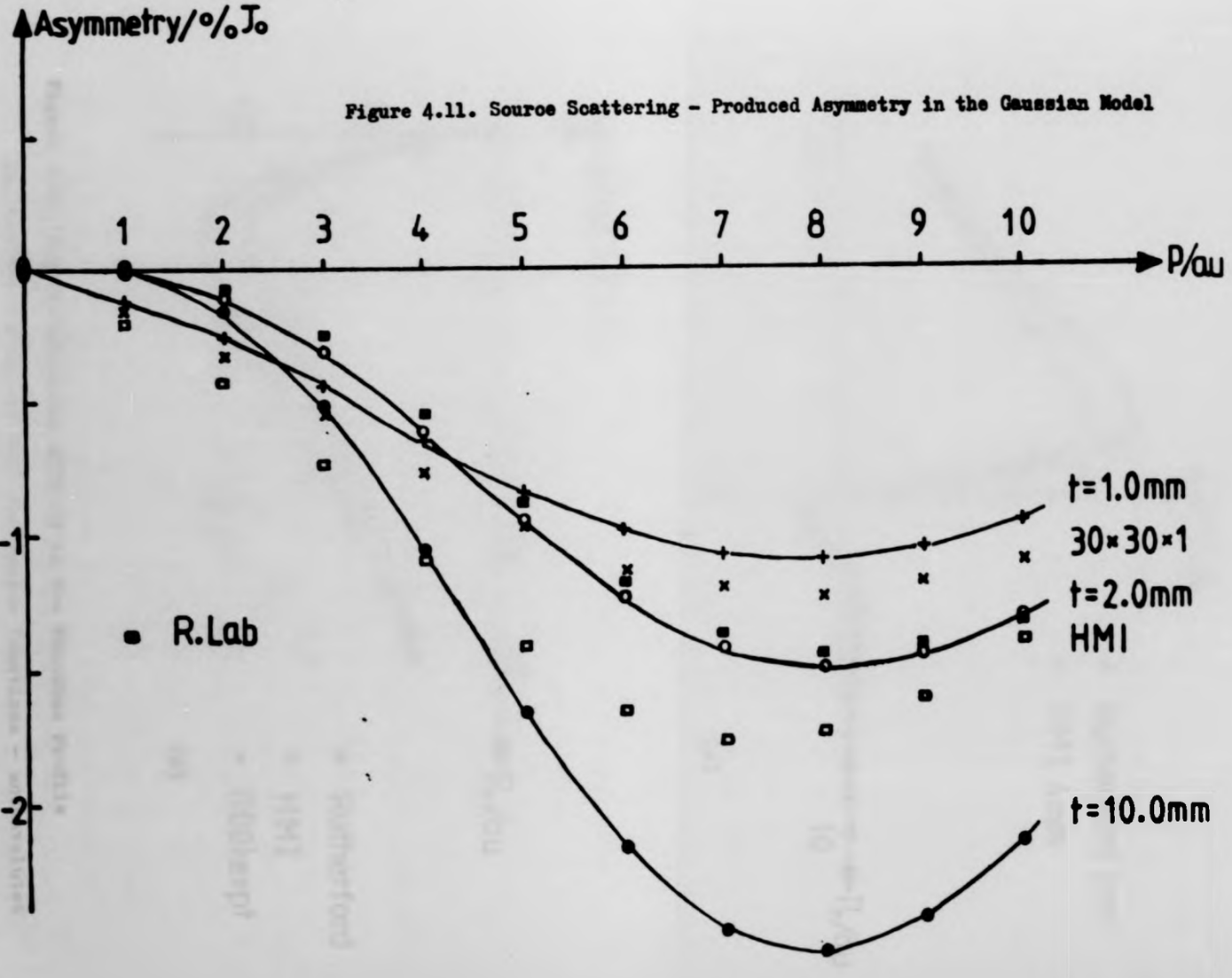

Figure 4.11. Source Scattering - Produced Asymmetry in the Gaussian Model

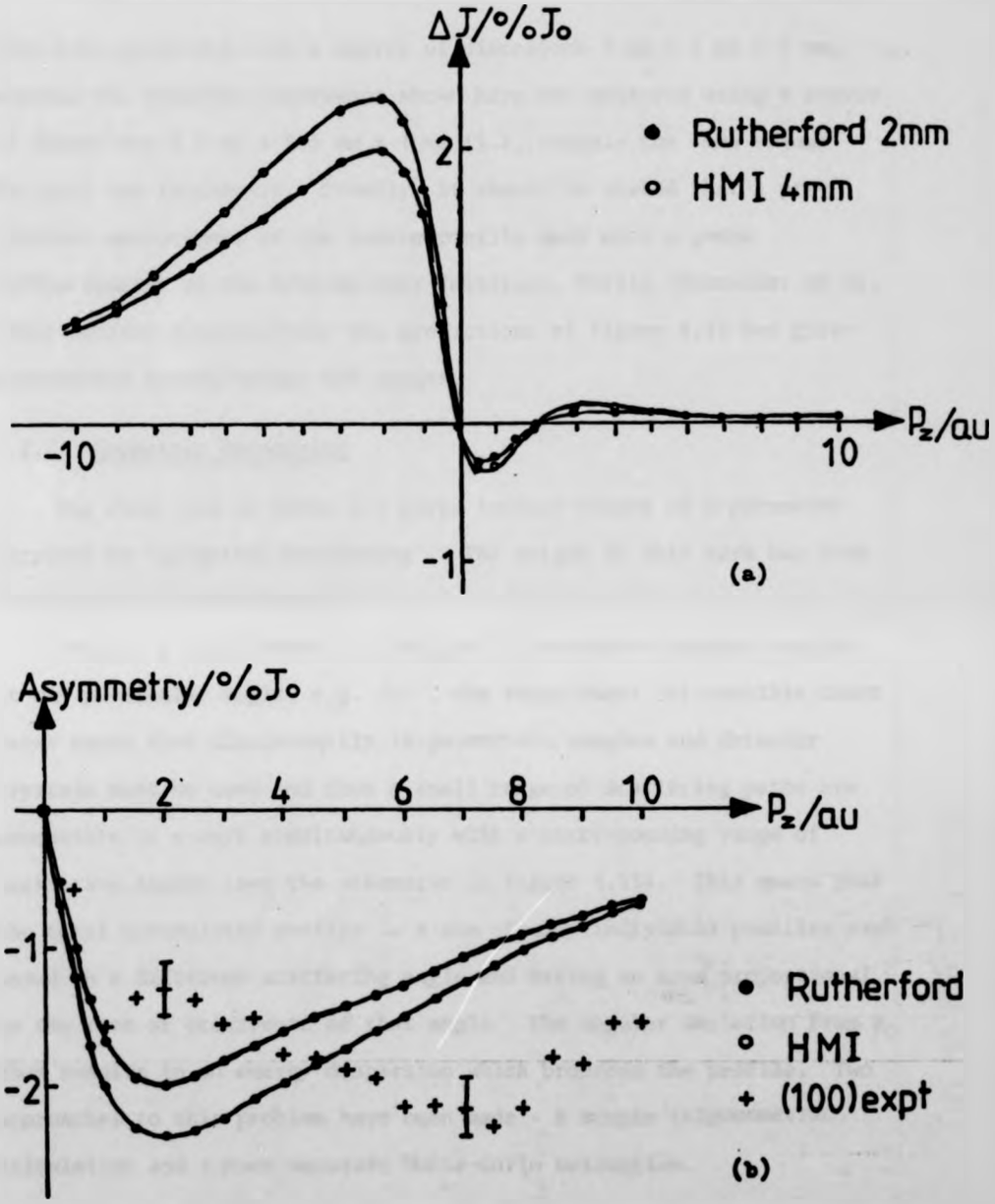

Figure 4.12. Source Scattering Effects in the Vanadium Profile

(a) Profile convoluted with two source functions - unconvoluted profile (b) Asymmetry produced by convolution with source function (The crosses show the experimentally measured asymmetry)

have been performed with a source of dimensions 3 mm x 5 mm x 2 mm, whereas the Vanadium experiment shown here was measured using a source of dimensions 6.5 mm x 6.5 mm x 1 mm (i.e. roughly the same volume but half the thickness). Finally, it should be stated that a preliminary measurement of the source profile made with a gamma diffractometer at the Hahn-Meitner Institute, Berlin (Schneider et al, 1983) confirm qualitatively the predictions of figure 4.12 but gives asymmetries approximately 50% larger.

4.2.2. Geometric Broadening

The final row in table 4.1 gives typical values of a parameter ascribed to 'geometric broadening'. The origin of this term has been investigated in some detail.

Whereas a spectrometer is designed to measure a Compton profile at one particular angle, e.g. 167°, the requirement for sensible count rates means that dimensionally large sources, samples and detector crystals must be used and thus a small range of scattering paths are accessible to γ-rays simultaneously with a corresponding range of scattering angles (see the schematic in figure 4.13). This means that the total accumulated profile is a sum of many individual profiles each based on a different scattering angle and having an area proportional to the rate of occurrence of that angle. The angular deviation from θ_o thus results in an energy dispersion which broadens the profile. Two approaches to this problem have been made - a simple trigonometric calculation and a more accurate Monte-Carlo evaluation.

The first method calculates the maximum range of angles subtended by the spectrometer components and assumes a triangular distribution of intensity representable by a Gaussian distribution of equal FWHM. Table 4.2a gives the results of the simple calculation for various Au spectrometer configurations. Referring back to equation 4.2, the total resolution

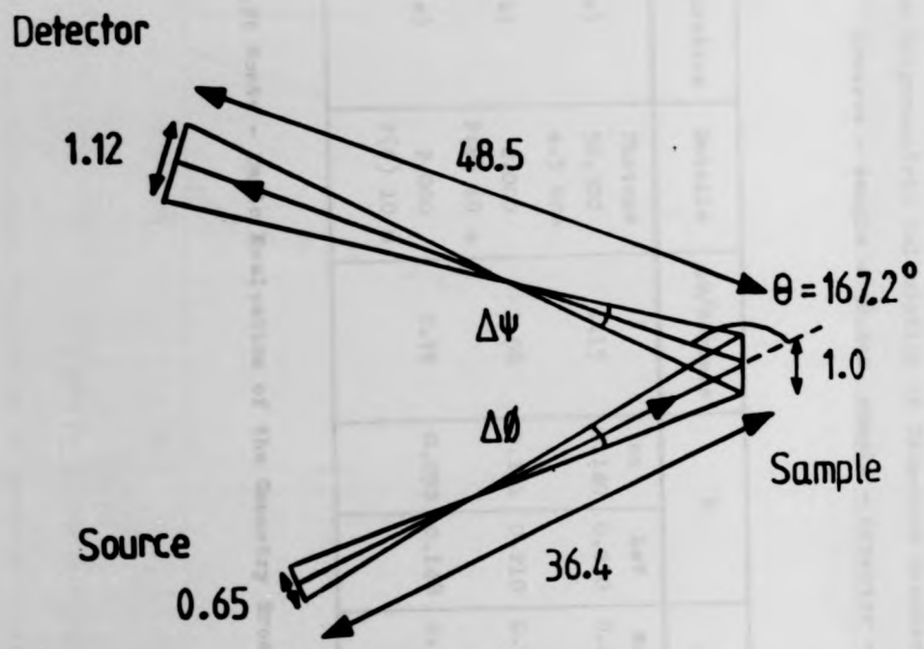

$\Delta\phi = 2.51°$

$\Delta\psi = 2.50°$

Total Divergence $= \sqrt{\Delta\phi^2 + \Delta\psi^2}$

$= 3.6°$

FWHM $= 1.8°$

$= 0.218$ au

Figure 4.13. Schematic for the Simple Trigonometric Calculation of the Geometric Resolution of the Cold Spectrometer

Sample	Dimensions/mm			2Δθ/degrees			FWHM			
	Source	Sample	Detector	Detector	Source	Total	γ		Total	
							au	keV	au	keV
(a)Vanadium	6.5	10.0	11.2	2.51	2.50	3.6	0.22	0.34	0.43	0.69
(b)Iron	6.5	8.0	11.2	2.27	2.28	3.2	0.19	0.30	0.42	0.67
(c)Iron	3.0	8.0	11.2	2.27	1.73	2.9	0.17	0.28	0.41	0.66

Table 4.2a Trigonometric Calculation of Geometric Broadening for Gold System (source - sample = 36.4cm, sample - detector = 48.5cm)

Configuration	Details	Δθ/degrees	γ		Total	
	Photons		au	keV	au	keV
(a)	54,300 4.5 hrs	1.15	0.140	0.230	0.400	0.639
(b)	2,000 P(6) 10 m	1.08	0.131	0.210	0.395	0.632
(c)	2,000 P(6) 10 m	0.76	0.092	0.148	0.384	0.615

Table 4.2b Monte - Carlo Evaluation of the Geometry Broadening Profile

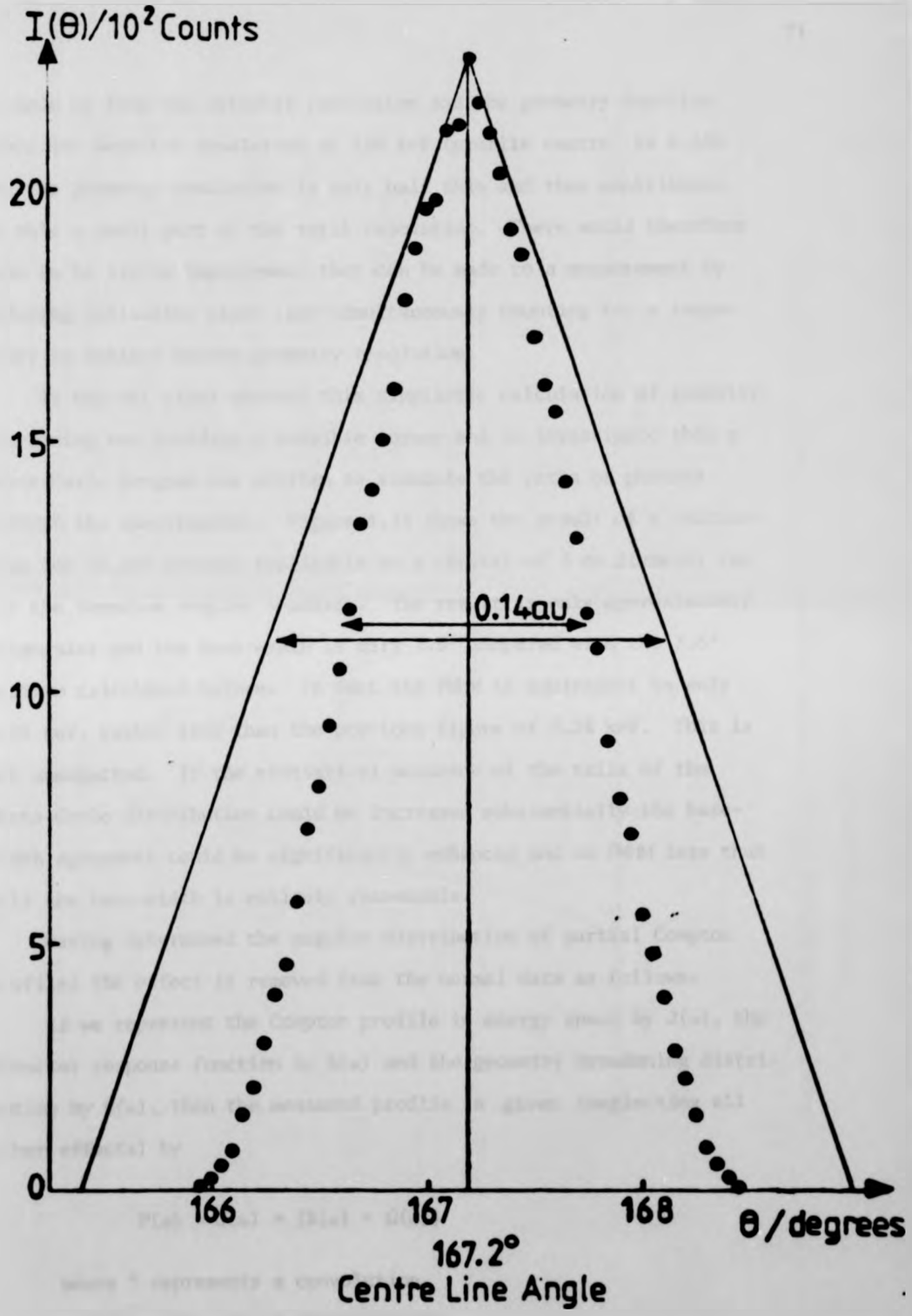

Figure 4.14. Monte-Carlo Simulation of Geometry Function. The triangular distribution represents the equivalent trigonometric calculation

is made up from the detector resolution and the geometry function. Since the detector resolution at 159 keV (profile centre) is 0.596 keV the geometry resolution is only half this and thus contributes to only a small part of the total resolution. There would therefore seem to be little improvement that can be made to a measurement by reducing collimator sizes (and simultaneously counting for a longer time) to achieve better geometry resolution.

It was not clear whether this simplistic calculation of geometry broadening was yielding a sensible answer and to investigate this a Monte-Carlo program was written to simulate the paths of photons through the spectrometer. Figure 4.14 shows the result of a calculation for 56,300 photons applicable to a crystal of 1 cm diameter (as for the Vanadium samples studied). The result is only approximately triangular and the base width is only 2.5° compared with the 3.6° maximum calculated before. In fact the FWHM is equivalent to only 0.23 keV, rather less than the previous figure of 0.34 keV. This is not unexpected. If the statistical accuracy of the tails of the Monte-Carlo distribution could be increased substantially the base-width agreement could be significantly enhanced and an FWHM less than half the base-width is entirely reasonable.

Having determined the angular distribution of partial Compton profiles the effect is removed from the normal data as follows.

If we represent the Compton profile in energy space by $J(\omega)$, the detector response function by $R(\omega)$ and the geometry broadening distribution by $G(\omega)$, then the measured profile is given (neglecting all other effects) by

$$P(\omega) = J(\omega) * [R(\omega) * G(\omega)]$$

where $*$ represents a convolution

and $*^{-1}$ represents a deconvolution.

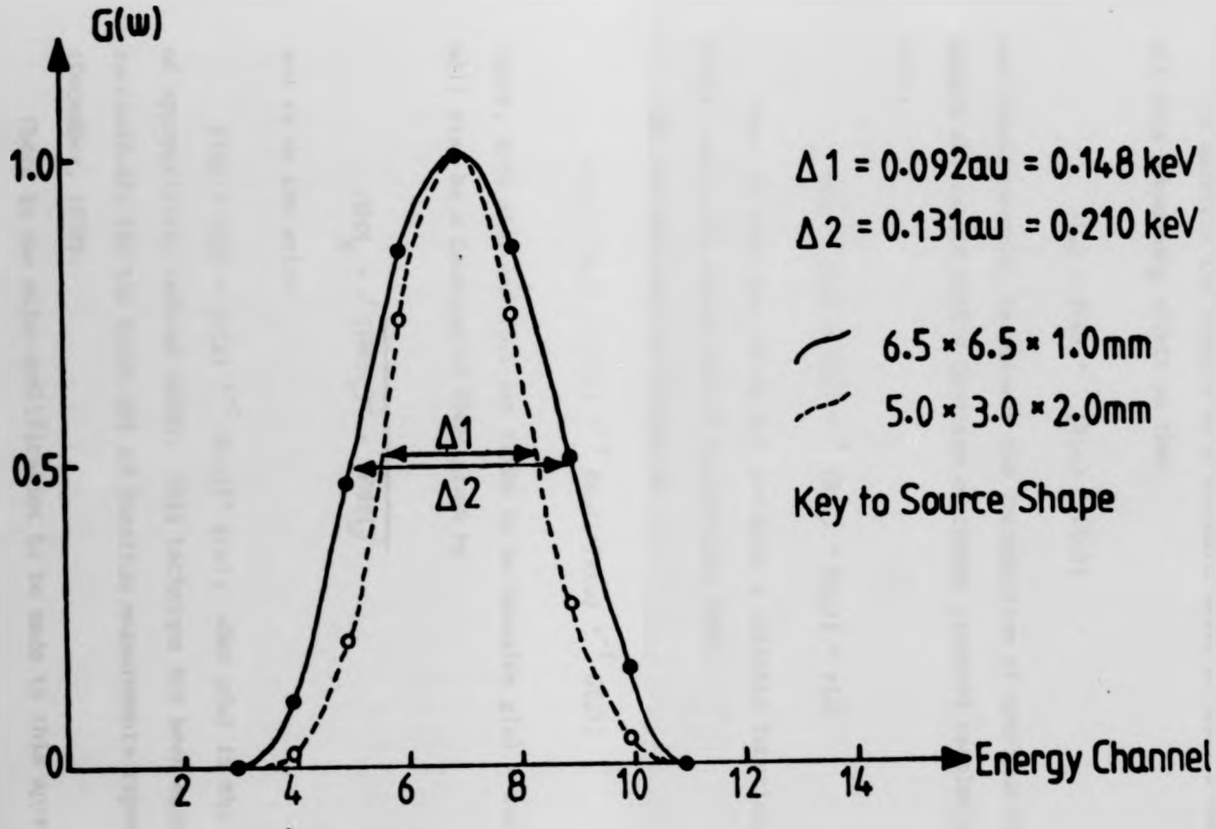

Figure 4.15. Polynomial-Fitted Geometry Functions for Two Source Configurations of the Au Spectrometer

To maintain the results on a standard basis we should remove all this broadening effect so that

$$J(\omega) = P(\omega) *^{-1} [R(\omega) * G(\omega)]$$

and simultaneously, to present the introduction of spurious oscillations, smooth the result with a Gaussian of chosen standard resolution $r(\omega)$, i.e.,

$$r(\omega) * J(\omega) = P(\omega) *^{-1} [R(\omega) * G(\omega)] * r(\omega) \qquad 4.4$$

Now, in practice, we do not yet have a suitable function $G(\omega)$(only $G(\theta)$), and so we create one of appropriate FWHM.

Eq. 4.4 can also be written as

$$r(\omega) * J(\omega) = [P(\omega) *^{-1} R(\omega)] * [r(\omega) *^{-1} G(\omega)]$$

Since, both $r(\omega)$ and $G(\omega)$ are taken to be Gaussian $g(\omega) = r(\omega) *^{-1} G(\omega)$ will also be a Gaussian of FWHM given by

$$FWHM_g = \sqrt{(FWHM_r)^2 - (FWHM_G)^2}$$

and so we can write

$r(\omega) * J(\omega) = [P(\omega) *^{-1} R(\omega)] * g(\omega)$, when $g(\omega)$ is the Gaussian of appropriately reduced width. This technique has been employed successfully for the first set of Vanadium measurements reported here (December, 1979).

There is one major qualification to be made to this approach. The geometry broadening function must be assumed Gaussian. This is obviously not the case and it is much better to convert the angular distribution to an energy distribution and utilize this function directly as $G(\omega)$ in Eq. 4.4. To use a function as statistically noisy as that given in

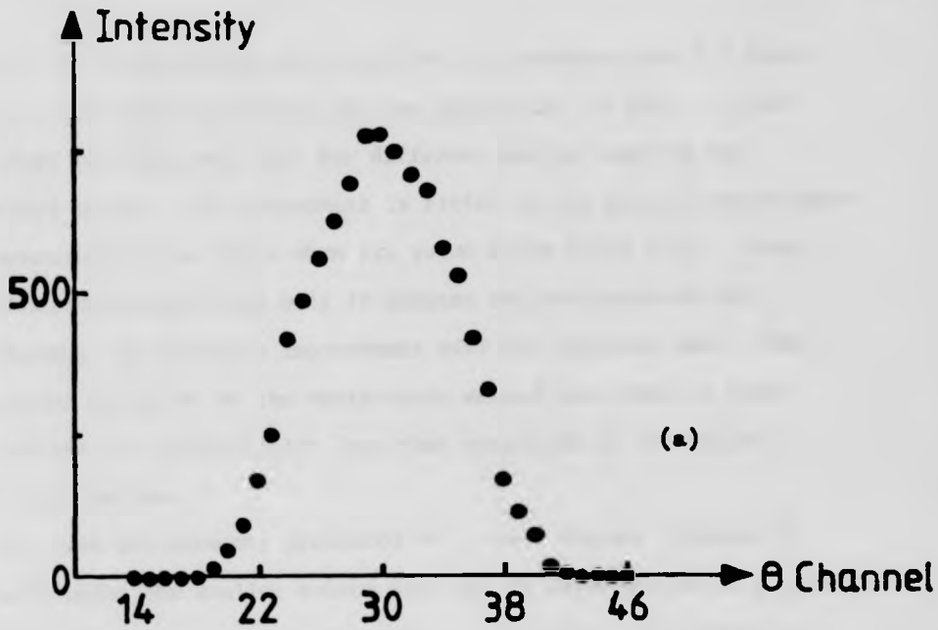

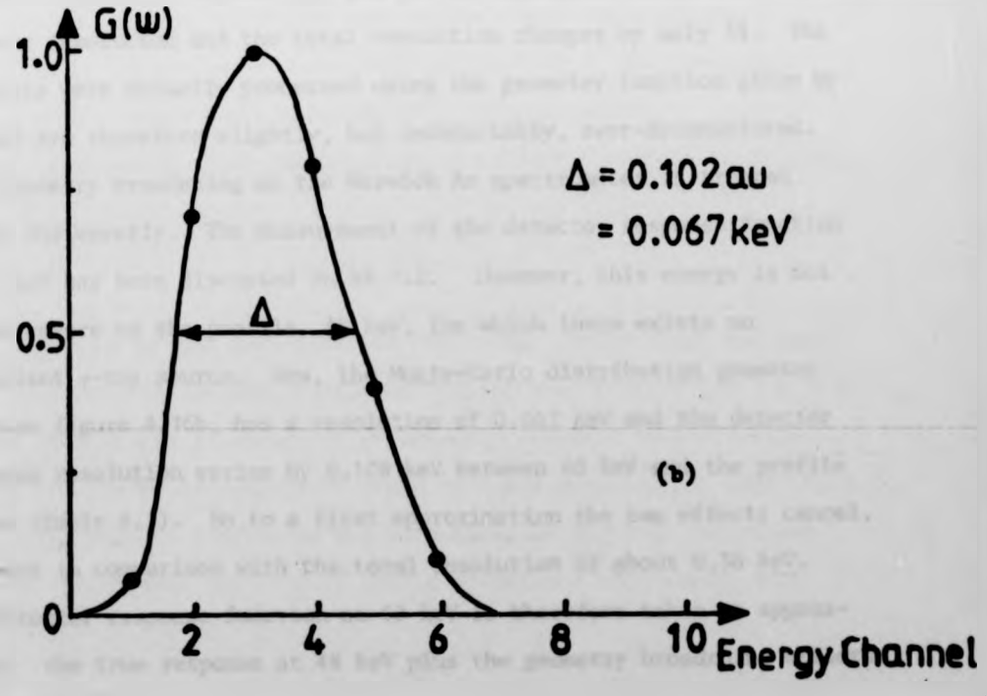

Figure 4.16. Americium Spectrometer Geometry Broadening Functions (a) Calculated intensity in angle space (b) Calculated intensity transformed to energy space.

Figure 4.14 is undesirable and since this calculation took 4.5 hours to run, a 6th order polynomial fit was applied to the data. Figure 4.15 shows two functions $G(\omega)$ for different source sizes in the Rutherford system. The polynomial is fitted to the data in angle space and terminated in the tails when its value drops below 0.01. These two calculations each took only 10 minutes and are based on only 2000 photons, an effective improvement over the previous case. The resolutions predicted by the Monte-Carlo method are given in Table 4.2b and are all substantially less that predicted by the trigonometric calculation.

The Iron measurements presented in a later Chapter (Chapter 6) were made using the smaller source size (c) in anticipation of a higher resolution. However, as has already been suggested, the change in geometry resolution between (b) and (c) is negligible compared to the detector resolution and the total resolution changes by only 3%. The Iron data were actually processed using the geometry function given by (b) and are therefore slightly, but undetectably, over-deconvoluted.

Geometry broadening on the Warwick Am spectrometer is treated rather differently. The measurement of the detector response function at 60 keV has been discussed in §4.1.2. However, this energy is not at the centre of the profile, 48 keV, for which there exists no convenient γ-ray source. Now, the Monte-Carlo distribution geometry function figure 4.16b, has a resolution of 0.067 keV and the detector response resolution varies by 0.109 keV between 60 keV and the profile centre (Table 4.1). So to a first approximation the two effects cancel, at least in comparison with the total resolution of about 0.36 keV. The detector response function at 60 keV is therefore taken to approximate the true response at 48 keV plus the geometry broadening effects $(R(\omega) * G(\omega))$.

One other interesting feature of the Warwick geometry is the asymmetry in energy space that can be seen in figure 4.16b. The distribution of angles is approximately symmetric (figure 4.16a) but conversion to an energy scale reveals a slight increase in the high energy tail. In practice this is so small as to be unnoticeable.

4.2.3. Normalisation Condition

During all stages of processing no attempt is made to apply absolute energy-varying corrections only the relative corrections which alter the profile shape are involved. While this makes the evaluation of the correctionssimpler, the resulting profile has a more-or-less arbitrary vertical scale. To obtain the Compton profile defined for a single atom (or molecule) it is therefore necessary to normalise the data to equal the area of the single atom Compton profile, i.e. the number of contributing electrons. When performed correctly, the normalisation correction is fairly trivial.

If there are N electrons per atom, the Compton profile is defined such that

$$\int_{-\infty}^{\infty} J(p_z)dp_z = N$$

and integration of the data over the same range should yield the same area. However the low energy side of the measured profile ($-\infty < p_z < 0$) is very susceptible to errors (e.g. detector response tail effects) and the total area may easily be wrong by a few percent. So only the high energy side is considered for normalisation and this introduces the requirement that the profile centre be defined accurately, such that

$$\delta \times J(o) < \sigma \frac{N}{2}$$

where σ is the required accuracy for the data.

For example, if σ = 0.5%, N = 26 and J(o) ≈ 6 (cf.Iron)

δ < 0.01 au momentum

or δ < 0.3 channels (50 eV per channel)

These accuracies are just achievable (see§4.4.1.).

In practice the profile cannot be measured above $p_z = p_{z\,max}$ where $\omega_1 - \omega(p_{z\,max}) = E_B$, the maximum electron binding energy, since for values of $p_z > p_{z\,max}$ the energy transfer is too small to eject all of the electrons. This defines an extreme limit for the range of normalisation. The limit chosen must also be such that for $p_z > p_{min}$ the profile is determined solely by the non-bonding core electrons. This contribution is then identical to that of a free atom, a model of which can therefore be used to calculate N* where

$$\int_o^{p_m} J\sigma(p_z)dp_z = \frac{N^*}{2}, \quad p_{min} \leq p_m \leq p_{max}$$

and $J\sigma(p_z)$ is the free atom model convoluted with the final resolution of the experimental data, σ. Choosing p_{max} as small as possible reduces the possibility of including spurious oscillations due to noise in the profile tail.

The following normalisation parameters have been commonly used for Vanadium, Iron and Aluminium.

	σ/au	pm/au	N*/2
V	0.40	10	10.85
Fe	0.40	10	12.15
Al	0.57	5	5.89

4.2.4. Multiple Scattering Profile

A significant proportion of the measured differential cross section is attributable to multiple scattering events in the target with the

incident photons scattering two or three times (elastically or inelastically) before emerging. A few "off-beam" experiments have been performed (e.g., Hulubei, 1934) where only those photons that have been scattered more than once are allowed through the collimators thus measuring the multiple profile directly, but these were not very successful for the reasons discussed in §2.5. A more profitable approach has been taken using a computer routine devised by Felsteiner et al (1974) which performs a Monte-Carlo simulation of the paths of γ-rays in a target to a level of three scattering events.

For the first measurement made on Vanadium with crystals of diameter 10 mm and 3 mm thick, the original simulation predicted a proportion of multiple scattering events varying from 10% at p_z = 0 au to 20% at p_z = 10 au. Over the momentum range initially of interest in considering anisotropies (0 au to $\sim$ 3 au), the average contribution to the measurement was about 12.2%. Thus the measured profile would contain 87.8% single scattering events and 12.2% multiple scattering events. Because of the normalisation of the profile with respect to only single events (cf. the Impulse Approximation, §2.4.3), the results must be further rescaled by a factor

$$F = \frac{1}{100\% - 12.2\%} = 1.14$$

i.e. an increase in the vertical scale of 14%, certainly a non-trivial correction.

With a correction as large as above, in order to be able to study individual profiles instead of anisotropies, it is important to apply a spectral correction to the data and to examine both high and low momentum sides of the resulting profile. Therefore the existing Monte-Carlo program was adapted to produce a spectral calculation over the entire momentum range and to generate a multiple scattering profile.

incident photons scattering two or three times (elastically or inelastically) before emerging. A few "off-beam" experiments have been performed (e.g., Hulubei, 1934) where only those photons that have been scattered more than once are allowed through the collimators thus measuring the multiple profile directly, but these were not very successful for the reasons discussed in §2.5. A more profitable approach has been taken using a computer routine devised by Felsteiner et al (1974) which performs a Monte-Carlo simulation of the paths of γ-rays in a target to a level of three scattering events.

For the first measurement made on Vanadium with crystals of diameter 10 mm and 3 mm thick, the original simulation predicted a proportion of multiple scattering events varying from 10% at p_z = 0 au to 20% at p_z = 10 au. Over the momentum range initially of interest in considering anisotropies (0 au to $\sim$ 3 au), the average contribution to the measurement was about 12.2%. Thus the measured profile would contain 87.8% single scattering events and 12.2% multiple scattering events. Because of the normalisation of the profile with respect to only single events (cf. the Impulse Approximation, §2.4.3), the results must be further rescaled by a factor

$$F = \frac{1}{100\% - 12.2\%} = 1.14$$

i.e. an increase in the vertical scale of 14%, certainly a non-trivial correction.

With a correction as large as above, in order to be able to study individual profiles instead of anisotropies, it is important to apply a spectral correction to the data and to examine both high and low momentum sides of the resulting profile. Therefore the existing Monte-Carlo program was adapted to produce a spectral calculation over the entire momentum range and to generate a multiple scattering profile.

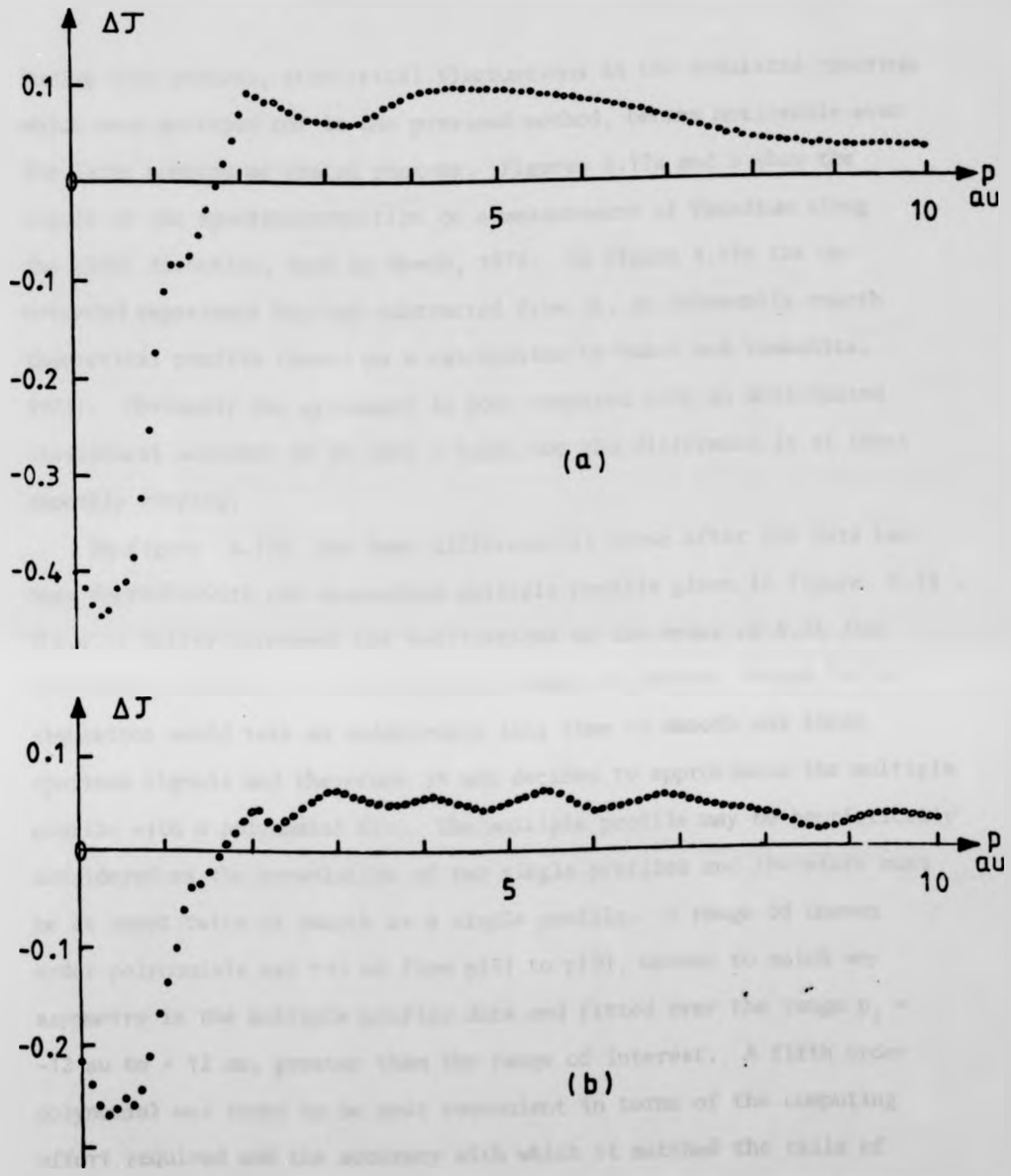

Figure 4.17. Effect of Multiple Scattering Correction on Vanadium: (a) Uncorrected Experimental Profile - Theory (see text); (b) Curve (a) with the Unsmoothed Multiple Profile Removed

During this process, statistical fluctuations in the simulated spectrum which were averaged out in the previous method, became noticeable even for large numbers of traced photons. Figures 4.17a and b show the result of the spectral correction on a measurement of Vanadium along the (100) direction, made in March, 1979. In figure 4.17a the uncorrected experiment has had subtracted from it, an inherently smooth theoretical profile (based on a calculation by Wakoh and Yamashita, 1973). Obviously the agreement is poor compared with an anticipated statistical accuracy of 1% J(o) ≡ 0.05, but the difference is at least smoothly varying.

In figure 4.17b the same difference is shown after the data has been correctedwith the unsmoothed multiple profile given in figure 4.18 . There is better agreement but oscillations of the order of 0.5% J(o) have been introduced. Increasing the number of photons traced in the simulation would take an undesirably long time to smooth out these spurious signals and therefore it was decided to approximate the multiple profile with a polynomial fit. The multiple profile may be heuristically considered as the convolution of two single profiles and therefore must be at least twice as smooth as a single profile. A range of uneven order polynomials was tried from p[3] to p[9], uneven to match any asymmetry in the multiple profile data and fitted over the range p_z = -12 au to + 12 au, greater than the range of interest. A fifth order polynomial was found to be most convenient in terms of the computing effort required and the accuracy with which it matched the tails of p_z = ± 10 au; and the fit over the positive half is shown in figure 4.18 . The effect on the Vanadium data was very promising and is shown in figure 4.19 . The spurious oscillations have disappeared and any other features observable are real, as are, for example, the bumps at the (100) reciprocal lattice translation distances 1.1 au and 2.2 au.

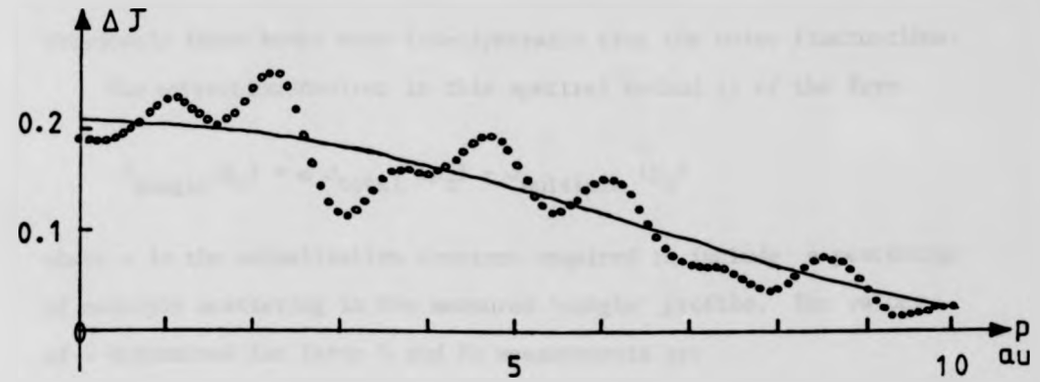

Figure 4.18. Calculated Multiple Scattering Profile of Vanadium (Points - unsmoothed results, curve - fifth order polynomial fit)

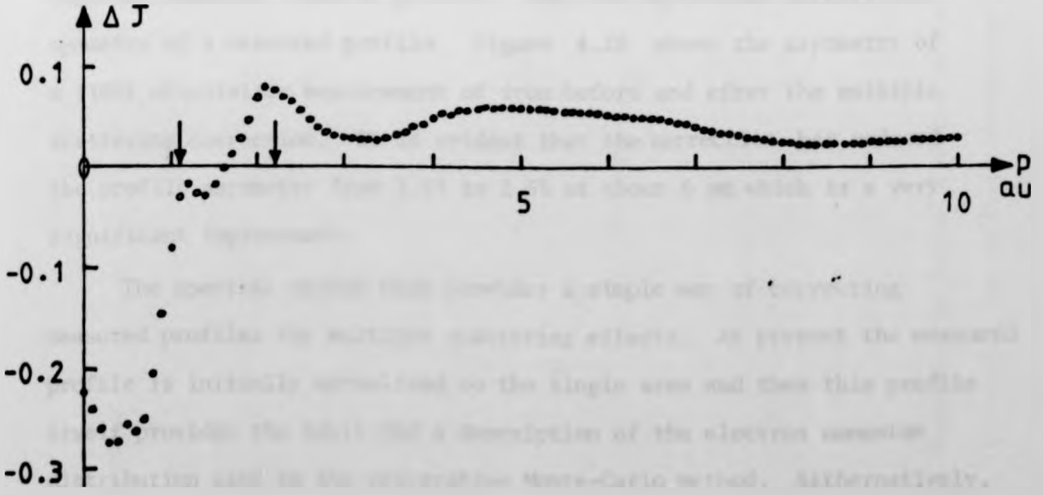

Figure 4.19. Vanadium Difference Profile (Experiment - Theory) Corrected with the Fitted Multiple Profile (The arrows indicate new features revealed at characteristic momenta)

Previously these bumps were indecipherable from the noise fluctuations.

The correction involved in this spectral method is of the form

$$J_{single}(p_z) = \alpha J_{total}(p_z) - J_{multiple}(p_z)$$

where α is the normalisation constant required to include a percentage of multiple scattering in the measured 'single' profile. The values of α determined for later V and Fe measurements are

	No. Photons	Dimensions	α
V	9×10^5	1.0 cm diam x 3mm	1.14
Fe	8×10^5	0.8 cm diam x 2 mm	1.17

Another important feature of the spectral correction is due to the fact that the multiple profile has slightly more electron density at negative momentum than at postive. Thus the correction affects the symmetry of a measured profile. Figure 4.20 shows the asymmetry of a (100) orientation measurement of iron before and after the multiple scattering correction. It is evident that the correction has reduced the profile asymmetry from 3.5% to 2.5% at about 6 au which is a very significant improvement.

The spectral method thus provides a simple way of correcting measured profiles for multiple scattering effects. At present the measured profile is initially normalised to the single area and then this profile itself provides the basis for a description of the electron momentum distribution used in the reiterative Monte-Carlo method. Althernatively, any other suitable profile (e.g. a free atom model) could be used as the basis and would yield an approximately equivalent multiple profile. The degree of approximation would be sufficiently close for the level of accuracy required and in fact any orientation of the profile can be used as the basis since the directional information is averaged out in the

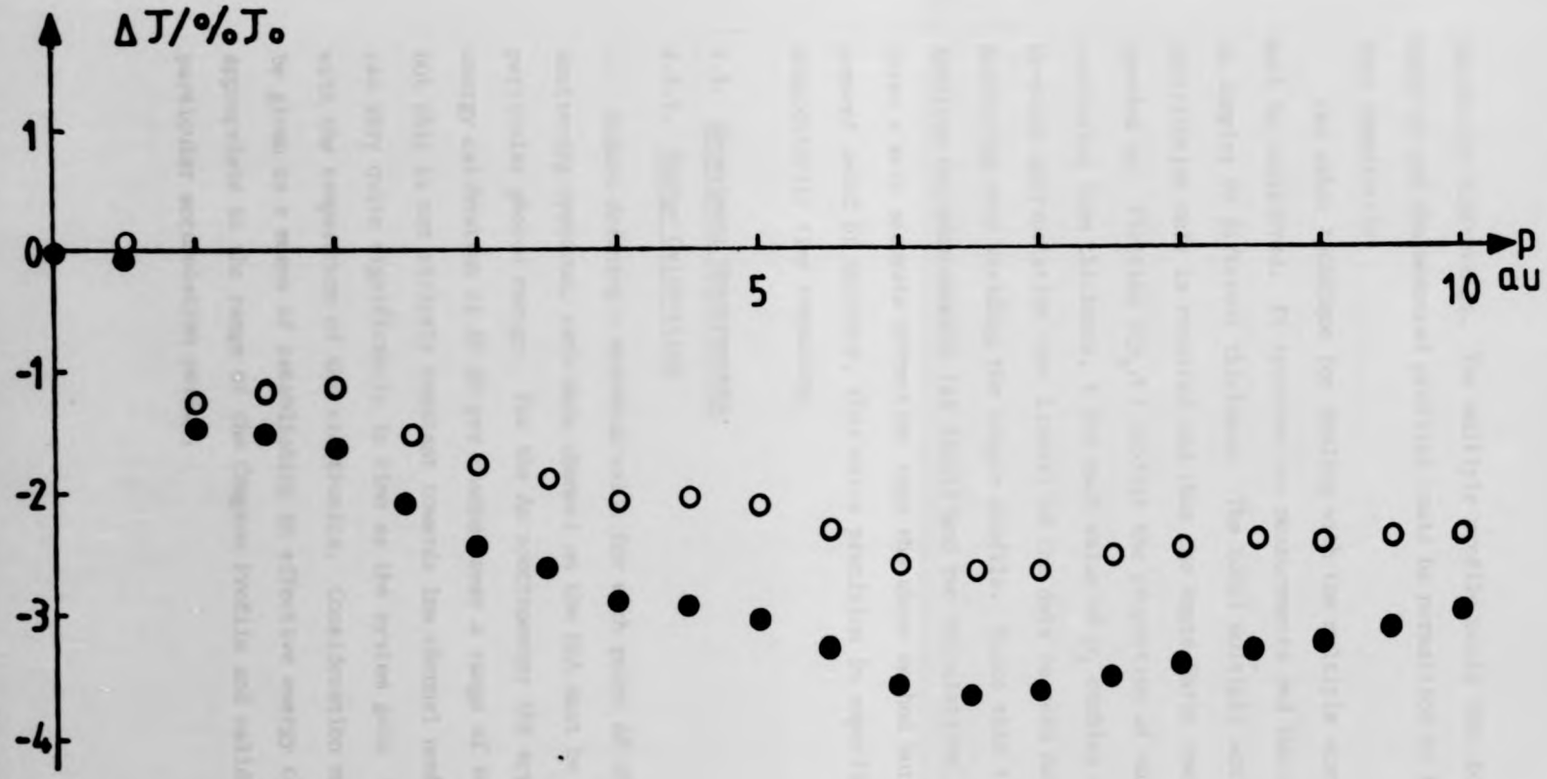

Figure 4.20. Asymmetry in Fe(100) Profile Before (closed circles) and After (open circles) Correction for Multiple Scattering

successive scatterings. The multiple profile could then be determined early on and the measured profiles could be normalised to the total area immediately.

One other technique for dealing with the multiple scattering must be considered. It involves two measurements and two calculations on samples of different thickness. The total multiple scattering contribution only is required and thus the Monte-Carlo routine may be speeded up. Plotting $J(p_z,t)$ against the proportion of multiple scattering from thickness, t for each value of p_z enables a point-by-point extrapolation (not linear) of the data to zero multiple scattering thus yielding the single profile. Since this technique involves two measurements (at least) and two calculations, it undoubtedly gives a more accurate correction than the above method but with the present level of accuracy, this extra precision is superfluous and unnecessarily time consuming.

4.3. Experiment Measurements

4.3.1. Energy Calibration

Before defining a momentum value for each point of the measured scattering spectrum, each data channel on the MCA must be assigned a particular photon energy. For the Au spectrometer the approximate energy calibration is 50 eV per channel over a range of 4096 channels but this is not strictly constant towards low channel numbers and also can vary quite significantly in time as the system gain fluctuates with the temperature of the electronics. Consideration must therefore be given to a means of establishing an effective energy calibration appropriate to the range of the Compton Profile and valid for a particular accumulation period.

successive scatterings. The multiple profile could then be determined early on and the measured profiles could be normalised to the total area immediately.

One other technique for dealing with the multiple scattering must be considered. It involves two measurements and two calculations on samples of different thickness. The total multiple scattering contribution only is required and thus the Monte-Carlo routine may be speeded up. Plotting $J(p_z,t)$ against the proportion of multiple scattering from thickness, t for each value of p_z enables a point-by-point extrapolation (not linear) of the data to zero multiple scattering thus yielding the single profile. Since this technique involves two measurements (at least) and two calculations, it undoubtedly gives a more accurate correction than the above method but with the present level of accuracy, this extra precision is superfluous and unnecessarily time consuming.

4.3. Experiment Measurements

4.3.1. Energy Calibration

Before defining a momentum value for each point of the measured scattering spectrum, each data channel on the MCA must be assigned a particular photon energy. For the Au spectrometer the approximate energy calibration is 50 eV per channel over a range of 4096 channels but this is not strictly constant towards low channel numbers and also can vary quite significantly in time as the system gain fluctuates with the temperature of the electronics. Consideration must therefore be given to a means of establishing an effective energy calibration appropriate to the range of the Compton Profile and valid for a particular accumulation period.

No.	Date	Am	PbK	PbK	Te	Measurement
		59.54 keV	72.79 keV	74.96 keV	159.0 keV	
1	3.3.80	1175.0	1442.0	1485.0	3175.0	-
1a	3.3.80	1175.0	1442.0	1485.0	3174.0	V(100)
2	5.3.80	1173.0	1439.5	1483.0	3171.0	V(110)
3	7.3.80	1172.5	1439.0	1482.5	3168.5	V(111)
4	11.3.80	1172.5	1439.0	1482.5	3167.5	

Table 4.3. Log of Calibration Line Drift During the March (1980) Series of Vanadium Measurements

Original processing involved establishing an energy calibration before and after a measurement using fluorescence lines of known photon energy excited by a 123 m Te source. For example, Table 4.3 depicts a series of five calibrations interspersed with a series of Vanadium measurements. The positions of the lines can be seen to vary by as much as 3 channels at 159 keV during a single measurement. This corresponds to a drift of $\sim$ 150 eV or 0.1 au momentum at the profile origin - a significant amount compared with the total system resolution of 0.4 au. Furthermore, there is no guarantee that the calibration obtained as an average in this way, represents that which exists during the measurement. This is borne out by the fact that scattering angles calculated from a knowledge of the position of the profile origin and the energy calibration have varied by as much as 3 degrees from the design value. This has a deteriorative effect on the cross-section and absorption corrections which both depend on the true value of θ. Reduction of temperature variation induced fluctuations in gain by installation of environmental control air conditioning was found to be only marginal. This ensured that the momentum smearing due to the gain variation would be maintained at a negligible value but could not ensure that the gain at any moment would be appropriate for the duration of a measurement lasting 3 days.

The effective solution adopted in all later measurements was to inspect the position of characteristic lines present in the data itself. The main lines are listed in Table 4.4. These can be taken to follow all the fluctuations in gain and should enable a much more realistic calibration. However, as can be seen from the table, no sharply-defined lines are found near the profile centre and it is necessary to extrapolate a linear calibration up to that region. Location of the profile centre then leads to slightly inaccurate values of θ showing the extrapolation

Identification	Energy/keV	Type	Used in Calibration
Ec ($AuK\alpha_1$,θ)	54.35	Compton	No
Ec ($AuK\beta_1$,θ)	59.92	Compton	No
$AuK\alpha_2$	66.98	Fluor.	Yes
$AuK\alpha_1$	68.79	Fluor.	Yes
$PbK\alpha_2$	72.79	Fluor.	Yes
$PbK\alpha_1$	74.96	Fluor.	Yes
$AuK\beta_1$	77.97	Fluor.	No
$AuK\beta_2$	80.17	Fluor.	No
$PbK\beta_1$	84.92	Fluor.	No
$PbK\beta_2$	87.34	Fluor.	No
Ec(^{99}Au,158)	98.25	Compton	No
Ec(^{199}Au,208)	115.38	Compton	No
Ec(^{149}Au,412)	158.94	Compton	Yes, finally

Table 4.4. Energy Calibration Lines Observed in a Data Spectrum from the Gold Spectrometer (θ = 167 degrees)

to be at fault. The final approach to fixing the energy scale is tied closely to the problems of determining the profile centre which is discussed in detail in §4.4.1. It involves a reiterative definition of the calibration taking the above as a first approximation while constraining the located profile origin to produce the correct value for θ. Only small alterations of the initial energy calibration are required by this technique and they are well within the experimental errors of the original determination.

This technique has proved itself to be entirely satisfactory to date. With regard to the Americium spectrometer, the energy calibration has never posed any problems since experiments can be performed more quickly in a more stable temperature environment and calibration lines exist on either side of the profile in a typical spectrum.

4.3.2. Background Spectrum

The determination of a suitable background radiation spectrum for a particular spectrometer system has come to be considered a trivial problem. However this is only the case when the signal-to-noise ratio (S/N) is high (> 100:1) compared with the accuracy desired for the profile ($\sim$ 0.5% J(o)). Recent measurements of Iron crystals of rather small dimension ($\sim$ 8 mm diameter) have produced S/N values of only 50:1 (see table 4.5). At this level, errors in determining the background start to affect the final profile significantly, as will be shown presently.

There are three main contributions to the noise in a Compton experiment -

(a) Cosmic ray interference

(b) Contamination of the source material producing γ-rays at energies other than that of the principal emission.

(c) Scattering of the primary radiation from some part of the apparatus rather than the sample.

Effect (a) can be reduced to a negligible level by adequate screening of the detector. For the Gold spectrometer the high density source block of Tungsten alloy has a cavity which houses the detector crystal. For the Americium spectrometer operating in a lower energy regime a special detector housing of lead was built, providing ∿ 5 cm of shielding over 360°. Thus the shielding in each system is sufficient to block the low energy extensive air showers resulting from the high energy Cosmic rays.

Contamination of the source emission with other energies is again simply dealt with. For the Gold spectrometer the secondary emission is at energies lower than the primary (Table 3.1) e.g. 208 keV and (more significantly) 159 keV. These are preferentially absorbed by the source itself and as was found during the design of the system (see Chapter 3), suitable choice of the source thickness removed their effect. With the Americium system (60 keV) there is a secondary emission at 100 keV which may indeed be detectable as significant additional scattering from the sample. Preferential absorption cannot be utilised here. It has been suggested by another Compton scattering research group at the University of Konstanz that a 2 mm thick filter of Tin, placed in front of the source may allow the higher energy contribution to the scattered profile to be measured on its own.

For both spectrometer systems, scattering from the sample chamber (c) has been shown to be generally the dominating contribution to profile noise. Chamber scattering is measured by removing the sample from the system (while retaining the sample mounting assembly) and performing a

normal experiment. With the Gold system the times of the "empty chamber" experiment and the sample experiment are recorded in order to allow for the decrease of intensity due to rapid source decay. It is assumed that to a first approximation, the presence of the sample does not interfere with the scattering from the apparatus and that the two signals thus add linearly. The errors introduced in a measurement by the subtraction of this background spectrum are derived in the following analysis.

Considering a data measurement $y_T(E)$ and a background measurement $y_{Bm}(E)$ over two time intervals differing by a factor R,

error in measured data, $y_T = \delta y_T$

error in measured background, $y_{Bm} = \delta y_{Bm}$

Correcting y_{Bm} for the different time interval

$$y_B = R y_{Bm}$$

This must be subtracted from the data,

Thus $y_D = y_T - y_B = y_T - R y_{Bm}$

and the error in the data now becomes

$$\delta y_D = \sqrt{\delta y_T^2 + \delta y_B^2}$$

$$= \sqrt{\delta y_T^2 + R^2 \delta y^2_{Bm}}$$

Supposing a measured signal-to-noise ratio of α

$$y_{Bm} = \frac{1}{\alpha} \; y_T$$

Measurement	Orientation	Compton Peak	Time Corrected	S/N	R	Accuracy %	P
R029	(111)	112,000	178,089	115	32.6	0.3 x	1.13
R030	(110)	47,000	164,739	106	14.8	0.5 x	1.07
R031	B.G.	30	1,555	-	-	18.3 ←	0.16
R032	(100)	89,000	141,449	125	10.5	0.3 x	1.04
R033	(110)	43,000	151,041	134	4.7	0.5 x	1.02
R034	B.G.	68	1,130	-	-	12.1 ←	0.10
R035	(100)	68,000	129,430	54	7.4	0.4 x	1.07
R036	(111)	60,600	166,294	69	5.1	0.4 x	1.04
R037	B.G.	170	2,400	-	-	7.7 ←	0.10

Table 4.5. Signal/Noise Ratios for Measurements of Iron Samples

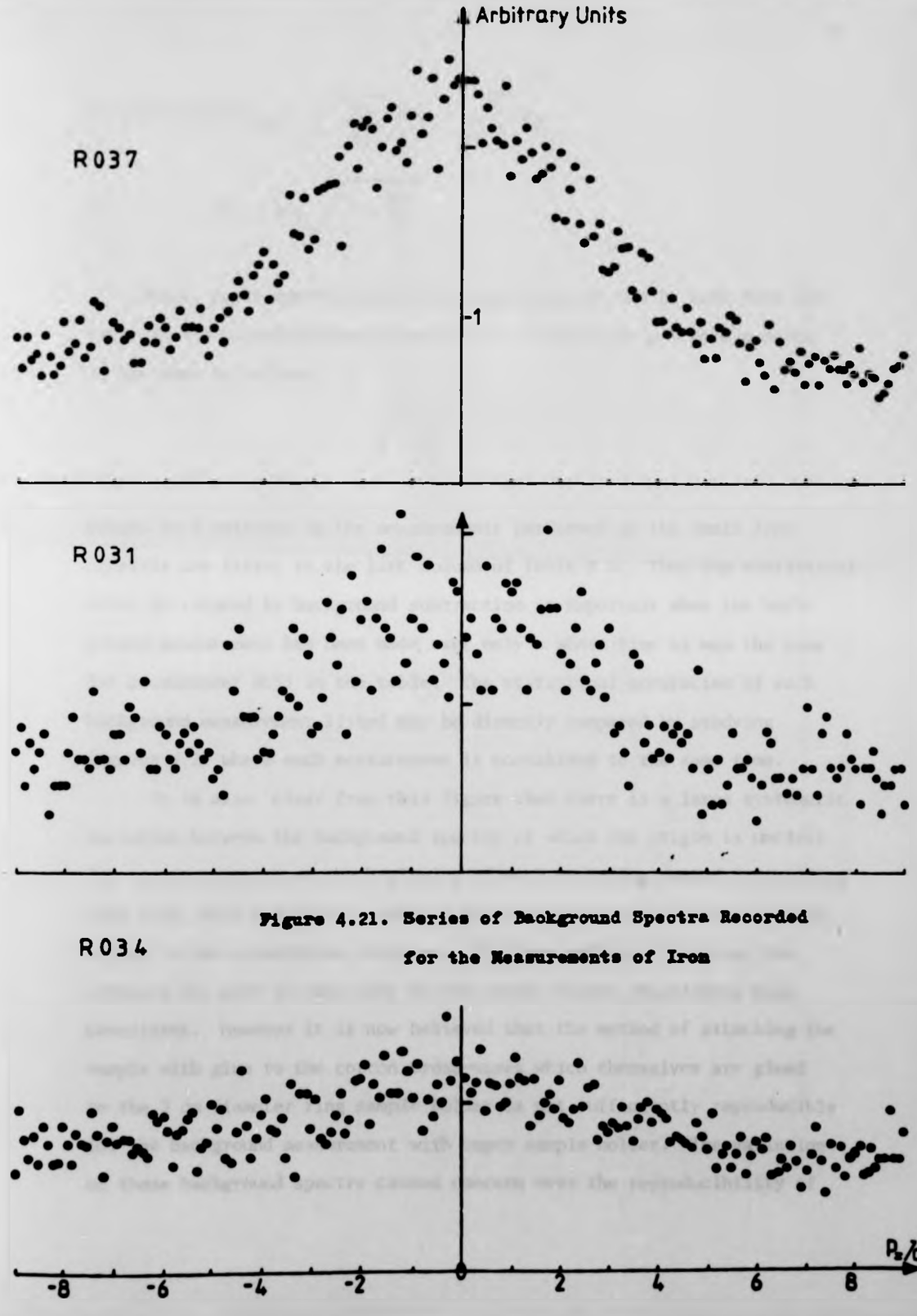

Figure 4.21. Series of Background Spectra Recorded for the Measurements of Iron

and therefore $\delta y_{Bm} = \sqrt{\frac{y_{Bm}}{y_T}}\ \delta y_T = \sqrt{\frac{1}{\alpha}}\ \delta y_T$

so, $$\delta y_D = \delta y_T \sqrt{1 + \frac{R^2}{\alpha}}$$

Since, y_D is approximately the same as y_T, it can be seen that the noise in the background measurement will increase the percentage error in the data by a factor of

$$\beta = \sqrt{1 + \frac{R^2}{\alpha}}$$

Values of β relevant to the measurements performed on the small Iron crystals are listed in the last column of Table 4.5. Thus the statistical error introduced by background subtraction is important when the background measurement has been made over only a short time as was the case for measurement R031 in the table. The statistical accuracies of each background measurement listed may be directly compared by studying figures 4.21 where each measurement is normalised to the same time.

It is also clear from this figure that there is a large systematic variation between the background spectra of which the origin is unclear. The source strength at the beginning of each measuring period (coinciding with R029, R032 and R035 in table 4.5) is assumed to be constant at 120 Ci due to the irradiation strategy. The same method of mounting the crystals was used in each case so the sample holder should have been consistent. However it is now believed that the method of attaching the sample with glue to the cotton cross-wires which themselves are glued to the 3 cm diameter ring sample holder is not sufficiently reproducible for the background measurement with empty sample holder. The variation of these background spectra caused concern over the reproducibility of

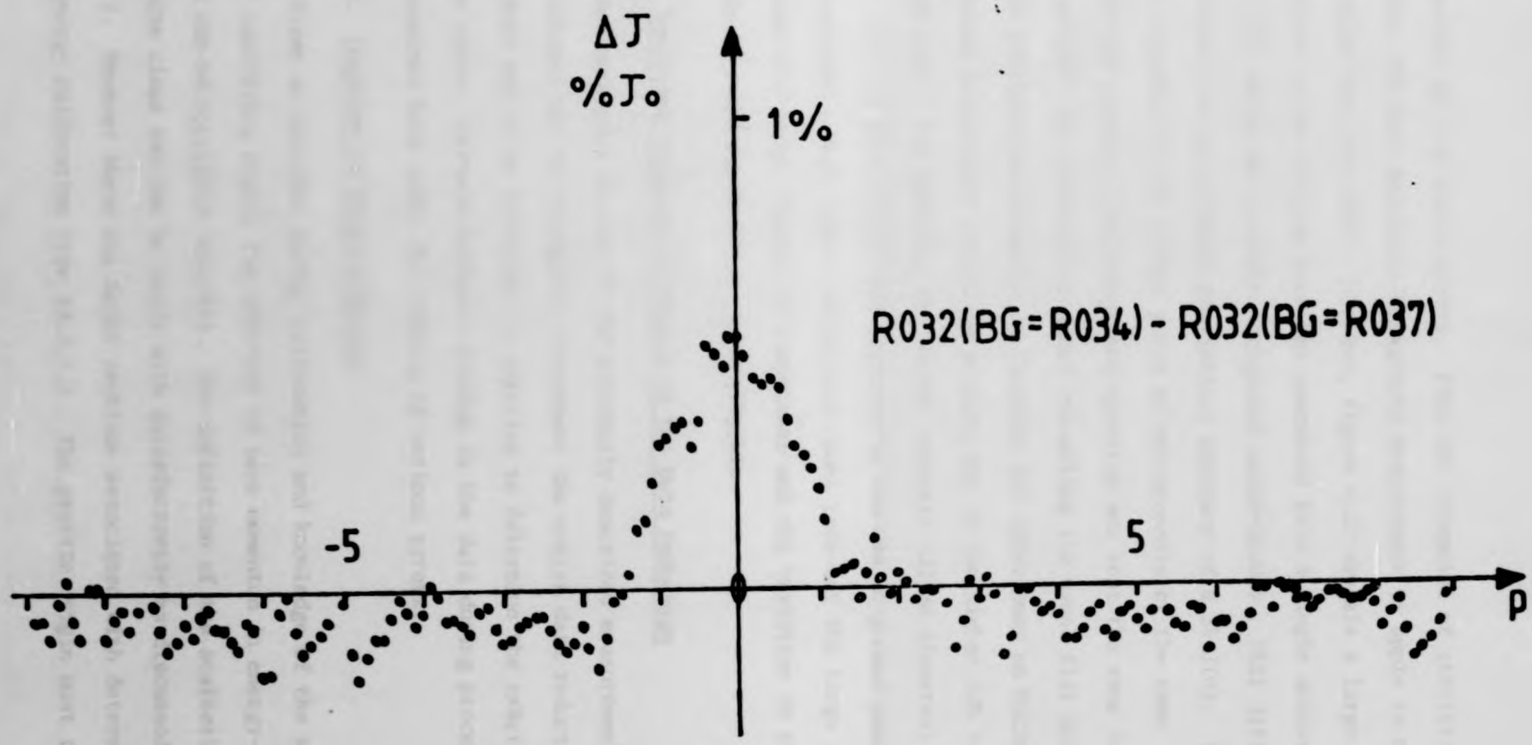

Figure 4.22. Effect of Using an Incorrect Background Spectrum (BG = R037) in the Data Reduction of a Measurement of Iron (R032)

this series of Iron measurements. From the viewpoint of statistical accuracy, the most desirable background measurement to apply to the data would have been R037. However, figure 4.22 reveals a large difference in the Compton profiles processed from a single measurement of Fe(100) using two separate background measurements. This difference far exceeds the anticipated statistical accuracy of 0.3% J(o). To ensure reproducibility within pairs of measurements of the same orientation crystal, the background spectrum was kept the same in each case and R037 was rejected as least resembling the usual flat spectrum.

In previous measurements on Vanadium and later ones on Nickel the background measurement proved no problem due to the higher S/N ratio in each case. For mounting the Nickel crystals (22 mm diameter) the cross wire and glue method was replaced by the use of gummed paper. This provided a much higher background count rate but the large crystals produced very large signals to compensate and the variation in cross section of mounting material was negligible.

4.4. Important Features of Stages in the Data Reduction

An inaccuracy in any of the previously described measurements or calculations may be propagated throughout the entire data reduction procedure and it is difficult in practice to determine the exact source of the error. Certain features arising in the data during processing are examined here under the effects of various errors.

4.4.1. Location of Profile Origin

Given an accurate energy calibration and knowledge of the spectrometer scattering angle, the position of zero momentum in energy-channel space can be specified exactly. The definition of the scattering angle is quite clear and can be dealt with satisfactorily as discussed in §4.2.2. However there are major problems associated with determining the energy calibration (see §4.3.1.). The profile origin must therefore

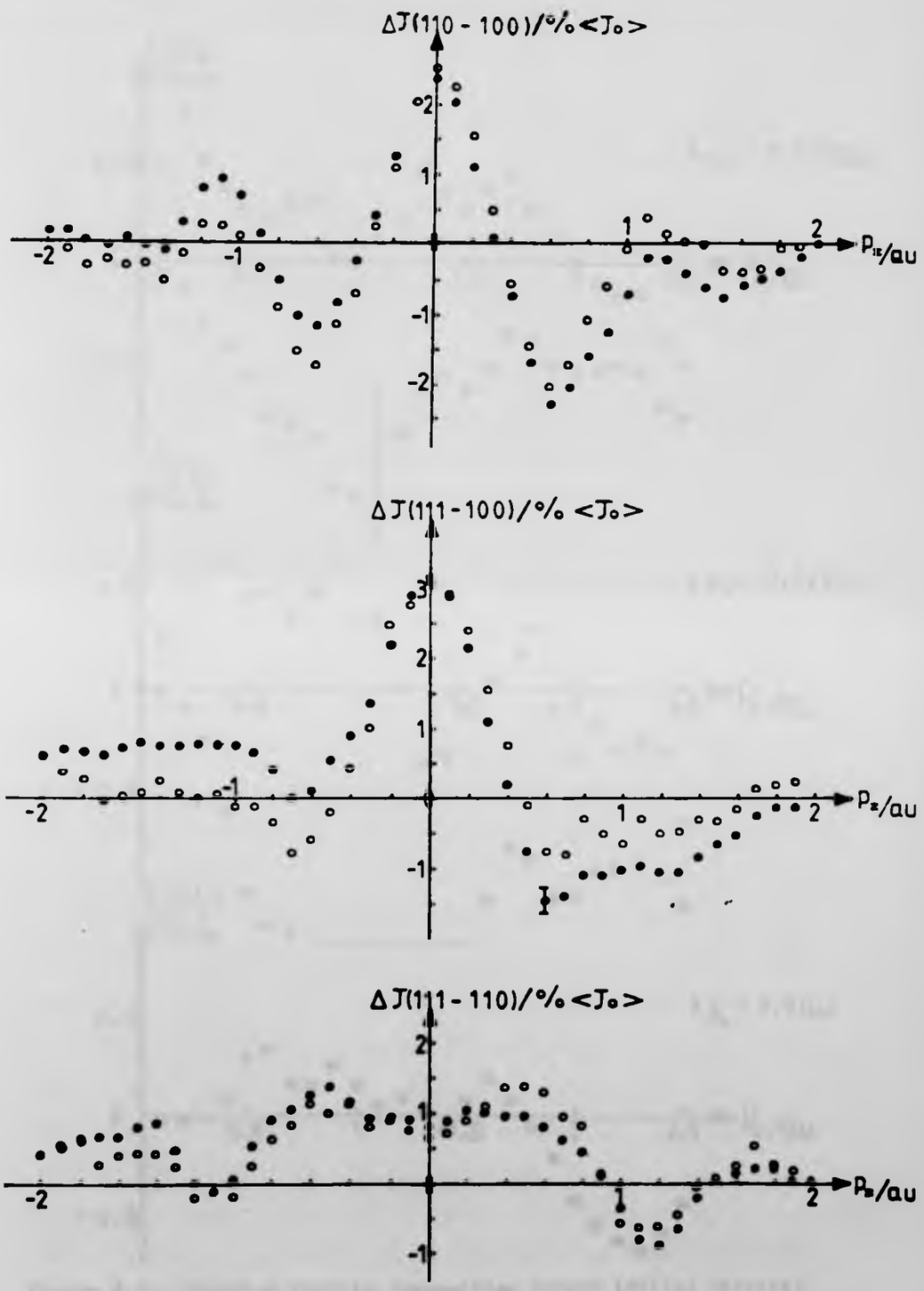

Figure 4.23. Vanadium Anisotropies Before (Filled Circles) and After (Open Circles) Relocation of Momentum Origin

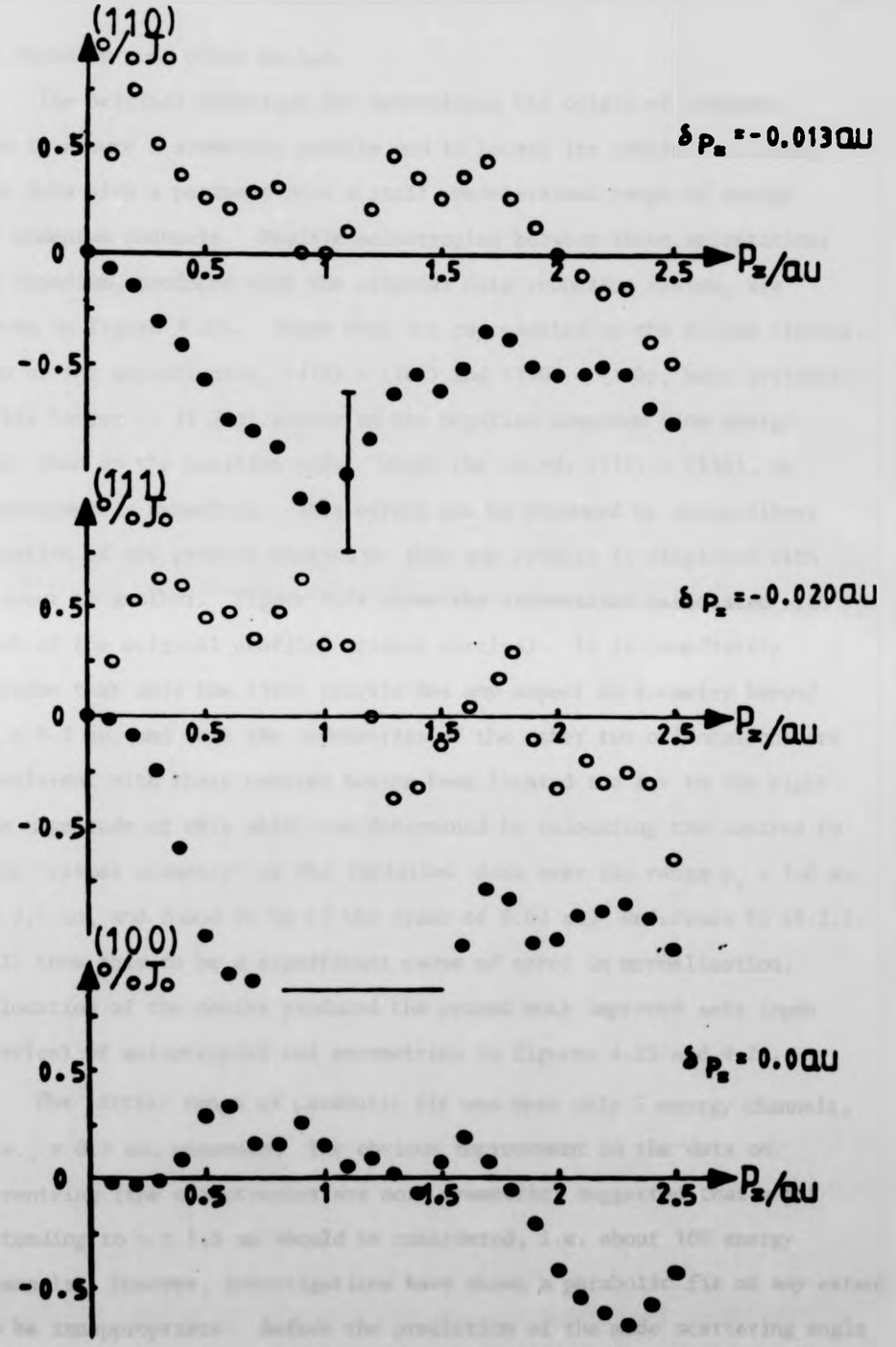

Figure 4.24. Vanadium Profile Asymmetries Before (Filled Circles) and After (Open Circles) Relocation of Origin

be found by some other method.

The original technique for determining the origin of momentum was to assume a symmetric profile and to locate its centre by fitting the data with a parabola over a small predetermined range of energy or momentum channels. Profile anisotropies between three orientations of Vanadium, produced with the original data reduction system, are shown in figure 4.23. where they are represented by the filled circles. Two of the anisotropies, (111) - (100) and (110) - (100), have systematically larger ($\sim$ 1% J(o) values on the negative momentum (low energy) side than on the positive side, while the third, (111) - (110), is approximately symmetric. This effect can be produced by inconsistent location of the profile centres so that one profile is displaced with respect to another. Figure 4.24 shows the asymmetries associated with each of the original profiles (closed circles). It is immediately obvious that only the (100) profile has any aspect of symmetry beyond $p_z \approx 0.1$ au, and that the asymmetries of the other two orientations are consistent with their centres having been located too far to the right. The magnitude of this shift was determined by relocating the centres to give "visual symmetry" of the replotted data over the range $p_z = 1.0$ au to 2.0 au, and found to be of the order of 0.02 au. Reference to §4.2.3. will show this to be a significant cause of error in normalisation. Relocation of the centre produced the second much improved sets (open circles) of anisotropies and asymmetries in figures 4.23 and 4.24.

The initial range of parabolic fit was over only 7 energy channels, i.e., ± 0.1 au, momentum. The obvious improvement in the data on recentring (the anisotropies are more symmetric) suggested that a fit extending to $\sim \pm$ 1.5 au should be considered, i.e. about 100 energy channels. However, investigations have shown a parabolic fit of any extent to be innappropriate. Before the prediction of the mode scattering angle by the geometry broadening simulation (§4.2.2.), the method of obtaining

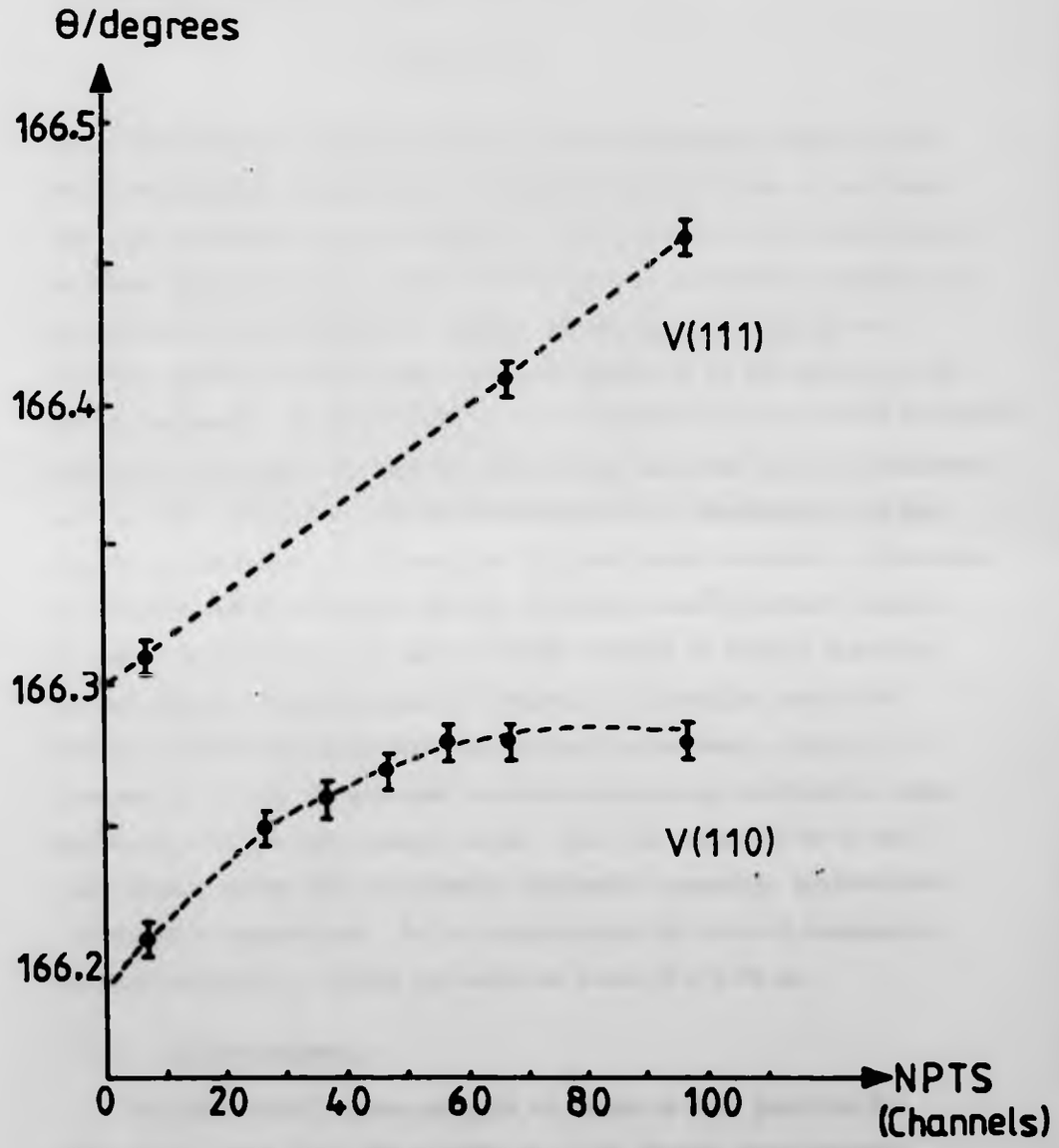

Figure 4.25. Variation of Scattering Angle θ Determined from Centre - Locating Parabolae of Varying Extent

θ (to be used in applying the cross-section correction and establishing the momentum scale) was to invoke eq. 1.2 -

$$\Delta\lambda = \frac{2h}{mc} \sin^2 \frac{\theta}{2}$$

after determining $\Delta\lambda$ from the centre position and known primary energy. While studying the effect of more extensive parabolic fits it was found that the scattering angle determined in this way would vary significantly as shown in figure 4.25. This variation in θ is explained by considering an asymmetric profile with the higher, low energy side pulling the centring parabola towards lower energies (higher θ) as the extent of the fit is increased. If the profile is always expected to be slightly asymmetric until all processing is complete, this method can never work satisfactorily and has been replaced by the procedure of §4.3.1. Furthermore, in the case of a (100) profile of Vanadium, the peak region exhibits a depression of electron momentum density due to the valence band structure (Chapter 5) and a simple parabola is not a suitable choice of fitting function. In anticipation of much closer fitting with all profiles around the origin, an 8th order polynomial is now constructed over a range of 37 channels (± 1.1 au) to generate the reiterated energy calibration which maintains θ at the spectrometer value. This has proved to be a very satisfactory method and consistently yields more symmetric anisotropies and sensible asymmetries. It is estimated that the zero of momentum is located correctly to within the required error of ± 0.01 au.

4.4.2. Profile Asymmetry

The theoretical Compton profile is symmetric over positive and negative momentum under the conditions of the Impulse Approximation. It should therefore be possible to use either side of an experimental result in any comparison with theory or indeed to average the two sides.

However, several experimental factors contribute to the destruction of this symmetry, particularly by enhancement of the low energy side, thus making interpretation more difficult. In the past only the high energy side results of measurements have been presented in the belief that these are less affected by the factors under consideration, and this attitude still exists amongst most contemporary research groups. Much of the current work has been involved with defining the asymmetry more precisely and to investigate its effect on the final profile. For example, the location of the profile centre has been found to be particularly sensitive to erroneous asymmetry and therefore, to some degree the normalisation of the high energy data must also be affected. Also if any significant asymmetry remains after all processing has been completed then there must be some unknown factor which has not been treated and there is no reason to assume that this does not affect the high energy data. Thus it is desirable to ensure through careful data processing that all possible asymmetry is removed and that both sides of the data should be regarded as equally valid.

The data reduction procedures recently developed go most of the way towards realizing this aim and the possibility of a symmetric result is no longer unrealisable. To comprehend more fully the magnitude of the asymmetry problem it is instructive to study the asymmetry after various corrections have been applied. The experimental factors which most affect the symmetry are

Detector efficiency
Detector response function
Source line broadening
Sample absorption
Cross-section
Multiple scattering

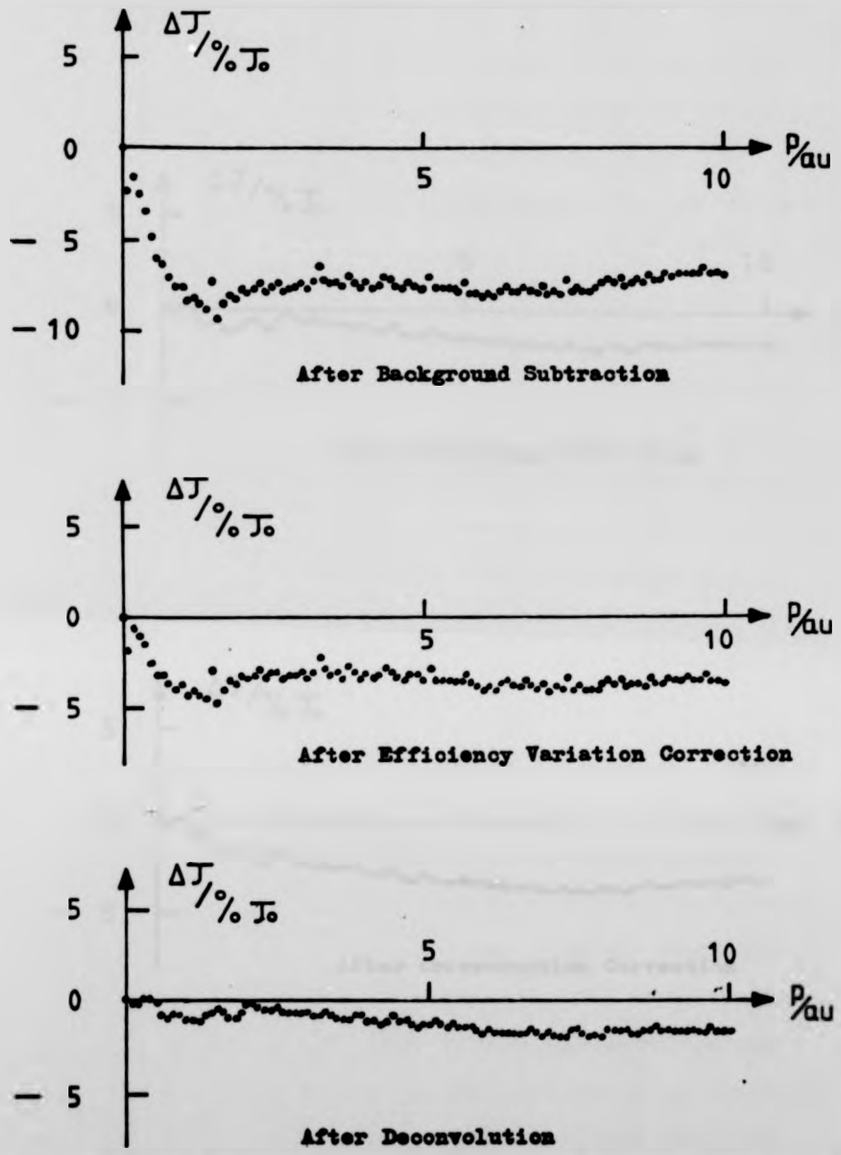

Figure 4.26a Fe(100) Profile Asymmetry Development During Data Reduction

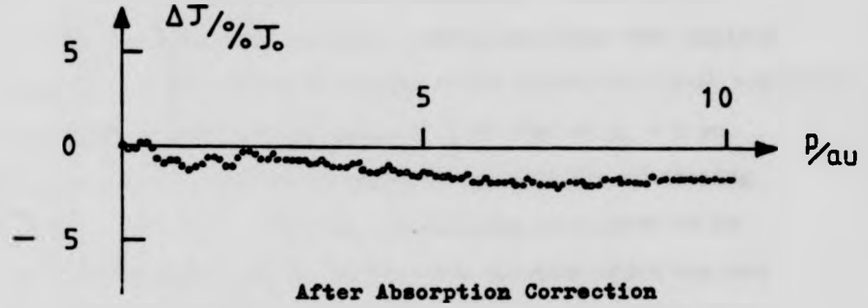

After Absorption Correction

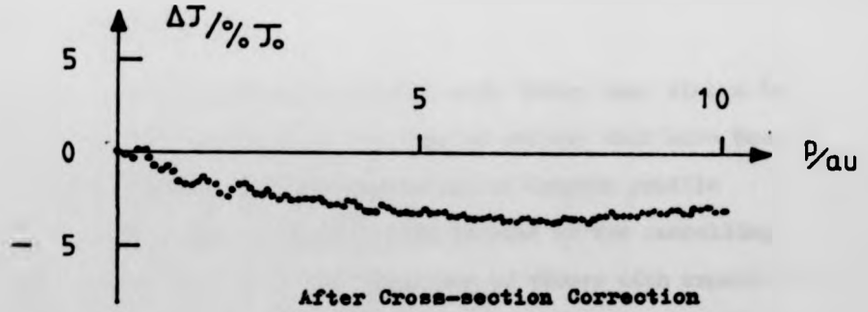

After Cross-section Correction

Figure 4.26b Fe(100) Profile Asymmetry Development During Data Reduction

The asymmetry of an Iron (100) profile after various stages of processing is shown in figures 4.26 a and b. The background correction is symmetric and so the first plot may be taken to represent the asymmetry of the raw data since no other corrections have been applied at this point. The second plot in figure 4.26b shows the final asymmetry of the total profile to be of the order of 3.5% J(o) at p_z = 6 au. Referring back to figure 4.20, the correction for multiple scattering reduces this to $\sim$ 2.5% J(o). The only outstanding correction to be applied is a deconvolution of the source line function which has yet to be justified by experiment. As can be seen from figure 4.12b, it is anticipated that the magnitude of this correction, which depends primarily on the source geometry, will be sufficient to remove all remaining asymmetry.

4.5. Profile Interpretation

Comparison of the experimental results with theory must always be performed with due consideration of the type of effects that have been discussed in this chapter. The interpretation of Compton profile anisotropies is always more straightforward because of the cancelling of systematic errors. However, the comparison of theory with experimental results in the form of the B-function (§1.3.2.) is likely to become popular in the near future since in this representation most of the systematic errors, as slowly varying functions of p_z, are expected to be confined to the region near the origin of position while the information about the bonding valence electrons appears at distances of the order of lattice translations. Recent results for transition metals are analysed in the light of these restraints in the following chapters.

CHAPTER 5

Vanadium

5.1. Introduction

The theoretical description of electron behaviour in Transition metals is complicated by the peculiar nature of the d electrons. In the first transition series from Sc to Zn, which is the subject of much present research, the 3d electrons have such a spatial extent that they cannot be classed neatly as conduction electrons or non-bonding free atom-like in the solid state. The 4d electrons of the second transition period are more diffuse than the 3d electrons, the crystal structure sometimes remaining the same from one period to the next. Thus there is the possibility of studying the effects of variation of electron density on the Compton profiles of these metals. No such systematic study has yet been undertaken. It has been discovered that there exists significant interaction between the 3d electrons themselves and between these and the 4s electrons in the conduction band. Such interactions lead to a complicated band structure and Fermi surface. A number of complete bandstructure calculations exist which include exchange-correlation energy functionals of the local density to account for these interactions. These calculations have been quite successful at predicting a number of observable quantities such as Fermi surface cross sections obtained byde Haas-van Alphen measurements and the energy widths of the d bands obtained from photo-emission measurements. On the other hand, predictions of the density of states have not been supported by measurements of the electronic specific heats of the metals and the scales of directional features of

both the momentum density and the charge density are seriously in error. Because of their semi-atomic character, discussion of the crystalline 3d wavefunctions in Vanadium often persists in terms of atomic orbitals configured to the symmetry of the body centred cubic lattice. In this arrangement the t_{2g} type d orbitals point towards nearest neighbours while the orbitals of e_g symmetry point in between to next-nearest neighbours. A simple redistribution of the spherically symmetric 60% t_{2g}, 40% e_g arrangement, as a result of crystalline effects leads in a clear way to anisotropy in the momentum and charge distributions with better agreement with experiment than is obtained from the band structure calculations. The measurement of Compton profile anisotropies and comparison with theory may therefore prove invaluable with regard to understanding transition metals.

The presentation of results from the current research is preceded in this chapter by a summary of the conclusions of earlier work on transition metals - both experimental and theoretical. Due to various experimental difficulties it has been customary to present results first in the form of differences of measurements - since this removes many systematic errors. The first results given are therefore for the momentum anisotropy (and the complementary charge asphericity measurements). The analysis of individual profiles is reserved for the last section.

5.2. Previous Research

The earliest attempts to describe the Compton profiles of transition metals in terms of free atom models were naturally very inadequate. As suggested in §1.4.2., the atom bonded in a solid has a higher kinetic energy than the free atom and this is evidenced in the Compton profile

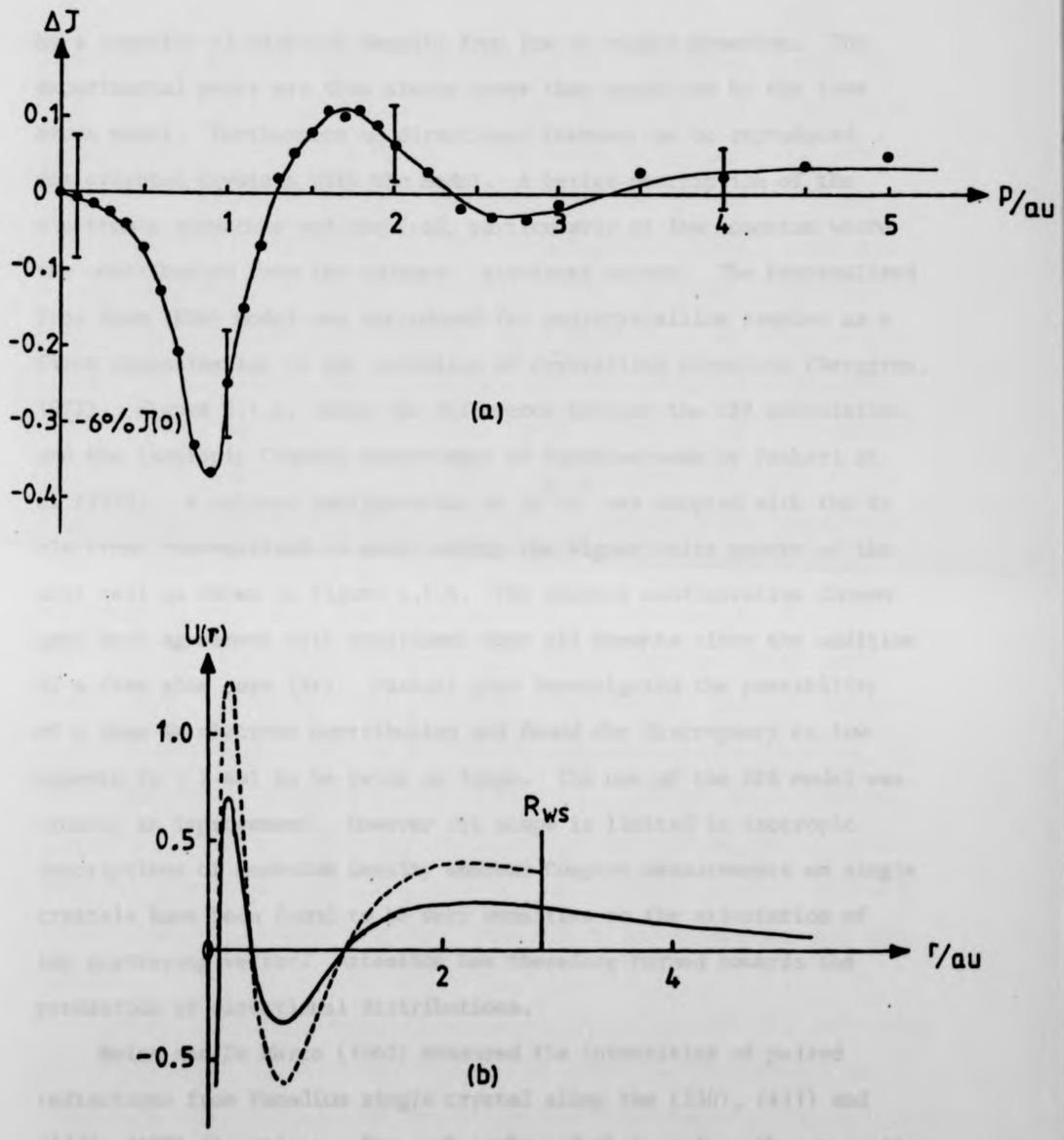

Figure 5.1. Early Investigation of the Isotropic Momentum Distribution in Polycrystalline Vanadium: (a) RPA Theory - Experiment (b) Renormalisation of 4s Radial Function within the Wigner - Seitz Sphere

by a transfer of electron density from low to higher momentum. The experimental peaks are thus always lower than predicted by the free atoms model. Furthermore no directional features can be reproduced for oriented crystals with the model. A better description of the electronic structure was required, particularly at low momentum where the contribution from the valence electrons occurs. The Renormalised Free Atom (RFA) model was introduced for polycrystalline samples as a first approximation to the inclusion of crystalline structure (Berggren, 1972). Figure 5.1.a. shows the difference between the RFA calculation and the isotropic Compton measurement of Vanadium made by Paakari et al (1975). A valence configuration of $3d^3 4s^2$ was adopted with the 4s electrons renormalised to unity within the Wigner Seitz sphere of the unit cell as shown in figure 5.1.b. The valence configuration chosen gave best agreement with experiment over all momenta after the addition of a free atom core (Ar). Paakari also investigated the possibility of a free 4s electron contribution and found the discrepancy at low momenta ($p < 2$ au) to be twice as large. The use of the RFA model was clearly an improvement. However its scope is limited to isotropic descriptions of momentum density whereas Compton measurements on single crystals have been found to be very sensitive to the orientation of the scattering vector. Attention has therefore turned towards the prediction of directional distributions.

Weiss and De Marco (1965) measured the intensities of paired reflections from Vanadium single crystal along the (330), (411) and (442), (600) directions. For each member of these pairs, the separation of the diffracting planes given by $d = a/(h^2+k^2+l^2)^{\frac{1}{2}}$ is the same and therefore so is the atomic density within each plane. Comparison of the scattered intensity from a pair of reflections thus yields information about the asphericity of the charge distribution around each atom. Weiss

found charge asphericities of the order of 4% which could be explained in terms of a simple atomic model with the 3d electrons distributed as 81% t_{2g} symmetry and 19% e_g symmetry. This should be compared with the spherically symmetric arrangement of 60% t_2g, 40% e_g. On the basis of this empirical distribution of d-orbitals, Weiss (1966[144]) predicted a Compton profile anisotropy between the (111) and (100) directions of $\Delta J(o) = 0.4$ electrons/unit momentum i.e., about 8% of the average peak value, J(o). However, this prediction was not confirmed in measurements with 241 Am γ-rays by Phillips (1973) ($\Delta J(o) \sim 0.1$) or by Paakari et al (1973) ($\Delta J(o) \sim 0.1$). The latter authors reworked Weiss's calculation using a 3d population of 67% t_{2g} character and found much better agreement with their results which were also qualitatively supported by the X-ray Compton measurements of Terasaki et al (1973). In an attempt to introduce solid-state effects into the atomic model Weiss (1978) varied the relative extent of the radial parts of the two types of d-orbital. This he achieved by substituting the Vanadium functions with a Chromium function for the t_{2g} orbital and a Titanium function for the e_g. This has the effect of contracting the t_{2g} orbitals which in a body centered cubic lattice point towards nearest neighbours while expanding the e_g. A slight reduction in anisotropy was the only result.

While this atomic model is not particularly suitable for describing the solid state, it still has a number of points in its favour. In comparison with the relevant band structure calculations it is conceptually very simple and leads to a distribution of d electrons between the two symmetries that is also predicted by the more rigorous theories and supported by experiment. Furthermore, although it cannot reproduce high momentum features arising from the periodicity of a lattice, the

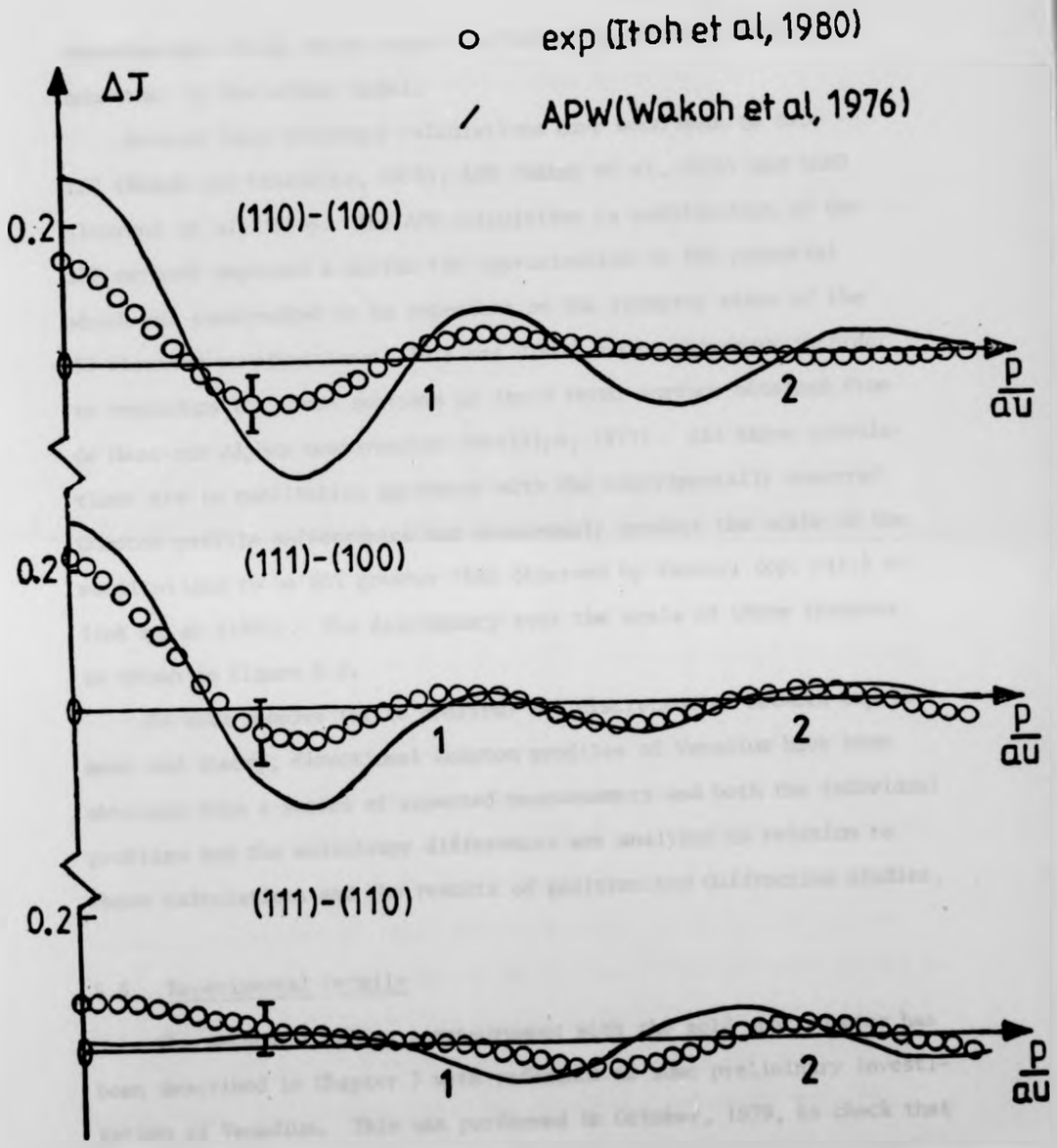

Figure 5.2. Vanadium Profile Anisotropy

momentum and charge anisotropies are better represented at low momentum by the atomic model.

Several band structure calculations have been made to date - KKR (Wakoh and Yamashita, 1973), APW (Wakoh et al, 1976) and LCAO (Laurent et al, 1978). The APW calculation (a modification of the KKR method) employed a muffin tin approximation to the potential which was constructed to be dependent on the symmetry state of the 3d electron wavefunctions. This was found to be necessary in order to reproduce the cross sections of the V Fermi surface obtained from de Haas-van Alphen measurements (Phillips, 1971). All three calculations are in qualitative agreement with the experimentally observed Compton profile anisotropies but unanimously predict the scale of the oscillations to be 50% greater than observed by Paakari (op. cit.) or Itoh et al (1980). The discrepancy over the scale of these features is shown in figure 5.2.

To help resolve (or to confirm) the discrepancies between experiment and theory, directional Compton profiles of Vanadium have been obtained from a series of repeated measurements and both the individual profiles and the anisotropy differences are analysed in relation to these calculations and the results of positron and diffraction studies.

5.3. Experimental Details

The method of making a measurement with the gold spectrometer has been described in Chapter 3 with reference to some preliminary investigation of Vanadium. This was performed in October, 1979, to check that the system was working as expected.

A more rigorous examination of Vanadium and the apparatus was initiated with two further series of measurements using the same samples in December 1979, and March 1980. The gold foil source of dimensions

6.5 mm square by 1 mm thick was for each series irradiated for 12 hours in the Dido Reactor at Harwll, giving an initial surface activity of 120 Ci (3.3×10^{11} Bq) at 412 keV. The half life of 2.7 days allows useful measurements to be performed for about one week and thus two sources were required to complete the six directional profile measurements of both series. The Vanadium samples were discs of 10 mm diameter and 2 mm thick oriented along the directions (100), (110) and (111). It would have been desirable to use larger diameter crystals up to the maximum beam size of 18 mm with a count rate increased by a factor of three but none could be found commercially available. After scattering through an angle of $\sim 167°$ the radiation was analysed in a 4096 channel Pulse Height Analyser with the gain set to approximately 50 eV (0.03 au) per channel.

A total of $\sim 5 \times 10^6$ counts were accumulated in each profile corresponding to a peak count of 5×10^4. Presentation of the results with the data interpreted at the conventional intervals of 0.1 au thus corresponds to a statistical accuracy of ± 0.3% J(o). Calibrations were performed before and after each measurement to establish the channel-energy relationship (see table 4.3) and the background profile was obtained using the empty sample holder at the beginning of each series of measurements. The background level at the profile centre position was found to be about 1% of the signal intensity and errors in its treatment should contribute little to the final accuracy (§4.3.2.).

The examination of individual directional profiles requires the use of very rigorous data reduction procedures and so the existing computer software was being reviewed during the course of these experiments. The results first presented for the anisotropy in Vanadium were obtained with the original software and show good agreement with the anisotropies obtained by another research group. The later results

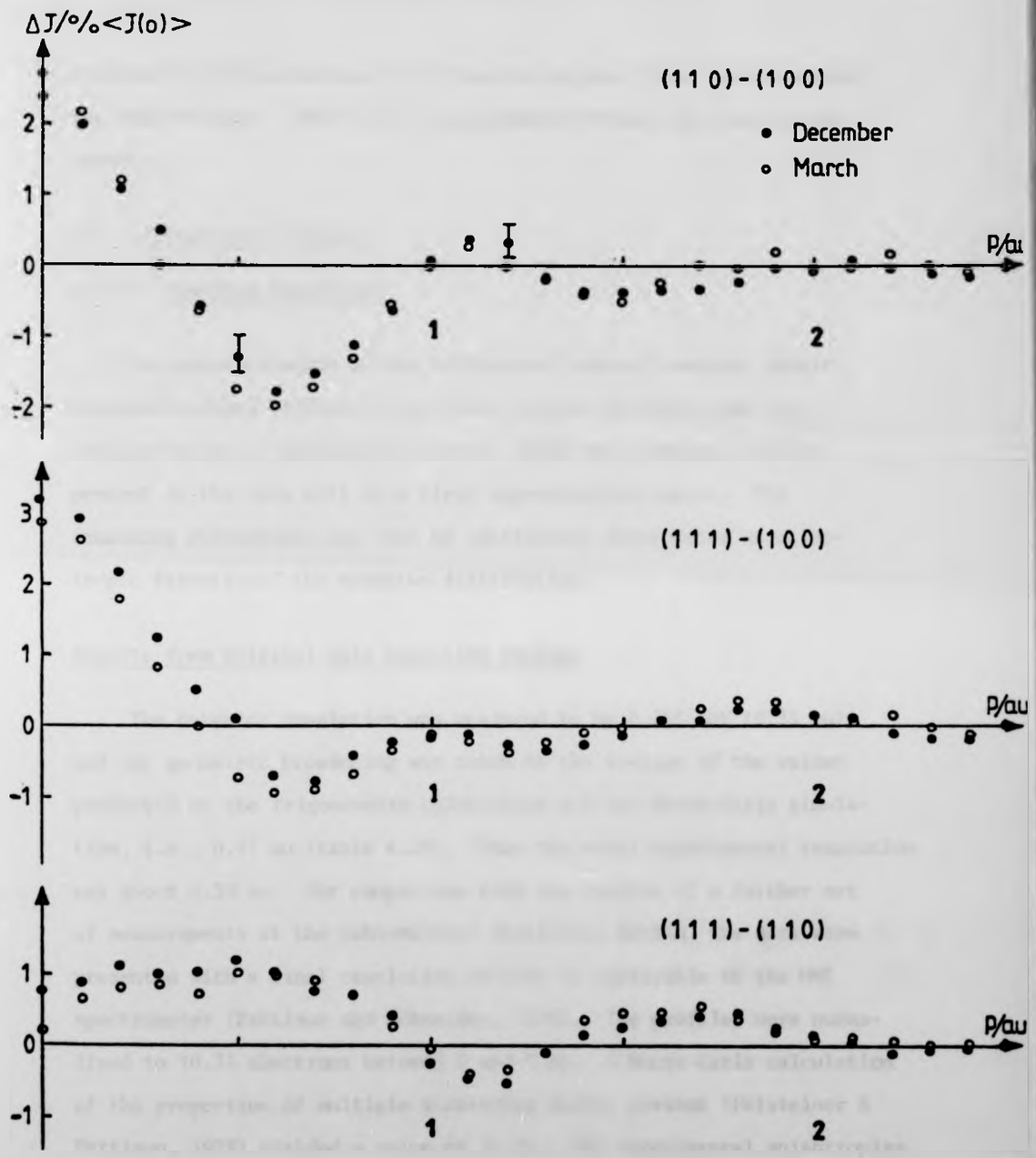

Figure 5.3. Reproducibility of Vanadium Anisotropy (Data are averaged over + ve and - ve momenta and are not corrected for multiple scattering contributions)

obtained for the anisotropy are from the original data reanalysed with the new software. There is no disagreement between the two sets of results.

5.4. Anisotropic Effects

5.4.1. Momentum Anisotropy

The interpretation of the differences between momentum density components along different directions is more reliable than the interpretation of individual profiles since any systematic errors present in the data will to a first approximation cancel. The remaining differences may then be confidently interpreted as anisotropic features of the momentum distribution.

Results from Original Data Reduction Package

The detector resolution was measured to be 0.565 keV (0.35 au) and the geometric broadening was taken as the average of the values predicted by the trigonometric calculation and the Monte-Carlo simulation, i.e., 0.17 au (table 4.20). Thus the total experimental resolution was about 0.39 au. For comparison with the results of a further set of measurements at the Hahn-Meitner Institute, Berlin, the data were presented with a final resolution of 0.41 au applicable to the HMI spectrometer (Pattison and Schneider, 1979). The profiles were normalised to 10.31 electrons between 0 and 7 au. A Monte-Carlo calculation of the proportion of multiple scattering events present (Felsteiner & Pattison, 1975) yielded a value of 12.2%. The experimental anisotropies were therefore rescaled by a factor of 1.14 to account for the necessary profile renormalisation (see §4.2.4.) and the result could now be compared with theory (Rollason et al, 1981).

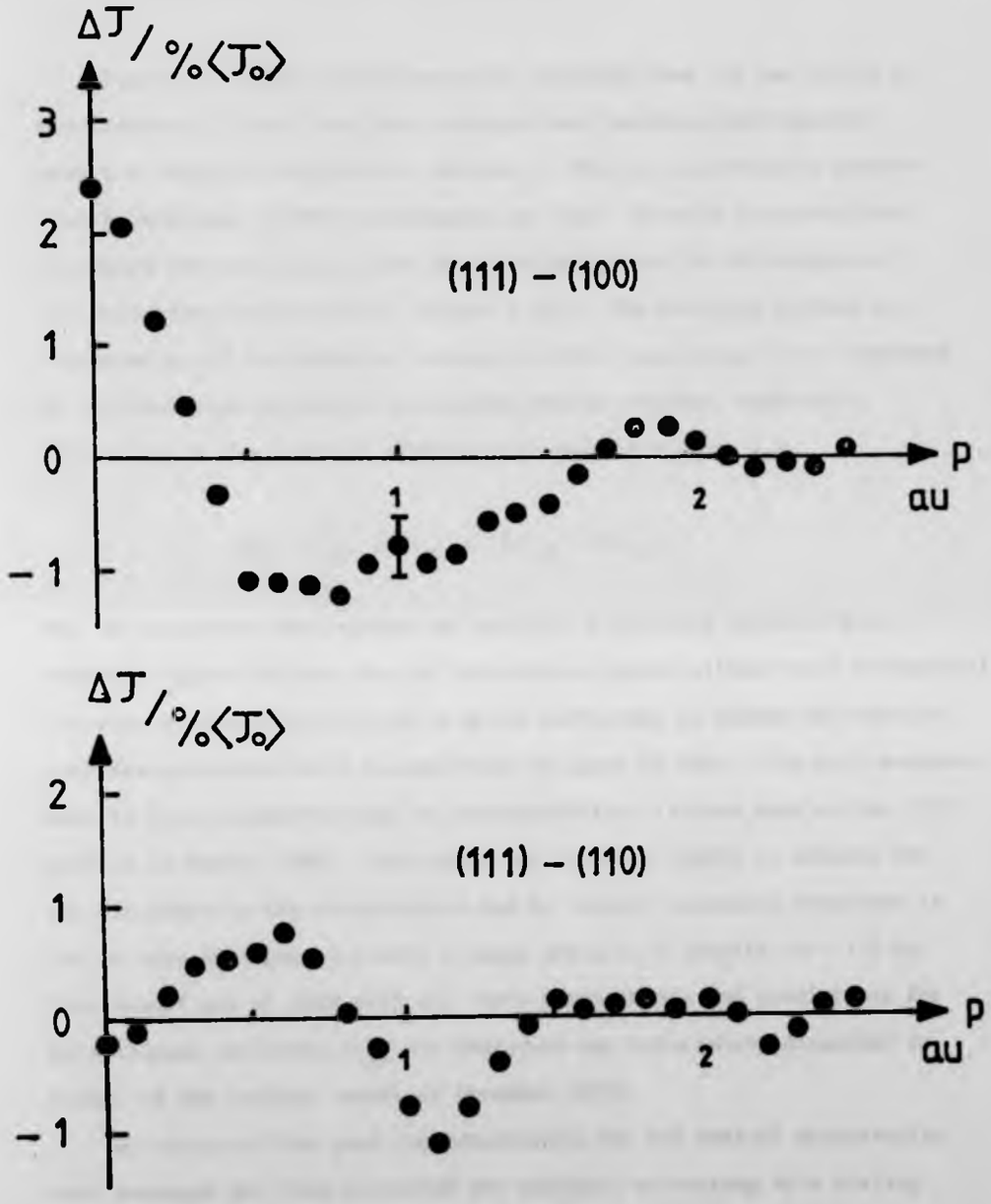

Figure 5.4. Vanadium Anisotropy Arising from the March Measurement of the (111) Profile

Figure 5.3 shows the anisotropies obtained from the two series of measurements. These have been averaged over positive and negative momentum values to improve the accuracy. This is justified in Chapter 6 with reference to the measurements on Iron. Briefly it served here to remove any remaining errors due to misalignment of the origins of the anisotropy profile pairs (figure 4.23). The data are plotted as a percentage of the spherical average profile peak value $\langle J(o) \rangle$ obtained by a linear combination of directional profile values, combined in proportion to the order of symmetry for each direction, i.e.,

$$\langle J_o \rangle = \frac{1}{26} \left[6J_{100} + 12J_{110} + 8J_{111} \right]$$

For the data here uncorrected for multiple scattering $\langle J(o) \rangle = 4.8$. From the figure the two sets of anisotropies agree within their statistical accuracy of ± 0.3% J(o) which is quite sufficient to define the oscillatory features which have an amplitude of about 3% J(o). The only measurement to have failed the test of reproducibility is that made on the (111) profile in March, 1980. The reason for this bad result is unknown but its inclusion in the anisotropies led to totally eccentric behaviour as can be seen in figure 5.4 with a large deficit of density at ∿ 1.0 au. This result was at odds with all other measurements and predictions for anisotropies involving J_{111} and therefore was reluctantly discarded in favour of the earlier result of December 1979.

By virtue of the good reproducibility, the two sets of anisotropies were averaged and then corrected for multiple scattering by a scaling factor of 1.14. Their comparison with up to date band structure calculations is shown in figure 5.5. The solid curve denotes the APW calculation by Wakoh et al (1976) and the dashed curve denotes the tight-binding calculation by Laurent et al (1978). Also shown as open circ les are the experimental results from HMI, Berlin.

Figure 5.5. Anisotropy in Vanadium (a) 110 - 100 (b) 111 - 100 and (c) 111 - 110 (The Rutherford Laboratory results ● are averaged over the two sets of measurements and corrected for multiple scattering. Also shown are the experimental results from HMI ○ and the predictions of two band - structure calculations, APW - Wakoh et al (1976) - solid curve; LCAO - Laurent et al (1978) - dashed curve.)

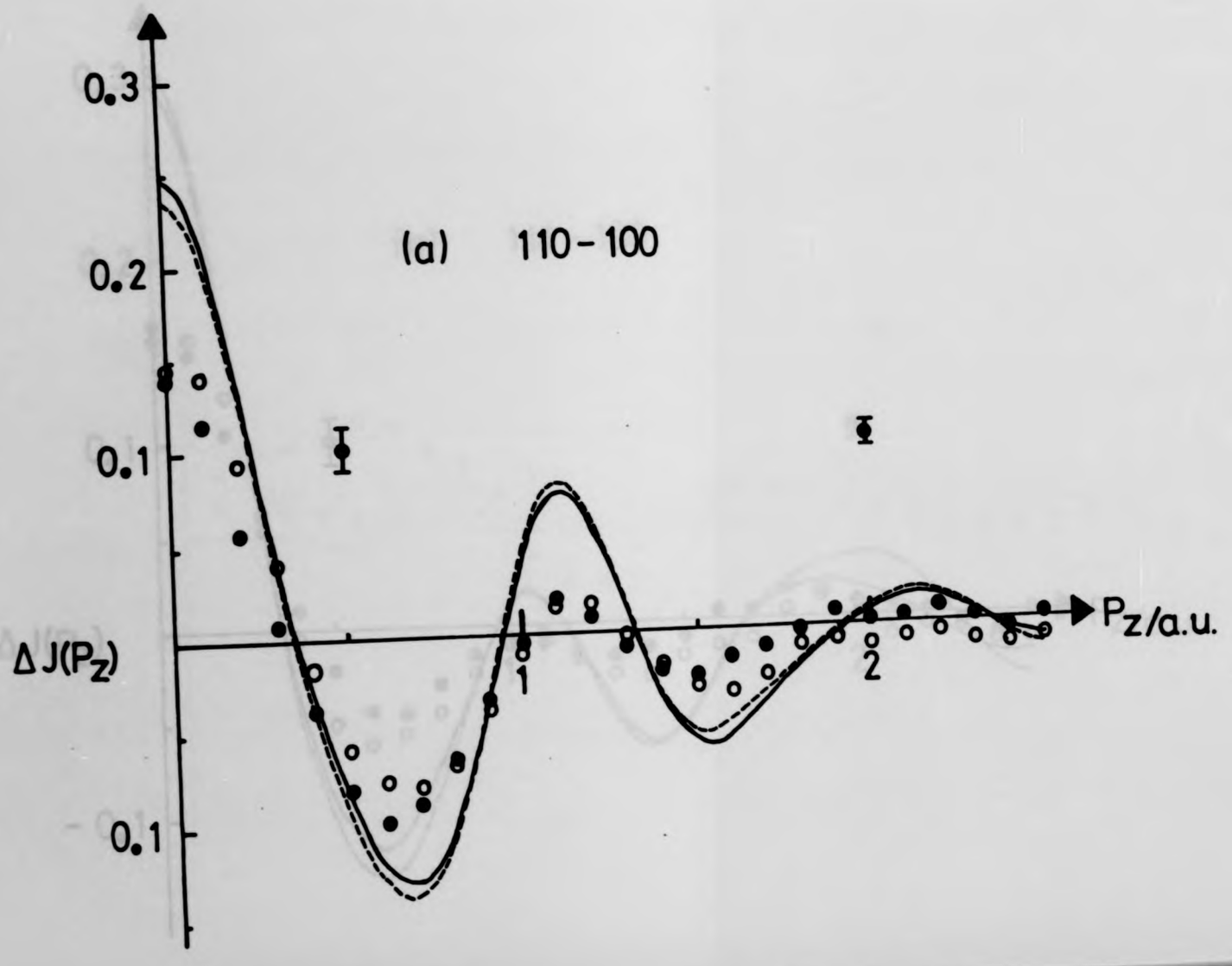
0.3
0.2
0.1
0.1
(a) 110 - 100
ΔJ(Pz)
Pz/a.u.
1
2

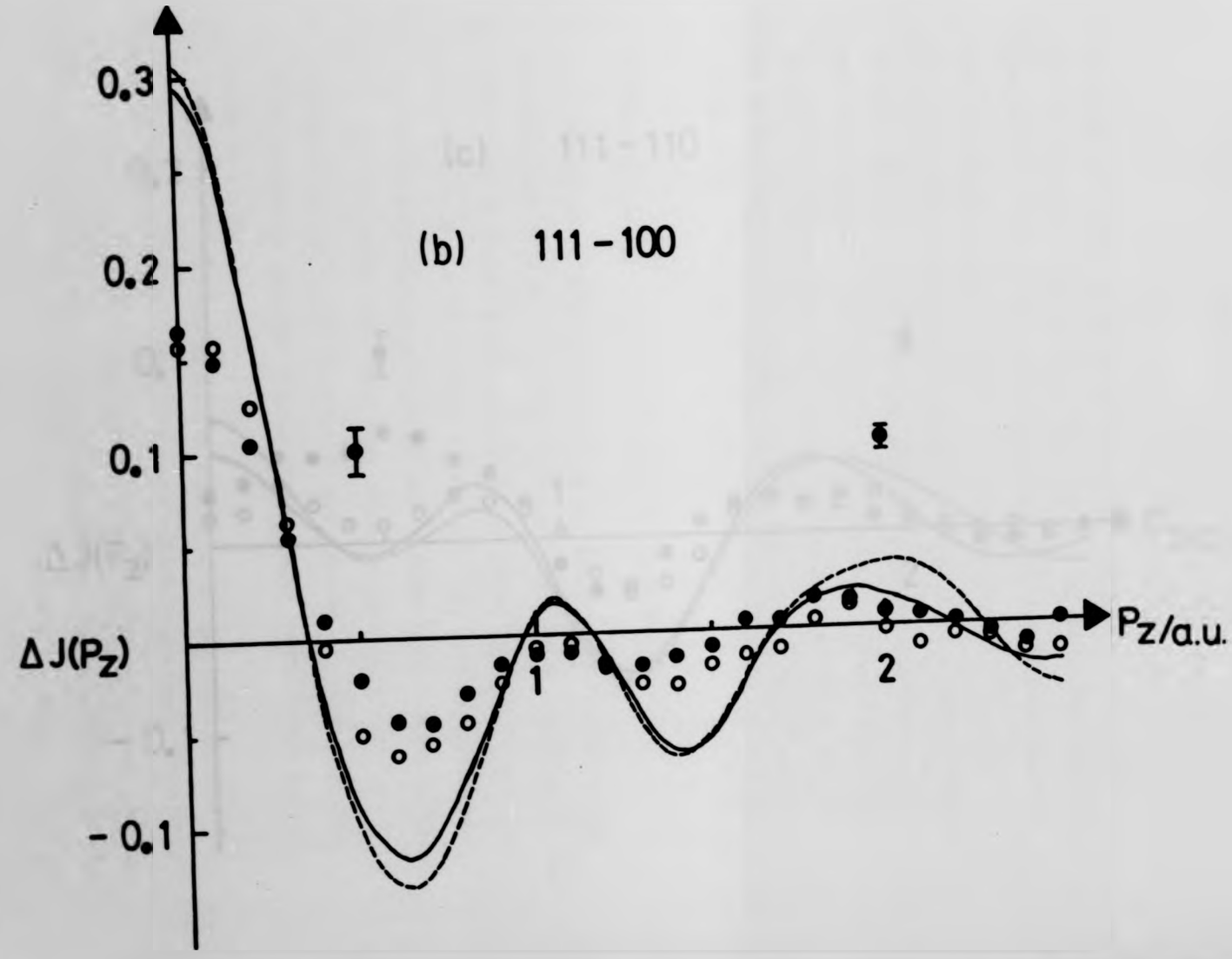
0.3
0.2
0.1
- 0.1
(b) 111 - 100
ΔJ(Pz)
Pz/a.u.
1
2

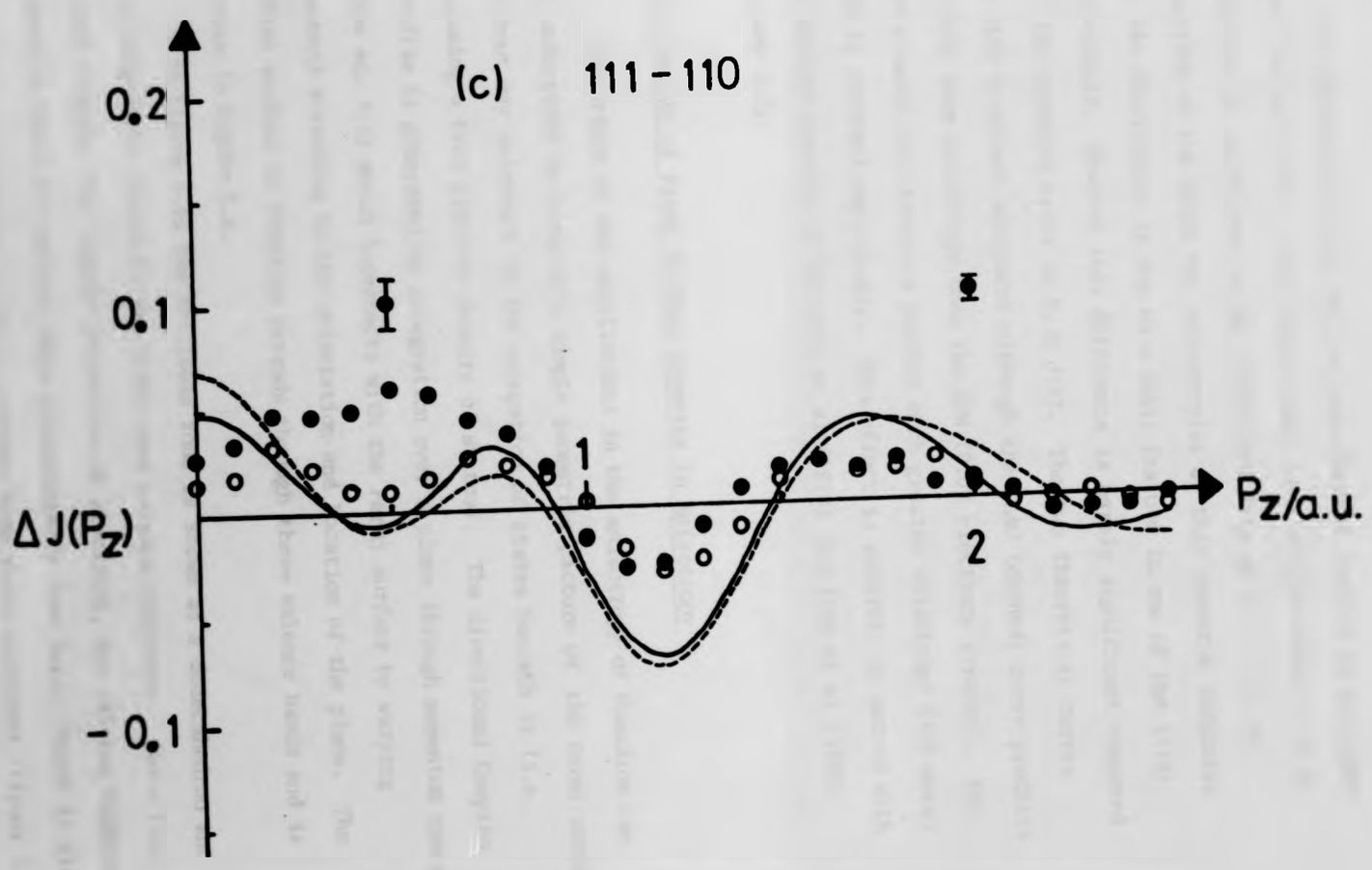
(c) 111 - 110
0.2
0.1
- 0.1
ΔJ(Pz)
1
2
Pz/a.u.

The agreement between the two experimental results is excellent except for the (111) - (110) where there is a slight excess ($\sim$ 0.05 electrons) of anisotropy in the Rutherford data at $p_z \sim$ 0.5 au. Inspection of the other two anisotropies at this momentum indicates that the discrepancy is due to a small feature in one of the (110) measurements. However this difference is barely significant compared with the standard error of 0.3% J(o). The two theoretical curves are also in mutual agreement although the LCAO (dashed) curve predicts slightly more anisotropy than the APW (0.02 electrons greater). But very clearly both theories predict much greater anisotropy (50% more) than is observed empirically. This effect is entirely in accord with the earlier results of Terasaki et al (1973) and Itoh et al (1980) (Figure 5.2).

Relationship of Fermi Surface Geometry to Anisotropy

The origin of the oscillations in the anisotropy of Vanadium can be understood in terms of a simple geometric picture of the Fermi surface without any reference to the occupation of states beneath it (i.e. assuming a free electron density of states). The directional Compton profile is generated by integration over a plane through momentum space (see eq. 1.1) which intersects with the Fermi surface by varying amounts according to the orientation and location of the plane. The Fermi surface in Vanadium extends through three valence bands and is shown in figure 5.6.

In figure 5.6a the Brillouin zone is shown as a dodecahedron and is completely filled by the first band valence electrons. Since this band contains the largest proportion of electrons, the valence Compton profile takes its general shape predominantly from here. There is also a small contribution to the anisotropy from these electrons (figure 5.7)

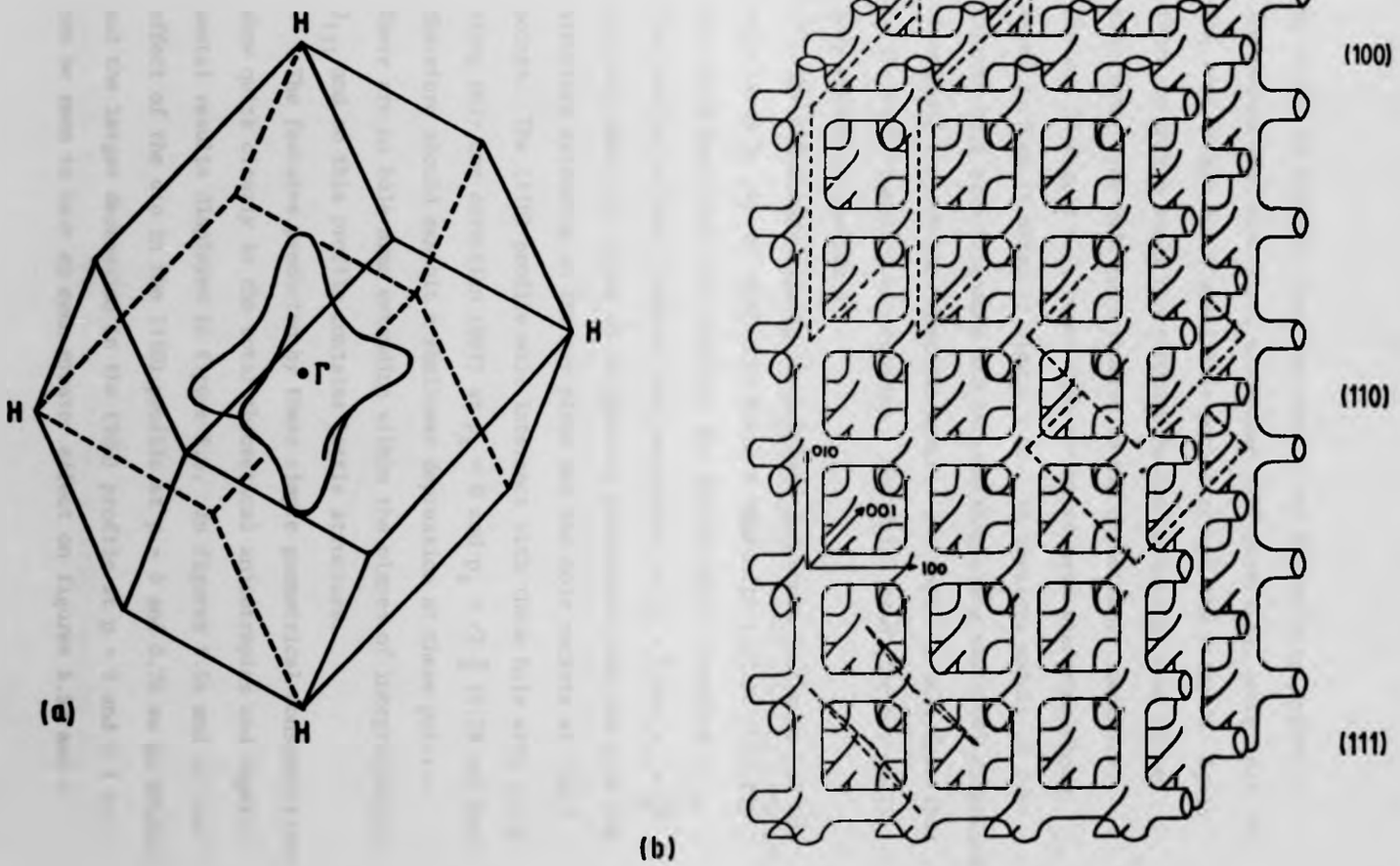

Figure 5.6. Fermi Surface of Vanadium : (a) Second Band with Hole Pocket at Γ Point

(b) Third Band "Jungle - Gym" Hole Surface

by virtue of the fact that the zone is not spherically symmetric. The second band electrons, also shown in figure 5.6a, occupy all of the zone except for a small hole pocket around the point Γ. Again there is only a small contribution to the anisotropy from these electrons. The main contribution to the anisotropy, immediately obvious in figure 5.7, comes from the third band electrons whose Fermi surface is shown in figure 5.6b. It consists mainly of continuous hole arms extending and intersecting along the (100) directions throughout the occupied momentum space. Its shape is well described by the term 'jungle-gym' structure. The third band also has small hole pockets at points N.

The anisotropy arising in each band and shown in figure 5.7 was calculated by the KKR method by Wakoh & Yamashita (1973). Clearly the third band electrons dominate the anisotropies involving J_{100}. The profile in this direction has large dips at $p_z = 0$ and $p_z = \frac{2\pi}{a}$ (1.1 au) where the plane of integration intersects with the hole arm structure extending in the x-y plane and the hole pockets at the N points. The (110) profile will intersect with these hole arms lying along only one direction (001) at $p_z = 0$ and $p_z = \sqrt{2}\,\frac{\pi}{a}$ (0.78 au) and therefore should exhibit a shallower depression at these points. There are no hole arms extending within the planes of integration for J_{111} and so this profile contains little structure.

The features predicted by these simple geometrical considerations show quite clearly in the total theoretical anisotropies and experimental results displayed in figure 5.5. In figures 5.5a and c, the effect of the dip in the (110) profile at p = 0 and 0.78 au is evident and the larger depression in the (100) profile at p = 0 and 1.1 au can be seen to have an even greater effect on figures 5.5a and b.

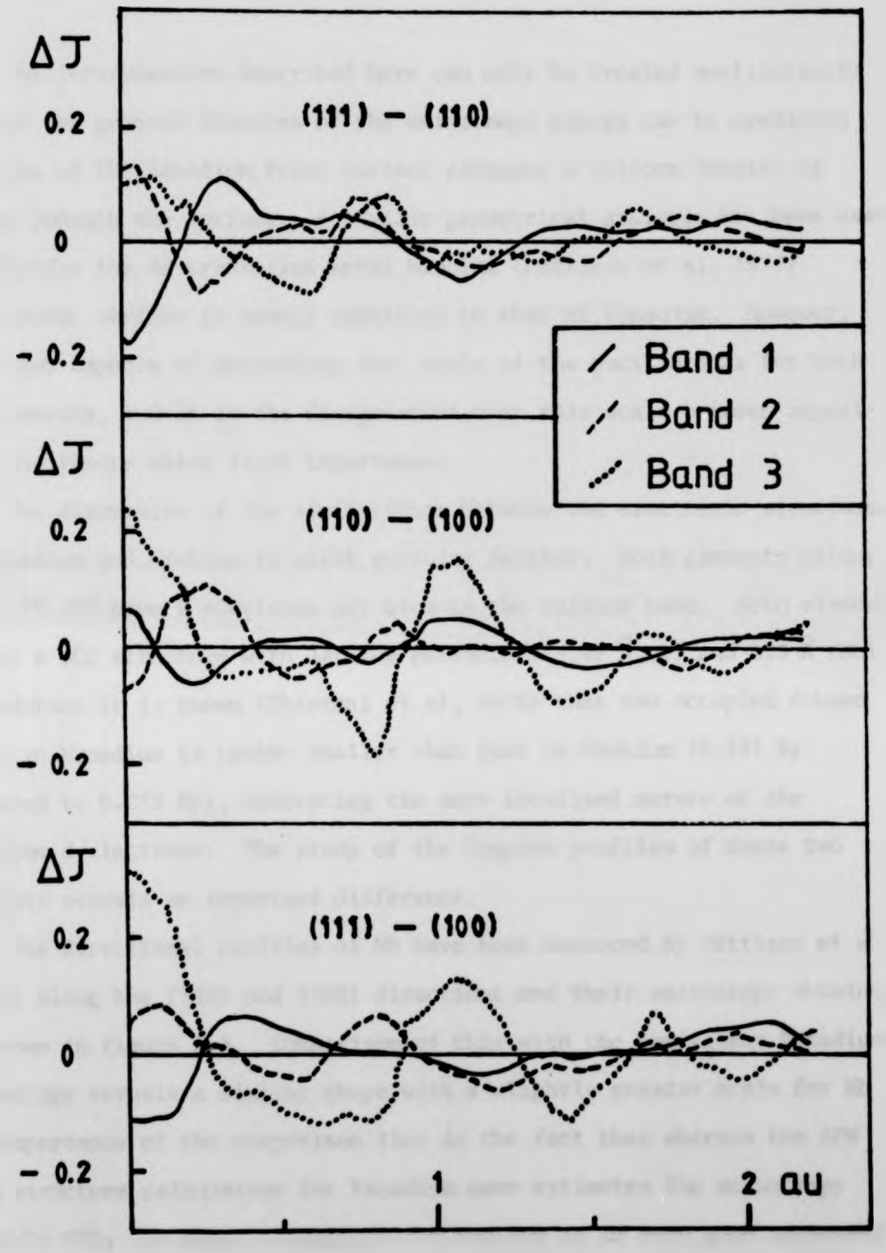

Figure 5.7. Partial Band Contributions to Total Vanadium Anisotropy

The interpreation described here can only be treated qualitatively in that the general features of the anisotropy curves can be predicted in terms of the Vanadium Fermi surface assuming a uniform density of states beneath the surface. A similar geometrical analysis has been used to describe the 4d transition metal Niobium (Pattison et al, 1977) whose Fermi surface is nearly identical to that of Vanadium. However, it is not capable of describing the scale of the oscillations for both these metals, and it is the disagreement over this scale between experiment and theory which is of importance.

The discussion of the similarities between the electronic structures of Vanadium and Niobium is worth pursuing further. Both elements belong to Group Vb and have 5 electrons per atom in the valence band. Both elements assume a BCC structure with lattice parameters 3.03 Å (V) and 3.3 Å (Nb). In addition it is known (Shiotani et al, 1975) that the occupied d-band width in Vanadium is rather smaller than that in Niobium (0.191 Ry compared to 0.275 Ry), indicating the more localised nature of the Vanadium d-electrons. The study of the Compton profiles of these two elements reveals an important difference.

The directional profiles of Nb have been measured by Pattison et al (1977) along the (110) and (100) directions and their anisotropy obtained is shown in figure 5.8. Comparison of this with the equivalent Vanadium anisotropy reveals a similar shape with a slightly greater scale for Nb. The importance of the comparison lies in the fact that whereas the APW band structure calculation for Vanadium over estimates the anisotropy scale by 50%, the same calculation for Niobium is in very good agreement with the experimental data. At present only the two directional profiles of Nb have been measured with a 412 keV spectrometer and further measurements of the other anisotropies are desirable to confirm this behaviour.

Additional information can be obtained from ACPAR studies (§3.1.2).

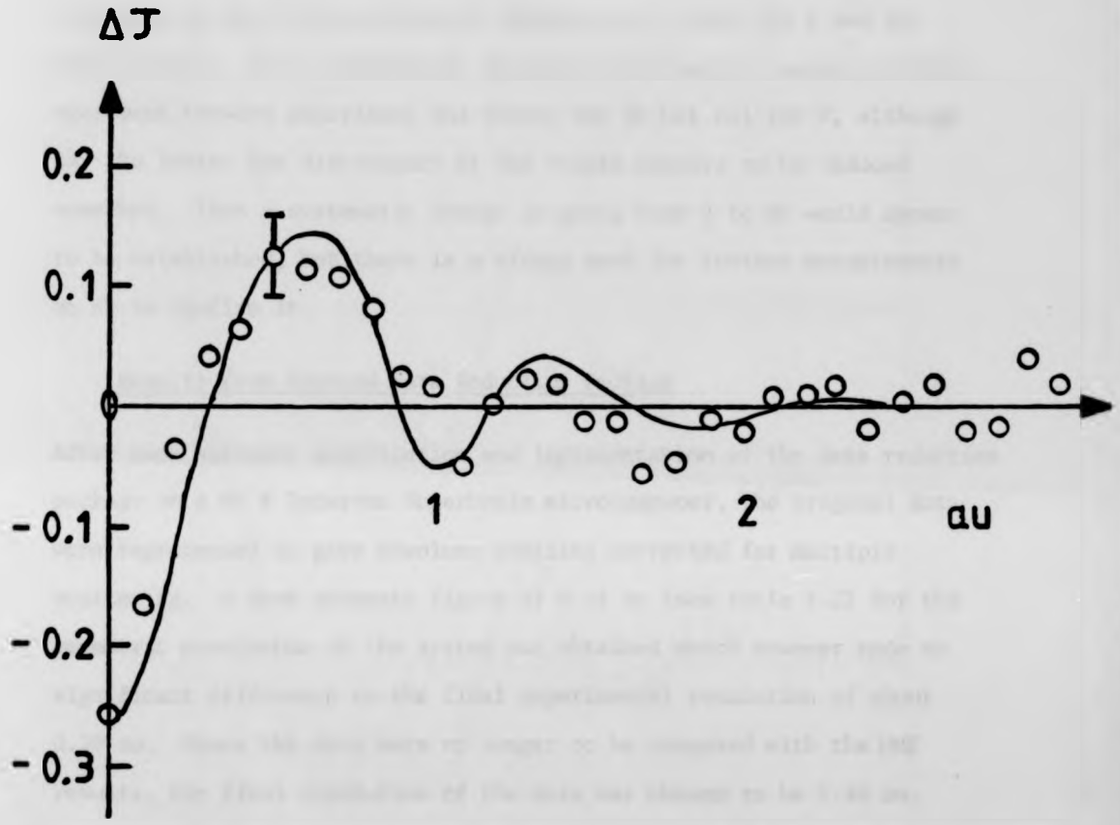

Figure 5.8. Anisotropy in Niobium (100) - (110) ; Circles - Experiment (Pattison et al, 1977) ; Curve - APW Calculation (Wakoh et al, 1976)

Figures 5.9 a and 5.9 b show the angular correlation difference curves (the equivalent of Compton profile anisotropies) obtained by experiment (Shiotani et al, 1975) and theory (Wakoh et al, 1975) for V and Nb respectively. It is immediately apparent that there is again excellent agreement between experiment and theory for Nb but not for V, although for the latter the discrepancy at the origin appears to be reduced somewhat. Thus a systematic change in going from V to Nb would appear to be established, but there is a strong need for further measurements on Nb to confirm it.

Results from Revised Data Reduction Package

After much software modification and implementation of the data reduction package on a 64 K Intertec Superbrain microcomputer, the original data were reprocessed to give absolute profiles corrected for multiple scattering. A more accurate figure of 0.14 au (see table 4.2) for the geometric resolution of the system was obtained which however made no significant difference to the final experimental resolution of about 0.39 au. Since the data were no longer to be compared with the HMI results, the final resolution of the data was chosen to be 0.40 au. Normalisation was performed over the extended range of 0 to 10 au including a total of 10.85 electrons. The multiple scattering spectrum for positive momentum values was calculated in a Monte Carlo simulation of 9×10^5 photon paths on a GEC 4080 computer with the program due to Felsteiner et al (1974). The proportion of multiple scattering predicted was 12% of the total, in agreement with the previous value quoted. After renormalisation of the experimental data the multiple spectrum was smoothed by fitting a fifth-order polynomial (see §4.2.4) and subtracted from the data to give a single profile result (Rollason et al 1983).

Figures 5.9 a and 5.9 b show the angular correlation difference curves (the equivalent of Compton profile anisotropies) obtained by experiment (Shiotani et al, 1975) and theory (Wakoh et al, 1975) for V and Nb respectively. It is immediately apparent that there is again excellent agreement between experiment and theory for Nb but not for V, although for the latter the discrepancy at the origin appears to be reduced somewhat. Thus a systematic change in going from V to Nb would appear to be established, but there is a strong need for further measurements on Nb to confirm it.

Results from Revised Data Reduction Package

After much software modification and implementation of the data reduction package on a 64 K Intertec Superbrain microcomputer, the original data were reprocessed to give absolute profiles corrected for multiple scattering. A more accurate figure of 0.14 au (see table 4.2) for the geometric resolution of the system was obtained which however made no significant difference to the final experimental resolution of about 0.39 au. Since the data were no longer to be compared with the HMI results, the final resolution of the data was chosen to be 0.40 au. Normalisation was performed over the extended range of 0 to 10 au including a total of 10.85 electrons. The multiple scattering spectrum for positive momentum values was calculated in a Monte Carlo simulation of 9×10^5 photon paths on a GEC 4080 computer with the program due to Felsteiner et al (1974). The proportion of multiple scattering predicted was 12% of the total, in agreement with the previous value quoted. After renormalisation of the experimental data the multiple spectrum was smoothed by fitting a fifth-order polynomial (see §4.2.4) and subtracted from the data to give a single profile result (Rollason et al 1983).

Figures 5.9 a and 5.9 b show the angular correlation difference curves (the equivalent of Compton profile anisotropies) obtained by experiment (Shiotani et al, 1975) and theory (Wakoh et al, 1975) for V and Nb respectively. It is immediately apparent that there is again excellent agreement between experiment and theory for Nb but not for V, although for the latter the discrepancy at the origin appears to be reduced somewhat. Thus a systematic change in going from V to Nb would appear to be established, but there is a strong need for further measurements on Nb to confirm it.

Results from Revised Data Reduction Package

After much software modification and implementation of the data reduction package on a 64 K Intertec Superbrain microcomputer, the original data were reprocessed to give absolute profiles corrected for multiple scattering. A more accurate figure of 0.14 au (see table 4.2) for the geometric resolution of the system was obtained which however made no significant difference to the final experimental resolution of about 0.39 au. Since the data were no longer to be compared with the HMI results, the final resolution of the data was chosen to be 0.40 au. Normalisation was performed over the extended range of 0 to 10 au including a total of 10.85 electrons. The multiple scattering spectrum for positive momentum values was calculated in a Monte Carlo simulation of 9×10^5 photon paths on a GEC 4080 computer with the program due to Felsteiner et al (1974). The proportion of multiple scattering predicted was 12% of the total, in agreement with the previous value quoted. After renormalisation of the experimental data the multiple spectrum was smoothed by fitting a fifth-order polynomial (see §4.2.4) and subtracted from the data to give a single profile result (Rollason et al 1983).

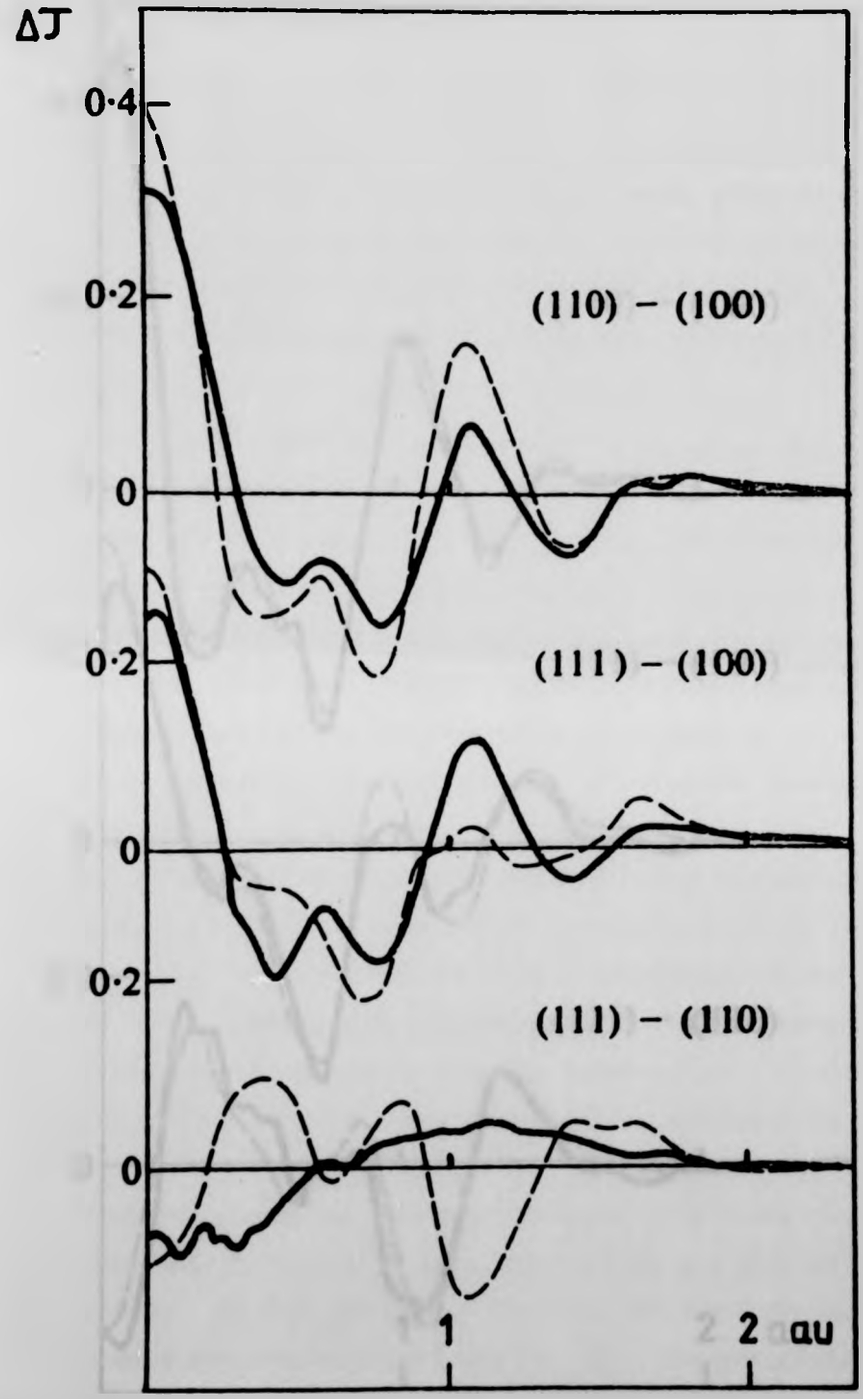

Figure 5.9a Angular Correlation of Positron Annihilation Radiation Difference Curves for Vanadium (Solid curve - experiment, Shiotani et al, 1975; dashed curve - APW calculation, Wakoh et al, 1975)

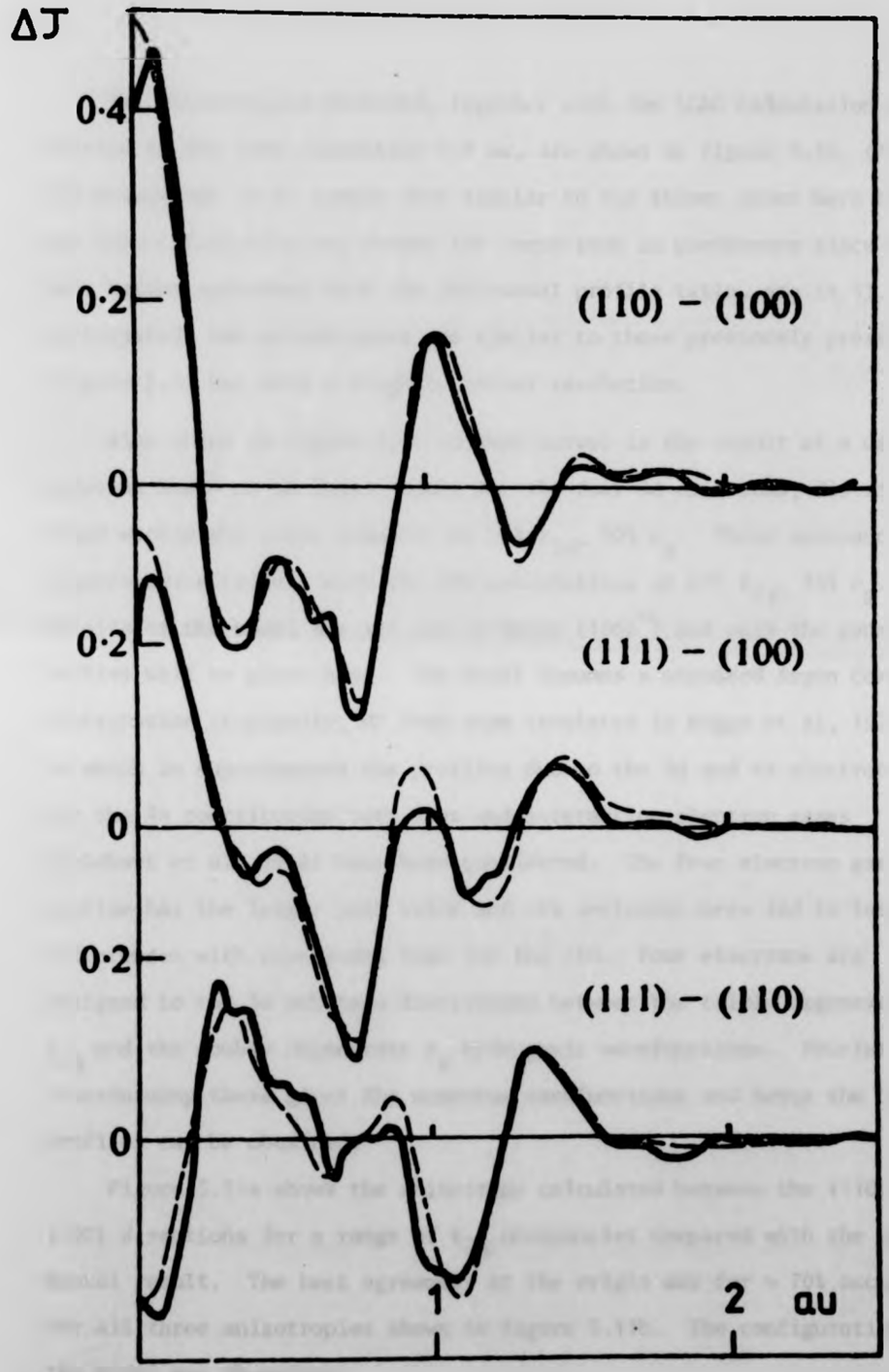

Figure 5.9b Angular correlation of Positron Annihilation Radiation Difference Curves for Niobium (Solid curve - experiment, Shiotani et al, 1975; dashed curve - APW calculation, Wakoh et al, 1975)

The anisotropies obtained, together with the LCAO calculation now smeared to the same resolution 0.4 au, are shown in figure 5.10. (The APW anisotropy is of course very similar to the theory given here but the LCAO calculation was chosen for comparison in preference since it gave better agreement with the individual profile tails, see §5.5). As anticipated, the anisotropies are similar to those previously presented (figure 5.5) but with a slightly better resolution.

Also shown in figure 5.10 (dashed curve) is the result of a calculation based on an atomic model for the four 3d electrons, distributed within the cubic symmetry as 70% t_{2g}, 30% e_g. These occupancy figures agree closely with the APW calculations of 67% t_{2g}, 33% e_g. Details of the model are set out in Weiss (1966[161]) and only the general outline will be given here. The model assumes a standard Argon core contribution (typically, HF free atom tabulated in Biggs et al, 1975) on which is superimposed the profiles due to the 3d and 4s electrons. For the 4s contribution both free and interacting electron gases (Geldhart et al, 1964) have been considered. The free electron gas profile has the larger peak value and its inclusion here led to larger differences with experiment than for the IEG. Four electrons are assigned to the 3d orbitals distributed between the triply degenerate t_{2g} and the doubly degenerate e_g hydrogenic wavefunctions. Fourier transforming these gives the momentum wavefunctions and hence the Compton profiles can be obtained.

Figure 5.11a shows the anisotropy calculated between the (110) and (100) directions for a range of t_{2g} occupancies compared with the experimental result. The best agreement at the origin was for $\sim$ 70% occupation for all three anisotropies shown in figure 5.11b. The configuration for the model was therefore

$$Ar^{18} \text{ core} + (70\% \; t_{2g}, \; 30\% \; e_g) \; 3d^4 + 4s^1 \quad \text{(IEG)}$$

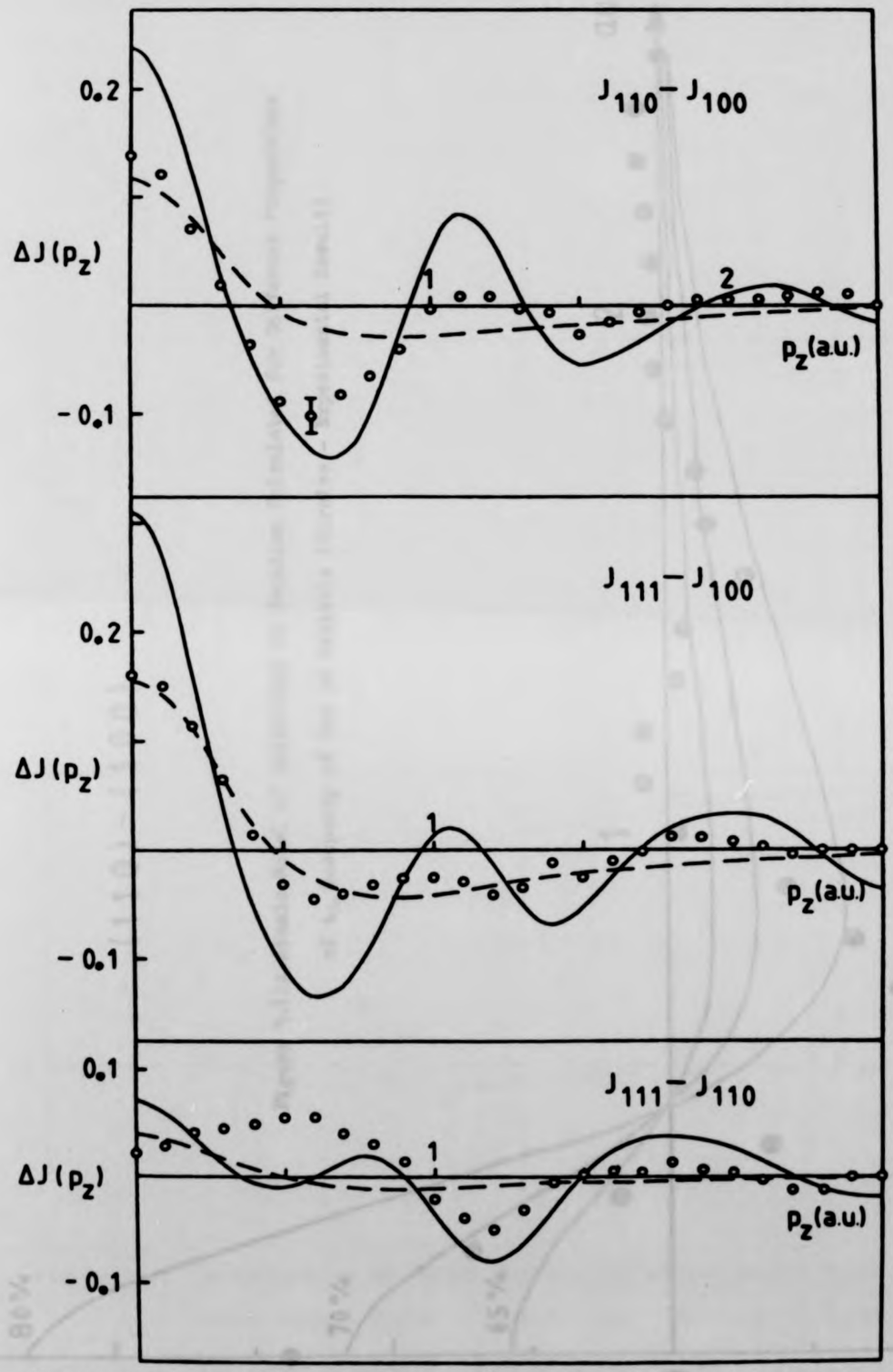

Figure 5.10. Anisotropy in Vanadium (circles - experiment, solid curve - LCAO, dashed curve - atomic model)

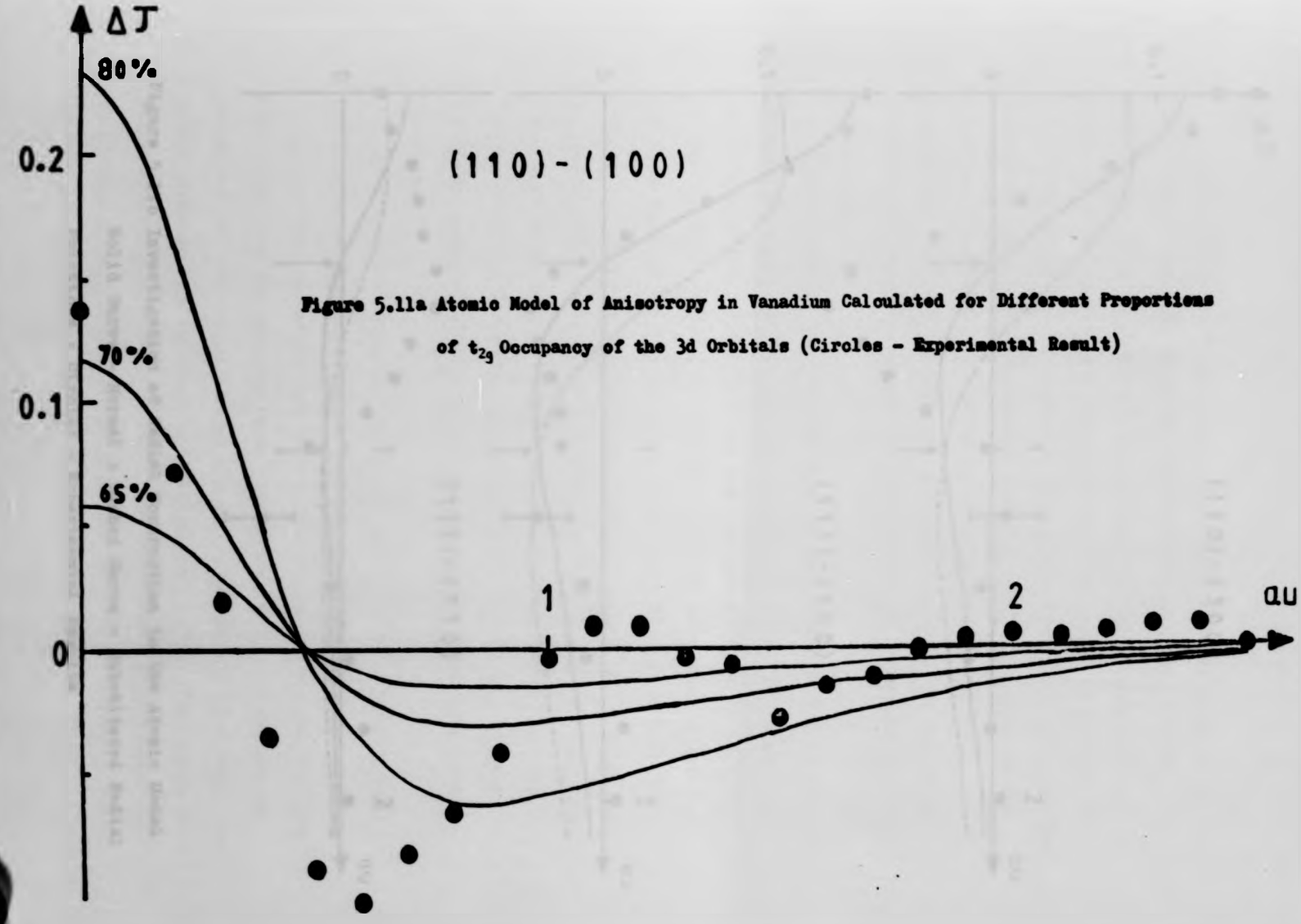

Figure 5.11a Atomic Model of Anisotropy in Vanadium Calculated for Different Proportions of t_{2g} Occupancy of the 3d Orbitals (Circles - Experimental Result)

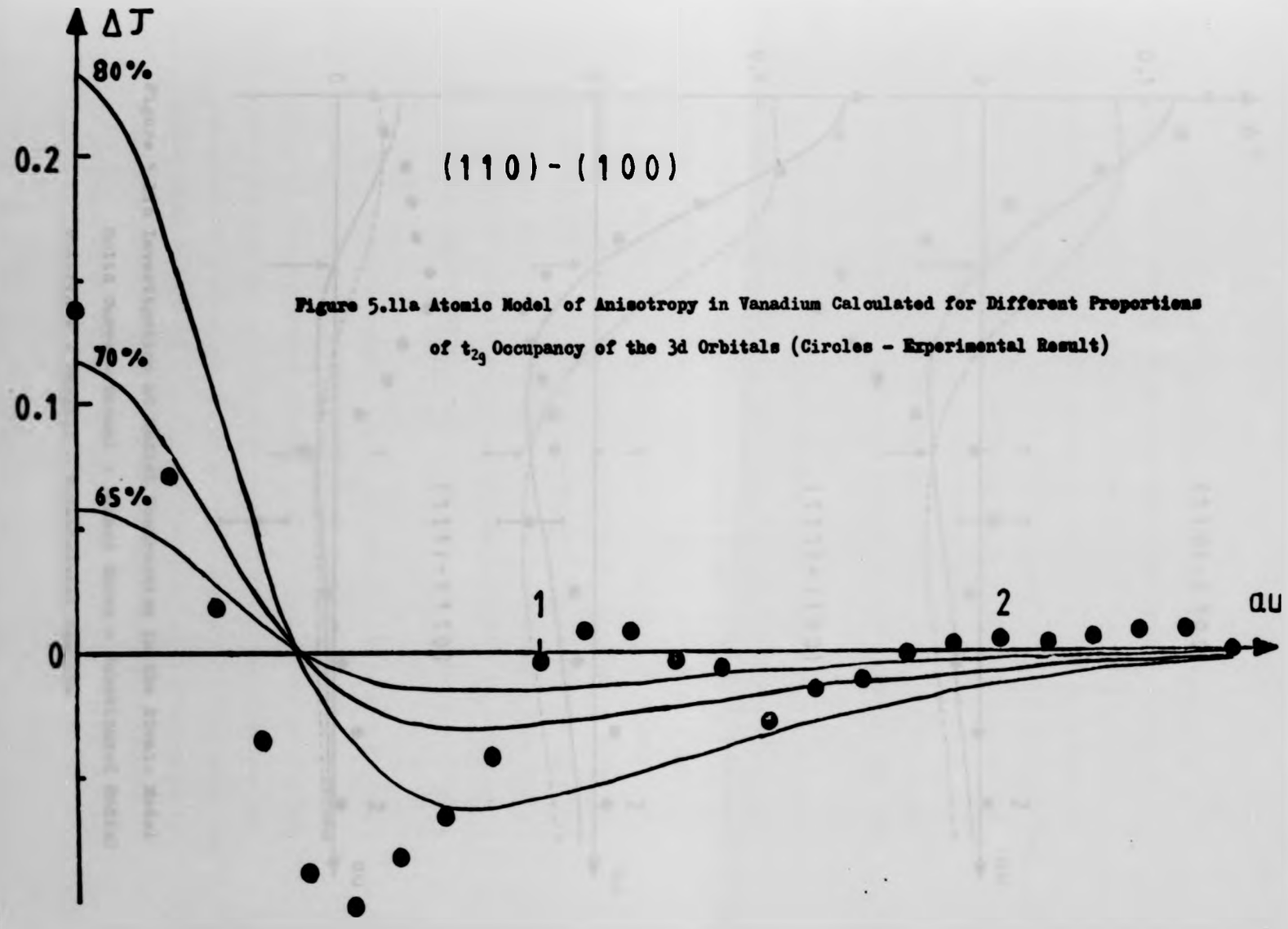

Figure 5.11a Atomic Model of Anisotropy in Vanadium Calculated for Different Proportions of t_{2g} Occupancy of the 3d Orbitals (Circles - Experimental Result)

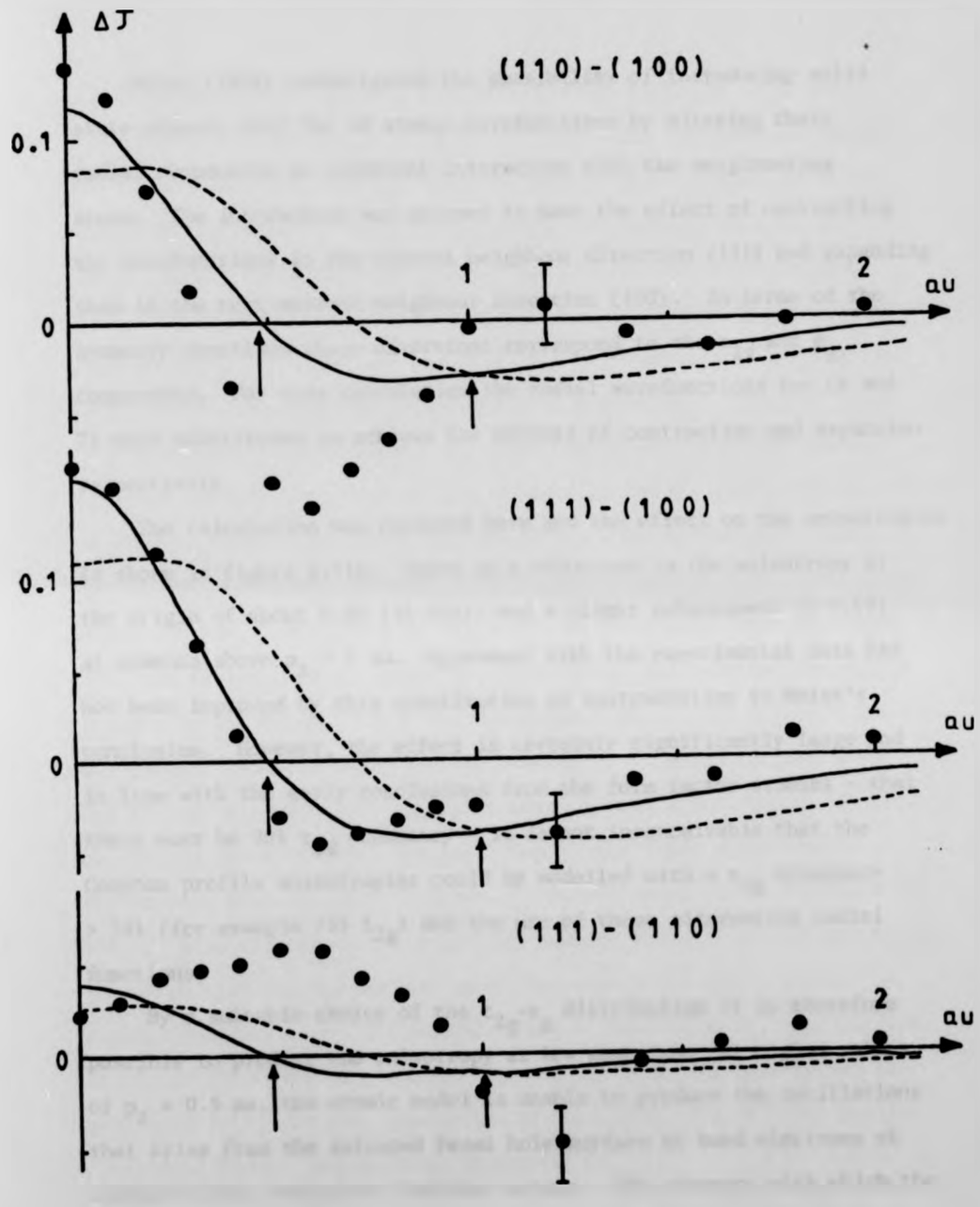

Figure 5.11b Investigation of Radial Contraction in the Atomic Model

Solid Curve - Normal ; Dashed Curve - Substituted Radial Functions ; Circles - Experimental Results

Weiss (1978) investigated the possibility of introducing solid state effects into the 3d atomic wavefunctions by altering their radial components to represent interaction with the neighbouring atoms. The interaction was assumed to have the effect of contracting the wavefunctions in the nearest neighbour direction (111) and expanding them in the next nearest neighbour direction (100). In terms of the symmetry functions these directions correspond to the t_{2g} and e_g components. For easy calculation the radial wavefunctions for Cr and Ti were substituted to achieve the effects of contraction and expansion respectively.

The calculation was repeated here and the effect on the anisotropies is shown in figure 5.11b. There is a reduction in the anisotropy at the origin of about 0.05 (1% J(o)) and a slight enhancement ($\sim$ 0.01) at momenta above p_z = 2 au. Agreement with the experimental data has not been improved by this substitution in contradiction to Weiss's conclusion. However, the effect is certainly significantly large and in line with the early conclusions from the form factor studies - that there must be 80% t_{2g} occupancy - it is not inconceivable that the Compton profile anisotropies could be modelled with a t_{2g} occupancy > 70% (for example 75% t_{2g}) and the use of these alternative radial functions.

By a suitable choice of the t_{2g}-e_g distribution it is therefore possible to predict the anisotropy at low momentum. At higher values of p_z > 0.5 au, the atomic model is unable to produce the oscillations that arise from the extended Fermi hole surface of band electrons at characteristic reciprocal lattice vectors. The accuracy with which the atomic model and the experimental anisotropies (111) - (100) agree is somewhat surprising - since at least the (100) direction is supposed to contain large fluctuations in density at $p_z = \frac{2\pi}{a}$. However these are not seen in the experimental data.

The question of whether such a simplistic model is worth while arises here. It is not only necessary to be able to reproduce momentum anisotropies but one must also be able to predict the values for individual profiles and the corresponding observables in position space. These are considered later. For the present it is proposed that a large part of the anisotropy observed in Compton profiles arises from an atomic contribution and that this is supplemented by a smaller contribution arising from the higher band electrons.

The disagreement between the calculated scale of oscillations from the band theories and the experimentally observed scle is considered to be related to the neglect of electron correlation. The use of the pseudo-one electron wavefunctions obtained from calculations which include a Local Density Approximation to the exchange potential ($X\alpha$, see §1.4.1), as the basis for determining the momentum density is thought to be inexact (Bauer and Schneider, 1983). The slightly better agreement of results from positron studies of Vanadium (figure 5.9a) is due to the non-uniformity of the e^+ wavefunction which, being repulsed by the positively charged nucleus, samples the inner dense charge region less than the outer regions. Thus the amount of e-e correlation seen is also reduced compared to that seen by a γ-photon, and any errors in calculating the appropriate momentum density are also reduced. A similar conclusion applies to both γ and e^+ studies of Nb (figures 5.8 and 5.9b) where the 4d electrons are more diffuse and correlation is generally less. Further discussion of the conclusions of Local Density Functional Theory is presented in Chapter 7.

5.4.2. Charge Asphericity

Table 5.1 lists the results of some important measurements of the X-ray paired reflection intensities (330) - (411) and (442) - (600) along

	f(110)	$f^2(330)/f^2(411)$	$f^2(442)/f^2(600)$
$\sin\theta/\lambda$	0.236	0.698	0.987
Experiment			
Weiss and DeMarco (1965)	15.75 ± 0.25	1.025 ± 0.010	1.048 ± 0.010
Diana and Mazzone (1975)	15.90 ± 0.25	1.017 ± 0.010	1.040 ± 0.020
Ohba et al (1981)	-	1.010 ± 0.014	1.014 ± 0.016
Kretschmar & Schneider (1984)	-	1.019 ± 0.006	1.030 ± 0.010
Band Theory			
Wakoh and Yamashita (1973)	15.74	1.012	1.019
Laurent et al (1978)	15.75	1.008	1.013
Atomic Model			
Weiss (1978)	16.01	1.020	1.040
80% t_{2g}	15.97	1.026	1.041
70% t_{2g}	15.96	1.013	1.021

Table 5.1. Summary of Vanadium Charge Density Asphericity Determinations

with the predicted asphericities from the two band-structure calculations and the atomic model described earlier. In the low energy regime of X-rays, there are many problems associated with making a diffraction measurement (extinction, absorption, etc.) and the reported results have tended to exhibit a wide scatter of values depending on the conditions of the measurement. Thus the measurement of Ohba et al (1981) is significantly lower than those of Weiss and DeMarco (1965) or Diana and Mazzone (1975). A recent γ-ray measurement by Schneider and Kretschmer (1984) has again resulted in somewhat lower values for the two ratios, i.e. 1.020 and 1.018 respectively. However, it appears that the measured asphericities are generally larger than those predicted by band theory, in contrast to the situation for momentum anisotropies, and in line with this result, Weiss and DeMarco (op. cit.) determined a t_{2g} population of 3d electrons of 80% while Wakoh and Yamashita (1973) predicted only 67% t_{2g}.

In §5.4.1. the Compton profile anisotropies were calculated from the atomic model with a distribution of 70% t_{2g}, 30% e_g. Accordingly, the paired intensity ratios were calculated for the same configuration. The Ar core and 4s IEG form factors were taken from the tables in Weiss and Phillips (1969) and the 3d contribution again calculated from the expressions given in Weiss (1966[164]). The resultant asphericities (see table) for 70% t_{2g} are in very good agreement with the band theory of Wakoh and Yamashita and the more recent X-ray and γ-ray measurements. The result labelled Weiss (1978) is the calculation for 70% t_{2g} occupancy with contracted and expanded radial wavefunctions. It leads to worse agreement with the recent measurements and band calculations and also with the momentum anisotropies reported earlier. The result of the atomic calculation for 80% t_{2g} and normal radial functions is also given for comparison. The agreement with the measurements of

P_z	Exp	BAND THEORY		HF Free Atom
		LCAO	APW	
0.0	5.105 ± 0.028	5.099	5.099	6.618
0.1	5.098	5.108	5.105	6.442
0.2	5.073	5.116	5.107	5.979
0.3	5.012	5.087	5.070	5.380
0.4	4.905	4.997	4.973	4.802
0.5	4.758	4.847	4.819	4.335
0.6	4.558	4.654	4.620	3.996
0.7	4.318	4.421	4.381	3.754
0.8	4.062	4.146	4.101	3.569
0.9	3.792	3.834	3.788	3.405
1.0	3.523 ± 0.021	3.515	3.469	3.246
1.2	3.024	2.994	2.940	2.912
1.4	2.580	2.613	2.554	2.565
1.6	2.225	2.232	2.177	2.230
1.8	1.890	1.888	1.831	1.926
2.0	1.633 ± 0.013	1.610	1.556	1.666
2.5	1.193	1.193	1.152	1.192
3.0	0.904	0.891	-	0.908
3.5	0.734	0.730		0.742
4.0	0.630	0.618		0.622
5.0	0.483 ± 0.009	0.465		0.465
6.0	0.365	-		0.355
7.0	0.269			0.269
8.0	0.197			0.203
10.0	0.129 ± 0.004			0.120

Table 5.2. Directional Compton Profile of Vanadium (100) Compared with Theory (LCAO and APW) and Free Atom Profile (HF)

anisotropies in both momentum and position space adds a great deal of support to justifying the use of an obviously over-simplified atomic model. However, its prediction of the absolute form factor for the (110) reflection was greater than most other values given by about 1.4%. By way of comparison, the predicted directional Compton profile was in error by about 4% at $p_z = 0$. Analysis of individual profiles is presented in the following section.

5.5. Absolute Distributions

5.5.1. Directional Compton Profiles

The generation of a new data processing package with an accurate channel-by-channel multiple scattering correction has enabled the production of individual Compton profiles in addition to profile differences. The positive momentum sides of the experimental profiles no longer appear to be significantly affected by any remaining systematic errors such as source line broadening (§4.2.1) which predominantly affect the low energy side, and therefore it is possible to make absolute comparisons with theory (Rollason et al, 1983).

The final experimental profiles for Vanadium are tabulated for positive momentum values in tables 5.2 and 5.3 against the corresponding results of the LCAO and APW band-structure calculations. Also given in table 5.2 is the Hartree Fock free atom profile (Biggs et al, 1975). All the profiles have a Gaussian FWHM resolution of 0.40 au and the experimental data have been normalised to the same area (10.85 electrons) as the free atom profile over the range 0 to 10 au. The agreement between the tails of the experimental and free atom profiles is excellent and provides strong justification of the multiple scattering correction.

The comparison of the band theory profiles with the experiment is shown graphically in figures 5.12a and b as the differences ΔJ (theory-

p_z	Exp [110]	BAND THEORY [110]		Exp [111]	BAND THEORY [111]	
		LCAO	APW		LCAO	APW
0.0	5.244 ± 0.028	5.343	5.319	5.266 ± 0.028	5.413	5.378
0.1	5.219	5.319	5.296	5.248	5.380	5.349
0.2	5.144	5.246	5.224	5.186	5.283	5.255
0.3	5.030	5.122	5.101	5.076	5.134	5.112
0.4	4.870	4.953	4.932	4.919	4.947	4.930
0.5	4.670	4.748	4.727	4.727	4.739	4.723
0.6	4.456	4.520	4.495	4.512	4.521	4.503
0.7	4.237	4.283	4.249	4.278	4.297	4.273
0.8	3.997	4.044	4.000	4.029	4.062	4.029
0.9	3.751	3.806	3.753	3.766	3.806	3.763
1.0	3.519 ± 0.021	3.563	3.505	3.498 ± 0.021	3.528	3.478
1.2	3.032	3.057	2.996	2.983	2.980	2.927
1.4	2.573	2.576	2.514	2.568	2.545	2.490
1.6	2.210	2.273	2.120	2.214	2.208	2.150
1.8	1.889	1.871	1.809	1.902	1.909	1.846
2.0	1.638 ± 0.013	1.620	1.559	1.641 ± 0.013	1.644	1.571
2.5	1.193	1.176	1.132	1.193	1.157	1.122
3.0	0.918	0.895	-	0.912	0.903	-
4.0	0.645	0.618		0.636	0.619	
5.0	0.490 ± 0.009	0.465		0.488 ± 0.009	0.463	

Table 5.3. Directional Compton Profiles of Vanadium for (110) and (111) Directions Compared with LCAO and APW Calculations

experiment) for each orientation. Generally, the APW profiles show greater differences from experiment than do the LCAO profiles although an assumption has been made here in that no data were available for the APW profiles beyond 2.5 au which were therefore fitted with a free atom tail out to 10 au. Data were available for the LCAO calculation out to 5 au and so the assumption is not so serious here.

Both calculations over-estimate the electron density at low momentum (i.e. over the range 0 to 1.0 au) and the APW result drastically under-estimate the profile between 1.0 and 3.0 au. It is unlikely that the calculation would predict any large excess of electron density above 3.0 au and therefore, by comparison with the LCAO curves which are known to have zero integrated difference, the negative excursion of the APW curve between 1.0 au and 3.0 au represents a real deficit of electron density. This must reduce the total number of electrons in the normalisation by about 0.1 in 11.5 (half the electrons in a V atom).

The missing electron density in the APW result is an artefact of the way the Compton profile are obtained from a band-structure calculation (Wakoh and Yamashita, 1973[160]). After calculating the Bloch wavefunctions at a number of k-points in $^1/_{48}$th of the Brillouin Zone, the momentum functions are extracted by summing the coefficients over a limited range of reciprocal lattice points, G. For the two calculations here, the sampling of momentum space is described by the following table.

Calculation	No. of k-points in $^1/_{48}$ BZ	No. of G's considered
APW	55	87
LCAO	506	3000

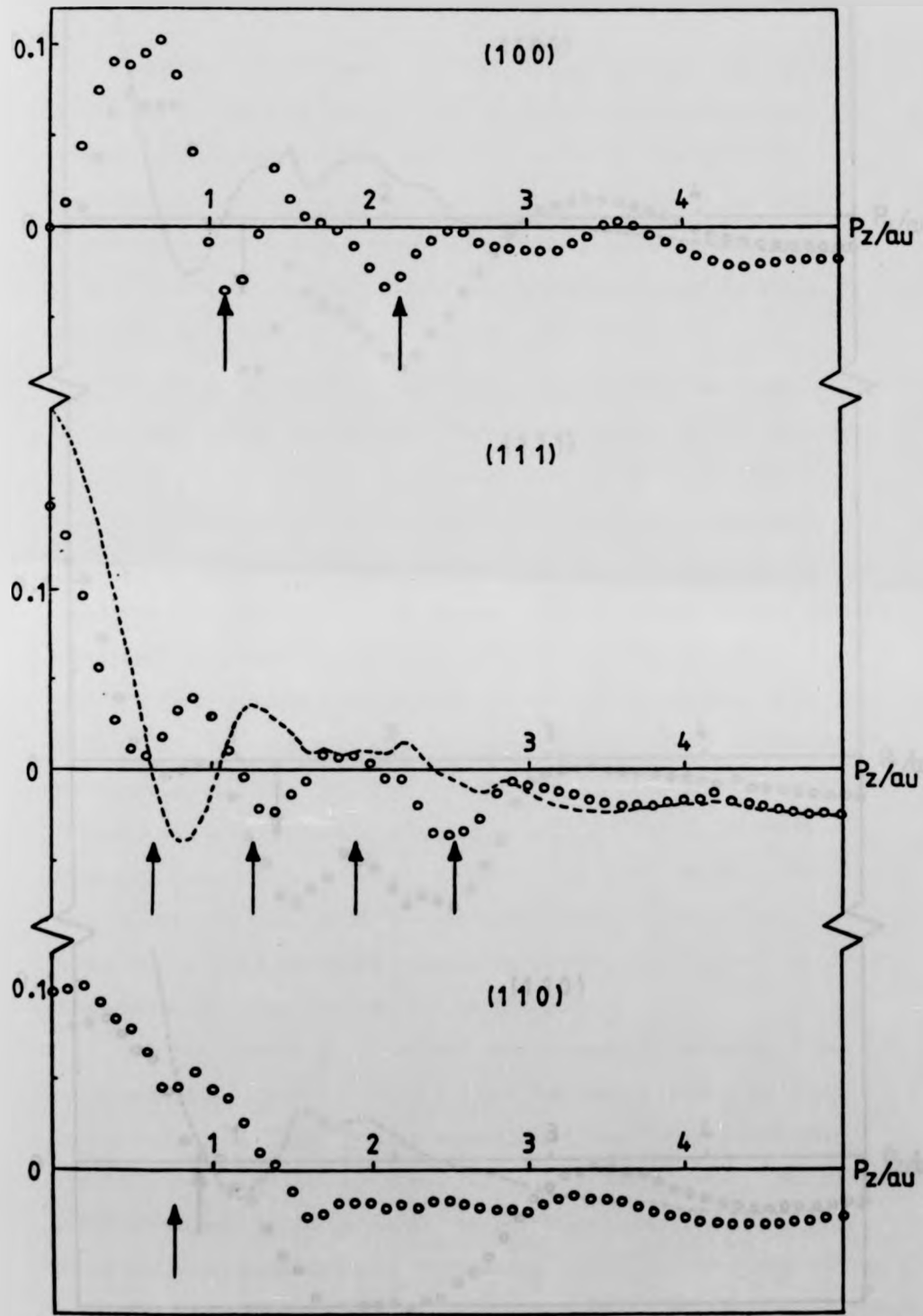

Figure 5.12a Vanadium Difference Profiles: LCAO - experiment (all directions) and 70% t Atomic Model - experiment (111 direction)

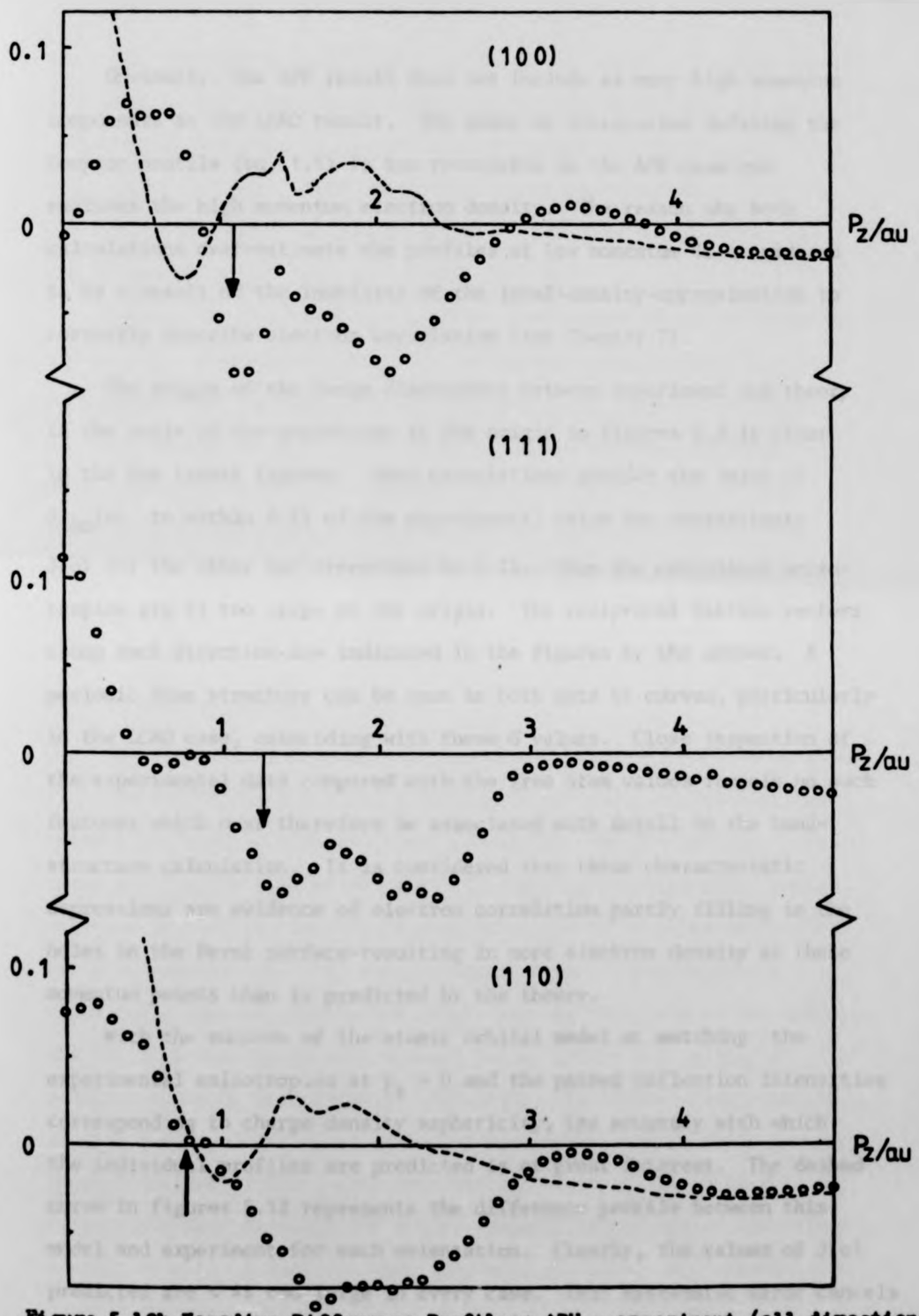

Figure 5.12b Vanadium Difference Profiles: APW - experiment (all directions) and 70% Atomic Model - experiment (100 and 110 directions)

Obviously, the APW result does not include as many high momentum components as the LCAO result. The plane of integration defining the Compton profile (eq. 1.1) is too restricted in the APW case and excludes the high momentum electron density. The reason why both calculations over-estimate the profiles at low momentum is considered to be a result of the inability of the local-density-approximation to correctly describe electron correlation (see Chapter 7).

The origin of the large discrepancy between experiment and theory in the scale of the ansiotropy at the origin in figures 5.5 is clear in the two latest figures. Both calculations predict the value of $J_{100}(o)$ to within 0.2% of the experimental value but overestimate J(o) for the other two directions by $\sim$ 2%. Thus the calculated anisotropies are 2% too large at the origin. The reciprocal lattice vectors along each direction are indicated in the figures by the arrows. A periodic fine structure can be seen in both sets of curves, particularly in the LCAO case, coinciding with these G values. Close inspection of the experimental data compared with the free atom values reveals no such features which must therefore be associated with detail in the band-structure calculation. It is considered that these characteristic depressions are evidence of electron correlation partly filling in the holes in the Fermi surface-resulting in more electron density at these momentum points than is predicted by the theory.

With the success of the atomic orbital model at matching the experimental anisotropies at $p_z = 0$ and the paired reflection intensities corresponding to charge density asphericity, the accuracy with which the individual profiles are predicted is of great interest. The dashed curve in figures 5.12 represents the difference profile between this model and experiment for each orientation. Clearly, the values of J(o) predicted are $\sim$ 4% too large in every case. This systematic error cancels

when calculating the anisotropies which is why there is good agreement in figure 5.11b. The use of a free electron gas model for the 4s contribution was rejected since it gave rise to an even larger discrepancy in J(o). This is in accord with the conclusion of Paakari et al (1975) who investigated its possible substitution in the RFA model.

Despite the crudeness of an atomic representation of the metallic system, the agreement of this model with individual profiles is not much worse than the band structure results - the worst fit being at $p_z = 0$. Indeed there is very little to choose between the theories at all momenta above 3 au. This is partly to be expected since at these momenta the main contribution to the Compton profile is from the core electrons which should remain free atom like even within the solid state.

5.5.2. Autocorrelation Function

The directional Compton profiles were Fourier transformed to give the autocorrelation functions according to eq. 1.9. Analysis of the results in terms of $B(\bar{r})$ has three advantages over the profile representations. The first is merely that it is perhaps conceptually simpler to think of electron density in position space. The other advantages are more significant. All the systematic errors associated with obtaining a Compton profile are slowly varying functions of the momentum and are thus compressed into a small region around the origin of position space on transforming. Similarly, the contribution from the localised core electrons is also confined to this region while the long range behaviour of B(z), free from systematic error, is related to the valence electron distribution alone. Thus investigation of the valence density from the B-function should be more reliable. Furthermore, the

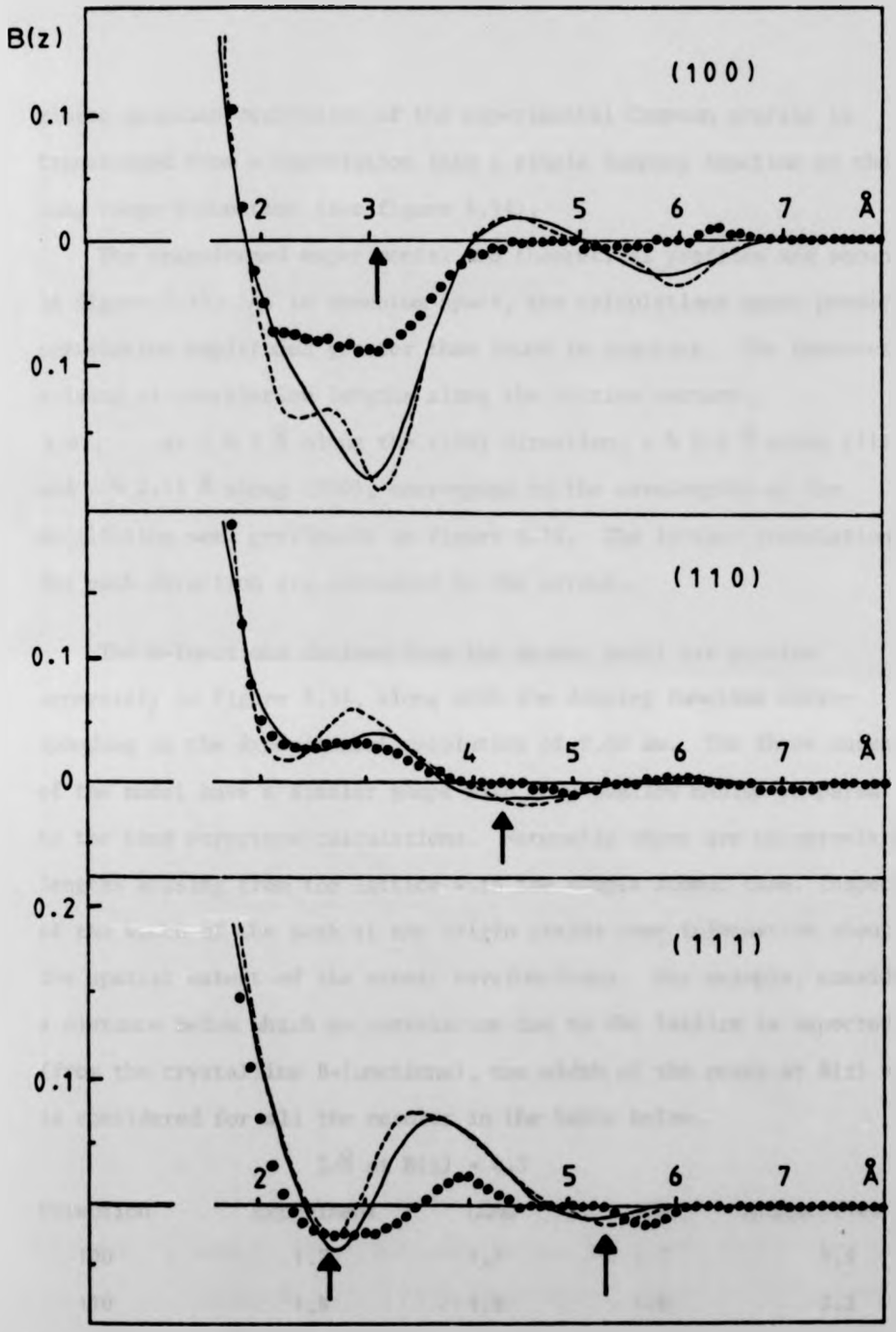

Figure 5.13. Autocorrelation (B-) Functions of Vanadium
(Full Curve - APW, Wakoh et al, 1976 ; Dashed Curve -
LCAO, Laurent et al, 1978 ; Circles - Experiment)

finite Gaussian resolution of the experimental Compton profile is transformed from a convolution into a simple damping function of the long range B-function (see figure 5.14).

The transformed experimental and theoretical profiles are shown in figure 5.13. As in momentum space, the calculations again predict correlation amplitudes greater than found in practice. The features arising at correlation lengths along the lattice vectors, i.e., at $z \approx 3$ Å along the (100) direction, $z \approx 2.5$ Å along (111) and $z \approx 2.15$ Å along (110), correspond to the wavelengths of the oscillation seen previously in figure 5.12. The lattice translations for each direction are indicated by the arrows.

The B-functions derived from the atomic model are plotted separately in figure 5.14, along with the damping function corresponding to the experimental resolution of 0.40 au. The three curves of the model have a similar shape with very shallow minima compared to the band structure calculations. Naturally there are no correlation lengths arising from the lattice with the simple atomic case. Inspection of the width of the peak at the origin yields some information about the spatial extent of the atomic wavefunctions. For example, considering a distance below which no correlation due to the lattice is expected (from the crystalline B-functions), the width of the peaks at B(z) = 0.1 is considered for all the results in the table below.

	Z/Å at B(z) = 0.1			
Direction	Experiment	LCAO	APW	Atomic (70% t_2g)
100	1.7	1.7	1.7	1.9
110	1.8	1.8	1.8	2.2
111	1.9	2.0	2.0	2.3

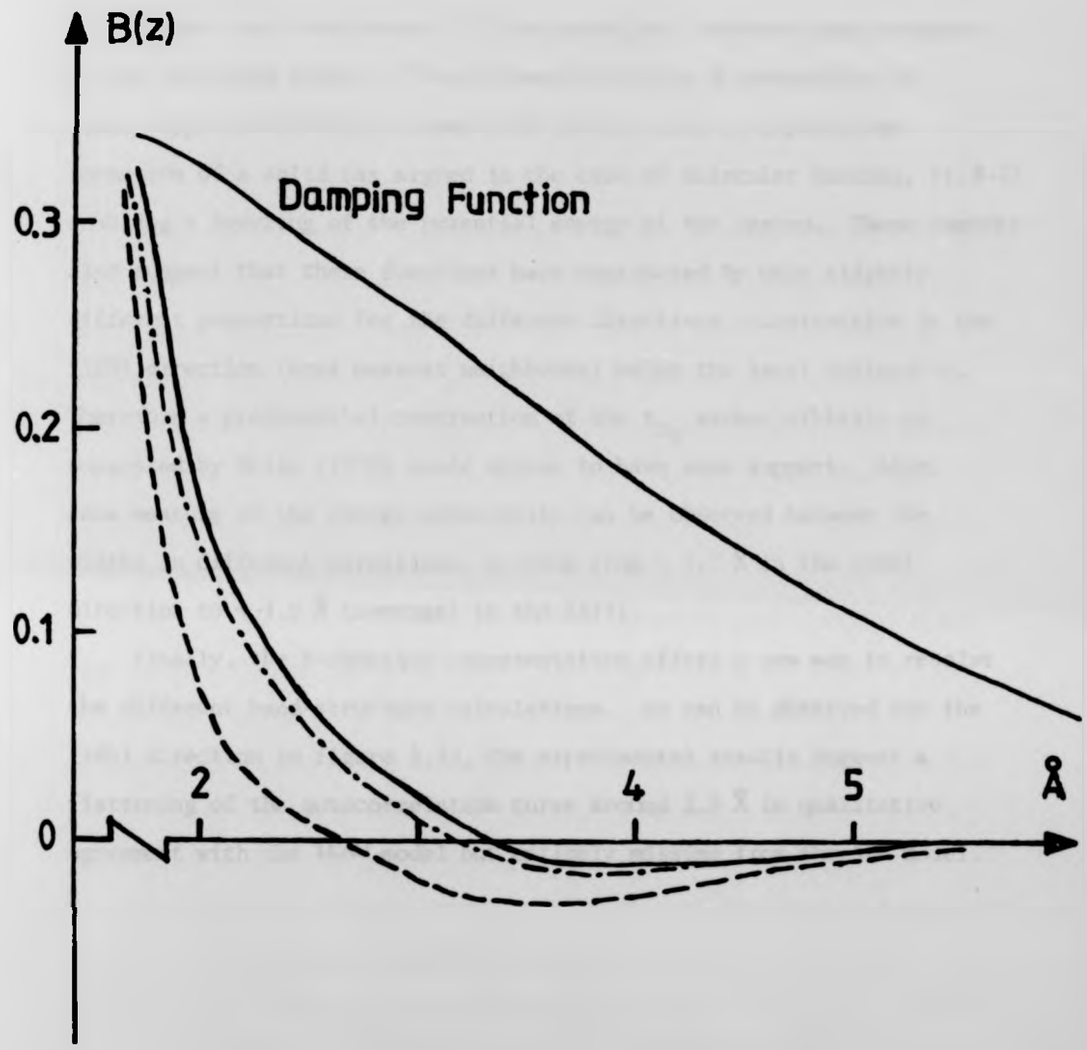

Figure 5.14. Atomic Model Autocorrelation Functions (70% t Occupancy) Solid Curve - (100), Dash-Dotted Curve - (110), Dashed Curve - (111). The experimental resolution appears as a multiplicative term labelled - Damping Function

It is clear that the solid state peaks are narrower than predicted by the free atom theory. This is sensible since a contraction of atomic-type wavefunctions about each lattice site is expected on formation of a solid (as argued in the case of molecular bonding, §1.4.2) enabling a lowering of the potential energy of the system. These numbers also suggest that these functions have contracted by only slightly different proportions for the different directions - contraction in the (100) direction (next nearest neighbours) being the least noticeable. Therefore a preferential contraction of the t_{2g} atomic orbitals as suggested by Weiss (1978) would appear to have some support. Also, some measure of the charge asphericity can be observed between the widths in different directions, varying from $\sim$ 1.7 Å in the (100) direction to $\sim$ 1.9 Å (average) in the (111).

Finally, the B-function representation offers a new way to resolve the different band-structure calculations. As can be observed for the (100) direction in figure 5.13, the experimental results suggest a flattening of the autocorrelation curve around 2.5 Å in qualitative agreement with the LCAO model but entirely missing from the APW model.

CHAPTER 6

IRON

6.1. Introduction

Body-centred cubic ferromagnetic iron has been the subject of many theoretical and experimental studies in an effort to understand the exchange interactions occurring between the 3d electrons which can account for its magnetic properties. Much more so than vanadium, the Fermi surface of iron is complicated by the presence of a high density of 3d electrons and extends throughout many energy bands which are further subdivided according to their spin orientation. While Compton scattering experiments with circularly polarised γ-rays, from magnetised samples can reveal information about the unpaired spin electron momentum density (Sakai and Ono, 1977), such experiments are difficult to perform and there is a low cross-section and correspondingly poor statistical accuracy to contend with. Of concern at present therefore is a rigorous study of the spin independent momentum density and the associated effects of electron correlation.

The study of charge density in BCC iron is rather more advanced than that of momentum density-measurements of the latter being mostly restricted to isotropic distributions. Figure 6.1a shows the result of a 60 keV Compton measurement of polycrystalline iron by Paakari and Manninen (1973) and the agreement with two simple models. The dashed curve represents a Hartree-Fock free atom calculation for the configuration $3d^7 4s^1$ which can be seen to greatly overestimate the height of the profile peak. Above q $\approx$ 2.5 au the data appear to be reasonably well represented by a free atom tail, however a small divergence ($\sim$ 1% J(o)) appears above 4 au. The significance of this

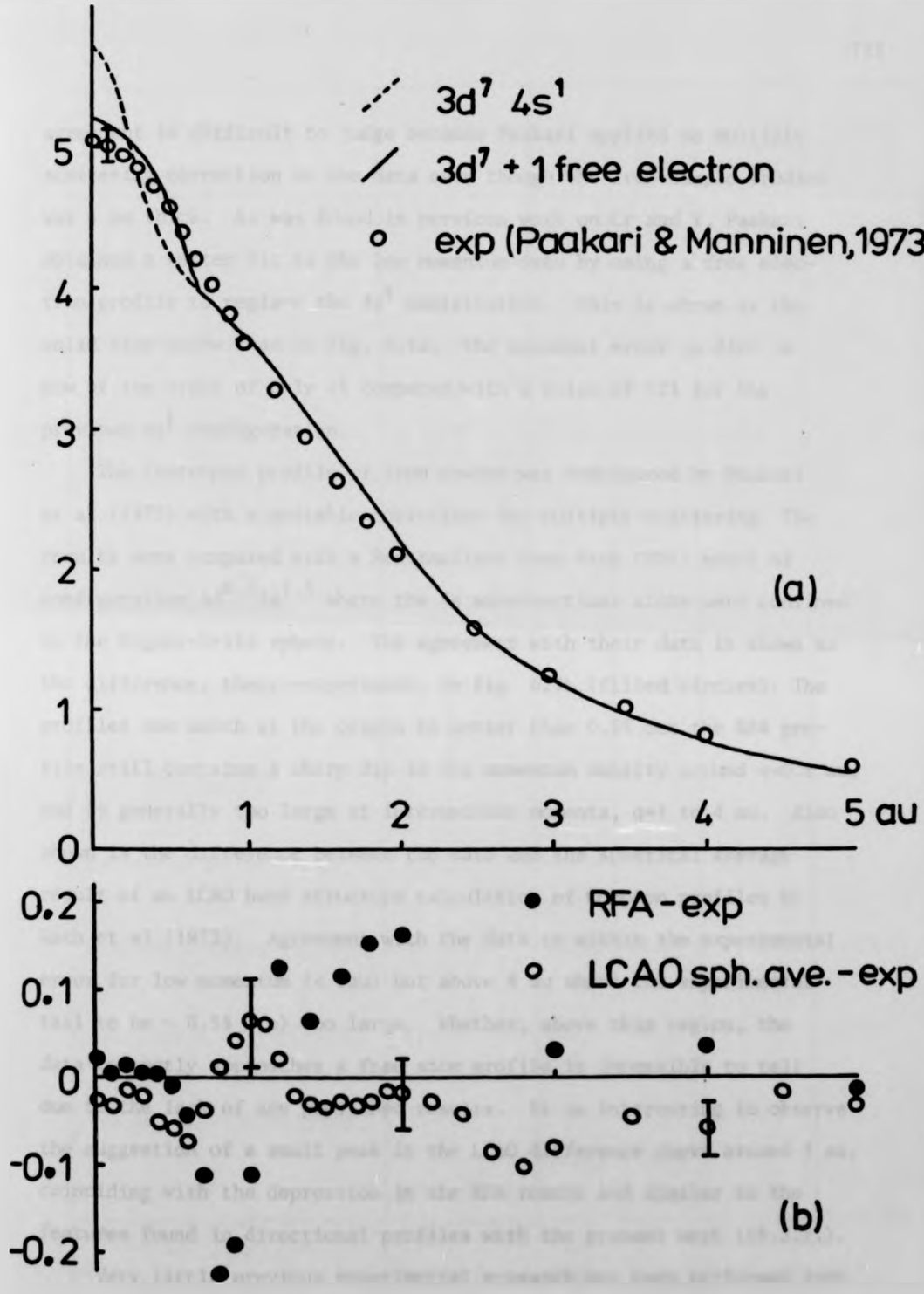

Figure 6.1. Early Studies of Iron Compton Profile : (a) Polycrystalline Compared with Free Atom (b) Powder Compared with RFA and LCAO

agreement is difficult to judge because Paakari applied no multiple scattering correction to the data even though the iron sample studied was 6 mm thick. As was found in previous work on Cr and V, Paakari obtained a better fit to the low momentum data by using a free electron profile to replace the $4s^1$ contribution. This is shown as the solid line below 1 au in fig. 6.1a. The residual error in J(o) is now of the order of only 2% compared with a value of 12% for the previous $4s^1$ configuration.

The isotropic profile of iron powder was remeasured by Paakari et al (1975) with a suitable correction for multiple scattering. The results were compared with a Renormalised Free Atom (RFA) model of configuration $3d^{6.5}4s^{1.5}$ where the 4s wavefunctions alone were confined to the Wigner-Seitz sphere. The agreement with their data is shown as the difference, theory-experiment, in fig. 6.1b (filled circles). The profiles now match at the origin to better than 0.5% but the RFA profile still contains a sharp dip in the momentum density around q=0.8 au, and is generally too large at intermediate momenta, q=1 to 4 au. Also shown is the difference between the data and the spherical average result of an LCAO band structure calculation of Compton profiles by Rath et al (1973). Agreement with the data is within the experimental error for low momentum (< 2au) but above 4 au shows the experimental tail to be $\sim$ 0.5% J(o) too large. Whether, above this region, the data correctly approaches a free atom profile is impossible to tell due to the lack of any published results. It is interesting to observe the suggestion of a small peak in the LCAO difference curve around 1 au, coinciding with the depression in the RFA result and similar to the features found in directional profiles with the present work (§6.3.2.).

Very little previous experimental research has been performed into directional Compton profiles of iron. Phillips and Weiss (1972) attempted

Author	Method	f(110)	f(200)	$\frac{f^2(330)}{f^2(411)}$	$\frac{f^2(442)}{f^2(600)}$
Theory					
Wakoh & Yamashita (1966)	Green's Fn V Wood,1966	18.55	14.89	1.003	1.005
DeCicco & Kitz (1967)	APW V W&Y, 1966	18.37	15.12	1.006	1.012
Duff & Das (1971)	HF TB OPW	17.59	14.28	1.015	-
Wakoh & Yamashita (1971)	Green's Fn V SCF	18.34	15.12	1.006	1.012
Tawil & Callaway (1973)	LCGO	18.38	15.08	1.005	-
Experiment					
Batterman et al (1961)		17.63 ± 0.2	14.70 ± 0.2	1.00(5)	-
DeMarco & Weiss (1965)		18.38	15.08	1.023(5)	1.05(1)
Phillips & Weiss (1972)	Atomic Fn*	17.97	14.55	1.054	1.028
Diana & Mazzone (1974)		17.54 ±0.25	14.55 ± 0.2	1.02	-

*5 t_{2g}, 2.2 e_g : Mn radial functions for t_{2g}, Cr radial functions for e_g : 0.8 free electrons

Table 6.1. Summary of Results of Diffraction Studies of BCC Iron

to measure the anisotropy between the (111) and (100) directions using both Mo and Ag Kα X-rays (∿ 20 keV). Within the limits of their errors (∿ 3% J(o)), no anisotropy was observed. This conclusion is in agreement with the scale of the anisotropy oscillations predicted by the LCAO calculation of Rath (op. cit.) who concluded that there is much less anisotropy than in vanadium or niobium.

The charge density asphericity in iron has been measured repeatedly and calculated by a wide variety of methods. The major results are listed in Table 6.1. DeMarco and Weiss (1965) measured the paired reflections (442) - (600) and (330) - (411) and concluded these must be a distribution of charge equivalent to a 70% t_{2g} and 30% e_g atomic 3d arrangement. Phillips and Weiss (op. cit.) tried to compile all the then-known results for charge, spin and momentum density within an atomic model scheme with expanded radial wavefunctions to account for the crystalline state. Their results for the charge asphericity are given in the table but did not lead to any firm conclusions or new insight.

The only definite conclusion that can be drawn from the tabulated results is that experiment is revealing a larger asphericity in the d-electrons than is predicted by theory. This is exactly the case that applied for vanadium (Chapter 5) where it was also shown that the reverse situation was true for studies of momentum anisotropy. Thus if the causes of these theory - experiment discrepancies are related, once can anticipate that the present study of Compton profile anisotropies will again reveal more smearing in practice than is predicted by the band-structure calculations.

6.2. Details of Experiment

Measurements with the gold spectrometer were made on three orientations of iron single crystals - (100), (110) and (111) - which were purchased from Metals Research, Cambridge. The largest diameter crystals that could be obtained from this (or any other) company were only 8 mm across with a thickness of 2 mm. These small samples therefore represented quite a serious loss of intensity since the primary beam of the spectrometer irradiates an area of diameter 18 mm - a reduction of possible intensity of $^{5}/_{6}$. Increasing the sample thickness would generate excessive amounts of multiple scattering compared with the single scattering cross section. The remedy for the low counting rate was to make repeated measurements. In total therefore, three separate gold sources of initial activity 120 Ci, were employed over a period of six months - this also allowing time for each measurement to be analysed during the course of the experiment. With this arrangement a great deal of attention was inevitably focussed on the reproducibility of a particular profile measurement.

Compared with the vanadium measurement the directional Compton profiles of iron were expected to exhibit only two thirds of the scale of the previous anisotropy - high accuracies ~ 0.2 % J(o) would therefore be required for comparisons with theory. Each profile was accumulated over a period of 1½ to 4 days, depending on the exact source activity, to record at least 6×10^4 counts in the peak (50 eV, 0.03 au) channel. Averaging over both measurements of one orientation and over both high and low energy sides of the profiles produced the required statistical accuracy.

Processing was performed in the same fashion that had been developed for the vanadium measurements and the profiles were finally extracted on a momentum grid of 0.1 au with a Gaussian resolution of FWHM 0.4 au. An 8×10^5 photon Monte-Carlo simulation of multiple

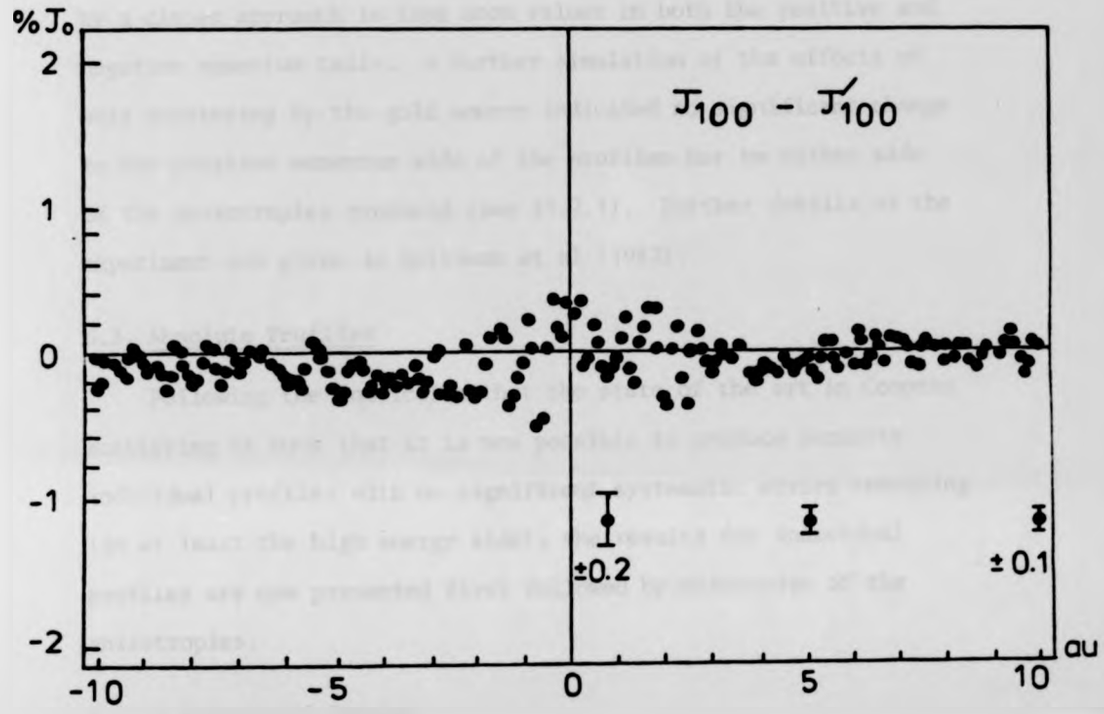

Figure 6.2. Reproducibility of Data : Difference Between Two Measurements of the (100) Profile of Iron

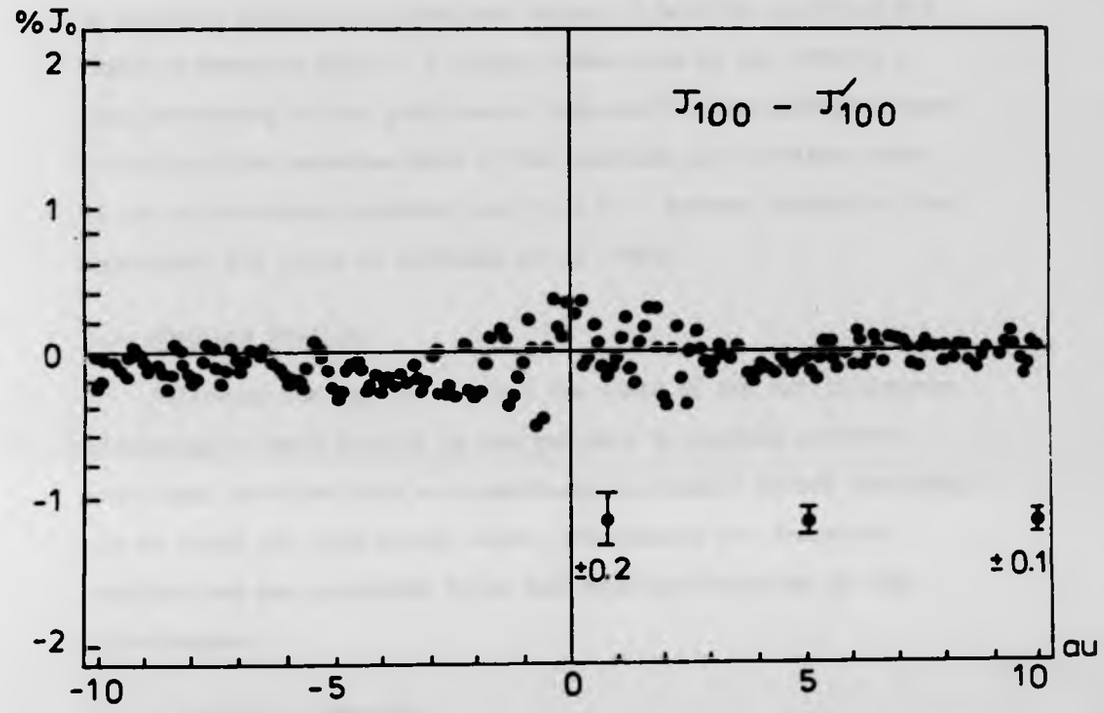

Figure 6.2. Reproducibility of Data : Difference Between Two Measurements of the (100) Profile of Iron

scattering yielded a point-by-point spectral correction for doubly and triply scattered photons which contributed 14.5% of the total accumulated profiles. The accuracy of the correction was indicated by a closer approach to free atom values in both the positive and negative momentum tails. A further simulation of the effects of self scattering by the gold source indicated no significant change to the positive momentum side of the profiles nor to either side of the anisotropies produced (see §4.2.1). Further details of the experiment are given in Rollason et al (1983).

6.3. Absolute Profiles

Following the conviction that the state of the art in Compton scattering is such that it is now possible to produce accurate individual profiles with no significant systematic errors remaining (in at least the high energy side), the results for individual profiles are now presented first followed by discussion of the anisotropies.

6.3.1. Quality of Results

Figure 6.2 shows the degree of reproducibility that is now possible in a repeated Compton measurement on the same crystal with an interval of several months. The slight systematic differences around the origin are well within the quoted statistical error of ± 0.2% J(o). The differences between the repeated measurements for the other orientations (110) and (111) were of the same appearance and the averaging of the two sets of results could be undertaken with some confidence.

The final asymmetries of the averaged experimental profiles in the three directions are shown in fig. 6.3 and correspond to the negative momentum sides of the profiles being 2.5% <J(o)> higher within the range 5-10 au. The origin of this remaining asymmetry is

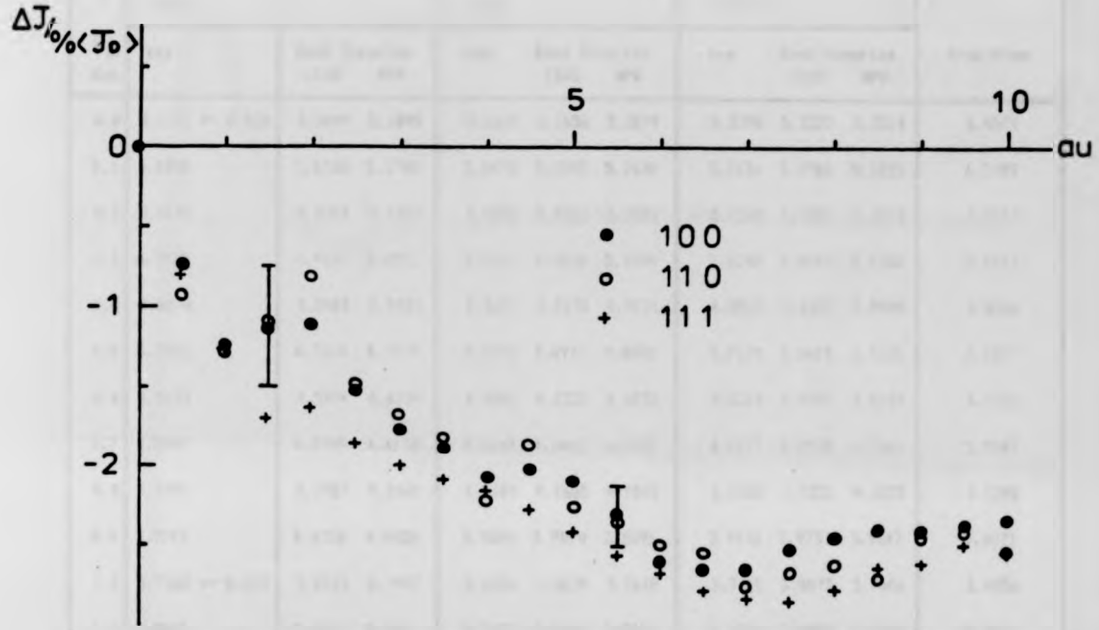

Figure 6.3. Residual Asymmetry in the Averaged Data After Processing
The persistence of this asymmetry is believed to derive from the non - monochromaticity of the source radiation which is not removed during data reduction.

Table 6.2. Experimental and Theoretical Compton Profiles of Iron

(All data are convoluted with the experimental resolution = 0.4au)

p_z au	[100]			[110]			[111]			Free Atom
	exp	Band Theories LCAO	APW	exp	Band Theories LCAO	APW	exp	Band Theories LCAO	APW	
0.0	5.1271 ± 0.020	5.0849	5.1895	5.1619	5.1656	5.2879	5.2390	5.2227	5.3324	6.4571
0.1	5.1098	5.0738	5.1749	5.1478	5.1447	5.2678	5.2136	5.1986	5.3223	6.3103
0.2	5.0690	5.0357	5.1303	5.0836	5.0822	5.2082	5.1360	5.1254	5.2373	5.9187
0.3	4.9970	4.9616	5.0531	4.9820	4.9806	5.1094	5.0248	5.0045	5.1088	5.4012
0.4	4.8870	4.8483	4.9403	4.8643	4.8470	4.9721	4.8863	4.8447	4.9480	4.8846
0.5	4.7458	4.7034	4.7919	4.7045	4.6911	4.8002	4.7120	4.6619	4.7634	4.4527
0.6	4.5633	4.5404	4.6139	4.5062	4.5221	4.6030	4.5214	4.4751	4.5629	4.1312
0.7	4.3547	4.3769	4.4178	4.3107	4.3467	4.3929	4.3217	4.2978	4.3563	3.9043
0.8	4.1501	4.1987	4.2141	4.1187	4.1685	4.1809	4.1188	4.1333	4.1525	3.7398
0.9	3.9392	4.0208	4.0058	3.9005	3.9878	3.9696	3.9172	3.9737	3.9547	3.6071
1.0	3.7268 ± 0.017	3.8329	3.7902	3.6906	3.8029	3.7618	3.7165	3.8075	3.7606	3.4856
1.2	3.3412	3.4369	3.3451	3.3198	3.4184	3.3511	3.3395	3.4388	3.3705	3.2301
1.4	2.9687	3.0456	2.9435	2.9548	3.0407	2.9593	2.9901	3.0650	2.9813	2.9519
1.6	2.6343	2.6789	2.5939	2.6351	2.6947	2.6022	2.6424	2.7276	2.6202	2.6611
1.8	2.3228	2.3530	2.2766	2.3284	2.3762	2.2797	2.3328	2.3990	2.2831	2.3729
2.0	2.0679 ± 0.013	2.0885	2.0126	2.0660	2.0862	1.9921	2.0549	2.0796	1.9663	2.1012
2.5	1.3511	1.3509	1.4871	1.3371	1.3452	1.4589	1.3386	1.3381	1.4574	1.3534
3.0	1.1706	1.1565	1.0879	1.1757	1.1582	1.0842	1.1794	1.1862	1.1095	1.1669
3.5	0.9259	0.9001	0.8447	0.9345	0.9005	0.8413	0.9143	0.8937	0.8216	0.9086
4.0	0.7621	0.7392	0.6821	0.7602	0.7398	0.6840	0.7642	0.7402	0.6887	0.7402
5.0	0.5581 ± 0.007	0.5336	0.4871	0.5673	0.5302	0.4862	0.5544	0.5342	0.4779	0.5336
6.0	0.4172			0.4253			0.4216			0.4053
7.0	0.3170			0.3210			0.3170			0.3141
8.0	0.2475			0.2478			0.2443			0.2441
9.0	0.1980			0.2016			0.1982			0.1906
10.0	0.1658 ± 0.006			0.1666			0.1656			0.1500

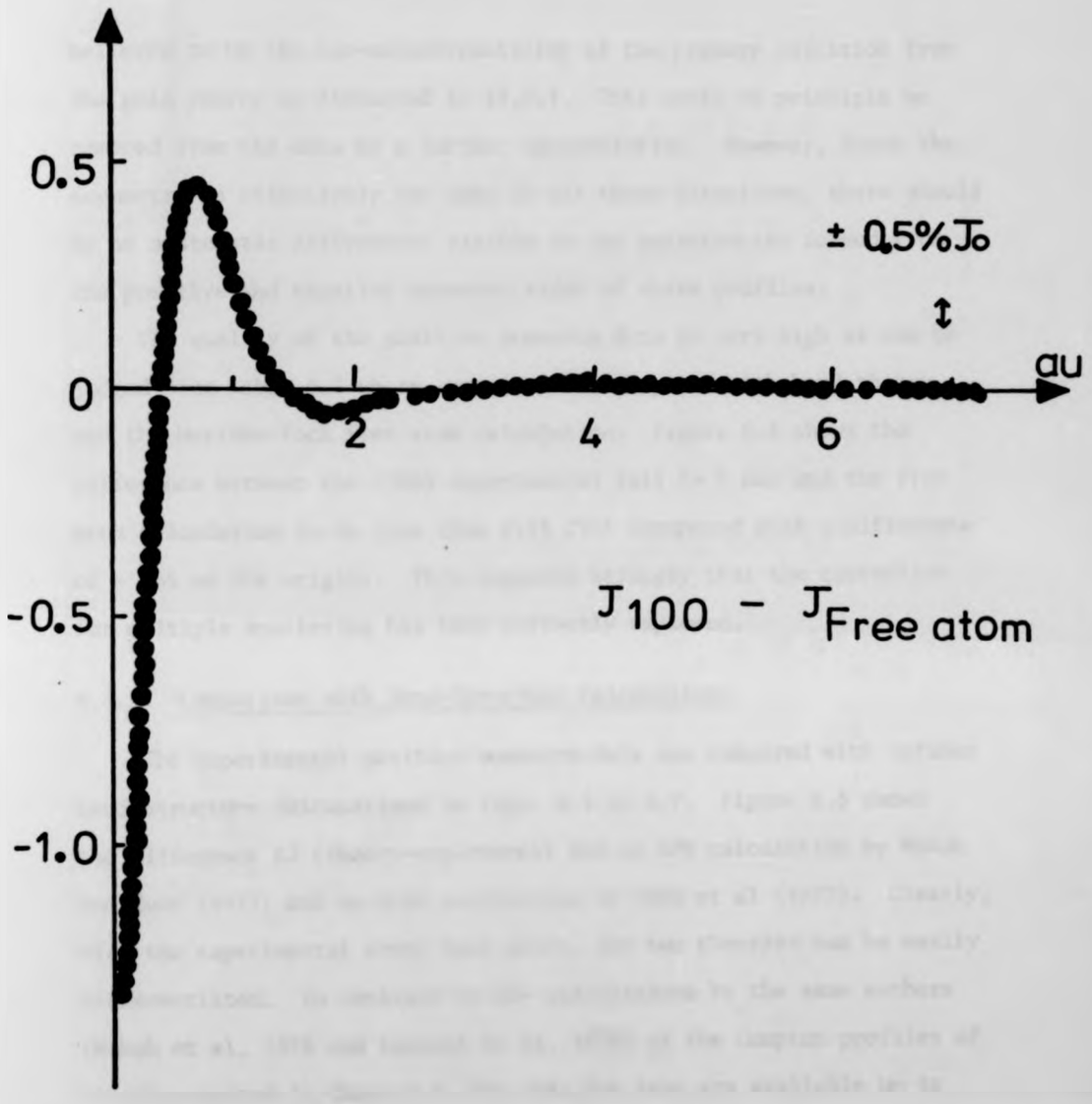

Figure 6.4. Divergence of Experimental Tail from HF Free Atom Value. Free atom values are approached from 5 au and above 7 au the difference is less than 0.5% Jo.

believed to be the non-monochromaticity of the primary radiation from the gold source as discussed in §4.2.1. This could in principle be removed from the data by a further deconvolution. However, since the asymmetry is effectively the same in all three directions, there should be no systematic differences visible in the anisotropies formed from the positive and negative momentum sides of these profiles.

The quality of the positive momentum data is very high as can be judged from Table 6.2 where experiment is compared with band theory and the Hartree-Fock free atom calculation. Figure 6.4 shows the difference between the (100) experimental tail (> 7 au) and the free atom calculation to be less than 0.5% J(o) (compared with a difference of ∿ 25% at the origin). This suggests strongly that the correction for multiple scattering has been correctly employed.

6.3.2. Comparison with Band-Structure Calculations

The experimental positive momentum data are compared with various band-structure calculations in figs. 6.5 to 6.7. Figure 6.5 shows the difference ΔJ (theory-experiment) for an APW calculation by Wakoh and Kubo (1977) and an LCAO calculation by Rath et al (1973). Clearly, with the experimental error bars given, the two theories can be easily differentiated. In contrast to the calculations by the same authors (Wakoh et al, 1976 and Laurent et al, 1978) of the Compton profiles of vanadium quoted in Chapter 5, the data for iron are available up to p_z = 5 au and these comparisons do not depend on any fitting of a free atom profile tail within the range shown. The reason for the extended data can be inferred from an inspection of the profile anisotropies (see §6.4 and fig. 6.8) which show significant features right out to 5 au.

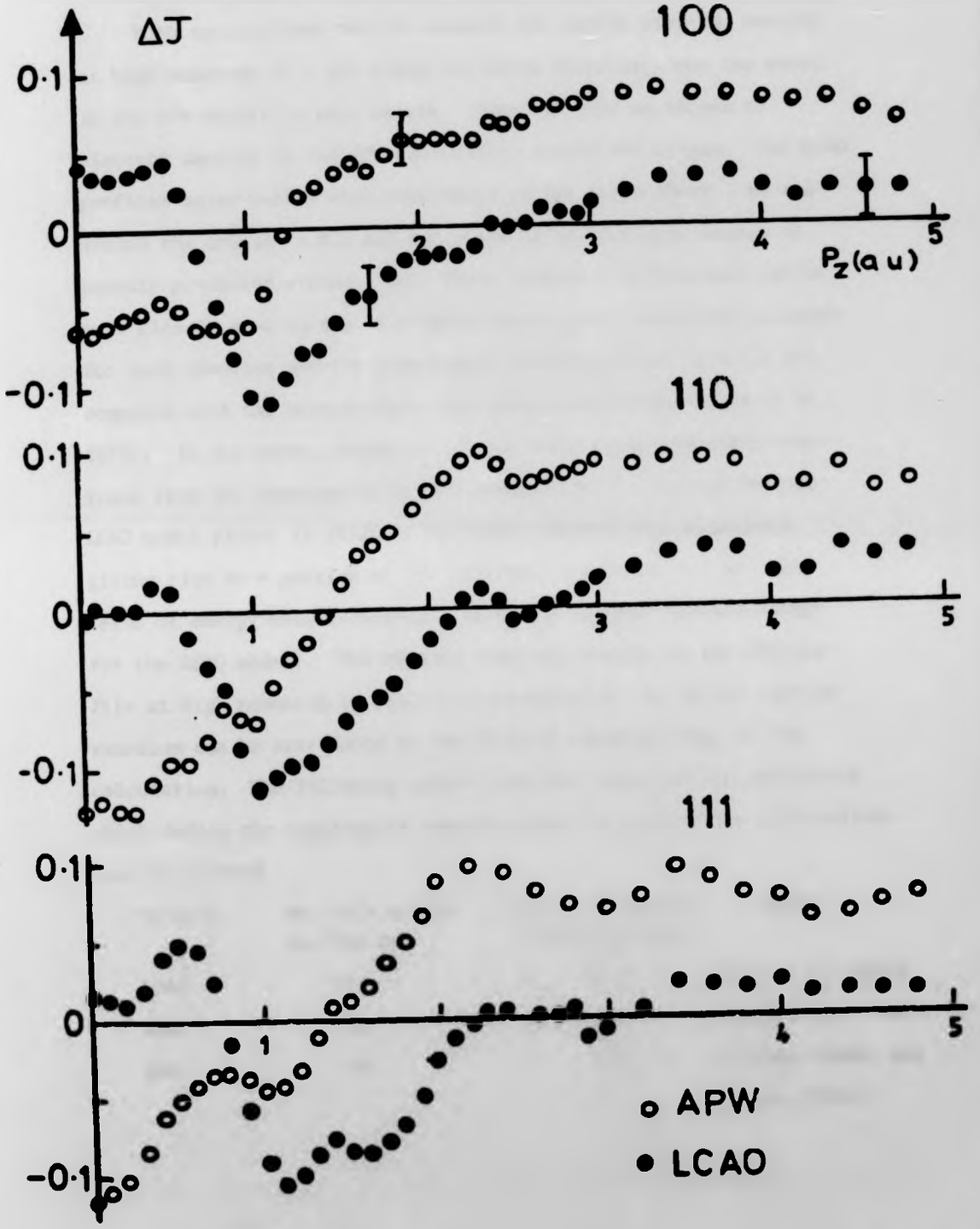

Figure 6.5. Difference Profiles (Theory - Experiment) for Iron

Both calculations tend to predict too little electron density at high momentum (> 3 au) along all three directions but the error in the APW result is very severe. There is also an excess of electron density in the APW calculation around the origin. The LCAO profiles agree better with experiment in the tails above 2 au and around the origin (< 0.5 au) but there is an isotropic excess of density predicted around 1 au. These isotropic differences can be more closely seen in fig. 6.6 where the weighted spherical averages for both theories and the experiment (obtained as in §5.4.1.) are compared with the Hartree-Fock free atom calculation (Biggs et al, 1975). In all cases, formation of the solid state transfers electrons from low momentum to higher momentum (0.5 - 1.5 au) but the LCAO model places it slightly too high compared with experiment giving rise to a portion of the isotropic excess at ∿ 1 au. (In terms of energy this corresponds to higher average kinetic energy for the LCAO model). The missing electron density in the APW profile at high momentum is readily discernible and as in the case of vanadium can be attributed to the limited momentum range of the calculation. The following table lists the values of the parameters which define the sampling of momentum space in each of the calculations considered here.

Method	No. of k points in 1/48 BZ	No. of reciprocal lattice vectors	Author
LCAO	140	3000	Rath et al (1973)
APW	55	249	Wakoh & Kubo (1977)
APW	19	141	Krishna-Gandhi and Singru (1982)

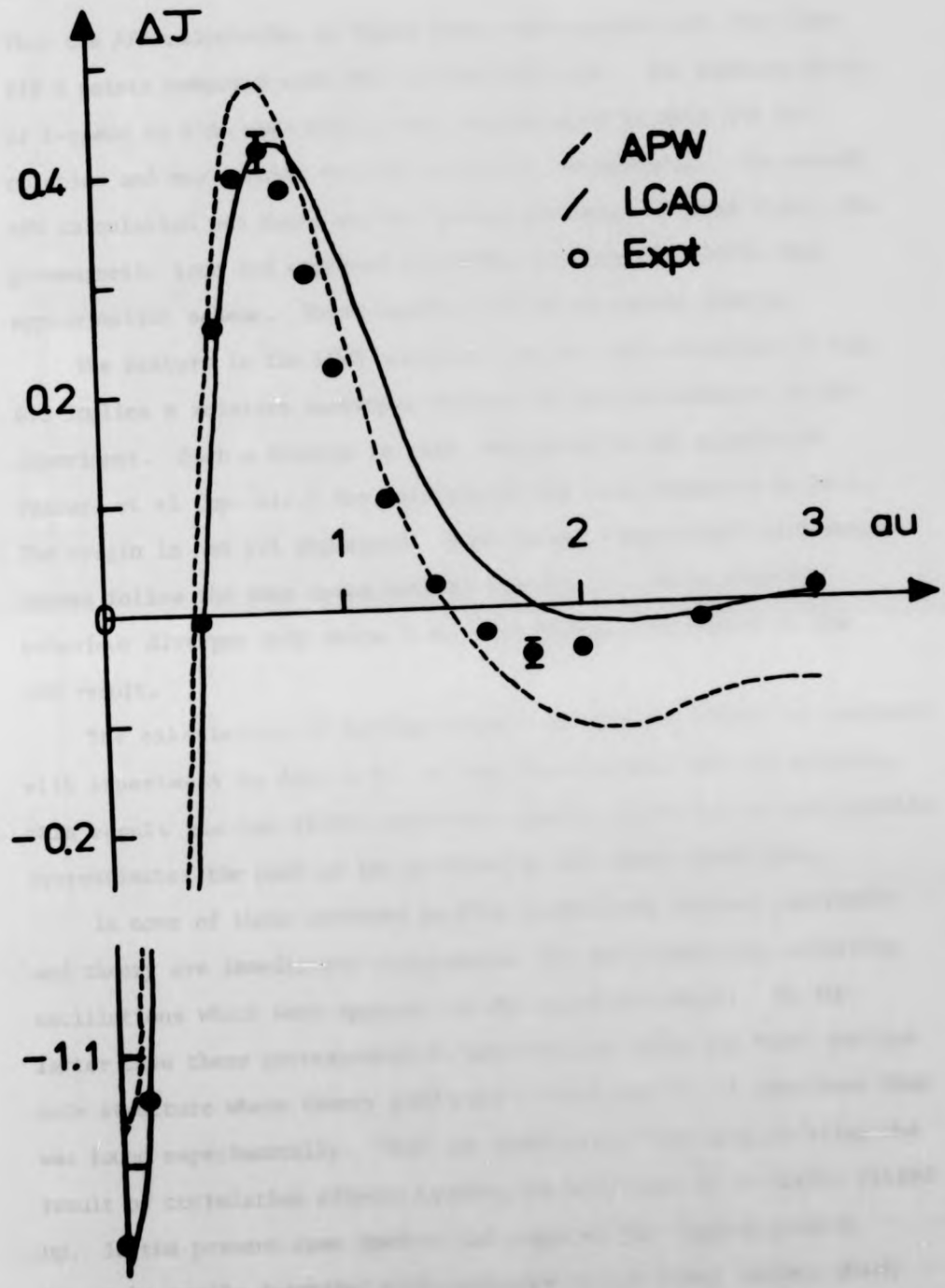

Figure 6.6. Difference of Isotropic Crystalline Profiles from HF Free Atom Value

Thus the APW calculation of Wakoh takes into account only the first 249 G points compared with 3000 in the LCAO case. The representation of k-space is also made with a much coarser grid in this APW calculation and may account for the errors at low momentum. The second APW calculation was based on the crystal potential of Wood (1962) for paramagnetic iron and employed the Hubbard-Mijnarends (1972) fast approximation scheme. These results will be discussed shortly.

The feature in the LCAO curves at 1 au for each direction in fig. 6.5 implies a relative isotropic deficit of electron density in the experiment. Such a feature is also suggested by the results of Paakari et al (op. cit.) for polycrystalline iron discussed in §6.1. The origin is not yet explained. Both theory - experiment difference curves follow the same trend between 1 and 5 au - their overall behaviour diverges only below 1 au, thus hiding this effect in the APW result.

The calculation of Krishna-Gandhi and Singru (1982) is compared with experiment in fig. 6.7. As for the previous APW calculation, this result has too little electron density above 1.5 au and greatly overestimates the peak of the profiles in all three directions.

In none of these absolute profile comparisons between experiment and theory are immediately recognisable the small regularly occurring oscillations which were apparent in the vanadium results. In the latter case these corresponded to intersections with the Fermi surface hole structure where theory predicted a lower density of electrons than was found experimentally. This was tentatively explained as being the result of correlation effects causing the hole arms to be partly filled up. In the present case however the shape of the Compton profile cannot be easily described with reference to its Fermi surface which contains much finer detail than that of vanadium - its complexity is expected to largely obscure any such correlation effects. However

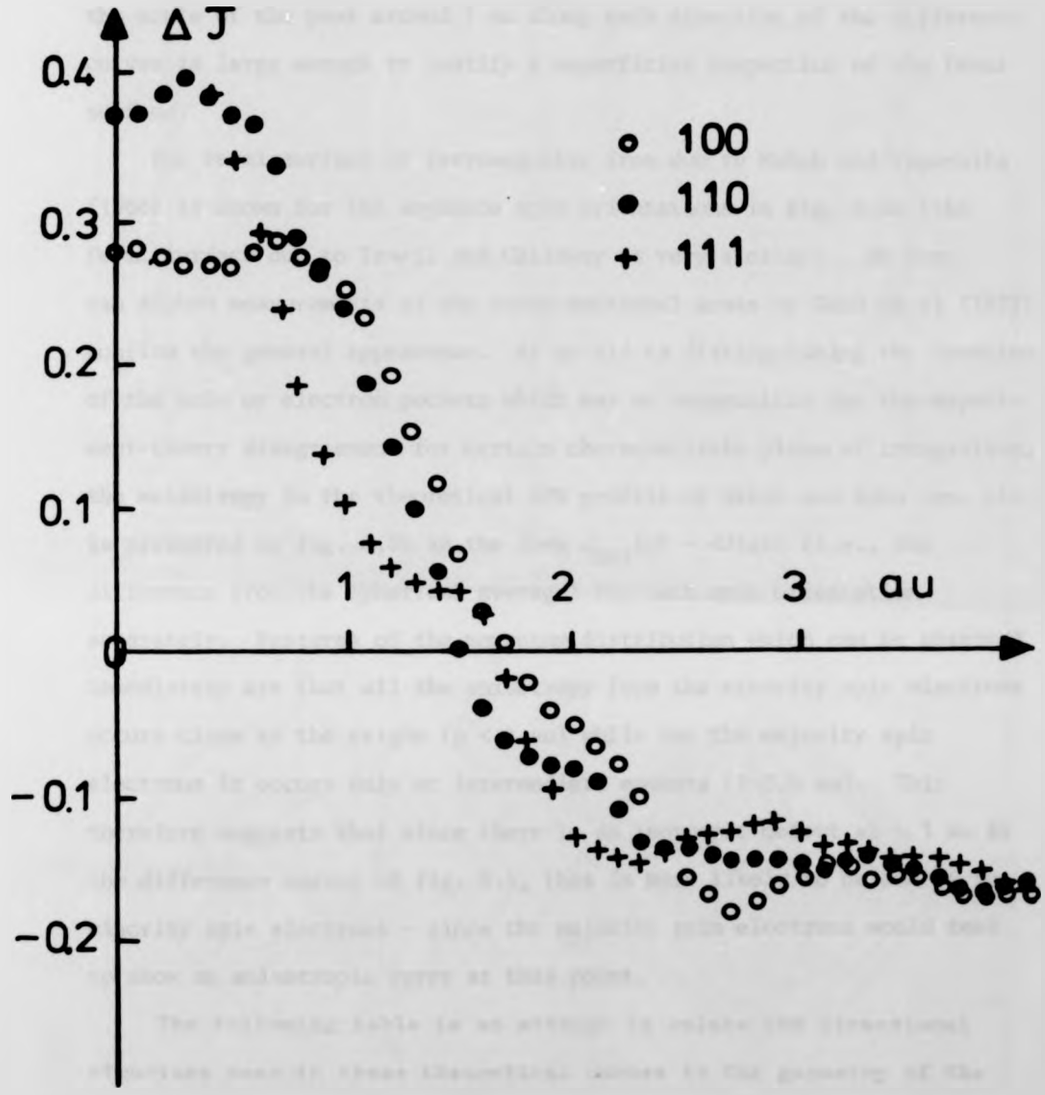

Figure 6.7. Comparison of the APW Calculation due to Krishna – Gandhi and Singru, 1982 with the Experimental Result. The differences at the origin are of the order of 7% Je.

the scale of the peak around 1 au along each direction of the difference curves is large enough to justify a superficial inspection of the Fermi surface.

The Fermi surface of ferromagnetic iron due to Wakoh and Yamashita (1966) is shown for the separate spin orientations in fig. 6.8a (the Fermi surface due to Tawil and Callaway is very similar). De Haas van Alphen measurements of the cross-sectional areas by Gold et al (1971) confirm the general appearance. As an aid to distinguishing the location of the hole or electron pockets which may be responsible for the experiment-theory disagreement for certain characteristic planes of integration, the anisotropy in the theoretical APW profile of Wakoh and Kubo (op. cit.) is presented in fig. 6.8b in the form $J_{hkl}(q) - \langle J(q) \rangle$ (i.e., the difference from the spherical average) for each spin orientation separately. Features of the momentum distribution which can be observed immediately are that all the anisotropy from the minority spin electrons occurs close to the origin ($p < 1$ au) while for the majority spin electrons it occurs only at intermediate momenta (1-2.5 au). This therefore suggests that since there is an isotropic defect at $\sim$ 1 au in the difference curves of fig. 6.5, this is more likely to be due to the minority spin electrons - since the majority spin electrons would tend to show an anisotropic error at this point.

The following table is an attempt to relate the directional structure seen in these theoretical curves to the geometry of the Fermi surface. The penultimate column indicates the nature of the error excursion that would be expected in the theory-experiment comparison of directional profiles if electron correlation smearing (as depicted in figure 1.10) were causing effects similar to those assumed in Vanadium. The final column confirms the appearance of these errors in figure 6.5.

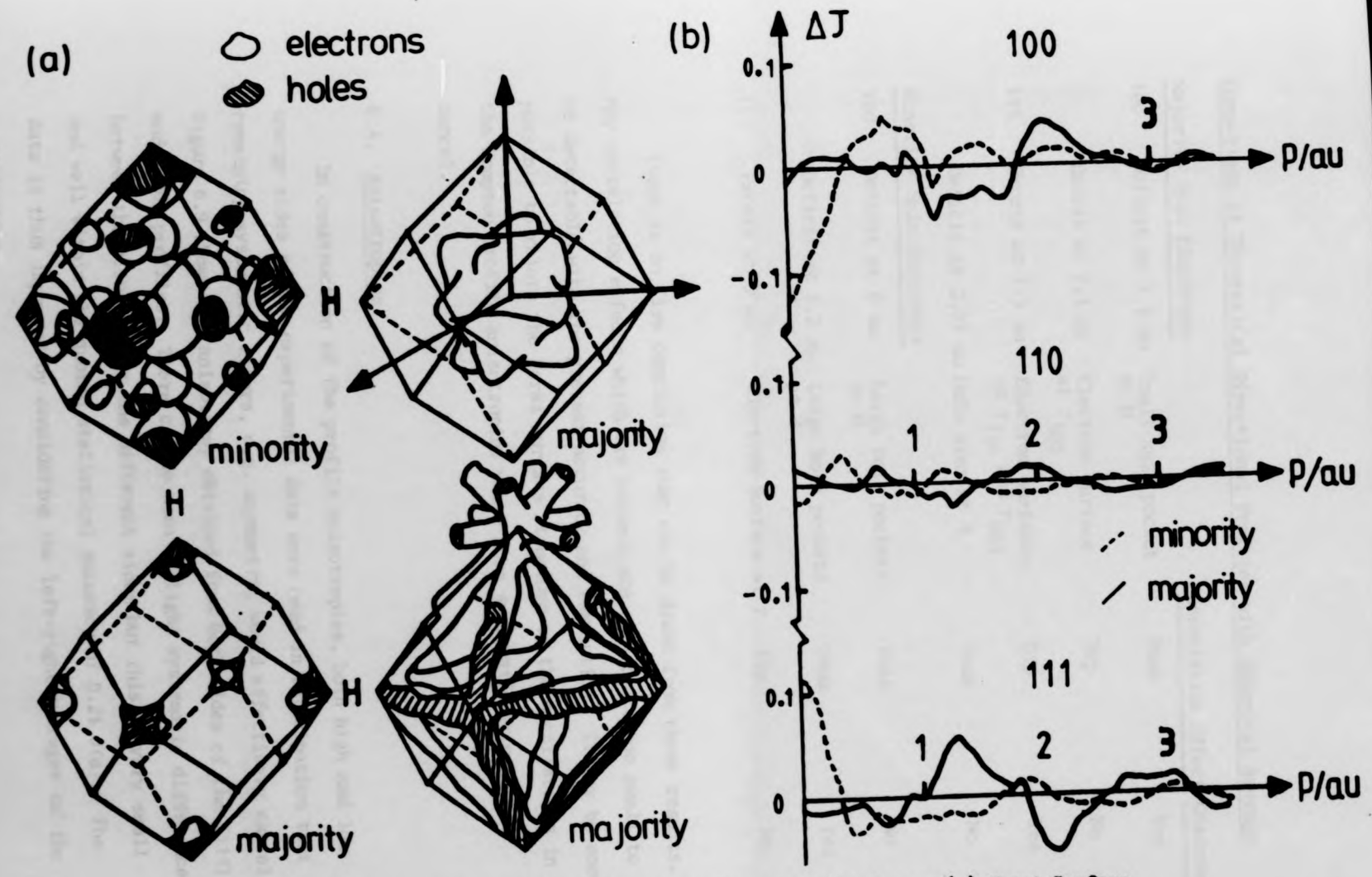

Figure 6.8. Investigation of Fermi Surface of Ferromagnetic Iron : (a) Fermi Surface

(b) Directional Differences from Spherical Average for Each Spin Orientation

Comparison of Theoretical Directional Profiles with Spherical Average

Majority Spin Electrons			Correlation Effect	Observed
100	Deficit at 1.2 au	Small hole pocket at H	Peak	Yes
	Excess at 2.1 au	Electron surface at Γ_{100}	Dip	No
111	Excess at 1.3 au	Electron surfaces at Γ_{110} and Γ_{001}	Dip	Yes
	Deficit at 2.05 au	Hole arms at H	Peak	No
Minority Spin Electrons				
100	Deficit at 0 au	Large hole pockets at H	Peak	No
	Deficit at 1.2 au	Large hole pockets at H	Peak	Yes
111	Excess at 0 au	Electron Surface at Γ	Dip	No

There is no firm conclusion that can be drawn from these results. Any correlation effects which are present are of a scale too small to be detectable with the present accuracy and resolution. It may be more possible to relate the Fermi surface structure to the oscillations in the Compton profile anisotropies where more systematic errors will cancel.

6.4. Anisotropies

In construction of the profile anisotropies, both high and low energy sides of the experimental data were used in anticipation that remaining systematic errors, e.g. asymmetry, would effectively cancel. Figure 6.9 shows the anisotropy obtained from both sides of the (111) and (100) profiles. There can be seen a slight systematic difference between the results from the different sides but this is very small and well within the quoted statistical accuracy of 0.2% J(o). The data is thus improved by considering the left-right averages of the anisotropies.

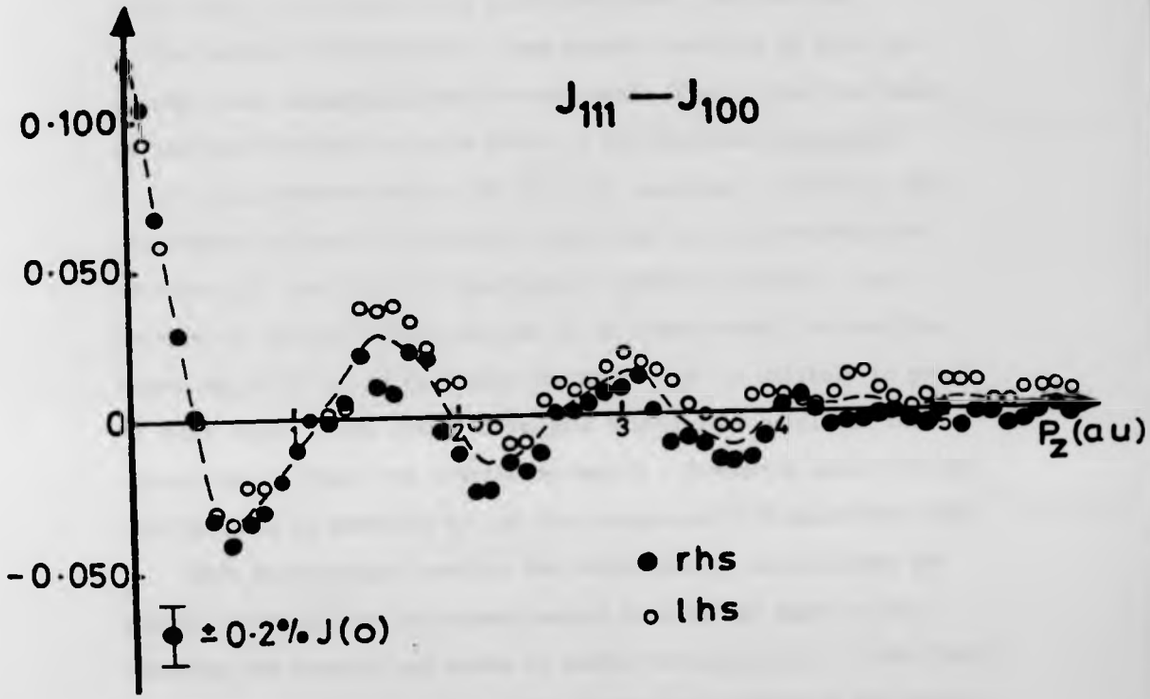

Figure 6.9. Reproducibility of Anisotropy between Data from High and Low Momentum Sides of the Profile

The results obtained after left-right averaging are shown in fig. 6.10a and compared with the band theory predictions. Within 0.5% J(o), the APW and LCAO results mutually agree but there are significant differences from experiment when the error bar of the latter is considered. Some general features of both the theory and experiment can be mentioned. One is that the scale of the oscillations is quite small at low momentum (amplitude $\sim$ 2.5% J(o) compared with $\sim$ 4% J(o) for vanadium). Secondly, the anisotropy in iron is detectable right out to $\sim$ 5 au whereas for vanadium the profiles are spherically symmetric beyond $\sim$ 3 au. Because of this situation the use of an atomic model (as used for vanadium, §5.4.1.) to represent the anisotropy is unlikely to prove of much value. This seems to suggest a different origin of the anisotropy in these two transition metals - depending mainly on the wavefunction in vanadium but on the occupation of k-space for iron.

Both calculations predict the occurrence of oscillations at momenta borne out by the experimental results but again as in vanadium the theoretical scale is rather too large (0.5 - 1.0% J(o)). Neither calculation is consistently better at predicting the experiment (in contrast to the comparison of individual profiles with theory where the APW result was found to be seriously deficient) over the entire range of p . The LCAO curves give better agreement below 0.5 au and above 2 au while the APW curves are slightly to be preferred for intermediate momenta.

Significant discrepancies between experiment and both theories are visible at $p_z \approx 0.7$ au and 2.2 au in the (111)-(100) curves and also in the (111)-(110) curves, where the calculations give values smaller by about 0.05 electrons/au. It is possible that this is due to small effects in the (111) profile alone at these positions and

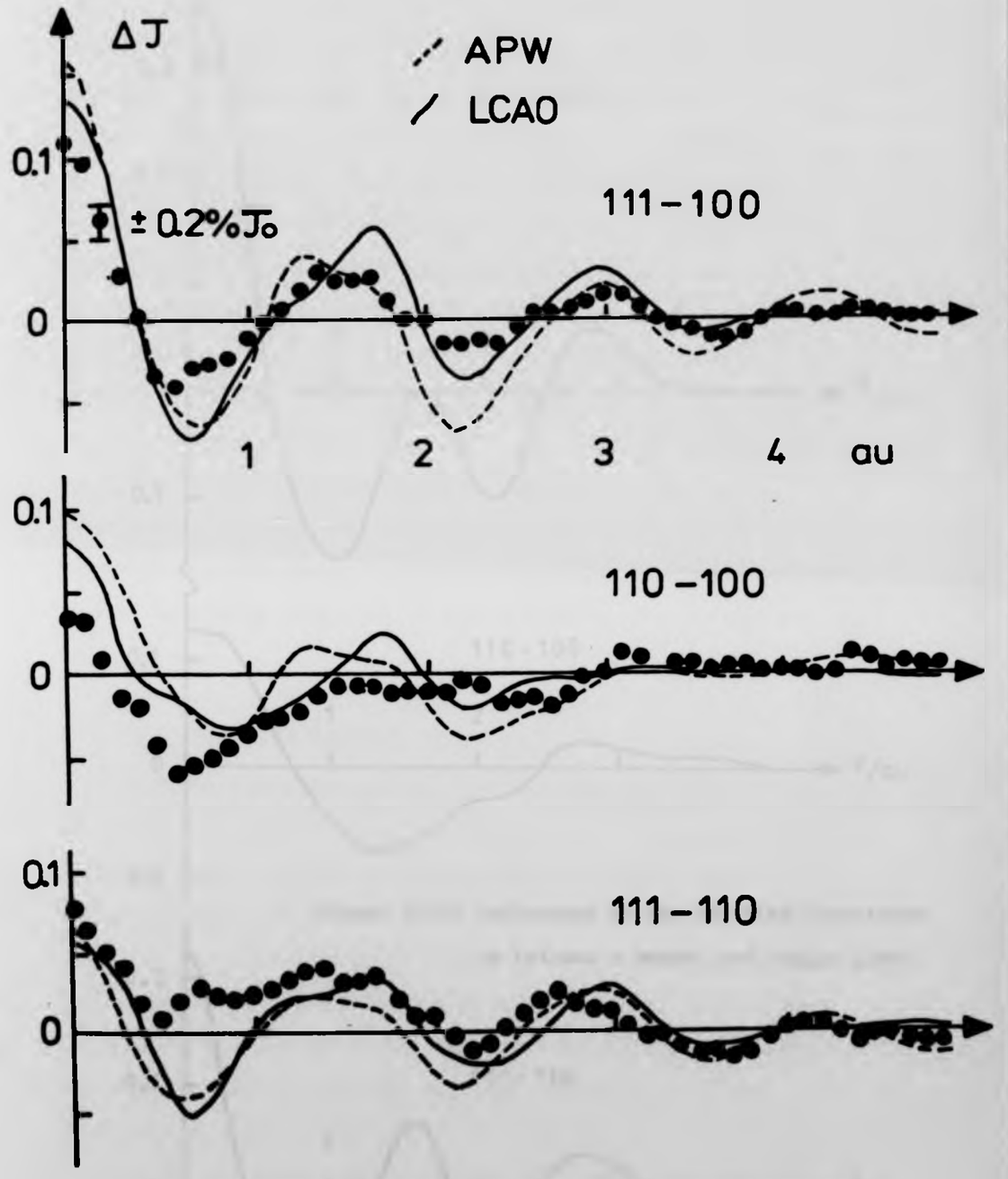

Figure 6.10a The Anisotropy Results for Iron (Data are averaged over positive and negative values of momentum)

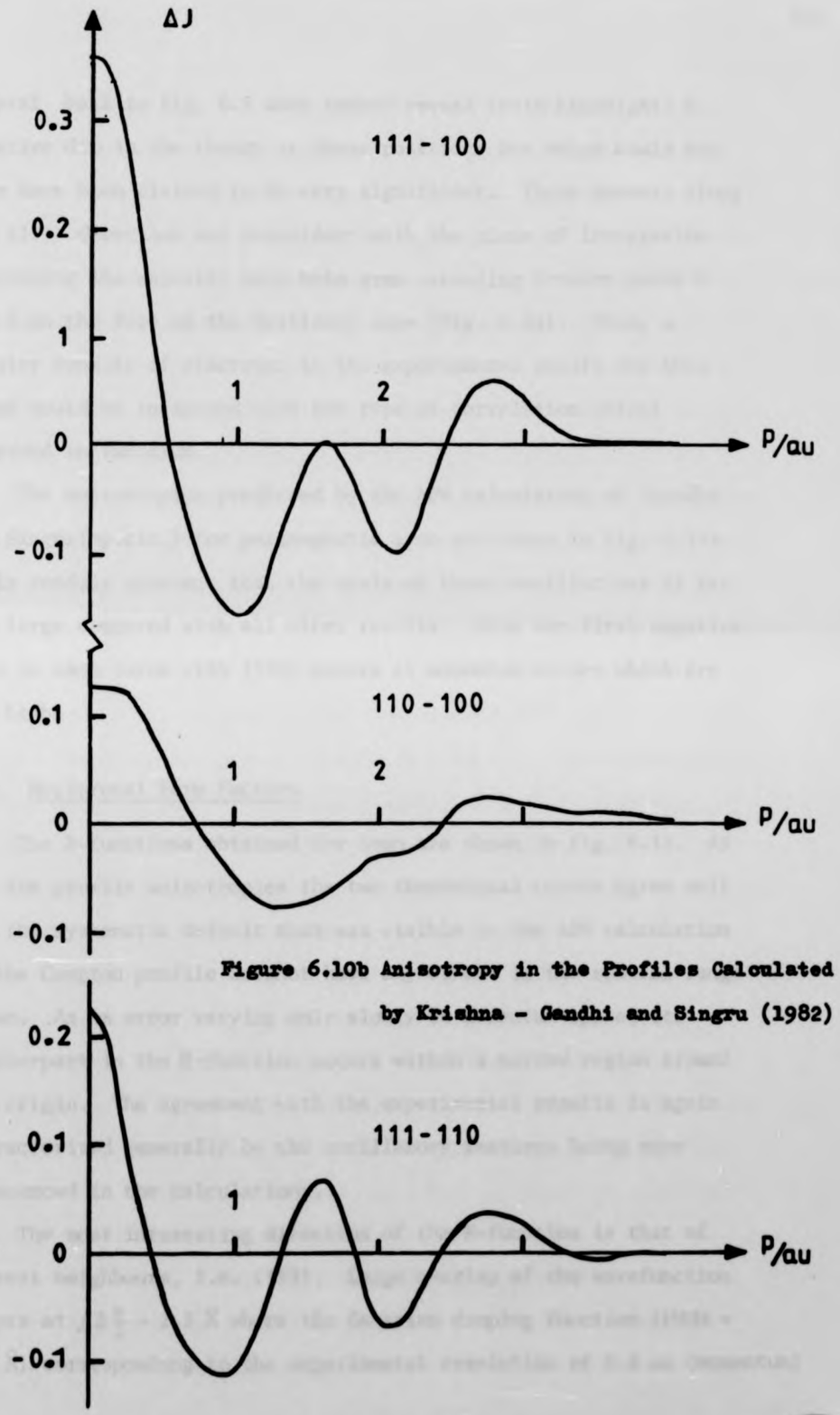

Figure 6.10b Anisotropy in the Profiles Calculated by Krishna - Gandhi and Singru (1982)

referal back to fig. 6.5 does indeed reveal (with hindsight) a relative dip in the theory at these positions but which could not then have been claimed to be very significant. These momenta along the (111) direction are coincident with the plane of integration containing the majority spin hole arms extending between point H and N on the face of the Brillouin zone (Fig. 6.8a). Thus, a greater density of electrons in the experimental result for this plane would be in accord with the type of correlation effect observed in vanadium.

The anisotropies predicted by the APW calculation of Gandhi and Singru(op.cit.) for paramagnetic iron are shown in fig. 6.10b It is readily apparent that the scale of these oscillations is far too large compared with all other results. Also the first negative peak in each curve with (100) occurs at momentum values which are too high.

6.5. Reciprocal Form Factors

The B-functions obtained for iron are shown in fig. 6.11. As for the profile anisotropies the two theoretical curves agree well and the systematic deficit that was visible in the APW calculation of the Compton profile doesnot have any effect in the spatial range shown. As an error varying only slowly in momentum space, its counterpart in the B-function occurs within a narrow region around the origin. The agreement with the experimental results is again characterised generally by the oscillatory features being more pronounced in the calculations.

The most interesting direction of the B-function is that of nearest neighbours, i.e. (111). Large overlap of the wavefunction occurs at $\sqrt{3}\frac{a}{2}$ = 2.3 Å where the Gaussian damping function (FWHM = 7.3 Å) corresponding to the experimental resolution of 0.4 au (momentum)

is still sufficiently large to allow features to appear. At this position both calculations predict a large localised peak which is visible only as a slight flattening of the experimental data. The B-function involves the overlap of integrals over planes in position space and thus the smaller theoretical peak at $\sim$ 3.4 Å ($2a/\sqrt{3}$) corresponds to the projection of (110) lattice translations onto the (111) direction. (This is the second (110) plane encountered along this direction - the first at $\sim$ 1.7 Å occurs too close to the origin for the small projection overlap to be distinguished from the (111) overlap itself). The experimental result shows no evidence of this small peak. The negative excursion in the calculation around $a/\sqrt{3} = 5.02$ Å corresponds to a lattice translation by the full body-diagonal of the unit cube. It is interesting to note that again the experimental result shows no sign of this feature. This position also corresponds to the periodicity of the proposed electron correlation defects found in the Compton profile for the (111) direction and the first feature at 2.3 Å represents slightly more than twice this periodicity. Thus the discrepancy between experiment and theory at these characteristic positions may be evidence of correlation effects.

The other two directions of the B-function do not show such large scale features as the (111). Along the (100) direction, there is a fairly strong peak in the theories at a distance seemingly related to the lattice translation a = 2.9 Å while the experiment shows only a small peak slightly closer to the origin (2.6 Å). Along the (110) direction a very small peak in the theory at the distance of projection of both the ($\frac{1}{2}$ $\frac{1}{2}$ $\frac{1}{2}$) and (100) positions is completely missing from the experiment.

In conclusion, it can be stated that the interpretation of Compton scattering data in terms of the B-functions is advantagous in that the slowly varying systematic errors of the Compton profiles,

is still sufficiently large to allow features to appear. At this position both calculations predict a large localised peak which is visible only as a slight flattening of the experimental data. The B-function involves the overlap of integrals over planes in position space and thus the smaller theoretical peak at $\sim$ 3.4 Å ($2a/\sqrt{3}$) corresponds to the projection of (110) lattice translations onto the (111) direction. (This is the second (110) plane encountered along this direction - the first at $\sim$ 1.7 Å occurs too close to the origin for the small projection overlap to be distinguished from the (111) overlap itself). The experimental result shows no evidence of this small peak. The negative excursion in the calculation around $a/\sqrt{3}$ = 5.02 Å corresponds to a lattice translation by the full body-diagonal of the unit cube. It is interesting to note that again the experimental result shows no sign of this feature. This position also corresponds to the periodicity of the proposed electron correlation defects found in the Compton profile for the (111) direction and the first feature at 2.3 Å represents slightly more than twice this periodicity. Thus the discrepancy between experiment and theory at these characteristic positions may be evidence of correlation effects.

The other two directions of the B-function do not show such large scale features as the (111). Along the (100) direction, there is a fairly strong peak in the theories at a distance seemingly related to the lattice translation a = 2.9 Å while the experiment shows only a small peak slightly closer to the origin (2.6 Å). Along the (110) direction a very small peak in the theory at the distance of projection of both the ($\frac{1}{2}$ $\frac{1}{2}$ $\frac{1}{2}$) and (100) positions is completely missing from the experiment.

In conclusion, it can be stated that the interpretation of Compton scattering data in terms of the B-functions is advantagous in that the slowly varying systematic errors of the Compton profiles,

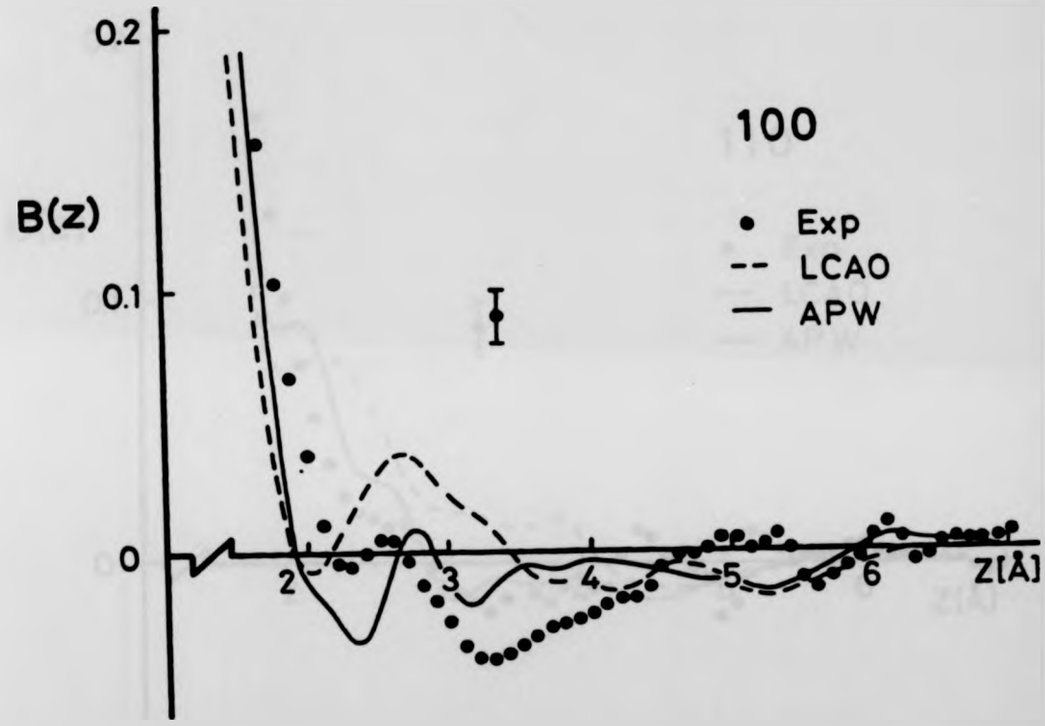

Figure 6.11a Reciprocal Form Factor for Iron (100)

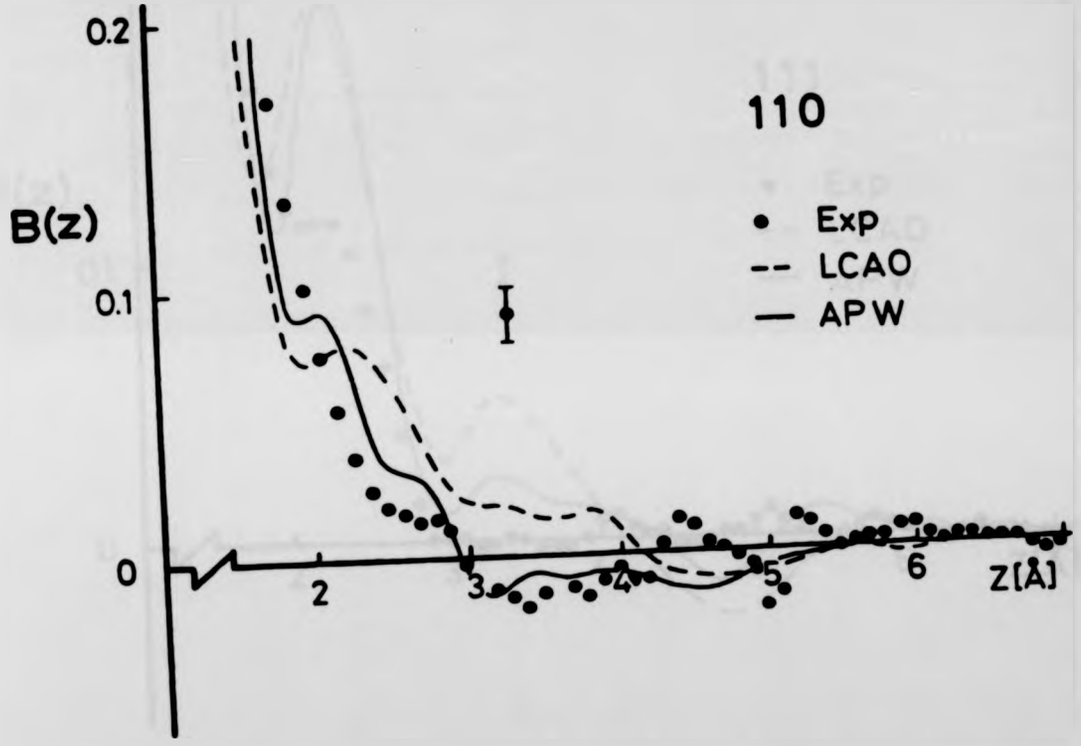

Figure 6.11b Reciprocal Form Factor for Iron (110)

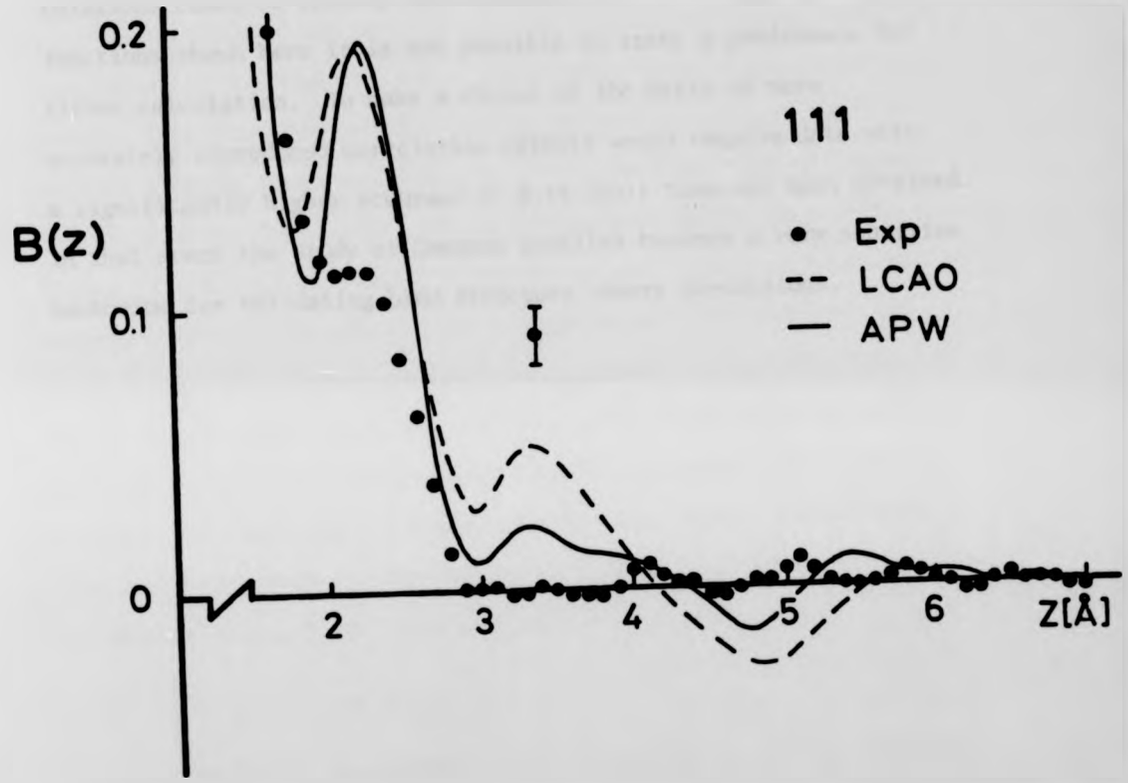

Figure 6.11c Reciprocal Form Factor for Iron (111)

both experimental and theoretical, are separated from the more localised errors which appear to be associated with correlation produced changes in the k-space occupation function. While in the Compton profile representation, the two band structure calculations could be clearly distinguished, on the basis of the B-functions shown here it is not possible to state a preference for either calculation. To make a choice on the basis of more accurately reproduced correlation effects would require data with a significantly higher accuracy (< 0.1% J(o)) than has been obtained. In that event the study of Compton profiles becomes a very sensitive technqiue for validating band structure theory predictions.

CHAPTER 7

DISCUSSION AND CONCLUSIONS

7.1. Studies of the First Transition Series

The results of the present study of Vanadium and Iron should be considered in the light of other investigations of the momentum density distributions in other transition series elements and compounds. Recent reviews of the scope of research to date are given for the Compton Scattering technique in general by Williams and Thomas (1983) and for transition metals in particular by Weiss and Mazzone (1981). The development of high energy spectrometers and solid state detectors has ensured that research is prolific and the field covered quite extensive. However, only a brief survey of the results is presented here with special consideration of the effects of correlation for d-electron systems. Where such comparisons would be pertinent, the results of allied experimental techniques and related research are also discussed.

7.1.1. Pure Transition Metals

Compton Profile measurements have been made on all the elements of the first transition series except Mn and Sc which are particularly difficult to obtain in pure crystalline form. The most accurate measurements at present are made with 412 keV spectrometer systems and have so far been restricted to V, Fe and Cu (current attention of several research groups has turned towards the 400 keV measurement of the profiles for Ni). However, lower energy (60 keV and 160 keV) measurements of the other members of the series have yielded results following the same trend of disagreement with theory as the former

set - namely, that the calculated anisotropy is generally greater than measured. There is also a tendency for the recent band-structure calculations to overestimate the value of J(o). Angular correlation of position annihilation radiation measurements reproduce the anisotropy disagreement but to a lesser degree. The reason is assumed to be related to the avoidance of the tightly bound d electrons by the position wavefunction and hence by implication, it is the behaviour of the electrons occupying these highly inhomogeneous d-type wavefunctions which is the source of error in the calculations. In contrast to the disagreement present for transition metals, anisotropies for the simple metals are more accurately reproduced by theory as is evidenced for example by Be (Hansen et al, 1979). But a slight overestimate of the value of J(o) still persists. Attempts to relate Compton scattering results to the measurements of structure factors and their paired-reflection intensity ratios have not been very revealing. Early X-ray diffraction measurements have suggested that the experimental asphericity may be actually greater than calculated values but these measurements have been very prone to error. Later high energy γ-ray measurements such as for Cu (Schneider et al, 1982) suggest that the disagreement may be less than originally thought. In addition, most recent band-structure calculations quite accurately predict the energy band dispersions and Fermi surfaces measured by Angle-Resolved Photoemission and de Haas - Van Alphen experiments respectively and therefore there is a possibility that the discrepancies evidenced by the momentum density measurements are unique to Compton scattering - at least within the limits to the accuracy of measurements obtainable for the other experimental techniques. Some recent consideration of this theoretical problem is presented in §7.2.

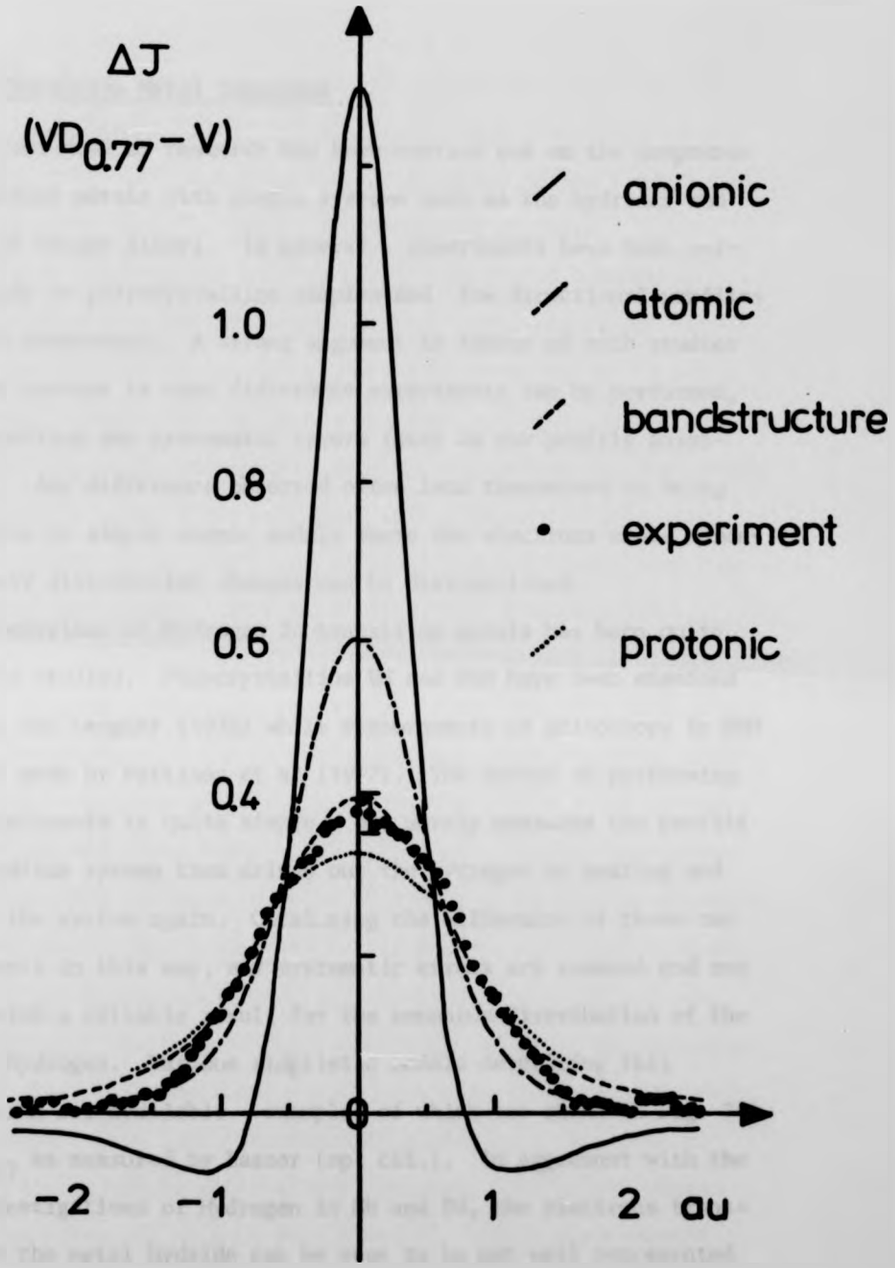

Figure 7.1. Study of Hydrogen in Vanadium - Comparison of the difference profile $VD_{0.77}$ - V with various models (Lässer & Lengeler,1978)

7.1.2. Transition Metal Compounds

A great deal of research has been carried out on the compounds of transition metals with simple systems such as the hydrides and oxides and binary alloys. In general , experiments have been performed only on polycrystalline samples and few directional profiles have been determined. A strong argument in favour of such studies of binary systems is that difference experiments can be performed, thus minimizing any systematic errors (just as for profile anisotropies). Any difference observed often lend themselves to being explainable by simple atomic models where the electrons whose momentum density distribution changes can be distinguished.

The behaviour of Hydrogen in transition metals has been quite rigorously studied. Polycrystalline VH and PdH have been examined by Lässer and Lengeler (1978) while measurements of anisotropy in NbH have been made by Pattison et al (1977). The method of performing these experiments is quite simple - one merely measures the profile of the hydride system then drives out the hydrogen by heating and measures the system again. Obtaining the difference of these two measurements in this way, any systematic errors are removed and one is left with a reliable result for the momentum distribution of the inserted Hydrogen. Various simplistic models describing this distribution are available - examples of which are shown in Fig. 7.1 for $VH_{0.77}$ as measured by Lasser (op. cit.). In aggrement with the other investigations of Hydrogen in Nb and Pd, the electrons transferred in the metal hydride can be seen to be not well represented by an anionic model ($V^+ H^-$) but rather indicate only partial charge transfer from the Hydrogen (atomic model) to the metal (V^- + proton).

Rather less work has been carried out on transition metal oxides and there remain a lot of interesting effects to be uncovered through

the use of Compton profiles. Phase transitions are abundant with these systems. Lässer et al (1978) investigated the effect of the Verwey (ferromagnetic - paramagnetic) transition on the profile of Fe_3O_4 (magnetite) which occurs at a temperature of 119 K. However no effect was found within an error of ± 0.5% J(o). Molecular cluster calculations for the oxides of V by Gupta and Ellis (1976) suggest that the Mott (metal-insulator) transition in VO_2 at 340 K may be readily observable by Compton scattering but as yet no experiments have been performed. More immediately pertinent to the present work, Magnesium Oxide (MgO) has been studied recently both experimentally (Aikala et al, 1982) and theoretically (Podloucky and Redinger, 1983) by the APW method. This has yielded the interesting result that again the experimental anisotropy is smaller than calculated (fig. 7.2) This is problematical to explain in terms of a redistribution of the momentum density due to e-correlations since Magnesium Oxide is presumed to form as an ionic insulator (Mg^{2+} O^{2-}) which should therefore not admit any Fermi surface effects. This is unresolved.

The technological importance of alloys of transition metals with either simple or other transition metals has recently been a strong incentive for experimental research. Compton scattering has been involved at both the fundamental electron ground state determination level and also at a macroscopic level of non-destructive analysis of bulk castings. This latter research is presented in Appendix B.

Considering simple metal alloys, Manninen et al (1981) have studied the alloys of Al with Fe, Co and Ni. Their measurements have revealed a charge transfer of $\sim$ 0.5 electrons from the conduction electrons of Al to the 3d bands of the host system. Another Group III metal alloy Ni_3Ga has been modelled by Wakoh and Kubo (1984) by the LAPW method in a detailed examination of the contributions to the

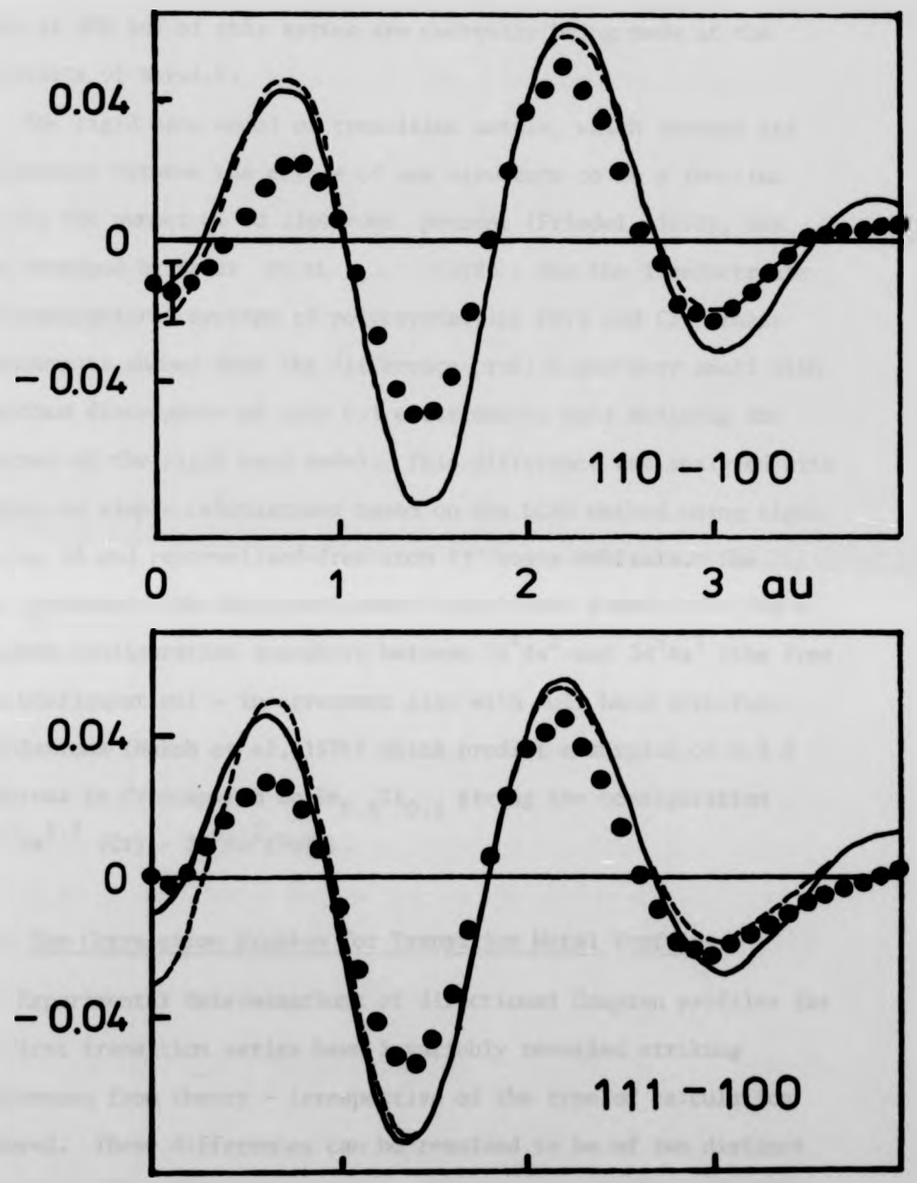

Figure 7.2. Anisotropy in MgO (Points - experiment of Aikala et al, 1982 ; curves - APW calculations by Podloucky and Redinger, 1983)

Compton profile from different bands, up to the 15th band. Measurements at 400 keV of this system are currently being made at the University of Warwick.

The rigid band model of transition metals, which assumes the differences between the metals of one structure to be a function of only the number of 3d electrons present (Friedel, 1958), has been examined by Bauer et al (1983) for the isoelectronic and isostructural systems of polycrystalline FeTi and Cr. Their measurements showed that the difference profile was very small with a maximum discrepancy of only 0.1 electrons/au thus defining the accuracy of the rigid band model. This difference was analysed with respect to simple calculations based on the LCAO method using tight-binding 3d and renormalised-free-atom 4s basis orbitals. The best agreement with the experimental result was found to be for a Chromium configuration somewhere between $3d^4 4s^2$ and $3d^5 4s^1$ (the free atom configuration) - in agreement also with full band structure calculations (Wakoh et al, 1976) which predict a surplus of 0.3 d electrons in Cr compared to $Fe_{0.5}Ti_{0.5}$ giving the configuration $3d^{4.3} 4s^{1.7}$ (Cr) - $3d^4 4s^2$(FeTi).

7.2. The Correlation Problem for Transition Metal Profiles

Experimental determinations of directional Compton profiles for the first transition series have invariably revealed striking differences from theory - irrespective of the type of calculation employed. These differences can be resolved to be of two distinct types - an isotropic part such that the theoretical value of J(o) is usually greater than the experimental one - and an anisotropic redistribution of momentum density such that theoretical anisotropies are greater than has been measured. Recent work by Bauer (1983) has

attempted to relate the origin of this discrepancy to the presence of electron interactions and suggests the particular sensitivity of the momentum density to such effects. This section discusses the progress made so far.

7.2.1. Single Particle Equations of Normal Use

Most recent band structure calculations employ a local-density approximation to the exchange-correlation potential in a set of independent one-electron equations after the manner of the Hartree-Fock-Slater method. The hope is to include correlation effects (interactions between electrons of opposite spins) in the same way as Slater included exchange effects (interactions between electrons of the same spin). It was shown by Hohenberg and Kohn (1964) and Kohn and Sham (1965) that these equations can be derived by density functional analysis of interacting electron systems. Density Functional Theory (Callaway and March, 1983) is directly descended from the Thomas-Fermi model of the atom (Thomas, 1926 and Fermi, 1927) which relates the central field potential to the electron density. The theory shows that the exchange-correlation energy is a unique functional of the charge density and that an energy minimisation procedure based on the variation principle can yield a set of self-consistent one electron equations,

$$\{-\nabla^2+V_H[\rho](\bar{r})+V_{ext}(\bar{r})+V_{xc}[\rho](\bar{r})\}\phi_i(\bar{r}) = \epsilon_i\phi_i(\bar{r}) \qquad \text{Eq. 7.1.}$$

where $V_H[\rho](\bar{r})$ = classical Hartree field for a distribution ρ

$V_{ext}(\bar{r})$ = external lattice potential

and $V_{xc}[\rho](\bar{r})$ = exchange-correlation potential $= \frac{\delta E_{xc}[\rho]}{\delta\rho(\bar{r})}$ Eq. 7.2.

where $E_{xc}[\rho]$ = total exchange-correlation energy

and $\rho(\bar{r}) = \sum_{i,\ \text{occupied}} |\phi_i(\bar{r})|^2$

attempted to relate the origin of this discrepancy to the presence of electron interactions and suggests the particular sensitivity of the momentum density to such effects. This section discusses the progress made so far.

7.2.1. Single Particle Equations of Normal Use

Most recent band structure calculations employ a local-density approximation to the exchange-correlation potential in a set of independent one-electron equations after the manner of the Hartree-Fock-Slater method. The hope is to include correlation effects (interactions between electrons of opposite spins) in the same way as Slater included exchange effects (interactions between electrons of the same spin). It was shown by Hohenberg and Kohn (1964) and Kohn and Sham (1965) that these equations can be derived by density functional analysis of interacting electron systems. Density Functional Theory (Callaway and March, 1983) is directly descended from the Thomas-Fermi model of the atom (Thomas, 1926 and Fermi, 1927) which relates the central field potential to the electron density. The theory shows that the exchange-correlation energy is a unique functional of the charge density and that an energy minimisation procedure based on the variation principle can yield a set of self-consistent one electron equations,

$$\{-\nabla^2+V_H[\rho](\bar{r})+V_{ext}(\bar{r})+V_{xc}[\rho](\bar{r})\}\phi_i(\bar{r}) = \varepsilon_i\phi_i(\bar{r}) \qquad \text{Eq. 7.1.}$$

where $V_H[\rho](\bar{r})$ = classical Hartree field for a distribution ρ

$V_{ext}(\bar{r})$ = external lattice potential

and $V_{xc}[\rho](\bar{r})$ = exchange-correlation potential $= \frac{\delta E_{xc}[\rho]}{\delta\rho(\bar{r})}$ Eq. 7.2.

where $E_{xc}[\rho]$ = total exchange-correlation energy

and $\rho(\bar{r}) = \sum_{i,\ \text{occupied}} |\phi_i(\bar{r})|^2$

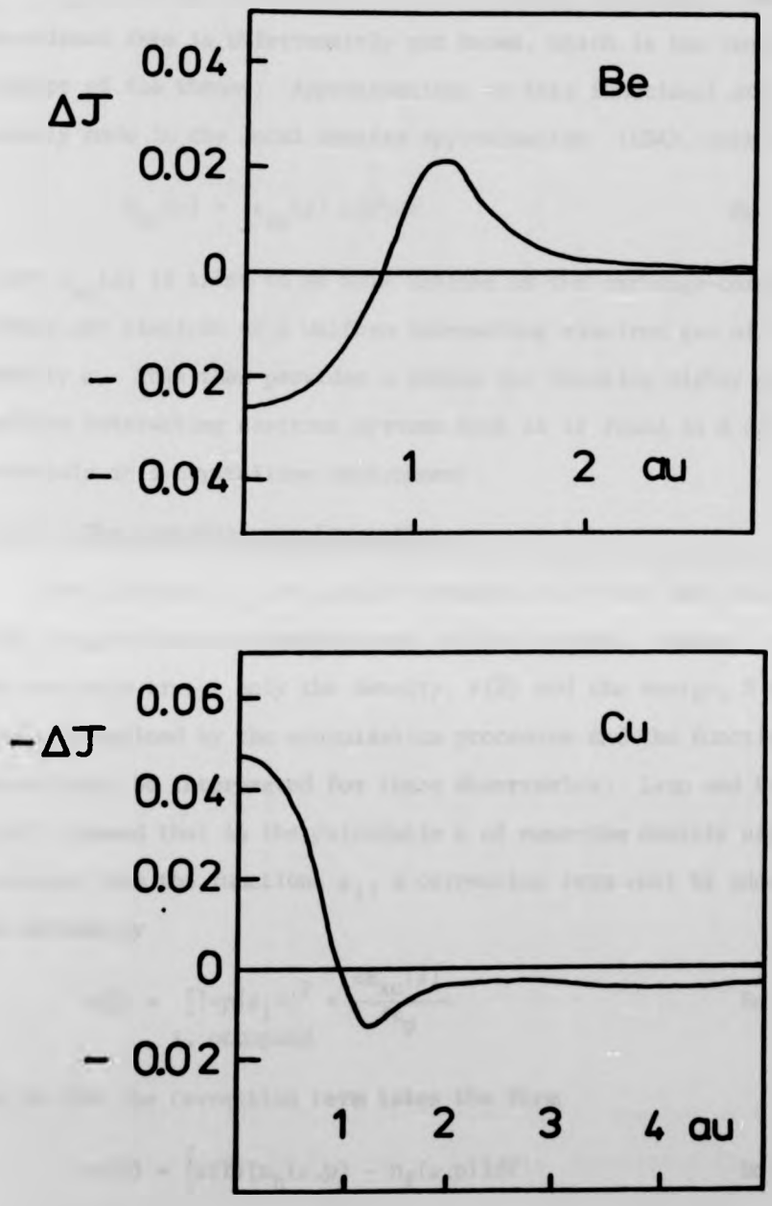

Figure 7.3. The Lam - Platzman Corrections for Beryllium and Copper Convoluted with 0.41 au (After Bauer and Schneider, 1983[8,9])

$E_{xc}[\rho]$ is the exchange-correlation energy functional, whose functional form is unfortunately not known, which is the central concept of the theory. Approximations to this functional are usually made in the local density approximation (LDA), such that

$$E_{xc}[\rho] = \int \epsilon_{xc}(\rho)\ \rho(\bar{r})d\bar{r} \qquad \text{Eq. 7.3.}$$

where $\epsilon_{xc}(\rho)$ is taken to be well defined as the exchange-correlation energy per electron of a uniform interacting electron gas of constant density ρ. This then provides a scheme for treating highly non-uniform interacting electron systems such as is found in d electron materials in a crystalline environment.

7.2.2. The Lam-Platzman Correction

The functions ϕ_i are usually treated as if they were the independent single electron wavefunctions for the system. However, this is not entirely true - only the density, $\rho(\bar{r})$ and the energy, E are formally defined by the minimisation procedure and the functions ϕ_i should only be interpreted for these observables. Lam and Platzman (1973) showed that in the calculatio n of momentum density $n(\bar{p})$, obtained from the functions ϕ_i, a correction term must be added which is defined by

$$n(\bar{p}) = \sum_{i,\ \text{occupied}} |\langle p|\phi_i\rangle|^2 + \frac{\delta E_{xc}[\rho]}{\delta \epsilon_p} \qquad \text{Eq. 7.4.}$$

In the LDA the correction term takes the form

$$\Delta n(p) = \int \rho(\bar{r})[n_h(\rho,p) - n_f(\rho,p)]d\bar{r} \qquad \text{Eq. 7.5.}$$

where $n_h(\rho,p)$ = momentum density of homogeneous interacting electron gas

and $n_f(\rho,p)$ = momentum density of free electron gas.

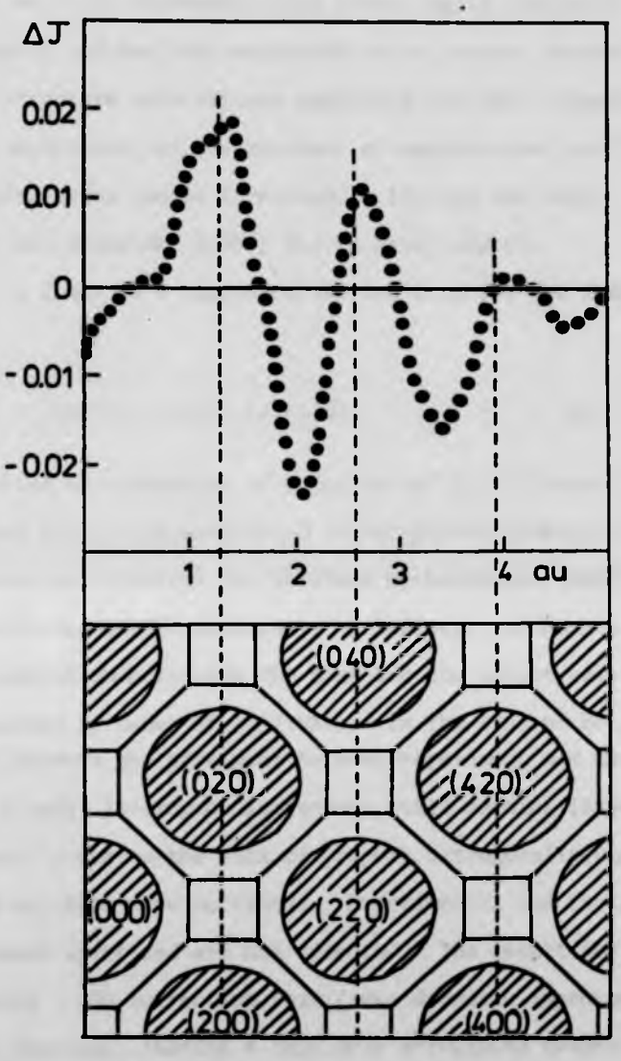

Figure 7.4. Theory - Experiment Difference Curve for Copper (110) after Application of the Lam - Platzman Correction (Theory - LCGO Calculation by Nagayoka et al, 1980 ; Experiment - Bauer and Schneider, 1984). The oscillatory features are clearly related to the passage of the plane of integration through the occupied regions of the Fermi surface shown at the bottom of the figure. (Taken from Bauer and Schneider, op. cit.)

In general, eq. 7.5. represents only a very small correction to the momentum density and has been neglected in all recent density functional band structure calculations employing the LDA. However with the recent improvement of the accuracy of experimental profiles, the correction term is no longer irrelevant. Its use has been revived by Bauer and Schneider (1983) for Be metal and Cu.

Equation 7.5. leads to a simple correction term for the Compton profile, i.e.

$$\Delta J(q) = \int \rho(\bar{r}) [J_h(\rho,q) - J_f(\rho,q)] d\bar{r} \qquad \text{Eq. 7.6.}$$

This term is plotted as a function of q for Be and Cu in figure 7.3. For Be, the values of $J_h(\rho,q)$ were based on occupation numbers of the homogeneous interacting electron gas obtained by Lundqvist (1968) and $\rho(\bar{r})$ was calculated self-consistently by Redinger and Hansen (1984). For Cu, the occupation numbers were the same and the density distribution was calculated by Bauer et al (1984). In the case of Be, the correction term improves the agreement between experiment and theory somewhat though a small isotropic discrepancy still remains (Bauer suggests that this is due to the lack of propert orthogonalisation of valence and core electron wavefunctions). Experimental and theoretical anisotropies already agree and are not affected. The result for Cu is more interesting - the correction term gives dramatic improvement of the isotropic features, leaving a regularly structured theory-experiment difference curve shown in figure 7.4 for the (110) direction (nearest neighbours). The structure corresponds strongly to the occupation of the extended Fermi surface - a section through which is shown in the lower half of the figure. The conclusion in this case is the same as that reached by Pattison et al (1982) using the Seitz model described in §1.5 -namely, that correlation effects in the real metal

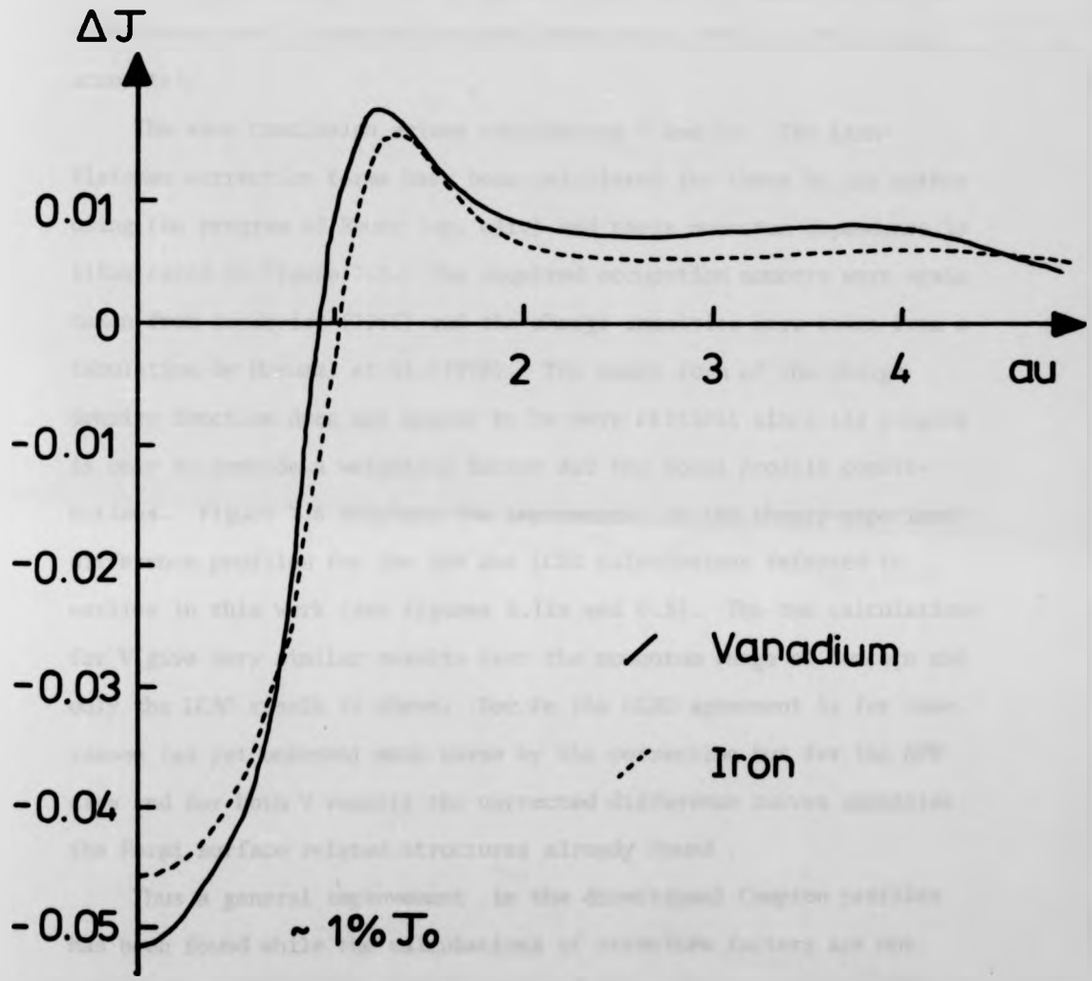

Figure 7.5. The Lan - Flatsman Correction Calculated for Vanadium and Iron with a Smearing of 0.4 au

have reduced the occupancy of the repeated Fermi spheres and populated the region in between. Thus it appears that the LDA employed in this calculation for Cu does not include correlation effects sufficiently accurately.

The same conclusion arises considering V and Fe. The Lam-Platzman correction terms have been calculated for these by the author using the program of Bauer (op. cit.) and their momentum dependence is illustrated in figure 7.5. The required occupation numbers were again taken from Lundqvist (1968) and the charge densities were taken from a tabulation by Moruzzi et al (1978). The exact form of the charge density function does not appear to be very critical since its purpose is only to provide a weighting factor for the local profile contributions. Figure 7.6 displays the improvement in the theory-experiment difference profiles for the APW and LCAO calculations referred to earlier in this work (see figures 5.12a and 6.5). The two calculations for V give very similar results over the momentum range of concern and only the LCAO result is shown. For Fe the LCAO agreement is for some reason (as yet unknown) made worse by the correction but for the APW case and for both V results the corrected difference curves emphasise the Fermi surface related structures already found .

Thus a general improvement in the directional Compton profiles has been found while the calculations of structure factors are not affected at all since the latter depend on ρ which is a well-defined variable in the Density Functional Theory. The source of the remaining anisotropic profile discrepancies is discussed briefly in §7.2.3.

7.2.3. Variation of the Local Potential

It is tempting to attribute the error in the anisotropy or, the same problem, the periodic structure of the theory-experiment difference

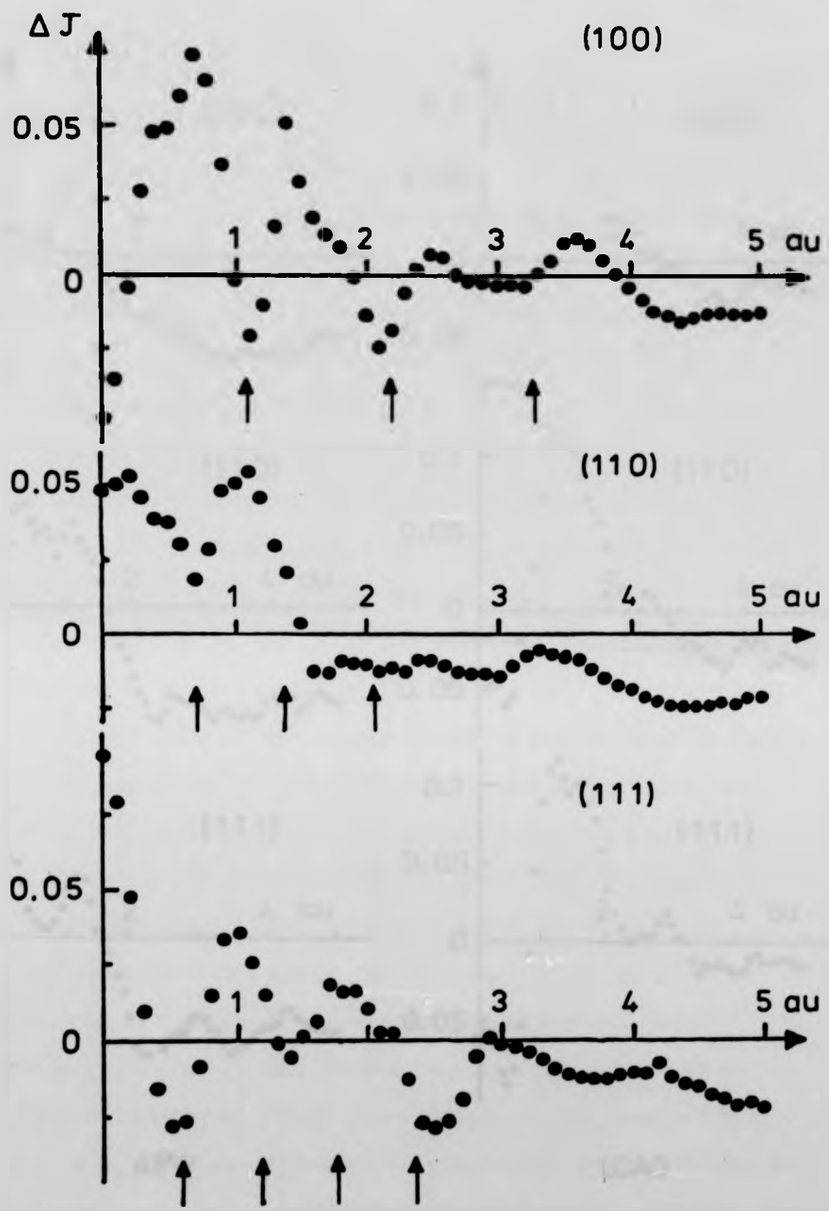

Figure 7.6a Theory - Experiment Difference Profile for Vanadium after Application of Lam - Platzman Correction (Theory - LCAO Calculation by Laurent et al, 1978 : Experiment - Bellasen et al, 1982). The arrows indicate the values of characteristic reciprocal lattice vectors in each orientation.

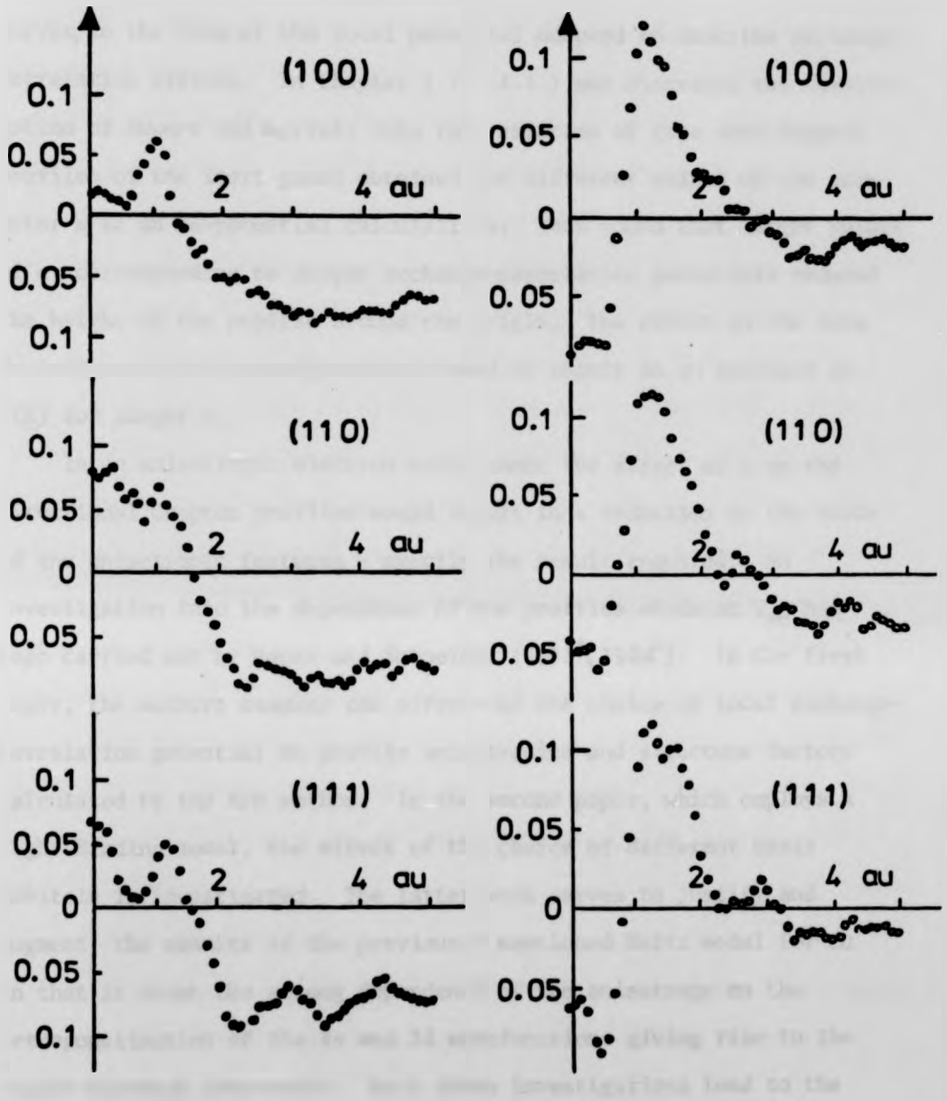

Figure 7.6b Theory - Experiment Difference Profile for Iron after Application of the Lee - Pietzman Correction (Theory - filled circles - APW Calculation by Wakoh and Kubo, 1977 ; open circles - LCAO Calculation by Rath et al, 1973 ; Experiment - Rollason et al, 1983)

curves, to the form of the local potential adopted to describe exchange-correlation effects. In Chapter 1 (§1.4.1.) was discussed the investigation of Euwema and Surratt into the variation of free atom Compton profiles of the inert gases obtained for different values of the parameter α in an Xα-potential calculation. They found that larger values of α, corresponding to deeper exchange-correlation potentials reduced the height of the profile around the origin. The effect on the form factors was also investigated and found to result in an increase of $S(\underline{k})$ for larger α.

In an anisotropic electron environment the effect of α on the directional Compton profiles would result in a reduction in the scale of the anisotropic features - exactly the result required. An investigation into the dependence of the profiles of Cu on V_{xc} has been carried out by Bauer and Schneider (1983[9], 1984[11]). In the first paper, the authors examine the effects of the choice of local exchange-correlation potential on profile anisotropies and structure factors calculated by the APW method. In the second paper, which employs a Tight Binding model, the effect of the choice of different basis orbitals is investigated. The latter work serves to justify and augment the results of the previously mentioned Seitz model for Cu in that it shows the strong dependence of the anisotropy on the orthogonalisation of the 4s and 3d wavefunctions giving rise to the higher momentum components. Both these investigations lead to the clear result that obtaining agreement between experimental and theoretical anisotropies produces unrealistically large values for the form factors. It was therefore concluded that it is not possible to obtain agreement with results in both momentum and position space when using a local approximation to the many electron interaction.

The use of a non-local exchange-correlation potential cannot be

expected to yield any better agreement between the two sets of results. Such a potential could still only alter the energy levels of the d-electron bands in the same manner as a local potential and therefore again cannot produce simultaneous agreement with measured anisotropies and form factors. Some investigations of non-local approximations to the exact exchange correlation energy have nevertheless been performed (see e.g. Bauer, 1983). No dramatic changes in the band structures have been observed at the level of approximation still invoked. However, in such approximations there will be a new form for the correlation correction functional (eq. 7.6. applies only in the LDA) which will automatically contain non-local and thus, hopefully, anisotropic effects. No derivation of such a correction term has yet been produced but it is anticipated that the proper use of such a correction would indeed yield agreement with the experimental anisotropies. The derived potential (eq. 7.2) which governs the structure factors could at the same time remain essentially unaltered maintaining the agreement there. It is greatly to be hoped that theoretical research along such lines will be stimulated by the rapid improvements in present experimental techniques.

7.3. Future Developments

There follows a brief survey of the topics in the field of Compton Scattering likely to receive attention in the immediate future.

7.3.1. Technique

The design of γ-ray Compton spectrometers has advanced significantly since their adoption in the 1970's and, with research into the problems of multiple scattering, geometric resolution and source broadening over the last few years, the design criteria have become much better understood. The result is that spectrometers are now practical which can measure profiles of accuracy $\leq$ 0.1% (for data measured at intervals of 0.1 au. momentum) in two days or less. The low cost of such systems

(due to their simplicity) compared with previous X-ray facilities means that new apparatus can be developed more frequently and new research groups may find γ-ray research more appealing. Certainly the use of high energy γ-rays removes a lot of problems associated with X-rays in Compton Scattering and diffractometry studies. In particular, two new spectrometers are currently being investigated - one a Cs-137 system (660 keV) at the University of Warwick, England - the other a Cr-51 system (320 keV) at the Hahn-Meitner Institut, Berlin. Both these spectrometers have been designed with some degree of variable scattering geometry so that the Compton cross-section at different scattering angles can be examined. Secondly there is a great advantage in having available high energy systems with a range of primary energies since this allows for very rigorous checks on the existing data processing techniques. For example, when only a single sample of one thickness is available, measurement at two energies enables a check on the multiple scattering correction.

Hand-in-hand with the development of these new spectrometers will go the implementation of the data reduction procedures investigated in the present work. It seems very probable that the long standing problem of profile asymmetry will very soon disappear completely and extremely accurate directional profiles will be reportable with complete confidence - a strong incentive for the production of more "realistic" calculations.

Other Compton techniques are also being investigated, such as high energy electron scattering - suitable for very small particles of material (Williams and Thomas 1983), photon-electron coincidence Compton Scattering - where the sample is itself a detector of the ejected electron (MacKenzie, 1981), rotating anode X-ray systems (high intensity and momentum resolution $\sim$ 0.1 au, not achievable with present solid-state detector γ-ray systems) and last but the most glamorous technique,

magnetic scattering experiments using circularly-polarised synchrotron radiation (Cooper and Holt, 1983).

7.3.2. Systems

There is no clear indication of any one particular field where the attention of experimental γ-ray Compton Scattering will be focussed in the near future. Rather, the applications of this technique will expand to a wider range of systems than has heretofore been examined. Measurements of the first transition series pure metals will be reasonably complete when data is obtained for Ni. It is anticipated that some investigations will be carried out on the second transition series elements Nb and Ag (corresponding to their first series counterparts V and Cu). A systematic study throughout the different series should give a revealing picture of d-electron effects as well as giving some indication of the problems associated with measurements of heavier materials. Investigation of f-electron systems can then proceed on a firm base. In particular, the 4f metal Ce has recently generated some interest with regard to its conductivity phase change. Calculations based on models promoting a 4f electron to the conduction band (Podloucky and Glötzel, 1983) have not been borne out by the experiment of Kornstadt et al (1980) and a repetition of this measurement would be highly desirable. The investigation of phase transition systems in general is a possible centre of activity for the future with the abundance of such effects amongst the compounds of the transition series (e.g. the oxides of V). Compounds are now likely to receive a great deal of attention. III-V and II-VI semiconductors have recently been measured at 412 keV (Itoh, 1984) and the Al alloys of Co, Ni and Cu are soon to be examined with a 320 keV or 412 keV system for comparison with the results for the charge transfer obtained at lower energy by Manninen et al (1981).

In conclusion it can only be stated that the whole field of Compton scattering research appears poised to rapidly expand into all corners of the field of electronic solid state physics.

References

1. Aikala,O., Paakari,T. & Manninen,S. (1982) Acta Cryst. A, 38, 155

2. Bagayoko,D., Laurent,D.G., Singhal,S.P. & Callaway,J. (1980) Phys. Lett. A, 76, 187

3. Barkla,C.G. & White,M. (1917) Phil. Mag. 34, 270

4. Barlas,A.D., Rueckner,W. & Wellenstein,H.F. (1977) Phil.Mag. 36, 201

5. Batterman,B.W., Chipman,D.R. & DeMarco,J.J. (1961) Phys.Rev. 122, 68

6. Bauer,G.E.W. (1983) Phys.Rev. B, 27, 10, 5912

7. Bauer,G.E.W., Felsteiner,J. & Schneider,J.R. (1984) unpublished

8. Bauer,G.E.W. & Schneider,J.R. (1983) S.S.Com. 47, 9, 673

9. Bauer,G.E.W. & Schneider,J.R. (1983) Z.Phys. B, 54, 17

10. Bauer,G.E.W. & Schneider,J.R. (1984) to be published

11. Bauer,G.E.W. & Schneider,J.R. (1984) J.Phys.Chem.Sol.(to be published)

12. Bauer,G.E.W., Schneider,J.R. & Welter,J.M. (1983) Phys.Lett. A, 100, 4, 207

13. Benesch,R. & Smith,V.H.jr. (1973) "Wave Mechanics - The First Fifty Years", ed. Price, Chissick & Ravensdale, Butterworths, London

14. Berggren,K.-F. (1972) Phys.Rev.B, 6, 6, 2156

15. Biggs,F., Mendelsohn,L.B. & Mann,J.B. (1975) Atomic & Nuclear Data Nuclear Data Tables, 16, 202

16. Bloch,B.J. & Mendelsohn,L.B. (1974) Phys.Rev. A, 9, 129

17. Borland,R.E. & Cooper,J.R.A. (1970) J.Phys. C, 3, Suppl. 253

18. Bragg,W.H. (1907) Phil.Mag. 14, 429

19. Callaway,J. & March,N.H. (1984) S.S.Phys. (to be published)

20. Clementi,E. (1965) IBM J.Research & Development, Suppl. 9, 2

21. Compton,A.H. (1923) Phys.Rev. 21, 207 & 483

22. Cooper,M.J., Pattison,P., Williams,B.G. & Pandey,K.C. (1974) Phil.Mag. 29, 167

23. Cooper,M.J. & Williams,B.G. (1972) Phil.Mag. 25, 6, 1499

24. Cooper,M.J., Williams,B.G., Borland,R.E. & Cooper,J.R.A. (1970) Phil.Mag. 22, 441

25. Coulson,C.A. & Duncanson,W.E. (1941)

Coulson,C.A. (1941)	Proc.Camb.Phil.Soc. 37, 55
Coulson,C.A. & Duncanson,W.E. (1941)	Proc.Camb.Phil.Soc. 37, 67
Coulson,C.A. (1941)	Proc.Camb.Phil.Soc. 37, 74
Duncanson,W.E. (1941)	Proc.Camb.Phil.Soc. 37, 397
Duncanson,W.E. & Coulson,C.A. (1941)	Proc.Camb.Phil.Soc. 37, 406
Coulson,C.A. & Duncanson,W.E. (1942)	Proc.Camb.Phil.Soc. 38, 100

26. Curratt,R., DeCicco,P.D. & Kaplow,R. (1971) Phys.Rev. B, 3, 243

27. Curratt,R., DeCicco,P.D. & Weiss,R.J. (1971) Phys.Rev. B, 4, 4256

28. Dauwe,Ch., Dorikens-Vanpraet,L. & Dorikens,M. (1972) S.S.Com. 11, 5, 717

29. DeCicco,P.D. & Kitz,A. (1967) Phys.Rev. 162, 2, 486

30. DeMarco,J.J. & Weiss,R.J. (1965) Phys.Lett. 18, 2, 92

31. Diana,M. & Mazzone,G. (1974) Phys.Rev. B, 9, 9, 3898

32. Diana,M. & Mazzone,G. (1975) Phil.Mag. 32, 1227

33. DuBard,J.L. (1979) J.Phys. E, 12, 302

34. Duff,K.J. & Das,T.P. (1971) Phys.Rev. B, 3, 7, 2294

35. DuMond,J.W.M. (1929) Phys.Rev. 33, 643

36. DuMond,J.W.M. (1930) Phys.Rev. 36, 1685

37. DuMond,J.W.M. & Kirkpatrick,H.A. (1937) Phys.Rev. 52, 419

38. Eisenberger,P., Lam,L., Platzman,P.M. & Schmidt,P.H. (1972) Phys.Rev. B, 6, 3671

39. Eisenberger,P. & Reed,W.A. (1972) Phys.Rev. A, 5, 2085

40. Eisenberger,P., Henneker,W.H. & Cade,P.E. (1972) J.Chem.Phys. 56, 1207

41. Eisenberger,P. & Platzman,P.M. (1970) Phys.Rev. B, 2, 415

42. Eisenberger,P. & Reed,W.A. (1974) Phys.Rev. B, 9, 3237

43. Epstein,I.R. (1973) Phys.Rev. A, 8, 160

44. Epstein,I.R. & Lipscomb,W.N. (1970) J.Chem.Phys. 53, 4418

45. Euwema,R.N. & Surratt,G.T. (1974) J.Phys. C, 7, 3655

46. Eve,A.S. (1904) Phil.Mag. 8, 669

47. Feinberg,M.J. & Ruedenberg,K. (1971) J.Chem.Phys. 54, 4, 1495

48. Felsteiner,J. & Pattison,P. (1975) Nucl.Instr. & Methods, 124, 449

49. Felsteiner,J. & Pattison,P. (1980) Nucl.Instr. & Methods, 173, 323

50. Felsteiner,J., Pattison,P. & Cooper,M.J. (1974) Phil.Mag. 30, 537

51. Fermi,E. (1928) Z.Physik, 48, 73

52. Finkelstein,B.N. & Horowitz,G.E. (1928) Z.Physik, 48, 118

53. Florance,D.C.H. (1910) Phil.Mag. 20, 921

54. Fock,V. (1935) Z.Physik, 98, 145

55. Friedel,J. (1958) Nuovo Cimento, 7 (Suppl), 287

56. Geldhart,D.J.W., Houghton,A. & Vosko,S.H. (1964) Can.J.Phys. 42,1938

57. Gold,A.V., Hodges,L., Panouris,P.T. & Stone,D.R. (1971) Int.J.Mag. 2 1, 357

58. Gray,J.A. (1913) Phil.Mag. 26, 611

59. Grossman,H. & Mendelsohn,L.B. (1975) Bull.Am.Phys.Soc. II, 20, 680

60. Gupta,M. & Ellis,D.E. (1976) Phys.Rev. 13, 8, 3405

61. Hansen,N.K., Pattison,P. & Schneider,J.R. (1979) Z.Physik B, 35, 215

62. Heisenberg,W. & Bewilogua,L. (1931) Z.Physik 32, 737

63. Hicks,B. (1937) Phys.Rev. 52, 436

64. Hohenberg,P. & Kohn,W. (1964) Phys.Rev. B, 136, 3, 864

65. Holt,R.S. (1978) PhD Thesis, University of Warwick, England

66. Holt,R.S. & Cooper,M.J. (1983) Nucl.Intsr.Methods Phys.Res. 213, 2-3, 447

67. Holt,R.S., Cooper,M.J., DuBard,J.L., Forsyth,J.B., Jones, T.L. & Knights,K. (1979) J.Phys. E, 12, 1148

68. Holt,R.S., DuBard,J.L., Cooper,M.J., Paakari,T. & Manninen,S. (1979) Phil.Mag. B, 39, 6, 541

69. Hubbard,J. & Mijnarends,P.E. (1972) J.Phys.C, 5, 2323

70. Hubbell,J.H., Veigele,W.J., Biggs,E.A., Brown,R.T., Cramer,D.T. & Howerton,R.J. (1975) J.Phys. & Chem.Ref.Data 4, 3, 471

71. Hughes,A.L. & Mann,M.M.J. (1938) Phys.Rev. 53, 50

72. Hulubei,H. (1934) Ann.Phys.(Paris) 1, 1

73. Itoh,F. (1984) private communication

74. Itoh,F., Honda,T., Asano,H., Hirabayashi,M. & Suzuki,K. (1980) J.Phys.Soc.Japan 49, 202

75. James,R.W. (1948) "The Optical Principles of the Diffraction of X - Rays - Vol.II", Cornell University Press, Ithaca, NY

76. Jauch,J.M. & Rohrlich,F. (1955) "Theory of Photons and Electrons ", Addison-Wesley, Cambridge, Massachusetts

77. Jauncey,G.E.M. (1924) Phys.Rev. 24, 204

78. Jepsen,O., Glötzel,D. & Mackintosh,A.R. (1981) Phys.Rev. B, 23, 2684

79. Klein,O. & Nishina,Y. (1929) Z.Physik, 52, 853

80. Kohn,W. & Sham,L.J. (1965) Phys.Rev. A, 140, 4, 1133

81. Kornstadt,U., Lässer,R. & Lengeler,B. (1980) Phys.Rev. B, 21, 5,1898

82. Kramer,B., Krusius,P., Schröder,W. & Schülke,W. (1977) Phys.Rev.Lett 38, 1227

83. Kretschmar,H.R. & Schneider,J.R. (1984) S.S.Comm. 49, 10, 971

84. Krishna-Gandhi,K.R. & Singru,R.M. (1982) Appl.Phys. A, 28, 119

85. Krusius,P. (1977) J.Phys. C, 10, 1875

86. Lam,L. & Platzman,P. (1973) Phys.Rev. B, 9, 12, 5122

87. Lässer,R. & Lengeler,B. (1978) Phys.Rev. B, 18, 687

88. Lässer,R., Singru,R.M. & Lengeler,B. (1978) S.S.Comm. 25, 345

89. Laurent,D.G.,Wang,C.S. & Callaway,J. (1978) Phys.Rev. B, 17, 455

90. Lederer,C.M., Hollander,J.M. & Perlman,I. (1967) "Table of Isotopes" Wiley

91. Lock,D.G., Crisp,V.H.C. & West,R.N. (1973) J.Phys. F, 3, 561

92. Lundqvist,B.I. (1968) Phys.Kondens.Mater. 7, 117

93. Lundqvist,B.I. (1971) Phys.Rev. B, 4, 10, 3360

94. Mackenzie,I.K. (1981) "Lecture Notes - Varenna, Italy": Enrico-Fermi International School of Physics

95. Manninen,S. (1974) Phil.Mag. 29, 167

96. Manninen,S., Sharna,B.K., Paakari,T., Lundqvist,S. & Richards,M.W. (1981) Phys.Stat.Sol.(b) 107, 749

97. March,N.H. (1957) Adv. in Physics, 6

98. Mendelsohn,L.B. (1978) private communication to M.J.Cooper

99. Mendelsohn,L.B. & Bloch,B.J. (1975) Phys.Rev. A, 12, 551

100. Mendelsohn,L.B., Bloch,B.J. & Smith,V.H.jr. (1973) Phys.Rev.Lett. 31 266

101. Mendelsohn,L.B. & Biggs,F. (1973) US Atomic Energy Conf. 720404, 3, 1142

102. Mendelsohn,L.B. & Grossman,H. (1977) AIP Conf.Proc. No.36, 249

103. Moruzzi,V.L., Janak,J.F. & Williams,A.R. (1978) "Calculated Electronic Properties of Metals", Pergamon Press Inc., NY

104. McCarthy,I.E. (1973) J.Phys. B, 6, 2358

105. McWeeny,R. & Coulson,C.A. (1949) Proc.Phys.Soc.London A, 62, 509

106. Nelms,A.T. (1953) NBS Circular, 542

107. Ohba,S., Sato,S. & Saito,V. (1981) Acta Cryst. A, 37, 697

108. Paakari,T., Berggren,K.-F., Ribberfors,R. & Halonen,V. (1976) Phys. Rev. B, 14, 2301

109. Paakari,T., Halonen,V. & Aikala,O. (1976) Phys.Rev. B, 13, 4602

110. Paakari,T. & Manninen,S. (1973) Phys.Rev. B, 8, 8, 3765

111. Paakari,T., Manninen,S. & Berggren,K.-F. (1975) Phys.Fenn. 10, 207

112. Paakari,T., Suortti,P., Halonen,V. & Manninen,S. (1973) Phys.Fenn. 8, 93

113. Pandey,K.C. & Lam,L. (1973) Phys.Lett. A, 43, 319

114. Pattison,P., Cooper,M.J., Holt,R.S., Schneider,J.R. & Stump,N. (1977) Z.Physik B, 27, 205

115. Pattison,P., Cooper,M.J. & Schneider,J.R. (1976) Z.Physik B, 25, 155

116. Pattison,P., Hansen,N.K. & Schneider,J.R. (1982) Z.Physik B, 46, 285

117. Pattison,P. & Schneider,J.R. (1979) Nucl.Instr. & Methods, 158, 145

118. Pattison,P. & Weyrich,W. (1979) J.Phys.Chem.Sol. 40, 213

119. Phillips,R.A. (1971) Phys.Lett. A, 36, 361

120. Phillips,W.C. (1973) Phys.Rev. B, 7, 1047

121. Phillips,W.C. & Weiss,R.J. (1968) Phys.Rev. 171, 790

122. Phillips,W.C. & Weiss,R.J. (1969) Phys.Rev. 182, 923

123. Phillips,W.C. & Weiss,R.J. (1972) Phys.Rev. B, 6, 11, 4213

124. Platzman,P.M. (1972) Comments on S.S.Physics, 4, 3, 85

125. Platzman,P.M. & Tzoar,N. (1965) Phys.Rev. A, 139, 410

126. Podloucky,R. & Glötzel,D. (1983) Phys.Rev. B, 27, 6, 3390

127. Podloucky,R. & Redinger,J. (1983) J.Phys. C, 16, 36, 6955

128. Rath,J., Wang,C.S., Tawil,R.A. & Callaway,J. (1973) Phys.Rev. B, 8, 11, 5139

129. Redinger,J. & Hansen,N.K. (1984) to be published

130. Reed,W.A. (1976) Acta Cryst. A, 32, 4, 676

131. Reed,W.A. & Eisenberger,P. (1972) Phys.Rev. B, 6, 4596

132. Ribberfors,R. (1975) Phys.Rev. B, 12, 2067

133. Ribberfors,R. & Berggren,K.-F. (1982) Phys.Rev. A, 26, 6, 3325

134. Rollason,A.J., Cooper,M.J., Holt,R.S., Bailey,I. & Jones,T.J.L. (1981) Phil.Mag. B, 43, 931

135. Rollason,A.J., Holt,R.S. & Cooper,M.J. (1982) Phil.Mag. B, 47, 1, 51

136. Rollason,A.J., Holt,R.S. & Cooper,M.J. (1983) J.Phys. F, 13, 1807

137. Röntgen,W.C. (1895) "The World of the Atom", 1, 396, ed. Boorse & Motz, NY, 1966

138. Sakai,N. & Ono,K. (1977) J.Phys.Soc.Japan, 42, 3, 770

139. Schiff,L. (1949) "Quantum Mechanics", McGraw-Hill, NY

140. Schlüter,M. & Sham,L.J. (1982) Phys.Today, February

141. Schneider,J.R., Hansen,N.K. & Kretschmar,H. (1981) Acta Cryst. A, 37 711

142. Schneider,J.R., Bauer,G.E.W., Hansen,N.K. & Kretschmar,H. (1982) Symposium Proc., "LDA in Quantum Chem. & S.S.Theory", Kopenhagen

143. Schülke,W. (1978) Jap.J. of Appl.Phys. 17, Suppl.17-2, 332

144. Seitz,F. (1935) Phys.Rev. 47, 400

145. Shiotani,N., Okada,T., Mizoguchi,T. & Sekizawa,H. (1975) J.Phys.Soc. Japan, 38, 2, 423

146. Slater,J.C. (1930) Phys.Rev. 36, 57

147. Slater,J.C. (1951) Phys.Rev. 81, 385

148. Snyder,L.C. & Weber,T.A. (1978) J.Chem.Phys. 68, 6, 2974

149. Tawil,R.A. & Callaway,J. (1973) Phys.Rev. B, 7, 9, 4242
8, 11, 5139

150. Terasaki,O., Fukamichi,T., Hosoya,S. & Watanabe,D. (1973) Phys.Lett. A, 43, 123

151. Thomas,L.H. (1927) Proc.Camb.Phil.Soc. 23, 542

152. Villard,P. (1900) "The World of the Atom", 1, 466, ed. Boorse & Motz NY, 1966

153. Wakoh,S. & Kubo,Y. (1977) J.Mag. & Mag.Mat. 5, 202

154. Wakoh,S. & Kubo,Y. (1984) to be published

155. Wakoh,S., Kubo,Y. & Yamashita,J. (1975) J.Phys.Soc.Japan, 18, 2, 416

156. Wakoh,S., Kubo,Y. & Yamashita,J. (1976) J.Phys.Soc.Japan, 40, 1043

157. Wakoh,S. & Yamashita,J. (1966) J.Phys.Soc.Japan, 21, 1712

158. Wakoh,S. & Yamashita,J. (1971) J.Phys.Soc.Japan, 30, 422

159. Wakoh,S. & Yamashita,J. (1973) J.Phys.Soc.Japan, 35, 1394

160. Wakoh,S. & Yamashita,J. (1973) J.Phys.Soc.Japan, 35, 1406

161. Weiss,R.J. (1966) Phil.Mag. 14, 403

162. Weiss,R.J. (1966) "X-Ray Determination of Electron Distributions", Amsterdam: North-Holland

163. Weiss,R.J. (1975) Phil.Mag. 32, 247

164. Weiss,R.J. (1978) Phil.Mag. B, 37, 645

165. Weiss,R.J., Cooper,M.J. & Holt,R.S. (1977) Phil.Mag. 36, 1, 193

166. Weiss,R.J. & DeMarco,J.J. (1965) Phys.Rev. A, 140, 1223

167. Weiss,R.J. & Mazzone,G. (1981) J.Appl.Cryst. 14, 401

168. Weiss.R.J. & Phillips,W.C. (1969) Tech.Note AMMRCTN, 69-02

169. West,R.N. (1973) Adv.Phys. 22, 263

170. Williams,B.G. (ed.) (1977) "Compton Scattering", McGraw-Hill, NY

171. Williams,B.G. & Halonen,V. (1975) Phys.Fenn. 10, 5

172. Williams,B.G. & Thomas,J.M. (1983) Int.Revs.Phys.Chem. 3, 39

173. Wood,J.H. (1962) Phys.Rev. 126, 2, 517

II